Characterization of Electroless Ni-P Coatings and Electrodeposition of Ni Coatings for Electrodes in Zinc-Air Flow Batteries

by

Hang Hu

A thesis submitted in partial fulfillment of the requirements for the degree of

Master of Science

in

Materials Engineering

Department of Chemical and Materials Engineering

University of Alberta

Abstract

Electrochemical energy storage devices such as Li-ion or Zn-air batteries (ZABs) are utilized to store energy generated by renewable sources, since these sources are intermittent. Li-ion batteries uses flammable organic electrolytes (less safe than nonflammable aqueous electrolytes) and have high material costs. ZABs, by comparison, have lower costs, higher safety, lower environmental impact, and higher theoretical energy density than Li-ion batteries. In practice, dendrite formation and passivation on the metallic Zn electrode are major obstacles towards widespread commercialization of ZABs. Circulating the electrolyte has been shown to alleviate these issues; Zn-air flow batteries (ZAFBs), therefore, have better electrochemical performance than ZABs. ZAFBs may be designed to use two sets of electrodes, one set each for the discharge and charge reactions. ZAFBs use "fuel", a slurry of KOH and Zn particles, that is stored in a "fuel" tank when the battery is not discharging or charging. This design allows energy and power to be decoupled. The ZAFB manufactured by Zinc8 Energy Solutions (shortened to Zinc8) uses a similar design. The regenerator of the ZAFB contains an oxygen evolution electrode for which Ni can be used; electroless Ni-P plating on Mg can be used to fabricate such an electrode.

The first study in this work involved using various materials characterization techniques to identify the composition and microstructure of various Ni-P coatings considered for use by Zinc8. The porosity of these Ni-P coatings was quantified using two methods, a dimple polishing coupled with optical microscopy technique developed in this study and cross sectional observations using scanning electron microscopy (SEM). Porosity quantified from the first technique is referred as macroscopic porosity, while porosity quantified from the second technique is referred as microscopic porosity.

The second study involved electrochemical testing of several coatings. Both immersion testing and cycle testing under OER and hydrogen evolution reaction (HER) conditions. The open circuit voltage (OCV), corrosion potential (E_{corr}), and corrosion current density (i_{corr}) were determined. Corrosion rates (CR) were estimated from i_{corr} values. CR values were correlated with microstructural changes (e.g., surface morphology and coating thickness), inherent porosity, and changes in electrolyte composition. High coating porosity generally correlated with high corrosion rates, although with no direct correlation between CR and observed Ni loss for many cases.

The third study focused on developing a low porosity Ni coating from a modified Watts bath. A design of experiments (DoE) approach was taken and Au-coated Si wafers were used as the substrates. Thick (40 μm) coatings were deposited over a fairly short plating time. This process will be adapted for Mg substrates and coating composition will be modified through alloying.

Preface

This thesis is the result of a partnership between the Ivey group and Zinc8 Energy Solutions Inc. (shortened to Zinc8). The goals of the partnership are microstructural characterization, porosity quantification, and electrochemical testing of electroless Ni-P coatings considered for use by Zinc8, and the development of an improved coating. The development of the improved coating is ongoing. The research presented in Chapters 3, 4, and 5 along with their supporting information is my original work. Dr. Douglas G. Ivey (my supervisor) aided in manuscript preparation and conceptual development across all chapters of my thesis.

Chapter 3 was conducted in collaboration with Dr. Ivey and Dr. Anqiang He. Dr. Ivey and Dr. He performed SEM, EDX, XRD, TEM, and HIM analyses on a standard Ni-P coating. Microscopic porosity characterization was conducted by Dr. He. Macroscopic porosity characterization was performed by me. The second coating #3 cross section sample was prepared and imaged by me.

Chapter 4 was conducted in collaboration with Dr. He, who performed SEM/EDX analysis on the cross sections of the electrochemical samples. The electrochemical tests were conducted by me. AAS and ICP-OES measurements of the electrolytes were obtained by Mr. Shiraz Merali and Zinc8, respectively. The beaker lid with openings for electrodes was developed in collaboration with Mr. Mark Cui and Dr. He.

Chapter 5 was conducted in collaboration with Dr. He. Dr. He performed preliminary testing that identified Au-coated Si wafers as a suitable substrate for Ni electroplating analogous to Mg substrates. The deposition and analysis of the coatings were performed by me.

Dedication

I dedicate this thesis to my friends and family who have shaped me into the person I am and pushed me to continue becoming a better man.

Acknowledgements

I would like to thank my supervisor, Dr. Douglas G. Ivey, for his support and guidance throughout my Master's degree. His dedication to his students, deep knowledge of materials science and engineering, and formidable work ethic have continuously inspired me.

I would like to thank the members of the Ivey research group for their guidance, support, and friendship. I would especially like to thank Dr. Anqiang He, Dr. Zahra Abedi, Mr. Matthew Labbe, Mr. Jiayao (Mark) Cui, and Mr. Qingping (Ken) Hou. Their assistance and advice were integral on overcoming many difficulties during experimental work and thesis writing.

I would like to thank Shiraz Merali (AAS), Dr. Anqiang He (sample characterization, training, preliminary experimentation), and Zinc8 Energy Solutions Inc. (ICP-OES) for their technical support and training.

I would like to thank my family and my friends for their support during my educational journey. Without their support, this degree would have been significantly more difficult to complete.

I am grateful to the Natural Sciences and Engineering Research Council of Canada, the Faculty of Graduate Studies and Research, the Graduate Student's Association, Future Energy Systems, and Zinc8 Energy Solutions Inc. for financially sponsoring my degree.

Table of Contents

List of Tables

List of Figures

1 Introduction

As the world shifts ever closer towards renewable, environmentally friendly energy sources to limit the extent of anthropogenic climate change caused by fossil fuels, greater and greater focus and efforts have been dedicated towards renewable energy research. A significant issue regarding these renewable energy sources is their intermittency. Renewable peak energy production time often does not match peak energy usage time. Another issue is that renewable energy is often dependent on the weather. Low amounts of sunshine or weak winds mean lower energy production from solar panels or wind turbines, respectively. Large-scale energy storage systems are, therefore, necessary to store energy when it is produced and release it when it is needed [1]–[3]. Pumped hydroelectric storage and compressed air energy storage have been commercially deployed and can already reach GW levels of energy storage with low life-cycle capital costs of $USD 50-200/kWh and storage efficiencies of 65-89% [2]. Special geographical considerations are required for these storage methods, however. Pumped hydroelectric storage requires water to be stored at a higher location so that when released, the flowing water is used to spin water turbines and generate electricity. Compressed air energy storage requires a large container/cavity to store the compressed air, so underground rock caverns, salt caverns, or porous media reservoirs made from materials such as sandstone or fissure lime are used. The compressed air is expanded through high pressure turbines to generate electricity. The former method requires a location with high elevation and the latter method requires large underground caverns. Such geographical considerations restrict the usage of these two energy storage systems. Electrochemical energy storage, by comparison, can be located anywhere and can be flexibly designed to accommodate kWh to MWh applications. Li-ion batteries (LIBs) have been widely commercialized and have long cycle lives exceeding 1,000

cycles, low self-discharge rates, high efficiency, and high specific energy density. LIBs are unsuitable for large-scale stationary energy storage, however, as their costs exceed $USD 1,000/kWh. For a storage system to be commercially viable, its cost must remain below $USD 200/kWh [2]. The fire hazard associated with the organic electrolyte used in LIBs is also a disadvantage [1], [2]. Metal-air batteries such as zinc-air batteries (ZABs), on the other hand, are low cost and Zn is both abundant and more environmentally compatible than Li [2]. The theoretical energy density of ZABs also far exceeds that of LIBs: 1,350 Wh/kg vs. 200 Wh/kg [3]. The electrolyte used for ZABs is also nonflammable. These factors have allowed ZABs to become the only commercialized metal-air battery [1]. Significant challenges exist for ZABs, as the metallic Zn electrode may passivate and form dendrites. The first challenge reduces the contact area between Zn and the electrolyte and the second challenge may result in short circuits. These issues can be resolved by circulating the electrolyte, like in flow batteries, which greatly reduces localized concentration gradients that lead to passivation or dendrite growth. Zn-air flow batteries (ZAFBs), therefore, capture the benefits of ZABs while minimizing their weaknesses. This results in lower costs; as an example, a 72 h ZAFB costs only $USD 60/kWh [4]. A schematic of a ZAFB is shown in Figure 1-1. During discharge, the "fuel" (a slurry of KOH and Zn particles) is pumped to the cell stack where the reactions shown in Equation 1-1 to Equation 1-3 occur at the anode and Equation 1-4 occurs at the cathode. The overall reaction during discharge is shown in Equation 1-5. After discharge, the spent "fuel" (now a slurry of KOH and ZnO and/or $Zn(OH)_4^{2-}$) is pumped back to the fuel tank. During recharge, the spent "fuel" is pumped to the regenerator, where the reverse of the reactions shown in Equation 1-1 to Equation 1-3 occur on the cathode and the reverse of Equation 1-4 occurs on the anode. The overall reaction in the regenerator is the reverse of Equation 1-5. The regenerated "fuel" is then pumped back to the "fuel" tank and the ZAFB is

ready for use again. Such a design allows energy and power to be decoupled. High energy simply means a larger "fuel" tank and high power means a larger cell stack. A single modular ZAFB design can therefore be used for many different applications [5].

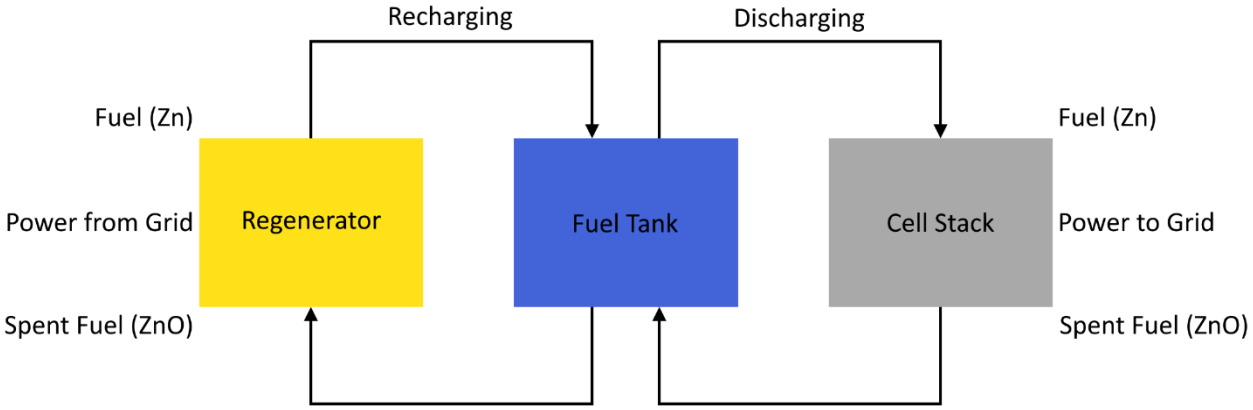

Figure 1-1: Schematic of ZAFB [5]

$$Zn \longrightarrow Zn^{2+} + 2e^{-} \qquad \text{Equation 1-1}$$

$$Zn^{2+} + 4OH^{-} \longrightarrow Zn(OH)_4^{2-} \qquad \text{Equation 1-2}$$

$$Zn(OH)_4^{2-} \longrightarrow ZnO + H_2O + 2OH^{-} \qquad \text{Equation 1-3}$$

$$O_2 + 2H_2O + 4e^{-} \longrightarrow 4OH^{-} \qquad \text{Equation 1-4}$$

$$2Zn + O_2 \longrightarrow 2ZnO \qquad \text{Equation 1-5}$$

This Master of Science degree is the result of a partnership between Zinc8 Energy Solutions Inc. (shortened to Zinc8) and the Ivey research group at the University of Alberta. Zinc8 is interested in developing new OER electrodes for the regenerator of their ZAFBs. Such electrodes may be fabricated by depositing an electroless Ni-P coating on Mg. Mg is lightweight and easy to machine but is highly reactive and, therefore, has poor corrosion resistance [6]–[10]. Ni is catalytic towards the oxygen evolution reaction (OER), which is the reverse reaction of Equation 1-4, but is difficult to machine and expensive [11], [12]. An electroless Ni-P coating deposited on Mg would, therefore,

result in a lightweight, relatively easy to fabricate electrode capable of catalyzing OER. The service lifetime of these coatings is, however, limited due to delamination. As such, the objectives of the partnership include characterization of various electroless Ni-P coatings deposited on Mg to understand the reasons behind coating delamination, with the ultimate goal of developing a coating less susceptible to delamination with improved OER catalytic activity. The characterization work has been completed, but the development of the improved coating is ongoing. This thesis has six chapters, with the current chapter (Chapter 1) serving as an introduction. Chapter 2 is a literature review of electroless Ni plating on Mg and its alloys, alternatives to electroless Ni coatings, the OER and hydrogen evolution reaction (HER) catalytic abilities of electroless Ni coatings, and possible failure mechanisms for electroless Ni coatings deposited on Mg. Chapter 3 discusses the microstructural and porosity characterization performed on the electroless Ni-P coatings supplied by Zinc8. The microstructure and composition of a standard Ni-P coating were analyzed in detail. The porosity of the Ni-P coatings was quantified using macroscopic porosity and microscopic porosity analyses. Macroscopic porosity analysis utilized dimple polishing coupled with optical microscopy. Microscopic porosity analysis used scanning electron microscopy (SEM) observations of the polished cross sections. Chapter 4 examines electrochemical testing of the electroless Ni-P coatings and correlates the results with the microstructural characterization from Chapter 3. Two test regimes, immersion testing (49 days) and cycle testing (2,000 cycles) were used. Open circuit voltage and potentiodynamic polarization (PDP) measurements were taken. The corrosion potential (E_{corr}) and corrosion current density (i_{corr}) were calculated from the PDP measurements, from which corrosion rates were determined and then compared with the porosity analysis in Chapter 3. Chapter 5 is an investigation into the development of an improved coating guided by a Design of Experiments approach. Ni electrodeposition from a modified Watts Ni bath

was utilized. Empirical models for various deposition metrics were developed and an optimal plating condition was identified. A 40μm coating was deposited from this plating condition and its microscopic porosity was determined. Chapter 6 discusses the conclusions, future work suggestions, and recommendations for the improved coating developed in Chapter 5.

2 Literature Review

2.1 Introduction

Magnesium and its alloys possess many qualities that are useful for engineering applications, such as abundance, low density, high strength-to-weight ratio, high thermal conductivity, good machinability, ease of recycling, high damping, high specific strength, and good vibration absorption. Magnesium is, however, limited by its high chemical reactivity and poor wear and corrosion resistance. Consequently, many surface treatment techniques have been investigated and employed to overcome these limitations. Electroless nickel deposition on magnesium is particularly attractive because of nickel's excellent corrosion and wear resistance, high hardness, and application simplicity [6]–[9], [13]–[30]. Additionally, nickel is catalytic to the oxygen evolution reaction (OER), which is necessary for secondary metal-air batteries, metal-air fuel cells, and metal-air flow batteries [12], [31]. As a result, using electroless Ni plating on Mg to form coated electrodes can leverage the advantages of both Mg and Ni while reducing overall cost. Consequently, this review discusses the pretreatment and application processes for electroless Ni coatings on Mg and its alloys, including coating types, the physical, electrochemical, and corrosion requirements of the coatings and breakdown mechanisms. In addition, the effectiveness of the coatings in catalyzing OER and the hydrogen evolution reaction (HER) is discussed [9], [28], [29], [31]–[35].

2.2 Pretreatments

Since the electroless nickel coating is less reactive than the substrate (magnesium or magnesium alloy), the coating acts only as a barrier against corrosion. Therefore, the coating must be as pore

and defect-free as possible and adherent to protect the substrate, making pretreatment prior to electroless deposition crucial [7], [8], [14]–[17], [22], [23], [25], [26], [28], [32], [36]–[40]. The general process for doing so is described below. The substrate is typically rinsed with distilled or deionized water between each step; this is performed rapidly to minimize oxidation [27], [28].

2.2.1 Mechanical Cleaning

Mechanical cleaning of the substrate in the form of grinding/abrading/polishing is performed to remove oxides and hydroxide layers, dirt, and other unwanted deposits from the surface to be coated [7]–[9], [14]–[16], [18], [20]–[25], [28], [29], [33], [34], [37], [38], [41], [42]. Typically, SiC emery paper or sandpaper with grit sizes ranging from 1000 to 5000, or sandblasting, or Al_2O_3 with mesh sizes of 60 to 400 or are used [7], [13], [14], [19], [21], [22], [27], [28], [33], [36]. Some researchers have utilized a water jet in addition to using SiC emery paper [13]. One paper wet polished their substrates with #240 SiC emery paper [43]. Some authors do not report using mechanical grinding/abrading/polishing for surface cleaning and use instead ultrasonic agitation in acetone or isopropyl alcohol or rely on acid etching/pickling to instead to obtain the same effect as mechanical grinding/abrading/polishing. These acids are mentioned in Section 2.2.3 [13], [15], [19], [32], [42], [44]. Some publications utilized ultrasonic cleaning in acetone, ethanol, or isopropyl alcohol after mechanical grinding/abrading/polishing to clean the substrate surface rather than rinsing with distilled or deionized water since this cleaning method is more thorough than a simple rinse [19]–[21], [27], [29], [39], [45].

2.2.2 Degreasing/Sensitization

Degreasing/sensitization is performed to remove greasy, oily, and other organic impurities from the surface [7]. This can be done by ultrasonic degreasing in acetone, or rinsing with an alkaline solution such as saturated $NaHCO_3$, NaOH, Na_3PO_4, KOH, and etc. [7], [14], [19], [29], [33], [39].

2.2.3 Pickling/Acid Etching

This process removes any leftover oxides and hydroxides from the substrate's surface and increases surface roughness. Higher surface roughness allows the coating to be smoother, more uniform and compact, improves the adhesion between coating and substrate, and also increases plating rate for better interlocking between the coating and substrate [7], [17], [21], [23], [27], [30], [38], [39], [46]. Acids used include HF, HNO_3 (usually alongside CrO_3), oxalic acid, H_2CrO_4, H_3PO_4, CrO_3 with NaF, CH_3COOH with $NaNO_3$ [13], [16], [21], [23], [24], [42], [44], [46]–[48]. Not all techniques in literature require pickling/acid etching [14], [20], [22], [36], [37], [42]. Bellemare reported using an undisclosed proprietary etchant that is compliant with the European Union's Restriction of Hazardous Substances Directive (RoHS) [17].

2.2.4 Activation/Conversion Coatings

Activation or conversion coating adds a temporary layer for further coating. The temporary layer has equal electric potential throughout for improved electroless plating reactions and improves adhesion [7]. Historically, activation involves fixating MgF_2 on substrate surface by using HF acid or NH_4HF_2 (somewhat easier to control than HF acid) in conjunction with another acid (such as H_3PO_4 or HNO_3), or the usage of hexavalent chromium [7], [13], [24]. For brevity, hexavalent chromium will be denoted as Cr(VI) hereafter. However, increasingly stringent environmental legislations has prompted the development of activation procedures or conversion coatings which

are less toxic and more environmentally friendly [14], [15], [17], [19], [21], [27], [30], [33], [37]–[39], [44], [48]. Some common activation techniques and conversion coatings are described below.

2.2.4.1 Zinc Immersion/Zincating

This process dissolves surface oxides and forms a thin Zn layer on the substrate to prevent Mg re-oxidation [9]. This process is not recommended for magnesium alloys with high aluminium content and is harder to control [40]. The benefit of this process is that there are more nucleation sites for electroless Ni plating, therefore improving adhesion between the electroless Ni coating and the substrate [7]. Wu et al. noted that zinc immersion conversion coating films typically do not completely cover the substrate surface and therefore electroless nickel plating should not be applied immediately afterwards. They recommend applying copper electroplating after zinc immersion using a cyanide or alkaline pyrophosphate electrolyte, and an acid electrolyte for the electroless nickel plating step [40]. The most common three zinc immersion processes are detailed in Section 2.2.4.1.1.

2.2.4.1.1 Dow, Norsk-Hydro, and WCM Processes

The three main zinc immersion treatment processes are the Dow, Norsk-Hydro, and WCM processes. The general sequence for these processes is tabulated in Table 2-1 [49].

Table 2-1: Overview of Dow, Norsk-Hydro, and WCM Processes [49]

Steps	1	2	3	4	5	6
Dow	Degrease	Cathodic cleaning	Acid pickle	Acid activation	Zincate	Copper plate
Norsk-Hydro		Acid pickle	Alkaline treatment	Zincate	Copper plate	
WCM			Fluoride activation			

The Dow process is complicated and its coating is often non-adherent. The Norsk-Hydro and WCM processes are based on the Dow process. The WCM process results in the most uniform zinc coating with the best adhesion, corrosion, and aesthetic properties. However, as previously mentioned these three processes are not suitable for magnesium alloys with aluminium content higher than 6-7 wt%. Preferential dissolution of the α-phase limits the effectiveness of these three pretreatment processes. CrO_3 and HF acid are used in acid pickling and activation, respectively, which are highly toxic and dangerous. Cyanide compounds are also frequently used during electroplating to improve the adhesion of the copper deposits to the substrate. Electroplating presents another challenge due to non-uniform plating caused by non-uniform current density distribution. These processes also require precise control of the acid pickling time to obtain adequate adhesion: excessive time leads to low amounts of deposition, whereas insufficient times leads to non-adherent deposits [40].

2.2.4.1.2 Improvements by Olsen et al. and Pearson et al.

Olsen et al. improved upon the issues mentioned in Section 2.2.4.1.1. The process they developed is tabulated in Table A-1 in Appendix A. Although Olsen et al. claimed that their patent can produce adherent copper deposits on zinc sub-layers, Wu et al. noted that the oxalic acid activation solution used tends to corrode and open underlying porosities on the substrate, resulting in poor corrosion behaviour and decorative appearance [40]. Pearson et al. improved upon Olsen et al.'s work and filed U.S. Patent 0039829A1. They noted that applying Olsen et al.'s patent to magnesium alloys with 12.5 wt% Zn content results in poor adhesion with obvious blistering and very poor cosmetic appearance ("frosted" effect) when immersion coated. Another test involving the same alloy and same treatment process, except for using electrolysis coating rather than

immersion coating, was noted to have good Zn layer adhesion, but still poor cosmetic appearance due to etching of the Mg substrate opening the underlying porosities in the substrate. An example provided in their patent, using a polished cast Mg tap handle with an alloy composition of 12.5 wt% zinc, 3.3 wt% aluminium, is shown in Table A-2 in Appendix A. The deposit adhesion of this process was excellent with no apparent blisters even after heating to 150℃ for 1 h and quenching in cold water. The cosmetic appearance of the deposit was also excellent, being mirror bright with no pits, pores, or frosting. Pearson et al. concluded that the sample's overall condition was acceptable for commercial use [50].

2.2.4.1.3 Fluoride and Chromate Free Zinc Immersion

Wang et al. reported a fluoride and chromate free zinc immersion process in 2012. After mechanical cleaning, alkaline cleaning, and acid pickling, the AZ91D substrates were immersed in a Zn immersion bath composed of $ZnSO_4 \cdot 7H_2O$, $Na_4P_2O_7 \cdot 10H_2O$, and Na_2CO_3. $Na_4P_2O_7 \cdot 10H_2O$ was used to improve Zn layer adhesion to AZ91D [48]. The performance of the electroless Ni-B coating deposited on this Zn layer is discussed in Section 2.6.2. Additional information about the pretreatment can be found in Table A-3 in Appendix A.

2.2.4.2 Chromium-based Conversion Coatings

Direct electroless nickel plating is simple and suitable for alloys with high aluminium content. However, electroless plating usually employs Cr(VI) compounds and HF acid during the etching and activation steps. As previously mentioned, this increases the danger of the plating operation and is harmful to the environment. As a result, much effort has been devoted towards developing pretreatment processes that do not utilize CrO_3 or HF acid [8], [51].

2.2.4.3 Phosphating Conversion Coating

Phosphating conversion coating utilizes the insolubility of the PO_4^{3-} ions in the phosphating bath to deposit them on the substrate surface. This treatment is commonly used in the automotive industry, and so shorter phosphating times are desired to reduce production times [8]. Additives are used to stabilize the phosphating bath and accelerate the phosphating process. For example, NaF and nitroguanidine in an 8.5:1 mass ratio are used as anticorrosion agents, while tartaric acid combines with the insoluble phosphate to form a solvable complex to prevent an insoluble phosphate sludge from forming and affecting the coating quality [33]. Additional information about phosphating conversion coatings can be found in Table A-4 in Appendix A.

2.2.4.4 Copper Immersion and Copper Striking

Copper immersion is a new process. Wu et al. noted that like Zn immersion, the Cu immersion formed coating typically also does not completely cover the substrate. Like in Section 2.2.4.1, they recommend applying copper electroplating after copper immersion for improved coverage of the substrate. More details regarding this can be found in Section 2.2.4.1. An example for plating on AZ91 was provided, but the pretreatment used was not specified. The Cu immersion coating bath specified in this example is tabulated in Table A-1 in Appendix A. Sonicating is performed during immersion to degas the substrate surface to form a continuous conversion coating. Electroless Ni-P plating can be applied on the Cu conversion coating; the plating bath specified in the patent is tabulated in Table A-5. The coating fabricated using the above process reportedly yields a uniform, dense coating without patchy areas [52].

2.3 Plating Procedure

Four major types of electroless plating baths exist, differentiated by the reducing agent (electron supplier for reducing of nickel) used: sodium hypophosphite, aminoboranes, sodium borohydride, and hydrazine. Table 2-2 compares the four types of baths. Most baths use sodium hypophosphite as the reducing agent due to its lower cost, greater ease of control, and higher corrosion resistance of deposits [26].

Table 2-2: Comparison of four major electroless nickel plating baths [23], [25], [26], [30], [46]

Reducing Agent	Characteristics
Sodium hypophosphite	• Most used • High plating rate, stability, ease of control, and corrosion resistance • Plating bath can be acidic (4-6) or basic (8-10) ○ Most are between 4-5.5 pH
Aminoboranes	• Primarily used to plate plastics and nonmetals • Limited to two compounds: N-dimethylamine borane (DMAB) – $(CH_3)_2$-$NHBH_3$, and H-diethylamine borane (DEAB) • Usable for wide pH range, but typically operated between pH 6-9 • Operating temperatures typically 50-80°C, but can be as low as 30°C • Deposition rates of 7-12 μm/h • Deposits usually have B content of 0.4-5%

Sodium borohydride	• Borohydride ion is most powerful reducing agent listed in this table
	  ○ Any water-soluble borohydride compound can be used, but sodium borohydride is preferred
	• Hydrolysis of borohydride ions very fast in acidic or neutral solutions, and in the presence of Ni ions, nickel boride may form spontaneously
	  ○ In plating solution with pH of 12-14, nickel boride formation is suppressed, and reaction production is mostly elemental Ni
	• Complexing agents like ethylene diamine (effective for pH 12-14) are used to prevent nickel hydroxide precipitation
	  ○ Such strong complexing agents typically reduce deposition rate
	• Operating temperature typically 90-95°C
	• Deposition rates of 25-30 μm/h
	• Deposits typically have 3-8 wt% B
	• Plating solution pH continually decreases during operation, requiring continual addition of alkali hydroxides
	• High operating pH prevents usage of aluminium substrates

Hydrazine	• Typically deposits 97-99 wt% Ni, but deposits lack metallic appearance, are brittle, highly stressed, and have poor corrosion resistance
	  ○ Stress is likely from codeposition of small quantities of basic nickel salts, $Ni(OH)_2$, and N
	• Deposit hardness has very little commercial use, unlike for hypophosphite and borohydride baths
	• Operating temperature of 90-95°C
	  ○ Instability of hydrazine at this temperature makes baths highly unstable and difficult to control
	• Operating pH of 10-11
	• Deposition rate of about 12 μm/h

2.4 Plating Reactions and Plating Bath Contents

The basic electroless plating reactions assuming no side reactions occur are shown in Equation 2-1 and Equation 2-2; the overall reaction is shown in Equation 2-3 [51].

$$Reductant \xrightarrow{catalytic\ surface} Oxidation\ product + Me^- \quad \text{Equation 2-1}$$

$$M^{z+} + ze^- \xrightarrow{substrate\ surface} M \downarrow \quad \text{Equation 2-2}$$

$$Reductant + M^{z+} \xrightarrow{catalytic\ surface} Oxidation\ product + M \downarrow \quad \text{Equation 2-3}$$

For example, electroless Ni-P deposition can be achieved if $NiSO_4$ is used as the metal salt and sodium hypophosphite (NaH_2PO_2) is used as the reducing agent as per Equation 2-4 and Equation 2-5 [44].

$$2H_2PO_2^- + 4OH^- + NiSO_4 \rightarrow 2HPO_3^- + SO_4^{2-} + 2H_2O + Ni \downarrow + H_2 \uparrow \quad \text{Equation 2-4}$$

$$2H_2PO_2^- + 10H^+ \rightarrow 4H_2O + 2P \downarrow + 3H_2 \uparrow \quad \text{Equation 2-5}$$

For example, electroless Ni-B deposition can be achieved if $Ni(CH_3COO)_2{\cdot}4H_2O$ is used as the metal salt and sodium borohydride ($NaBH_4$) is used as the reducing agent. In alkaline plating solutions, Equation 2-6 and Equation 2-7 provide electrons for Ni^{2+} reduction, and Equation 2-7 provides B content in the coating. Equation 2-8 provides B content to the coating for acidic plating solutions [48].

$$BH_4^- + 8OH^- \rightarrow BO_2^- + 6H_2O + 8e^- \quad \text{Equation 2-6}$$

$$BH_4^- \rightarrow B \downarrow + 2H_2 \uparrow + e^- \quad \text{Equation 2-7}$$

$$2BH_4^- + 2H_2O \rightarrow 2B \downarrow + 2OH^- + 5H_2 \uparrow \quad \text{Equation 2-8}$$

In addition to a metal salt and a reducing agent, electroless plating baths typically also contain complexing agents, stabilizers, accelerators, buffers, wetting agents, brightening agents, and pH

adjustment agents [53]. The alloy content of the substrate also affects the plating reactions/rate [16], [42]. These are described in greater detail in Sections 2.4.1 to 2.4.9, respectively.

2.4.1 Metal Salt

The metal salt provides the metal ions which are deposited onto the substrate. The number and type of metal salts determines what alloy deposit is obtained [53].

2.4.2 Reducing Agent

The reducing agent donates electrons to reduce metal ions to metals, and usually provides the nonmetal elements present in the alloy deposits. For example, NaH_2PO_2 supplies P and $NaBH_4$ supplies B. Ternary alloy deposits therefore require two reducing agents. For example, Ni-P-B alloys use NaH_2PO_2 and $NaBH_4$ [53].

2.4.3 Complexing Agent

The complexing agent (also known as a chelator or chelating agent) complexes the Ni^{2+} ions and reduces the excess free metal ion concentration, which prevents metal salt precipitation and stabilizes the bath. Experiments have shown that a plating bath with an appropriate complexing agent has a higher deposition rate than without any complexing agents. The complexing agent also acts as a pH buffer. Almost all modern plating baths contain a complexing agent due to the above reasons [53].

2.4.4 Stabilizer

The stabilizer prevents the spontaneous decomposition of the plating solution, as the solution is typically a metastable system [53]. Spontaneous decomposition can be exacerbated by the substrate being reactive, as is the case for magnesium and magnesium alloys [23], [30], [53], [54].

The stabilizer is sometimes called a catalytic inhibitor and its concentration must be carefully controlled, as excessive usage decreases and even possibly inhibits the plating reaction. Trace amounts are used typically, with few being used more than 10 ppm [53].

2.4.5 Accelerator

The accelerator accelerates deposition and, therefore, increases the plating rate and can also activate the reducing agent. The accelerator is also called the exultant in some literature and acts antagonistically to the stabilizer [53].

2.4.6 Buffer

The buffer modulates the pH of the bath to stabilize the deposition rate and deposit quality [53].

2.4.7 Wetting Agent

The wetting agent is a surfactant used to increase the wettability of the substrate. This reduces the contact angle between the solution and the substrate and aids in the escape of H_2 bubbles, decreasing deposit porosity [53].

2.4.8 Brighteners

Brighteners are used to make the electroless deposits visually brighter; the deposits are typically semi glossy but adding brighteners into the bath can cause the surface to become more uniform and increase its lustre. Brighteners are, therefore, not necessary for plating baths [53].

2.4.9 pH Adjustment Agents

The pH adjustment agents maintain the pH value of the bath within a certain range during the plating process. The plating process typically generates some H^+ ions, thus necessitating pH

adjustment agents. Most pH adjustment agents are compatible with the bath; these include H_2SO_4, HCl, NaOH, $NH_3 \cdot H_2O$, and etc. [53].

2.5 Effect of Alloy Content on Plating Rate

Liu and Gao reported that Mg alloys with higher alloy content have higher surface roughness after etching and fluoride activation. After 110 min of plating, the coating surface roughness on AZ31 and AZ91 was lowered, while the coating surface roughness on Mg increased. The overall deposition rate is also higher for AZ31 and AZ91 than for pure Mg. This is attributed to the finer and heterogeneous microstructure of AZ31 and AZ91. Nucleation, growth, and coalescence of the three-dimensional crystallites (collectively termed 3DCs) are promoted by the increased density of grain boundaries (GBs) and the galvanic coupling effect between the α and β phases, resulting in higher deposition rates for the alloys. The gradual reduction in coating surface roughness is due to the fine microstructure and the leveling effect inherent to electroless plating. More Ni is deposited on recessed areas since they are close to grain or phase boundaries, which are more energetically advantageous for 3DCs. This, therefore, results in a more uniform deposit and reduces roughness. It should be noted that this mechanism may not be valid for recessed areas exceeding tens of microns in size. The coarser microstructure of pure Mg, therefore, has a rougher coating surface roughness. Of the three substrates, AZ31 was found to have the lowest coating surface roughness and highest deposition rate due to its fine microstructure, enhancing 3DCs. The adhesion strength (evaluated by measuring the critical load L_c of a scratch tester) of the electroless nickel coating is lowest on Mg due to the reduced surface roughness and mechanical interlocking with the coating and is highest for AZ31 [16], [42].

2.6 Electroless Nickel Coating Types

2.6.1 Ni-P Coatings

The most researched electroless nickel coating type in literature is the Ni-P coating [21], [25], [30]. As mentioned previously, this coating is typically made from a hypophosphite reducing agent like NaH_2PO_2 and has high corrosion and wear resistance [26]. As mentioned in Sections 2.2.1 to 2.2.3, the standard pretreatment process in the past involved sandpaper grinding of the Mg substrate, followed by degreasing using acetone or ethanol, acid pickling using H_2CrO_4 and HNO_3 or H_3PO_4, and fluoride activation using HF or NH_4HF_2. The electroless Ni-P plating bath would typically also contain HF and/or NH_4HF_2 [17], [20], [23], [55] to prevent corrosion of the Mg substrate during electroless plating by forming a protective MgF_2 film [56]. With increasing restrictions on the usage of Cr(VI) [51] and increased mindfulness of the dangers of fluorides such as HF or NH_4HF_2 [21], recent reports in the literature increasingly do not use these chemicals [57], [58]. The pretreatment and electroless Ni-P plating processes employed by Ambat and Zhou in their 2004 paper are tabulated in Table 2-3 and Table 2-4, respectively. The processes and chemicals reported in this paper are typical of electroless Ni-P research of that time. The substrate is rinsed with water between each step of the pretreatment process. Further information about the pretreatment process and electroless Ni-P plating bath can be found in Table A-6 and Table A-7 in Appendix A. Later papers do not use HF and H_2CrO_4 in their pretreatment processes [38], [43], [57]–[60] and/or do not use HF or NH_4HF_2 in their electroless plating baths [21], [43], [57], [58], [60].

Table 2-3: Typical pretreatment process involving Cr(VI) and HF or NH_4HF_2 [23]

Mechanical Polishing	Wet grinding with SiC paper Diamond wheel polishing with diamond paste
Ultrasonic Degreasing	Performed in acetone
Alkaline Degreasing	NaOH 60°C 5 min
Pickling	H_2CrO_4 HNO_3 45 s
Activation	HF 10 min

Table 2-4: Typical chemicals and operating conditions in electroless Ni-P plating bath involving HF and/or NH_4HF_2 [23]

Basic Nickel Carbonate
Citric Acid
NH_4HF_2
HF
TU
$NaH_2PO_2 \cdot H_2O$
NH_4OH
pH 7-8
80°C
Mild Mechanical Agitation

Newer papers in the literature typically do not use HF or Cr(VI) for pretreatment or electroless plating [18], [43], [51], [57]–[60]. These papers typically focus on novel conversion coatings; the key findings of several such papers are discussed below [18]–[21], [51], [58].

Huo et al. introduced a pretreatment process involving a stannate conversion coating followed by $SnCl_2$ sensitization, $PdCl_2$ activation, and NaH_2PO_2 reduction. A $MgSnO_3 \cdot H_2O$ layer formed on the AZ91D substrate surface after stannate conversion coating to protect the substrate from corrosion in the electroless plating bath. The $SnCl_2$ sensitization step formed $Sn(OH)Cl_2$ on the $MgSnO_3 \cdot H_2O$ layer, which was activated using $PdCl_2$ to deposit free Pd on the substrate surface. To prevent excess Pd from destabilizing the electroless plating bath, a reduction step using NaH_2PO_2 was used to reduce the amount of free Pd available on the surface. Potentiodynamic polarization (PDP) measurements following electroless plating indicated that this coating system exhibited excellent corrosion resistance against 3.5 wt% NaCl solution. The P content of this coating was 10 wt% [20]. Additional information about the pretreatment process and electroless plating bath used can be found in Table A-8 and Table A-9 in Appendix A.

Lian et al. applied a phosphate conversion coating to AZ91D from a bath consisting of H_3PO_4, ZnO, NaF, nitroguanidine, tartaric acid, $NaNO_3$, and Na_2MoO_4. NaF and nitroguanidine were used as anticorrosion agents, tartaric acid was used to stabilize the phosphating bath, $NaNO_3$ was used to accelerate the phosphate coating formation process, Na_2MoO_4 was used to reduce microcracks, and ZnO was used to form nucleation clusters for the phosphate coating. The final Ni-P/phosphate coating system withstood 150 h in the salt spray test (5 wt% NaCl salt fog at 35℃), indicating good corrosion resistance. The Ni-P coating was deposited from a bath containing HF, but bath formulations without HF should also be usable with the phosphate conversion coating [20]. Additional information about the pretreatment process can be found in Table A-10 in Appendix A.

Zhao et al. vertically dipped AZ91D samples in 8604 organosilicon varnish, then roughened the varnish surface using NaOH solution. The roughened varnish surface was activated using a Pd

colloid activator and the activated surface was electroless Ni-P plated. The adhesion of the coating to the substrate was very good based on cross cut testing and PDP measurements in 3.5 wt% NaCl at 30°C indicated very low corrosion rates (very high corrosion resistance). The P content of the coating was 12.3 wt% [44]. Additional information about the pretreatment and electroless plating bath can be found in Table A-11 and Table A-12 in Appendix A, respectively.

Yang et al. applied a molybdate conversion coating on Mg-8Li by immersing AZ91D in $Na_2MoO_4 \cdot 2H_2O$. The Ni-P deposited on this molybdate conversion coating was compact and uniform with no obvious surface defects. Immersion testing and PDP measurements in 3.5 wt% NaCl solution showed that the coating exhibited high corrosion resistance. The P content of the Ni-P coating was 4.7 wt%. NH_4HF_2 was used in the plating bath, but a plating bath without HF or NH_4HF_2 should also be usable with the molybdate conversion coating [27]. Additional information about the pretreatment process can be found in Table A-13 in Appendix A.

Seifzadeh and Rajabalizadeh applied a cerium-lanthanum-permanganate (CLP) conversion coating to AZ61 composed of $Ce(NO_3)_3$, $La(NO_3)_3$, and $KMnO_4$. The conversion coating was homogeneous and porous, allowing mechanical interlocking with the coating for improved adhesion. The porosity of the coating also enabled the electroless plating bath to contact the substrate, allowing phases composed of Al, Mg, and Zn to catalyze the electroless plating reactions without requiring special activators such as Pd colloids as proposed in the processes by Huo et al. [20] and Zhao et al [44]. PDP and EIS measurements in 3.5 wt% NaCl solution showed that the coating provided substantially higher corrosion resistance than the AZ61 substrate. The high corrosion resistance of the coating was attributed to its fine grain structure and very low porosity. The Ni-P coating was deposited from a bath containing HF and NH_4HF_2, but Ni-P plating baths

that do not use HF or NH_4HF_2 should be usable with the CLP conversion as well [38]. Additional information about the pretreatment process can be found in Table A-14 in Appendix A.

Ghavidel et al. immersed their AZ31 substrates in saturated $NaHCO_3$ to form a carbonate conversion coating. This carbonate conversion coating effectively reduced the corrosion of the substrate in the electroless plating bath. Ni-P coatings with and without SiC nanoparticles (NPs) were deposited on the conversion coatings. Adding 1 g/L SiC NPs led to the highest hardness and corrosion resistance (per PDP measurements). A heat treatment temperature of 300°C resulted in the highest corrosion resistance and coating hardness, but heat treatment was noted to embrittle the coating and cause crack growth [19]. Additional information about the pretreatment and electroless plating bath can be found in Table A-15 and Table A-16 in Appendix A, respectively. An electroless plating bath formulation that does not use NH_4HF_2 should be used to deposit the Ni-P/SiC coatings to make the electroless plating step safer [19].

He et al. utilized mechanical attrition enhanced electroless plating (MAEP) to deposit a Ni-P coating on AZ31. The mechanical attrition was provided by Al_2O_3 balls 1-1.5 mm in diameter that were agitated by the continuous stirring of the solution. Compared to a coating deposited from the same bath without mechanical attrition (EP coating), the MAEP coating had slightly lower P content and a much smoother and compact surface morphology. This is consistent with previous reports on surface mechanical attrition treatment enhancing diffusion kinetics and yielding homogenous, pore-free, adherent coatings with excellent corrosion resistance. The MAEP coating had significantly higher corrosion resistance than the EP coating. Although He et al. utilized a pretreatment process involving HF and Cr(VI) and their electroless plating bath contained HF, mechanical attrition should still result in appreciable reductions in coating porosity and increases

in corrosion resistance even when used with different pretreatments and electroless plating bath formulations [29]. Additional information about the pretreatment and mechanical attrition assisted electroless plating bath can be found in Table A-17 and Table A-18 in Appendix A, respectively. An electroless plating bath that does not use HF and NH_4HF_2 should be used [19].

Heshmati et al. utilized a maleic acid conversion coating for AM60B substrates. The AM60B substrates were immersed in maleic acid (prepared by dissolving maleic anhydride in water) to form magnesium maleate dihydrate, aluminium maleate, MgO, and Al_2O_3. Immersion in maleic acid also etched the AM60B surface, resulting in a coarse surface finish that increased mechanical interlocking between the final composite electroless coatings and the substrate. The composite coating is discussed in greater detail in Section 2.6.4. Heshmati et al. also commented that some of the conversion coatings described above are typically more complex (stannate conversion coating by Huo et al. [20] and organosilicon varnish followed by activation by Zhao et al. [44]) or still used toxic compounds (molybdate pretreatment by Yang et al. [27]) [61]. Additional information about the pretreatment and electroless plating baths can be found in Table A-19 and Table A-20 in Appendix A, respectively. An electroless plating bath that does not use HF and NH_4HF_2 should be used [19].

Petro and Schlesinger tested the coatings deposited from 13 different Ni-P plating baths on AZ91D. No special pretreatment process was used. The AZ91D substrates were simply polished with #240 SiC sandpaper before being immediately inserted in the electroless plating baths. The plating baths are tabulated in Table A-21 and Table A-22 in Appendix A. Alkaline baths were found to be better than acidic baths. Chloride ions resulted in bath breakdown independent of pH controlling chemical and their use should be avoided. NH_4OH was found to be better than NaOH as a pH

controlling chemical, as continuous deposits formed more quickly and baths using solely NH_4OH were more stable than baths using NaOH. Bath S4 was determined to be the optimal bath, as it produced reasonably well adhering, continuous, and defect free coatings in as quickly as 60 s. This bath used NH_4OH only as the pH controlling chemical. The capability of depositing such a coating without the complex pretreatment processes described above is attractive [43].

In addition to NaOH, $Na_3PO_4 \cdot 12H_2O$ [29], [35]–[37] or $Na_2CO_3 \cdot 10H_2O$ [20], [55] have also been used in the alkaline degreasing step in some papers. Lian et al. used KOH instead of NaOH in the alkaline degreasing step [33]. Other commonly used Ni salts include $NiSO_4 \cdot 6H_2O$ [25], [28], [33]–[37] and $Ni(CH_3COO) \cdot 4H_2O$ [20], [55]. Petro and Schlesinger have also utilized $Ni(H_2NSO_3)_2 \cdot 4H_2O$ as a Ni salt [43]. The following electroless Ni-P plating bath additives have been used by various authors: $NaCH_3COO$ [30], [33]–[35], [37], [38], [61], [62], $Na_4P_2O_7$ [44], succinic acid or disodium succinate [32], [43], [62], trisodium citrate [18], [39], [43], KF [39], Na_2CO_3 [36], [62], maleic acid [30], glycine [18], [24], glyceraldehyde [18], $ZnSO_4 \cdot 7H_2O$ [43], and lactic acid [46].

2.6.2 Ni-B Coatings

Electroless Ni-B coatings are typically harder and have higher wear resistance but lower corrosion resistance than Ni-P coatings. The pretreatment process of these coatings is similar, if not identical, to Ni-P coatings [21], [26], [48]. The electroless Ni-B plating bath used by Wang et al. in their 2008 paper is tabulated in Table 2-5 [48]. A similar bath was used by Zhang et al. in their 2008 paper [34]. As previously mentioned in Section 2.3, the main difference between Ni-B and Ni-P baths is their reducing agent: Ni-P baths use NaH_2PO_2 and Ni-B baths use aminoboranes or $NaBH_4$ [26]. Ethylenediamine is used as a complexing agent. TU and saccharin (from sodium dihydrate)

is added for grain refinement [48]. Both Zhang et al. and Wang et al. reported that the Ni-B coatings significantly improved the corrosion resistance of their substrates [34], [48]. Additional information about the pretreatment and electroless plating bath can be found in Table A-3 and Table A-23 in Appendix A, respectively.

Table 2-5: Ni-B plating bath composition in 2008 paper by Wang et al. [48]

$Ni(CH_3COO)_2 \cdot 4H_2O$
Ethylenediamine
NaOH
$NaBH_4$
Sodium saccharin dihydrate
TU
pH 13.6
85℃
1 h

2.6.3 Ternary Coatings

Petro and Schlesinger tested the efficacy of four Ni-P-Zn plating baths for deposition on AZ91D. The chemicals used are tabulated in Table 2-6. The baths use different concentrations of these chemicals and had Ni:Zn molar ratios of 25-50%. No pretreatment was used, only grinding with #240 SiC sandpaper. Continuous coatings, that were largely homogenous, formed in as little as 15 min. A temperature of 80℃ and pH above 10 were necessary for rapid deposition rates and continuous deposits. Zn content in the coating rose and P content fell with higher pH, and vice versa. As a result, the P and Zn content of the coatings can be controlled by changing the pH and temperature of the plating bath. A coating composition of 15 at% P and 12 at% Zn led to optimal corrosion resistance. The plating baths were stable even at 80℃ for over 10 h over multiple uses. The exclusion of Cl^- and SO_4^{2-} ions was necessary for improved bath stability; this is why $NiCl_2$

or $(NH_4)_2SO_4$ was not used, as these both attacked Mg and destabilized the bath. Using NH_4OH instead of NaOH for pH control was also noted to improve bath stability [60]. Additional information about the plating baths can be found in Table A-24 in Appendix A.

Table 2-6: Chemicals utilized in Ni-P-Zn plating bath by Petro and Schlesinger [60]

$NiSO_4 \cdot 6H_2O$
$ZnSO_4 \cdot 7H_2O$
Trisodium citrate dihydrate
$NaH_2PO_2 \cdot H_2O$
NH_4OH
pH 11.6-12.0
80°C
> 15 min

Zhang et al. deposited Ni-Sn-P coatings on AZ91D from the bath tabulated in Table 2-7. The coatings had good uniformity and dense coverage over the substrate. The Sn and P content of the coatings were 2.5 and 8.5 wt%, respectively. The deposition rate was fairly low at 6 μm/h due to the SnO_3^{2-} ions in the plating bath adsorbing on the substrate and inhibiting the plating reactions. A porosity test utilizing phenolphthalein was done to determine the thickness required for through-thickness porosity to disappear. The Ni-Sn-P coating required a 6 μm thickness, while a Ni-P coating with pretreatment involving Cr(VI) conversion coating required a 28 μm thickness. This indicates that the coating has much lower porosity than a Ni-P coating deposited on AZ91D using the classic Cr(VI) based pretreatment. This porosity test is explained in greater detail in Section 3.1 (Introduction). PDP measurements in 3 wt% NaCl solution showed that the Ni-Sn-P coating was more corrosion resistant than the Ni-P coating and, therefore, confirmed the porosity test results. An immersion test in 10% HCl solution was also performed, with the time taken for the first H_2 gas bubble used as the metric. The trends observed in the porosity and PDP measurement

were also observed for this test. The low coating porosity (and high corresponding corrosion resistance and coating density) was attributed to the presence of SnO_3^{2-} inhibiting the electroless plating reactions [25]. Additional information about the pretreatment and electroless plating bath can be found in Table A-4 and Table A-25 in Appendix A, respectively. The electroless plating bath should be reformulated to omit NH_4HF_2 to make it safer for use [19].

Table 2-7: Ni-Sn-P plating bath used by Zhang et al. [25]

$NiSO_4 \cdot 6H_2O$
$Na_2SnO_3 \cdot 3H_2O$
$NaH_2PO_2 \cdot H_2O$
Trisodium citrate dihydrate
NH_4HF_2
TU
pH 9.0 ± 0.2
90 ± 2°C

Zhang et al. also deposited a Ni-W-P coating on AZ91D from the plating bath tabulated in Table 2-8. Na_2CO_3 acted as a complexing agent, accelerator, and pH buffer in the plating solution. Without Na_2CO_3, almost no Ni-W-P deposition occurred despite a 1 h plating time. A 20 g/L concentration of Na_2CO_3 led to a plating rate of ~7 μm/h. Lower Na_2CO_3 concentrations led to lower plating rates and higher concentrations destabilized the bath. The W and P contents of the coating were 4.5 and 4.9 wt%, respectively. The same porosity test, PDP measurement, and HCl immersion tests used in Zhang et al.'s Ni-Sn-P paper were used. The Ni-W-P coating exhibited high corrosion resistance. This high corrosion resistance was attributed to the low porosity and high compactness of the coating [36]. Additional information about the pretreatment and electroless plating bath can be found in Table A-4 and Table A-26 in Appendix A, respectively. The electroless plating bath should be reformulated to omit NH_4HF_2 to make it safer for use [19].

Table 2-8: Ni-W-P plating bath used by Zhang et al. [36]

$NiSO_4 \cdot 6H_2O$
Na_2CO_3
Na_2WO_4
$NaH_2PO_2 \cdot H_2O$
Trisodium citrate dihydrate
NH_4HF_2
TU
pH 9.0
80 ± 2°C

2.6.4 Multilayer Coatings

Hsu and Yang reported in 2012 a composite coating composed of an electroplated Ni layer on an electroless Ni-P layer. The AZ91D substrate was ultrasonically cleaned in isopropyl alcohol for surface cleaning, then acid pickled, surface activated, and zincated. A Cu strike layer was electrodeposited on the zincated substrate because Zn is not catalytic towards electroless Ni-P deposition. Specific details regarding the acid pickling, surface activation, zincating, and Cu strike electrodeposition process were not provided; therefore, these may involve HF and/or Cr(VI). The adhesion strength of the composite coating was high. PDP measurements were taken in 3.5 wt% NaCl solution. The Ni/Ni-P coating had identical corrosion potential (E_{corr}) but slightly lower corrosion current density (i_{corr}) than the Ni-P coating, indicating that the additional Ni layer increased the overall corrosion resistance. The total thickness of the composite coating was 28.6 µm [32]. Additional information about the pretreatment and plating baths can be found in Table A-27 and Table A-28 in Appendix A, respectively.

Gu et al. reported a similar coating system as Hsu and Yang in 2005. The pretreatment and electroless Ni-P plating processes used HF and Cr(VI). This composite coating also exhibited high corrosion resistance, which was attributed to the low porosity and fine nanocrystalline grain structure of the coating [28]. Although a slightly different electrolyte was used (3 vs. 3.5 wt% NaCl solution), Hsu and Yang's composite coating exhibited significantly lower i_{corr} (~1 μA/cm^2 vs. 0.67 nA/cm^2 for Gu et al. and Hsu and Yang, respectively) [28], [32]. This is likely caused by the higher overall coating thickness provided by the Cu and Zn layers [32]. Additional information about the pretreatment, electroless plating bath, and electroplating bath can be found in Table A-29 to Table A-31 in Appendix A, respectively. A pretreatment process and an electroless plating bath without HF and NH_4HF_2 should be used for to make the electroless plating step safer [19].

Luo et al. reported a Ni-P/Ni-P composite coating on Mg-Li-Zn alloy (9.3 wt% Li, 2.0 wt% Zn) obtained by two different electroless Ni-P plating steps. The pretreatment process used involves alkaline cleaning, acid cleaning, and activation. The activation step used NH_4HF_2, which is also dangerous like HF [7]. The first plating step was 10 min long to obtain a thin layer. The first Ni-P layer was ~4 μm thick, and the second Ni-P layer was ~16 μm thick. The composite coating was fully covered with a relatively uniform surface morphology. No gaps or inclusions were observed between the coating and substrate, indicating good adhesion. SEM observations of the interface between the first and second Ni-P layers showed good integration between the two coatings, indicating good adhesion. The P content of the both Ni-P layers was ~13.6 wt%. PDP measurements of the composite coating in 3.5 wt% NaCl solution showed that the composite coating had high corrosion resistance [46]. Additional information about the pretreatment and electroless plating baths can be found in Table A-33 and Table A-34 in Appendix A, respectively.

A pretreatment process that does not involve NH_4HF_2 should be used, as should a reformulated electroless plating bath that does not utilize HF [19].

Zhang et al. reported a Ni-B/Ni-P composite coating on AZ91D obtained from Ni-P and Ni-B electroless plating processes. The pretreatment process involved mechanical cleaning, alkaline cleaning, and a manganese dihydrogen phosphate phosphating conversion coating bath. The Ni-P layer was deposited first and was ~20 μm thick. The Ni-B layer was deposited on the Ni-P layer and was ~15 μm thick. The P content of the Ni-P layer was 7.7 wt%. The B content of the Ni-B layer was not reported. Some pores were observed in the Ni-P layer, possibly originating from H_2 evolution during electroless plating. No pores were observed in the Ni-B layer. SEM observations of the coating cross section showed good uniformity and compatibility between the coating and substrate, suggesting high adhesion. The composite coating was heat treated. As expected, the microhardness increased from 740 to 1245 HV after heat treating at 350°C for 2 h. PDP measurements in 3 wt% NaCl showed that the composite coating significantly improved the corrosion resistance of the substrate. Compared to a Ni-P coating, the composite coating had higher E_{corr} and lower i_{corr} (higher overall corrosion resistance). This is beneficial because as the Ni-B layer corroded, through-thickness pinholes would form and eventually contact the Ni-P layer. Once this occurred, the corrosion mode would switch from longitudinal pinhole corrosion to transverse corrosion, dispersing the corrosion current across the entire Ni-B layer and allowing the Ni-B layer to sacrificially protect the Ni-P layer [34]. The concept of a multilayer coating system where outer layers are less corrosion resistant than inner layers may be useful for components with long service lives. Additional information about the pretreatment and electroless plating baths can be found in Table A-4 and Table A-34 in Appendix A, respectively. The Ni-P electroless plating bath should be reformulated to not use HF and NH_4HF_2 [19].

Zhang et al. reported a Ni-P/Ni-B composite coating on AZ91 obtained from alkaline electroless Ni-B plating followed by acidic electroless Ni-P plating. The pretreatment process employed involved two activation steps, both of which use fluorides. A 1 h Ni-B plating time was used to prevent corrosion of the AZ91D substrate in the acidic Ni-P plating bath. The open circuit voltage (OCV) of the coating rapidly stabilized in a few seconds in 3.5 wt% NaCl solution, suggesting high corrosion resistance. The P content of the Ni-P coating was 12.1 wt%. The adhesion of the composite coating to the substrate was good, as shown by the connectedness of the composite coating to the substrate during cross sectional SEM analysis and a thermal shock test repeated 20 times with no blister or exfoliation observed. The Ni-B layer was ~6 μm thick and the Ni-P layer was ~13 μm thick. Electrochemical impedance spectroscopy (EIS) measurements of the composite coating in 3.5 wt% NaCl solution showed that the electrolyte did not penetrate the Ni-P layer. PDP measurements in the same electrolyte showed that the composite coating had high corrosion resistance [21]. Additional information about the pretreatment and electroless plating baths can be found in Table A-35 and Table A-36 in Appendix A, respectively. The activation 2 process should be revised to replace NH_4HF_2 to make it safer [19].

Heshmati et al. deposited a Ni-P/Ni-Zn-Cu-P composite coating on AM60B. After the pretreatment involving a maleic acid conversion coating (discussed in Section 2.6.1), electroless Ni-P and electroless Ni-Zn-Cu-P coatings were deposited successively. The final composite coating was uniform and compact, with 6.6 wt% P in the Ni-P layer and 10.3 wt% P, 7.6 wt% Zn, and 2.5 wt% Cu in the Ni-Zn-Cu-P layer. Per PDP and EIS measurements, both the Ni-P and composite coatings showed high corrosion resistance in 3.5 wt% NaCl solution, with the composite coating being better. The coatings exhibited high adhesion per ASTM B733 and ASTM D4541

adhesion tests. Additional information about the pretreatment and electroless plating baths can be found in Table A-19 and Table A-20 in Appendix A.

Song et al. deposited a composite coating of Ni-P-ZrO_2 (15 µm)/electroplated Ni (20 µm)/Ni-P (5 µm) on AZ91D. The first layer was an electroless Ni-P coating with 5 wt% of 20 nm diameter ZrO_2 NPs. The Ni coating (second layer) was electroplated from a Watts bath. The Ni-P plating bath was the same as the Ni-P-ZrO_2 plating bath apart from omitting the ZrO_2 NPs. The pretreatment process used was not described in detail but did not involve HF acid. PDP measurements of the composite coating in 3.5 wt% NaCl solution showed a significant increase in corrosion resistance compared to a 15 µm thick Ni-P coating or the bare AZ91D substrate. The composite coating was, therefore, well suited for protecting AZ91D in 3.5 wt% NaCl solution. Immersion testing per the Chinese GB-10124-88 standard and SST in accordance with the ASTM B117 standard both supported the conclusion drawn from the PDP results. EIS measurements in 3.5 wt% NaCl solution showed no pitting corrosion. The cross section morphology of the composite coating showed that the coating layers were compact and uniform and that the coating was well attached to the substrate. These results suggest high adhesion between the coating and substrate. Adhesion testing per the ASTM B571 standard did not result in blister or crack formation, indicating good adhesion [39]. Additional information about the pretreatment and plating baths can be found in Table A-37 and Table A-38 in Appendix A.

2.7 Alternatives to Electroless Nickel Plating

2.7.1 Electroplated Ni Coatings

Ghamari and Amadeh electroplated a Ni-Al_2O_3 coating on AZ91D using pulse current (PC) electroplating. The pretreatment involved zincating and Cu electroplating. The Cu layer was used

to protect the Zn layer from the acidic Watts Ni electroplating bath. The Zn layer was likely an adhesion layer between the AZ91D and Cu layer. Al_2O_3 was present as NPs 50 nm in diameter, with 5 g/L added to the plating bath. PC electroplating was used because it is believed to lead to continuous and uniform distribution of Al_2O_3 NPs in the Ni matrix and to provide better ion distribution in the electrolyte to improve the coating quality. Comparing the PDP measurements in 3.5 wt% NaCl solution of the Ni-Al_2O_3 coating with a Ni coating deposited from the same plating bath without Al_2O_3 added, showed that the Ni-Al_2O_3 coating had significantly better corrosion resistance (lower i_{corr} and higher E_{corr}). This was attributed to the NPs, which (1) decreased the contact area between the Ni and the corrosive media; (2) occupied the grain boundaries, which have lower corrosion resistance, to impede corrosion progress, and (3) prevented grain growth to form a nanocrystalline and more uniform coating. The microhardness of the Ni-Al_2O_3 coating was significantly higher than the Ni coating. This increase was solely due to Al_2O_3 incorporation and not oxide dispersion strengthening since the Ni grains were smaller than the Al_2O_3 NPs. A corresponding increase in wear resistance from higher hardness was also observed [13]. Additional information about the pretreatment, zincating, Cu electroplating, and Ni electroplating baths can be found in Table A-39 and Table A-40 in Appendix A, respectively. A pretreatment process that does not use Cr(VI) and NH_4HF_2 and a Cu electroplating bath that does not use cyanide compounds should be used to make these processes safer [15], [49], [51].

Huang et al. deposited a Cu/Ni composite coating on AZ31 using Cu and Ni electroplating. An alkaline $CuSO_4$ was used for galvanostatic etching and Cu electroplating. The Ni electroplating bath used was the Watts Ni bath. Galvanostatic etching (electroetching) was used to create an activated surface where a strongly adhering, uniform, and pore-free Cu coating could be deposited from the alkaline $CuSO_4$ bath. This coating was used to protect the AZ31 substrate from corrosion

in the acidic $CuSO_4$ bath. The acidic $CuSO_4$ bath was utilized to increase the combined Cu layer thickness and to further improve adhesion between the Ni and AZ31. The Ni coating was ~15 μm thick. The corrosion resistance of the composite coating after each electroplating step was determined using PDP measurements in 3.5 wt% NaCl solution. As expected, E_{corr} increased and i_{corr} decreased with each additional coating layer [15]. The composition and operating conditions of the alkaline $CuSO_4$ bath can be found in Table A-41 in Appendix A. The alkaline $CuSO_4$ bath discussed here may be used instead of the CuCN bath previously discussed in Ghamari and Amadeh's work [13], [15].

2.7.2 Electroplated Ni-P Coatings

Alleg et al. reported a Ni-P electroplating bath for polished Cu substrates. The pretreatment process of this report is not discussed, since this is not a Mg substrate. Three applied potentials (-1, -1.15, and -1.3 V) and two plating times (10 and 20 min) were tested. P contents of 8.6-12.2 at% were obtained, with P content increasing from along the substrate to surface direction. All deposits were dense, regular, and uniform with some cracks and a smooth surface [63]. Additional information about the Ni-P electroplating bath can be found in Table A-42 in Appendix A.

Hu and Bai also electroplated Ni-P coatings on Cu substrates. The pretreatment process used is also not discussed because Mg substrates were not used. A design of experiments (DoE) approach was taken to identify the effects of plating bath temperature, applied current density, plating bath pH, $NaH_2PO_2 \cdot H_2O$ concentration in plating bath, and electroplating bath stirring rate on the P content of the coatings. Temperature and applied current density had the strongest effect on P content. The P content of coatings deposited from a bath containing 1 M $NaH_2PO_2 \cdot H_2O$ decreased from 28 to 13 at% as temperature decreased, applied current density increased, and pH decreased

to 1. The P content of coatings deposited from baths containing 0.5 M $NaH_2PO_2 \cdot H_2O$ decreased from 12 to 4 at% with simultaneous decreases in temperature and increases in applied current density [64]. Additional information about the Ni-P electroplating bath can be found in Table A-43 in Appendix A.

2.8 Electrocatalytic Activities of Electroless Ni Coatings

Crystalline nickel phosphide is kinetically favourable for OER and HER because it is an n-type semiconductor. Its high electrical conductivity is also beneficial towards catalyzing OER [65]. Considering that Ni-P coatings can transform from an amorphous phase to crystalline Ni and Ni_3P with heat treatment, the electrocatalytic properties of heat treated Ni-P coatings should be like that of crystalline nickel phosphides [6], [24], [66]. Since heat treatment is commonly applied to improve a Ni-P coating's hardness, reduce internal stresses, and increase wear and possibly corrosion resistance, the assumption that electroless Ni-P coatings are catalytic towards OER and HER applies for most applications of electroless Ni-P coatings [19], [22], [24], [33], [34], [60], [66]. The crystalline phase of a material holds the dominant influence over the electrochemical property of that material. As such, heat treatment of electroless Ni coatings should improve electrochemical properties such as HER and OER catalytic activity by crystallizing the coating. Guo et al.'s work on hollow dendritic Ni-P structure and Surendran et al.'s work on interweaved Ni-P sponges demonstrate that heat treated electroless Ni-P coatings and nickel phosphides can catalyze both HER and OER [65], [67]. Details regarding their work are described below.

2.8.1 OER on Electroless Ni Coatings

Ni itself is catalytic for OER [31]. Therefore, various publications have utilized Ni foams, nanosheets, and other Ni structures (including mesoscale and nanoscale structures) to catalyze

OER [31], [68]. Modifying the structure of Ni is known to improve OER kinetics. Paul et al. utilized nanostructured Ni electrodes with recesses and pillars for increase surface area. They found that bubbles detach more easily from these electrodes and, therefore, improve mass transfer and OER activity and reduce reaction overpotential. Such improvements can be applied to improve the performance of secondary metal-air batteries [31]. Guo et al. applied electroless Ni-P plating on the blue wings of the Morpho butterfly and then dissolved the wings using phosphoric acid to form a hollow dendritic Ni-P structure. LSV measurements of this structure show that it has comparable OER catalytic activity as RuO_2. The Tafel plot slope for the Ni-P structure is like that of RuO_2 as well, which further suggests favourable reaction kinetics for OER. CV testing at a scan rate of 100 mV/s for 1,000 cycles showed negligible current loss, indicating that the Ni-P structure also has high durability. The cathodic current remained stable for over 24 h at an overpotential of 350 mV. A portion of this structure's high OER activity is due to its high Brunner-Emmett-Teller (BET) surface area of 43.6 m^2/g. The overall water electrolysis capability of the electrode was assessed by constructing an electrolyzer using the hollow dendritic Ni-P structure as both the anode and cathode in a two-electrode system and comparing it to another electrolyzer made with Pt/C and RuO_2-modified glass carbon electrode as cathode and anode, respectively. Both systems used 1 M KOH as the electrolyte. The Ni-P || Ni-P system required 1.63 V to maintain a water splitting current density of 10 mA/cm^2, while the Pt/C || RuO_2 system required 1.57 V. This result was considered impressive compared to other Ni-based bifunctional electrocatalysts in alkaline media reported at the time (2018). The stability of the hollow dendritic Ni-P electrode was tested by applying 10 mA/cm^2 for 24 h. A stable cell voltage of 1.60-1.63 V was obtained, indicating good durability [67].

Surendran et al. used Ni-P NPs to form an interweaved Ni-P sponge electrode. This sponge is a mixture of interlinked Ni_2P, $Ni_2P/Ni_{12}P_5$, and $Ni_{12}P_5$. Three electrode types were manufactured and tested: Ni_2P, $Ni_2P/Ni_{12}P_5$, and $Ni_{12}P_5$. The OER electrocatalytic activity of the electrodes and carbon cloth were tested by LSV. The $Ni_2P/Ni_{12}P_5$ electrode showed the best OER catalytic activity due to its low onset potential and overpotential. However, this is still lower than other Ni-based electrodes reported in literature. Continuous gas bubble formation and negligible behavioural changes were noted during chronoamperometry testing of $Ni_{12}P_5$ electrode at a constant potential for 25 h. Such stability indicates that the $Ni_2P/Ni_{12}P_5$ is highly stable for OER [65]. Amorphous Ni-P may result in better OER catalytic activity than crystalline nickel phosphide phases.

In short, electroless Ni-P coatings are known to be electrocatalytic towards OER, and this catalytic activity can be improved upon by increasing the surface area of the Ni-P coating [31], [67]. The Ni-P coated electrode manufactured by Guo et al., intended for use in water splitting applications, performed better than other Ni-based bifunctional catalysts reported at the time due to their lower overpotentials and high durability in cycling and 24 h continuous electrolysis tests. Presumably other electroless Ni coatings, such as Ni-B and Ni-W-P, and composite coatings like Ni-P/nano SiC may also be catalytic towards OER. Ni-P coatings may exhibit higher OER catalytic activity in the amorphous phase than in crystalline phases [65].

2.8.2 HER on Electroless Ni Coatings

H_2 evolution is observed when substrates corrode because their electroless Ni coatings were unable to protect them. Visible H_2 evolution (bubble formation on coatings) is, therefore, an indicator of the coating unable to protect its substrate [27], [38]. H_2 evolution may also occur during the electroless plating process, which could generate porosity in the coating. The effect of this porosity

on coating performance is discussed in Section 2.9.3.2 [36], [41]. The catalytic activity of Ni-P coatings towards HER is discussed below. HER should be avoided for Zn-air batteries, so the findings discussed below are for information purposes [68], [69]. The reasons for avoiding HER in Zn-air batteries are detailed in Section 2.8.3.

The HER activity of the hollow dendritic Ni-P structure manufactured from blue Morpho butterfly wings, described in Section 2.8.1, was also tested by Guo et al. The Ni-P structure had excellent electrocatalytic behaviour towards HER comparable with other Ni-based catalysts in alkaline electrolytes. The Tafel slope of this Ni-P structure was higher than of Pt/C and is considered to be moderate for Ni-based alloys. The current loss after 1,000 CV cycles was negligible and a stable current density was maintained for 24 h at ~37.5 mA/cm^2 at an overpotential of -200 mV. These values indicate that the stability of this structure for catalyzing HER is also excellent [67]. Electroless Ni-P coatings used in in Zn-air batteries should, therefore, avoid such a structure to minimize HER.

Shibli et al. created coated electrodes by electroless Ni-P-TiO_2-MnO_2 plating mild steel. TiO_2 and MnO_2 were secondary phase particles embedded in the Ni-P coating. These secondary phase particles were chosen as they are known to be photo- and electroactive and could modify the electrochemical properties of the Ni-P coating. The coatings were heat treated after plating. The effect of different NaH_2PO_2 content in the plating bath and different heat treatment temperature were assessed. A NaH_2PO_2 content of 25 g/L and a heat treatment temperature of 200°C were found to be optimal. The coatings had low porosity and high HER catalytic activity (as indicated by low overpotentials, high exchanged current densities, and low Tafel slopes). The optimal coating was highly stable in 32% w/v NaOH solution. The high catalytic activity of the coating

was due to synergistic interactions between the TiO_2 and MnO_2 NPs and the Ni-P present at the coating surface. The optimized coating had 11.3 at% P and 14.4 at% O contents at the surface [58]. To minimize HER in Zn-air batteries, the electroless plating baths should not incorporate MnO_2 or TiO_2 NPs.

LSV was performed on Surendran et al.'s interweaved nickel phosphide sponge electrodes to evaluate their HER catalytic activity. The $Ni_2P/Ni_{12}P_5$ electrode's onset potential was -0.17 V vs. RHE at a scan rate of 5 mV/s and an overpotential of 234 mV was needed to obtain a current density of 10 mA/cm^2. These values are lower than other values reported for Ni-based HER electrodes. Gas evolution occurred continuously during 25 h of CA, and no major changes in the electrode's morphology were observed by FESEM after the CA test. These results indicate that the $Ni_2P/Ni_{12}P_5$ electrode is well suited for catalyzing HER. Ni_2P was found to inhibit HER the most [65]. The Ni-P coating should remain amorphous to prevent nickel phosphide phases from forming, which would minimize HER catalytic activity.

Hu et al. reviewed the HER catalytic activities of electroplated Ni-P alloy electrocatalysts and concluded that although the electroplating process requires only mild preparation, and has low costs and high safety, the formed Ni-P alloy was generally amorphous, which may limit the alloy's intrinsic activities, and the structures and morphologies were difficult to control. These effects result in relatively inferior HER activities compared to Ni-P catalysts made from other methods like the solution-phase method [70]. These findings confirm that the Ni-P coating should be amorphous to minimize HER catalytic activity.

In short, many publications have reported on the HER catalytic abilities of nickel phosphides and electroless Ni coatings. These publications find that nickel phosphide electrodes, such as

$Ni_2P/Ni_{12}P_5$, and Ni-P coatings, such as the hollow dendritic Ni-P structure made from blue Morpho butterfly wings and Ni-P-TiO_2-MnO_2 composite coatings, are highly catalytic towards HER. HER activity can be reduced by reducing the coating surface area, not incorporating TiO_2 and MnO_2 NPs, reducing surface P and O contents, and by avoiding heat treatment [58], [65], [67], [70].

2.8.3 Electroless Ni Coated Zn-Air Battery Components

HER poses a problem for metal-air batteries like Zn-air batteries that may use electroless Ni plated components as the air electrode [68], [69]. Chiefly, the problem with HER for Zn-air batteries is that it reduces the battery's storage capacity and the generated hydrogen gas can be explosive [2], [3]. The high pH electrolyte used in most Zn-air batteries does decrease the quantity of hydrogen evolution [5], [36]. It should be noted that the issue of HER from the Zn electrode is well known and many solutions have been formulated against it. Techniques applicable to Ni-coated air electrodes include increasing the KOH and zincate ion concentration of the electrolyte [5], [69]. Nano- and mesoscale features are known to alter the kinetics of OER and HER by easing gas bubble detachment [31]. Given that many electroless Ni-P coatings are amorphous as-deposited, or in a mixed crystalline-amorphous phase after heat treatment, electroless Ni coated Zn-air battery components likely somewhat inhibit HER since the amorphous phase shows reduced HER activity [6], [24], [25], [34], [38], [61], [70]–[72].

2.9 Breakdown Mechanisms for Electroless Ni Coatings

2.9.1 Thermal Expansion Coefficient Differences

Buchtík et al. investigated the effect of heat treatment on Ni-P coatings deposited on AZ91 substrates. Although the differences in thermal expansion coefficient (TEC) between the AZ91

substrate and the Ni-P coating may lead to tension at the interface, they did not observe visible cracks or delamination at the substrate/coating interface [6]. Iranipour et al. observed microcracks after heat treating their Ni-P coating deposited on a WE43 substrate at 400℃ for 1 h. They attributed this to tensile stresses generated by the different TECs (~27 μm/m·K for WE43 and 11-13 μm/m·K for the coating) [72]. For reference, tensile internal stresses of 15 to 45 MPa have been reported for electroless Ni-P coating by other authors arising from differences in TEC between the substrate and coating. The internal stresses are believed to promote cracking and porosity in the coatings. P content has a significant effect on TEC. For reference, the TEC of high P coatings is approximately equal to that of steel. The TEC of electroless Ni-B is also similar to that of electroless Ni-P: 12.6 μm/m·K for 5 wt% B borohydride-reduced Ni-B coating and 12 μm/m·K for a hypophosphite-reduced Ni-P coating containing 10.5 wt% P [26].

In summary, despite the low number of publications reporting on the TEC differences causing cracks in electroless Ni coatings, the likelihood still exists and should be considered carefully when heat treatment is applied to electroless Ni coatings [6], [26], [72].

2.9.2 Internal Stresses from Structural Changes and Codeposition

Structural changes during heat treatment above 220℃ for Ni-P coatings can lead to volumetric shrinkage of the coating by up to 4 to 6 %, increasing internal tensile stresses and reducing internal compressive stresses. The codeposition of orthophosphites or heavy metals and the presence of excess complexing agents can also increase the tensile stresses of Ni-P coatings. For example, adding 5 mg/L Bi and Sb to most plating baths using hypophosphite as the reducing agent may increase coating stress as much as 350 MPa, severely reducing the coating's ductility and increasing cracking. The internal tensile stress of Ni-B coatings deposited from plating baths using

borohydride as the reducing agent is generally quite high at 110 to 200 MPa, but may be as high as 480 MPa for coatings deposited using pyrophosphate as a complexing agent with a B content of 0.4 wt% [26].

2.9.3 Adhesion Failures

2.9.3.1 General Notes on Electroless Ni Coating Adhesion

The adhesion of electroless Ni coatings to most metals is excellent, but good adhesion requires proper cleaning of the substrate during pretreatment. The replacement reactions shown in Equation 2-9 and Equation 2-10, which occur for catalytic materials like Ni, establish mechanical bonds between the coating and the substrate that increase the overall adhesion [24], [26].

$$3Ni^{2+} + 2Al \longrightarrow 3Ni + 2Al^{3+} \qquad \text{Equation 2-9}$$

$$Ni^{2+} + Zn \longrightarrow Ni + Zn^{2+} \qquad \text{Equation 2-10}$$

Conversely, noncatalytic or passive materials like stainless steels do not have these replacement reactions and, therefore, have reduced adhesion; however, proper pretreatment and activation can provide bond strengths exceeding 140 MPa. Metals like Al can be heat treated after electroless plating for 1.5 h at 190 to 210℃ for increased adhesion. The heat treatment relieves hydrogen from the coating and the substrate and allows a very small amount of codiffusion between the substrate and coating. Heat treatment is recommended for parts with inadequate pretreatments and low adhesion strengths, but properly applied coatings do not see significant increases in bonding strength with baking [24], [26].

2.9.3.2 Adhesion Failures from Corrosion

Corrosion through the coating can lead to coating debonding and delamination. Corrosive media that corrodes through the coating could provoke a strong galvanic response between the coating and the Mg or Mg alloy substrate, which would lead to etch pit formation, debonding of coating, and interfacial delamination [14]. Since electroless Ni coatings are cathodic to Mg and Mg alloy substrates, these coatings act only as barriers against corrosion, meaning that the coatings need to be as pore and defect free as possible to protect the substrate from corrosion [8], [14], [15], [22], [26], [28], [36]. Heat treatment, noted for improving or otherwise altering the properties of electroless Ni coatings, can affect the corrosion morphology of the coating, but not the coating's porosity, making heat treatment ineffective at reducing coating porosity [24]. Continuous porosity through the coating may form from HER during the plating process as hydrogen gas bubbles escape from the coating/substrate interface [25], [29], [34]–[36], [41]. Electroless plating from alkaline baths has been noted to reduce HER since the bath's pH is quite high. Plating baths should, therefore, be alkaline for reduced coating porosity [5], [36]. The continuous pores act as electric current paths, leading to strong galvanic corrosion between the coating and the substrate and reducing the overall corrosion resistance of the coating. It is for this reason that HER should be avoided during the plating process [41]. Note that discontinuous pores lead to improved corrosion resistance since there is no continuous electric current path to enable corrosion. Discontinuous pores are, therefore, preferrable to continuous pores [24], [25], [28], [29], [33], [35], [36], [39], [41].

2.10 Summary

Magnesium, despite possessing many attractive qualities such as low density, good machinability, ease of recyclability, has seen limited usage due to its poor wear resistance and high chemical activity (leading to a correspondingly low corrosion resistance). Electroless Ni plating has emerged as a promising method of coating Mg for widespread usage. The high chemical activity of Mg necessitates a robust pretreatment process to remove the oxide/hydroxide films that may form on the surface. The plating processes and plating bath compositions and operating conditions have similarly stringent requirements. Electroless Ni-P coatings remain the most researched coating type, although Ni-B coatings and composite coatings involving multiple electroless Ni coating layers, nanoparticle incorporations, and electroplated Ni and Ni-P layers have also been researched. Ternary alloy coatings, such as Ni-P-Zn and electroplated Ni and Cu coatings, have also been explored. The corrosion resistance of the reported coatings varies, as does the environmental impact of the manufacturing processes (judged in this work by the usage of Cr(VI) and HF acid or NH_4HF_2). Electroless Ni-P coatings, and other Ni-P coatings have been studied for use as electrocatalysts for OER and HER. Some of these coatings are competitive with other Ni-based electrocatalysts in terms of OER and HER performance. However, electroless Ni coatings, being typically amorphous, likely show limited HER catalytic activity. Electroless coatings are beneficial for Zn-air battery applications, which require high OER activity and low HER activity. Electroless Ni coatings may break down from TEC differences, internal stresses from structural changes and codeposition, and adhesion failures from corrosion. Of these three, adhesion failure from corrosion is the most well-known, and effort should be concentrated on improving corrosion resistance when developing long-lasting electroless Ni coatings.

3 Coating Characterization

3.1 Introduction

The protective ability of electroless Ni-P coatings on many engineering materials is limited by coating porosity. Properties such as coating density and toughness are also significantly affected by porosity [62]. A Ni-P coating on Mg also exemplifies the classic example of a cathodic coating on an anodic substrate. In this case, the coating cannot offer any sacrificial protection and is purely a barrier protection. Consequently, any through-thickness porosity exposes a very small anodic area to corrosion, leading to rapid corrosion of the Mg substrate due to the large corrosion current density i_{corr} generated [73]. As a result, quantification, characterization, and reduction of coating porosity is crucial in determining and enhancing the protective ability [62].

Some authors have suggested using a colour-changing reagent solution to quantify the porosity for Ni-P coatings on Mg and its alloys. This involves utilizing an aqueous solution that is reactive with Mg or Al (for the case of alloys containing Al) [25], [33], [36], [37], [62]. The subsequent reaction products interact with the reagent solution, causing it to change colour. Lian et al. and Zhang et al. used a reagent solution with the primary components being NaCl and phenolphthalein. They soaked a filter paper in this reagent solution and then applied the paper to their coatings for 10 min. They then removed the filter paper and noted the ratio of red spot areas to zone area (the area in contact with the filter paper) on the coating and used this ratio to quantify the porosity of their coatings. The principle behind this technique is that as Mg corrodes and H_2 is evolved, a pH change will occur that causes the phenolphthalein indicator to change from colourless to red or pink. This is shown in Equation 3-1 and Equation 3-2 [25], [33], [36], [37].

$$Mg \longrightarrow Mg^{2+} + 2e^{-}$$ Equation 3-1

$$2H^{+} + 2e^{-} \longrightarrow H_2 \uparrow$$ Equation 3-2

Li et al. devised a similar porosity test by first soaking their coatings in a "corrodkote" solution, whose primary components are HCl and NaCl, for 5 min. The coatings were soaked in a reagent solution for 3 min. Three reagent solutions were tested: eriothrome black T, magneson, and sodium alizarinesulfonate. The coatings were then drawn onto a filter paper, and the porosity of the coating was calculated using Equation 3-3, where *n* is the number of colour spots present on the filter paper and *s* is the surface area of the coating.

$$\text{Porosity} = \frac{\text{n}}{\text{s}}$$ Equation 3-3

The *n* value is worth one count for spots less than 1 mm in diameter, three counts for spots 1-3 mm in diameter, and 10 counts for spots greater than 3 mm in diameter. Li et al. found that eriothrome black T worked the best since it formed a soluble Mg complex that passed through the pores and wetted the filter paper better. Magneson formed an insoluble Mg complex that did not transfer easily from the pores to the filter paper, resulting in many smaller pores not being counted. Sodium alizarinesulfonate formed an insoluble Al complex, but since their tests were performed on AZ91D, which contains only 9.1 wt% Al, this reagent solution only revealed larger pores [62].

Such reaction-based porosity testing can only document porosity present at the surface and large pores visible only with the naked eye. Additionally, the reagent solution may spread slightly due to high wettability and inflate the subsequent porosity measurement. This author attempted to use Lian et al.'s technique on Ni-P coatings deposited on Mg with inconclusive results. As such, Lian et al.'s technique was not used to quantify the porosity for the coatings in this project. Instead, a

novel porosity characterization technique was developed by the author and members of Ivey's research group that is capable of documenting through-thickness porosity that is much smaller in size than that in the reaction-based methods across a larger area than conventional cross section samples [25], [33], [36], [37], [62]. Through-thickness dimples less than 2 mm in diameter were machined into Ni-P coatings using a dimple grinder and pores observed using an optical microscope (OM) were then characterized (Figure 3-1). This technique permits plan-view characterization of porosity present through the coating's thickness using a simple polishing method. The sample preparation process for this technique is less labour intensive than that for making cross section samples as required by the ASTM B748-90 standard [74].

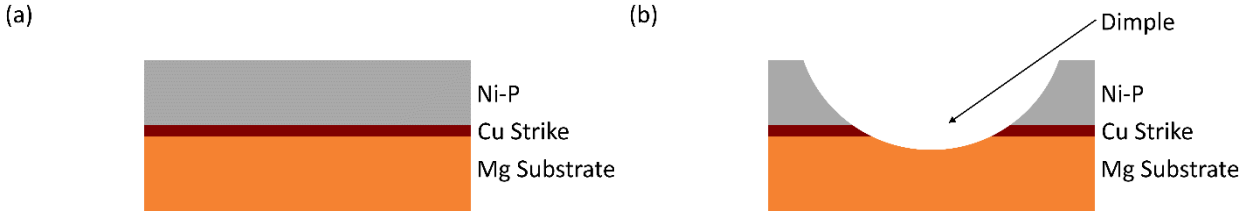

Figure 3-1: Side-view dimple grinding schematic of a) pristine coating and b) dimple in coating.

In this work, the macroscopic scale porosity (defined as pores larger than 4 µm) and microscopic scale porosity (defined as pores smaller than 4 µm) within various electroless Ni-P coatings deposited on Mg were characterized using dimple polishing coupled with OM and scanning electron microscopy (SEM) and SEM observation of coating cross sections, as specified by the ASTM B748-90 standard, and carried out by the author and Dr. Anqiang He, respectively [74]. The 4 µm limit for macroscopic pores was set by the minimum resolution of the OM camera, as this corresponds to a length of approximately 5 pixels, which is the minimum length needed to distinguish between porosity and surface contaminants.

3.2 Experimental

3.2.1 Coating Deposition Process

The exact deposition process for the Ni-P coated bars analyzed in this project is not known. The coated bars were provided by Zinc8 Energy Solutions, who received them from a third party. The overall deposition process is tabulated in Table 3-1. Generally, Mg samples are first mechanically ground or sandblasted and then chemically cleaned and acid pickled. Mechanical grinding or sandblasting is used to remove surface contaminants and to ensure uniform surface roughness across all samples. The chemical cleaning further removes any surface contaminants and greases and can be performed by ultrasonically cleaning the samples in acetone or an alkaline substance such as NaOH. Acid pickling is used to remove surface oxides and roughen the substrate surface to create sites for mechanical interlocking to improve adhesion. This can be done with acids such as CH_3COOH or H_2CrO_4 with HNO_3. Acid activation creates a chemical conversion coating on the substrate to prevent reoxidation and is traditionally performed using HF or NH_4HF_2 with an acid like H_3PO_4 to create a MgF_2 conversion coating [7], [24]. A Cu strike may be applied after activation to create a base layer for electroless Ni-P plating [10], [20], [23], [28], [49]. The electroless Ni-P coating is likely deposited from a NaH_2PO_2 bath. Such a bath typically uses $NiSO_4$ as the Ni source, NaH_2PO_2 as the reducing agent to supply electrons and P, complexing agents such as citric acid or succinic acid to reduce the amount of free Ni^{2+} in solution and to prevent Ni salt precipitation, a pH buffering agent such as acetate or succinate salts to control pH changes, accelerators such as succinic acid to counter the reduced reaction speed caused by the complexing agents, and stabilizers such as thiourea to prevent spontaneous bath decomposition since the plating bath is a metastable system. Ammonia or hydroxides are also periodically added to

neutralize the acid formed during plating [26]. The addition of an appropriate complexing agent has been shown to increase the plating rate [53]. Stabilizers are especially important for reactive substrates such as Mg and its alloys [23], [53], [54].

Table 3-1: General electroless Ni-P deposition process [10], [49]

Mechanical grinding or sandblasting
Chemical cleaning
Acid pickling
Acid activation
Copper striking
Electroless Ni-P plating

3.2.2 Examined Coatings

Various electroless Ni-P coatings were examined. All coating samples were 15 cm X 15 cm X 1 cm in size. The list of coatings examined are tabulated in Table 3-2. Some coatings (coatings #1 and #6, for example) were single layer whereas some had multiple layers (e.g., coatings #2 and #3). Some coatings had a Cu strike layer (such as coatings #2 and #3). The purpose of the Cu strike layer was to improve adhesion between its underlayer (layer beneath it) and overlayer (layer above it). Some coatings contained a Cu strike layer between two Ni-P layers (such as coating #2), while others had a Cu strike layer adjacent to the Mg substrate (such as coating #3). The P content of the Ni-P layers also varied; some layers had low P content (1-4 wt%), some had medium P content (5-8 wt%), and some had high P content (greater than 10 wt%). LPEN, MPEN, and HPEN are the acronyms used for low, medium, and high P content Ni-P layers [75]. The sandblasting grit number used for each coating varied from 80-240 grit number, with most using 120 grit number. The uppermost layer is listed first, with subsequent layers listed afterwards. For example, the top layer

of coating #3 was a medium P content Ni-P layer, and beneath that was a high P content Ni-P layer, followed by a Cu strike layer, and finally the Mg substrate at the bottom.

The effect of P content, sandblasting grit number, Cu strike presence, and total coating thickness on coating porosity were determined through comparative analysis between different coatings; e.g., the effect of sandblasting grit number was determined by comparing coatings #6, #7, #8, and #11, with all other deposition parameters being the same. Coatings #6-#19 were specifically commissioned to identify the effects of the four plating parameters on coating porosity. The coatings were provided by four manufacturers, so their P content may vary slightly despite all coating conforming to the classifications of LPEN, MPEN, and HPEN.

Table 3-2: List of analyzed coatings and their sandblasting grit number; layer structure is from top surface to substrate

Coating Number	Layer Structure	Sandblasting Grit Number
1	MPEN Mg	120
2	MPEN Cu Strike MPEN Mg	120
3	MPEN HPEN Cu Strike Mg	120
4	LPEN HPEN Cu Strike Mg	120
5	LPEN HPEN Cu Strike Mg	120

6	MPEN Mg	80
7	MPEN Mg	150
8	MPEN Mg	240
9	LPEN Mg	120
10	LPEN Cu Strike LPEN Mg	120
11	MPEN Mg	120
12	MPEN Cu Strike MPEN Mg	120
13	HPEN Mg	120
14	MPEN Cu Strike MPEN Mg	120
15	MPEN Cu Strike MPEN Mg	120
16	MPEN Cu Strike MPEN Mg	120
17	MPEN Cu Strike MPEN Mg	120

18	MPEN Cu Strike MPEN Mg	120
19	MPEN Cu Strike MPEN Mg	120

3.2.3 Preliminary Crystallographic and Compositional Characterization

Preliminary microstructural characterization of the Ni-P coatings was performed on coating #1. This involved topographical and compositional analysis of the coating in cross section and in plan view orientations using an SEM (TESCAN VEGA 3) with an attached energy dispersive X-ray analysis detector (EDX, OXFORD), Vickers hardness measurements (Wilson HV3100), and crystallographic analysis, using X-ray diffraction (XRD, Rigaku XRD Ultima IV) and transmission electron microscopy (TEM, JEOL JEM-200 CF S/STEM). For XRD analysis, Cu K_{α} radiation was used at an operating voltage and current of 40 kV and 44 mA, respectively. The TEM was operated at an accelerating voltage of 200 kV. For helium ion microscopy (HIM, Zeiss Orion NanoFab) analysis of the cross section, the bar was sectioned using a Ga focused ion beam (FIB) instrument attached to the HIM. Both HIM and FIB utilized a 30 kV accelerating voltage and ~10 nA beam current. For TEM sample preparation, coating #1 was scraped from the substrate and ground using an agate mortar with reagent alcohol added. The powder was collected and placed on a carbon grid. The sample preparation process for plan view and cross section analyses samples are detailed in Sections 3.2.4 and 3.2.5.

3.2.4 Plan View SEM and EDX Analysis

The coated bars were heated alongside the sample mounts from the low-speed diamond saw on a hot plate at 140°C for 5 min before applying Crystalbond™ 509 adhesive to the sample mount. The bars were then pressed for 5 s onto the adhesive applied to the sample mount. The mounted bars were removed from the hot plate and cooled to room temperature over a 30 min period to allow the adhesives to fully harden. After cooling, the mounted bars were clamped onto the low-speed diamond saw's goniometer and 1.5 cm long bar segments were sectioned from the bars using triethanolamine-based, water-soluble coolant and a medium/fine grit - low concentration diamond wafering blade (Figure 3-2). The bars and bar segments were released from the sample mount by using the hot plate (heated to 140°C for 5 min to melt the Crystalbond™ 509 adhesive). The segments were ultrasonically cleaned using reagent alcohol and acetone and dried with dry compressed air before mounting on SEM stubs using carbon tape for plan view SEM and EDX analysis. The accelerating voltage used was 20 kV, with a working distance of 10 and 15 mm for SEM and EDX analysis, respectively.

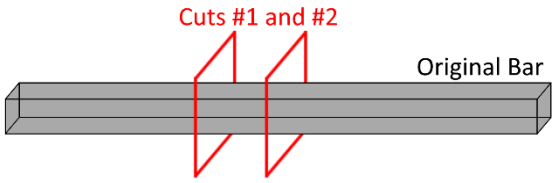

Figure 3-2: Sample preparation schematic for plan view SEM and EDX analysis (not drawn to scale).

3.2.5 Cross Section Sample Preparation and Analysis

The initial fabrication steps for cross section samples are t detailed in Section 3.2.3. One face was sectioned from each bar segment (Figure 3-3a). The faces removed were approximately 2 mm thick. The faces were sectioned in half to expose the cross section (Figure 3-3b) and one portion was then placed vertically upright into an epoxy mould, and Buehler EpoThin 2 epoxy hardener

and EpoThin 2 epoxy resin were then mixed at a mass ratio of 0.45:1 for 2 min using a clean wood stirring stick. The epoxy mixture was carefully poured into the mould, while ensuring that the coating piece did not topple, and allowed to harden over 9 h. After hardening, the mounted samples were removed from the mould and ground sequentially with 240, 400, 800, and 1200 grit SiC sandpapers. The samples were polished using 1 µm Al_2O_3 polishing suspension followed by 0.05 µm Al_2O_3 polishing suspension. The samples were then rinsed in deionized water for 2 min and ultrasonically cleaned in reagent alcohol for 10 min. After ultrasonic cleaning, the samples were rinsed with reagent alcohol and dried using dry compressed air. The epoxy resin blocks of the samples were carbon coated and a piece of carbon tape was used to connect the sample to the block's underside for electrical connectivity in the SEM. The cross sections of the samples were analyzed using a SEM equipped with EDX detector, with EDX being used to measure layer composition. Secondary electron (SE) and backscattered electron (BSE) imaging modes were used to analyze surface topography and distinguish between coating layers, respectively. At least three different locations were selected per coating and the measured thicknesses across the locations were averaged to obtain the layer thickness values. An example of cross section analysis from coating #3, is shown in Figure 3-4: Figure 3-4a shows the different layers of coating #3 and Figure 3-4b shows the composition of each layer. The Cu strike, MPEN, and HPEN layers are easily distinguishable using EDX analysis. Additional examples are shown in Appendix B (Figure B-1).

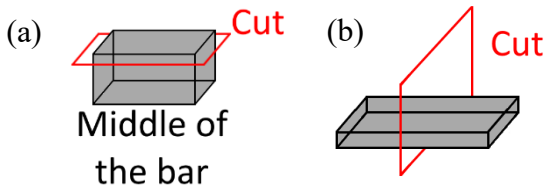

Figure 3-3: Sample preparation schematic for cross section analysis. a) Sectioning of one face from the bar segment and b) sectioning the face in half. Figure is not drawn to scale.

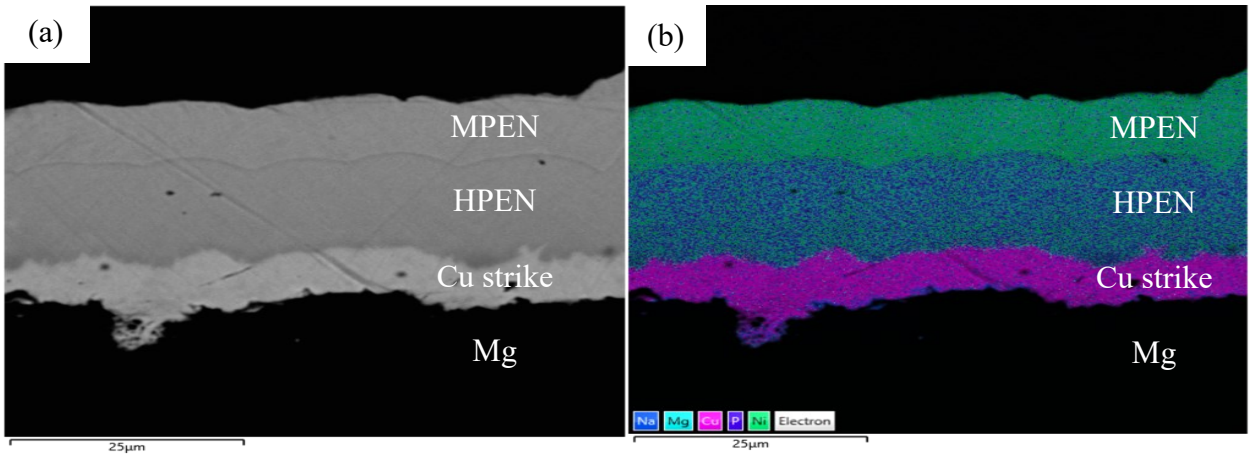

Figure 3-4: SEM BSE image of a) coating with Cu strike (#3), and b) layer composition analysis using EDX.

3.2.6 Microscopic-Scale Porosity Analysis

Cross section samples were used to characterize the microscopic-scale porosity (shortened to microscopic porosity) in the layers of each coating. The same locations utilized in Section 3.2.5 were used for this characterization. An accelerating voltage of 20 kV and a working distance of either 10 or 15 mm were employed. SEM BSE imaging mode was used to distinguish porosity from the coating. The number and longest length of each pore was measured, with data from all locations pooled together to calculate the microscopic porosity of each coating. The pores were assumed to be circular and their longest lengths were assumed to be their diameters. Equation 3-4 and Equation 3-5, and histograms were used to calculated microscopic pore areal density (MiPAD), microscopic pore area percentage (MiPAP), and pore length distributions. These lengths do not exceed 4 µm.

$$\text{Pore Areal Density} = \frac{\text{Number of pores}}{\text{Area of Analyzed Region}} \qquad \text{Equation 3-4}$$

$$\text{Pore Area Percentage} = \frac{\text{Total pore area}}{\text{Area of Analyzed Region}} \qquad \text{Equation 3-5}$$

3.2.7 Dimple Analysis Sample Preparation

The initial fabrication steps of dimple analysis samples are similar to that plan view SEM and EDX analysis samples (Section 3.2.4), with one face from each segment being removed by another cut (Figure 3-5). The faces were then secured to the dimple grinder's sample mount with the Ni-P side facing up (Figure 3-6), using the hot plate and adhesive method described above.

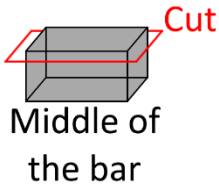

Figure 3-5: Sample preparation schematic for dimple analysis. Not drawn to scale.

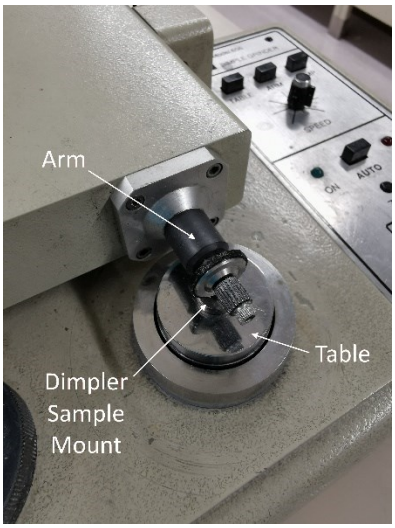

Figure 3-6: Labelled image of dimpler.

3.2.8 Macroscopic-Scale Porosity Analysis

After mounting, the sample was placed on the dimple grinder table and adjusted so that a dimple was machined away from the edges of the faces. A felt polishing wheel was used. A polishing suspension composed of 3 µm diamond paste mixed with a drop of distilled water and approximately 5 mL of reagent alcohol was used for dimple grinding. This suspension was applied to the grinding location, and the arm of the dimple grinder was lowered onto the face. The dimpler

grinder was then turned on and stopped every 2-10 min and the extent of dimpling was examined using an optical microscope. The process was continued until the Mg substrate was reached and is shown schematically in Figure 3-7. Three dimples were machined per sample. After dimpling, the samples were unmounted using the above procedure and cleaned ultrasonically in acetone for 5 min and then in reagent alcohol for 15 min before drying in air.

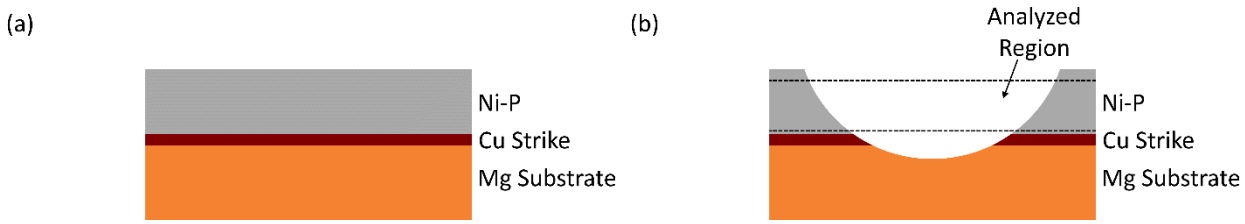

Figure 3-7: Schematic of dimpling process for coating containing Cu strike and one Ni-P layer, (a) before polishing and (b) after polishing. Figure is not drawn to scale.

Each dimpled face was placed onto the stage of a Leica DM2500M optical microscope, and each dimple was photographed with a Lumenara Infinity 1 camera attached to the microscope using a 5X objective lens. A composite image was created by piecing together the various images using Paint.net software. Macroscopic-scale porosity (shortened to macroscopic porosity) was calculated through analysis of the "Analyzed Region" labelled in Figure 3-7b. Two circles were then drawn using Paint.net and the regions between the circles ("Analyzed Region") were analyzed for porosity. This region represents the depth of the coating and provides through thickness macroscopic porosity measurements. The size of each circle and the number and length of the pores (measured by drawing the longest line from edge to edge for each pore) were recorded to calculate the pore areas (assuming each pore is circular). The outer circle corresponds to a coating depth just below the surface and the inner circle corresponds to a depth just above the substrate. For samples with Cu strike layers, the inner circle was drawn around the Cu strike ring. Two examples of the above are shown in Figure 3-8. Additional examples of dimple analysis are shown in Appendix B (Figure B-2). The macroscopic pore areal density (MaPAD), macroscopic pore area

percentage (MaPAP), and pore length distributions were then calculated using Equation 3-4 and Equation 3-5, and a histogram, respectively.

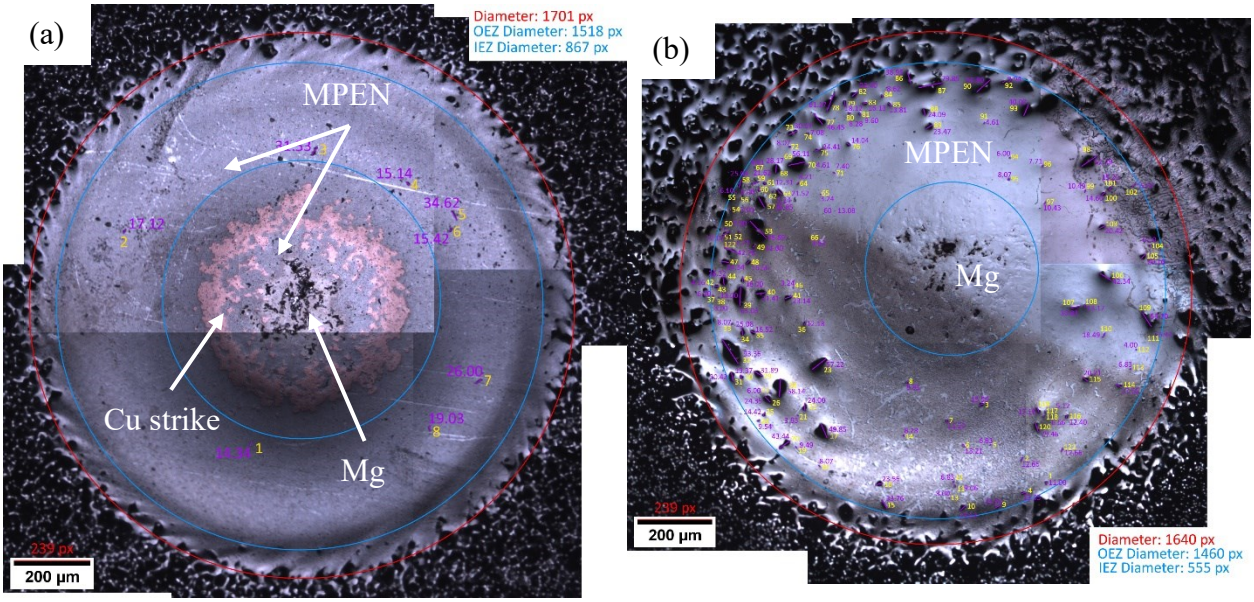

Figure 3-8: Example of dimple analysis on a) coating with Cu strike (#19) and b) coating without Cu strike (#6).

The validity of the dimple analysis method was confirmed using a TESCAN Vega 3 SEM with a 10 kV accelerating voltage and a working distance of 10 mm operating in SE imaging mode. The aim was to confirm that features identified as pores from the OM micrographs were indeed pores. An example of this analysis is shown in Figure 3-9. It is clear from the SEM image in Figure 3-9b, that the OM features in Figure 3-9a are pores that extend through the Ni-P layer.

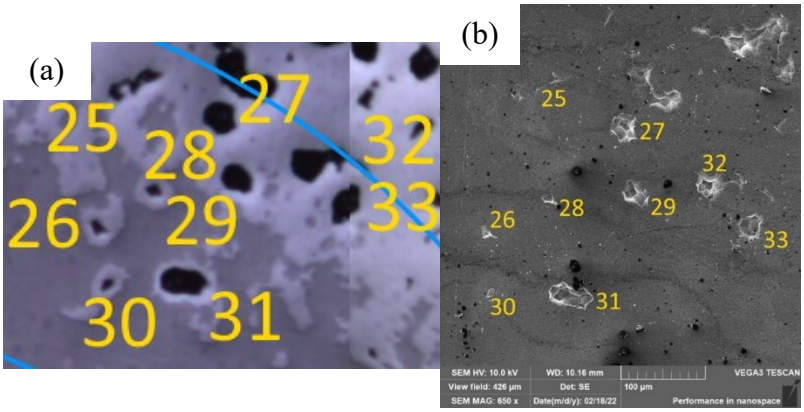

Figure 3-9: Pores observed from dimple on coating #4 identified by a) OM micrograph from dimple analysis and (b) SEM SE micrograph.

3.3 Results and Discussion

3.3.1 Preliminary Characterization of Coating #1

The surface morphology of coating #1 was analyzed using plan view SEM SE images (Figure 3-10). A compact, spherical nodular, "cauliflower-like" surface morphology with no cavities or crevices typical for electroless Ni-P deposits was observed [20], [24], [32], [37].

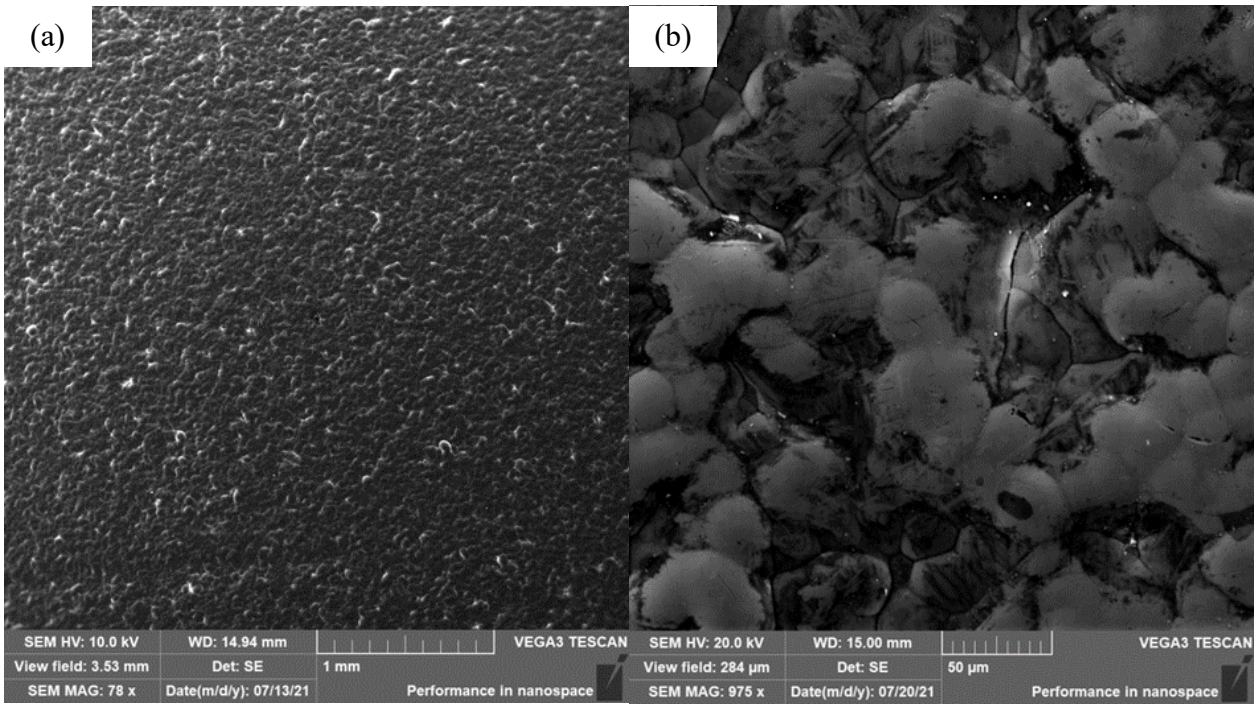

Figure 3-10: Plan view SEM SE images of the surface morphology of coating #1 at a) low and b) high magnification.

Cross section samples of coating #1 were prepared using manual polishing, autopolishing, and FIB milling using a Ga^+ ion beam. Manual polished and autopolished samples were analyzed using a SEM in SE mode and FIB samples were analyzed using a HIM (Figure 3-11). Manual polishing created slightly flatter samples than autopolishing. The striations in the HIM image are artifacts from the Ga^+ beam; these artifacts are less significant in the harder Ni-P layer. The Mg/MPEN interface is quite rough due to sandblasting of the Mg substrate during pretreatment.

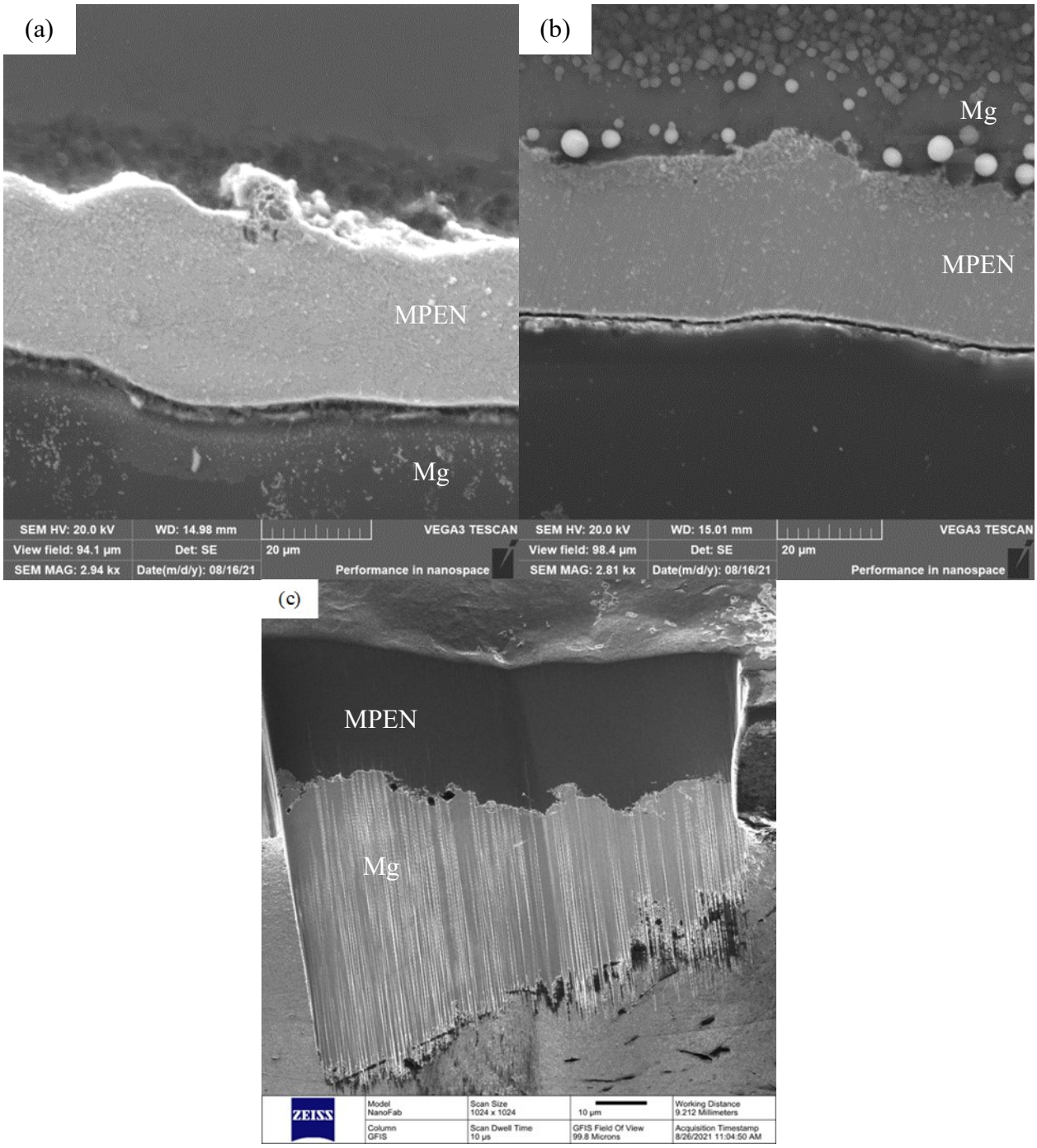

Figure 3-11: Coating #1 cross section prepared and imaged after a) autopolishing and SEM, b) manual polishing and SEM, and c) FIB milling and HIM.

Compositional analysis was performed using EDX in plan view and in cross section orientations (Figure 3-12). The plan view sample shown in Figure 3-12a was imaged using the SEM in SE mode. An EDX map of this sample is shown in Figure 3-12b and shows uniform Ni-P coating

coverage over the Mg substrate. The cross section sample shown in Figure 3-12c was prepared from Ga^+ ion focused ion beam sectioning. An EDX map of the cross section sample is shown in Figure 3-12d. The F enrichment at the interface is likely from the fluoride activation step during pretreatment [10], [24], [28], [35], [71]. The P enrichment at the interface could be from fluoride activation as well (H_3PO_4 in conjunction with NH_4HF_2) [24], [46]. The P content of coating #1 is 6-7 wt%; according to the literature, this corresponds to a mixed crystalline (Ni solid solution) and amorphous microstructure [76].

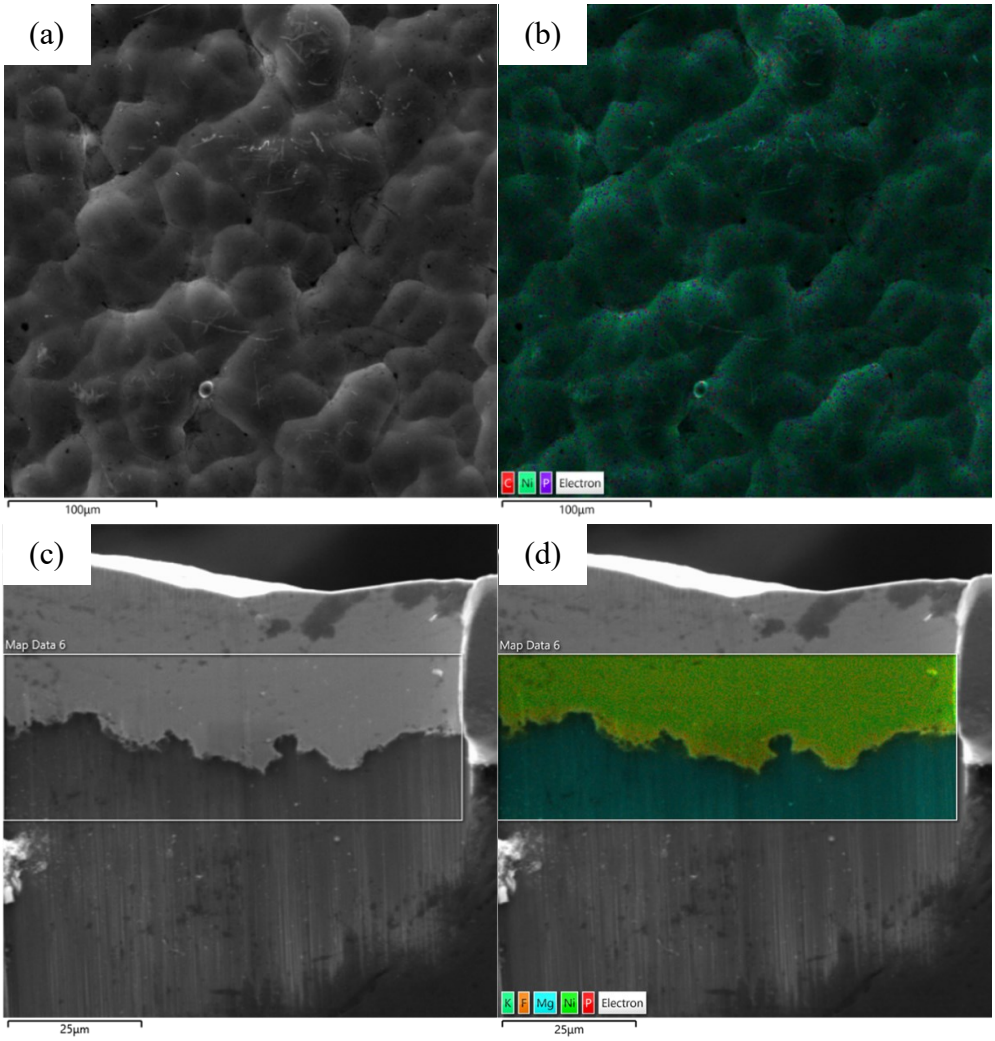

Figure 3-12: SEM SE image and EDX overlay map of coating #1 in a) plan view and b) cross section orientations, prepared by FIB.

Vickers hardness measurements were taken and are tabulated in Table 3-3. This hardness corresponds well to a mixture of Ni solid solution and amorphous phases heat treated at 365-400°C for 1 h [75].

Table 3-3: Vickers hardness measurements of coating #1

Measurement	Hardness (HV)
1	945.6
2	916.0
3	989.2
4	1041.6
5	1031.7
Average	984.8
Standard deviation	54.1

To confirm the presence of a mixed phase microstructure, XRD analysis was performed on coating #1 (Figure 3-13). Broad peaks were observed, suggesting a nanocrystalline (NC)/amorphous mixture that was indexed to Ni solid solution, confirming the EDX results.

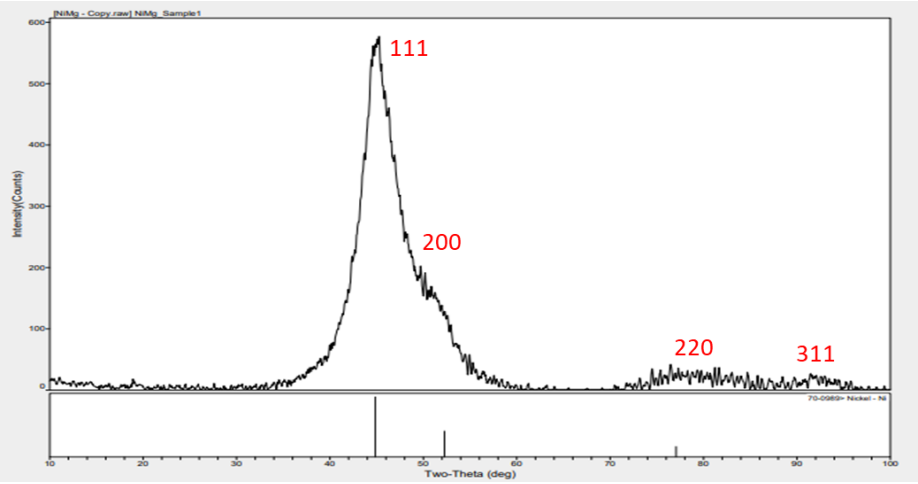

Figure 3-13: XRD pattern of coating #1.

Additional confirmation of the coating's microstructure was performed using TEM (Figure 3-14). A mixture of nanocrystalline (NC) and amorphous regions was observed: NC regions are shown

in blue and amorphous regions are shown in red (Figure 3-14a-b). The amorphous regions do not display regular repeatability in the crystal planes. Grains visible in the TEM bright field (BF) image are clearly NC and are between 5-21 nm in size. The rings of the selected area diffraction (SAD) patterns (Figure 3-14c) were indexed to Ni (PDF#87-0712), and the spots (S1-S5) were indexed to residual Mg from the substrate (PDF#89-5003). These findings further confirm the conclusions drawn from the SEM and XRD results that coating #1 is a mixture of NC and amorphous phases. A TEM dark field (DF) image was generated from the part of the first two rings of the SAD pattern and clearly shows the NC grains of the coating (Figure 3-14d).

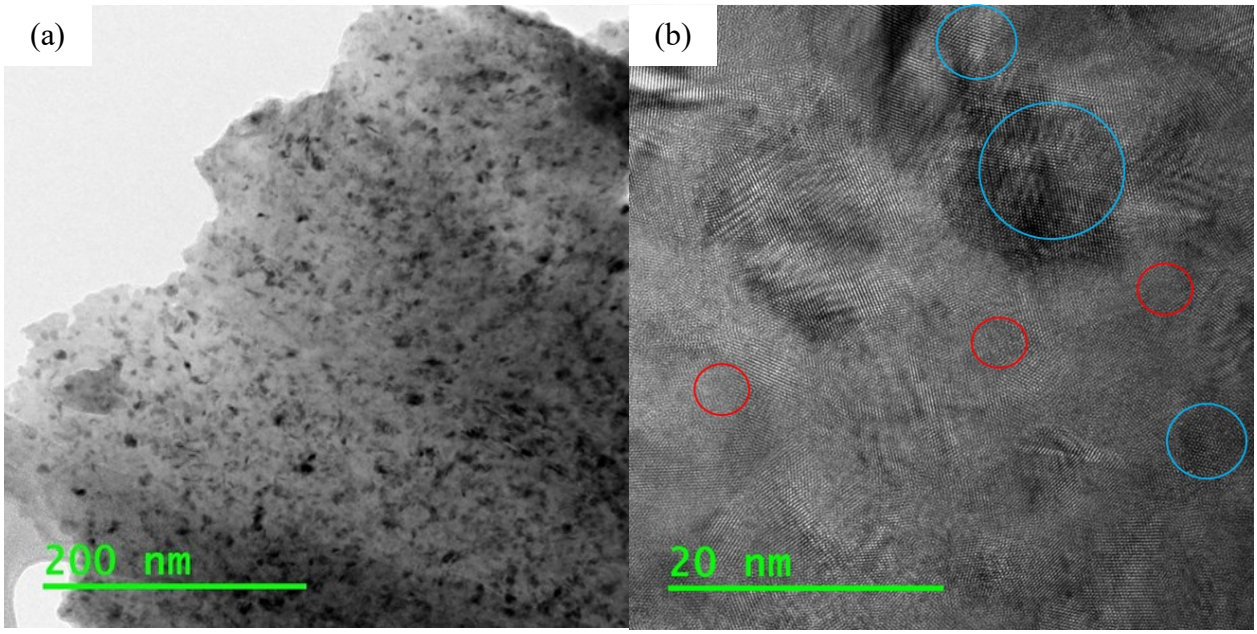

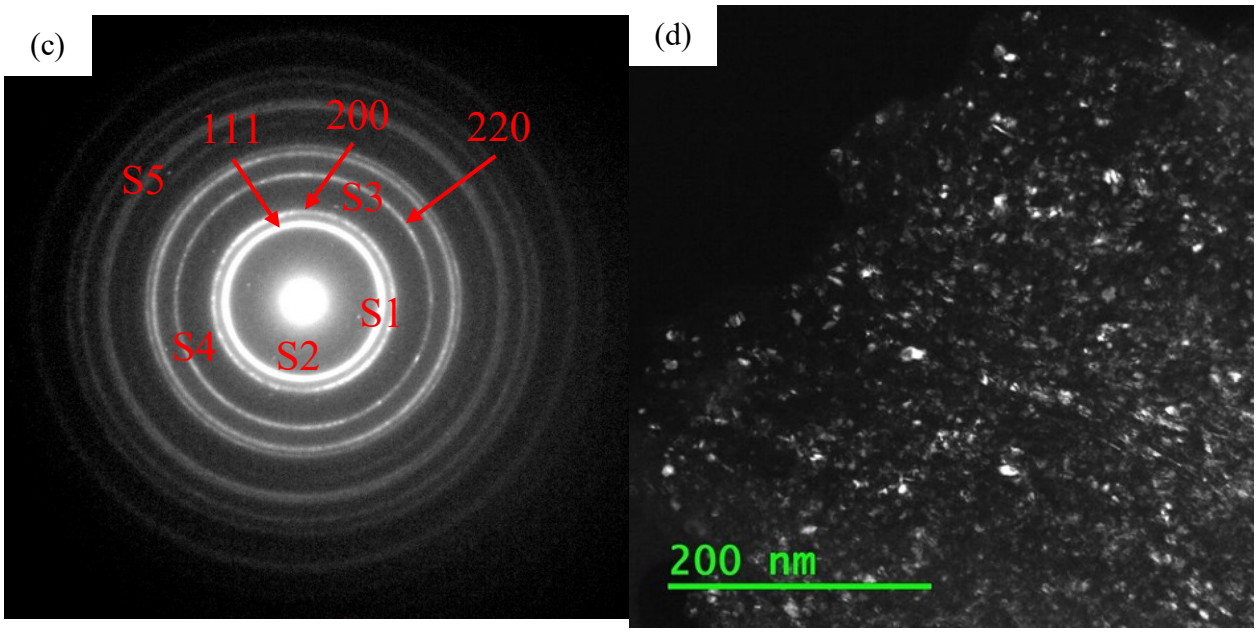

Figure 3-14: a) TEM BF image of coating #1, b) HRTEM of coating #1 with nanocrystalline regions circled in blue and amorphous regions circled in red, c) SAD pattern of coating #1, and d) TEM DF image generated from first two rings of SAD pattern.

3.3.2 Microscopic Porosity

The microscopic porosity of each coating is tabulated in Table 3-4 and shown in Figure 3-15 and Figure 3-16. The MiPAD axis in Figure 3-15 is in log-scale so that all data points can be displayed distinctly. Coating #3 had by far the highest Ni-P microscopic porosity while #2, #12, and #19 had the lowest. To confirm that the high Ni-P microscopic porosity of coating #3 was not a sampling error, another cross section sample was prepared and imaged using SEM (Figure B-3 in Appendix B). The second sample had visually similar amounts of porosity as the first. Apart from coating #3, #4 had the highest Ni-P microscopic porosity. Coating #12 had smaller pores than #2 and #19 (Figure 3-17), leading to a smaller MiPAP value despite the three coatings having comparable MiPAD values. The outer Ni-P layer of coating #3 had many large pores (Figure 3-17) which is why it has much higher MiPAP and MiPAD values than the other coatings. Coating #14 had the highest Cu strike microscopic porosity while coating #5 had the lowest (Figure 3-16). The

Cu strike of coating #14 had many larger pores, which is why its MiPAP is higher than #15 despite #15 having more pores. On the other hand, coating #5 had both few pores and small pores, resulting in it having the lowest Cu strike microscopic porosity of all analyzed coatings (Figure 3-16).

Table 3-4: Microscopic porosity results for outer Ni-P and Cu strike layers

	Ni-P		Cu Strike	
Coating Number	MiPAD (#/mm^2)	MiPAP (%)	MiPAD (#/mm^2)	MiPAP (%)
1	$6.47 \cdot 10^3$	0.152	-	-
2	$2.67 \cdot 10^3$ (inner and outer)	0.0889 (inner and outer)	-	1.71
3	$4.28 \cdot 10^5$ (outer) $1.80 \cdot 10^4$ (inner)	16.0 (outer) 0.581 (inner)	-	2.38
4	$2.15 \cdot 10^4$ (outer) $2.50 \cdot 10^4$ (inner)	2.19 (outer) 0.517 (inner)	-	0.332
5	$1.13 \cdot 10^4$ (outer) $8.93 \cdot 10^3$ (inner)	0.992 (outer) 0.511 (inner)	$2.00 \cdot 10^5$	0.271
6	$2.50 \cdot 10^4$	0.0800	-	-
7	$6.30 \cdot 10^3$	0.0700	$1.10 \cdot 10^5$	-
8	$1.60 \cdot 10^4$	0.0800	-	-
9	$1.80 \cdot 10^4$	0.290	$1.80 \cdot 10^5$	-
10	$3.40 \cdot 10^3$	0.0200	$2.90 \cdot 10^5$	1.87
11	$2.90 \cdot 10^3$	0.0300	$1.60 \cdot 10^5$	-
12	$2.60 \cdot 10^3$	0.0200	$2.00 \cdot 10^5$	1.34
13	$2.30 \cdot 10^4$	1.40	$1.60 \cdot 10^5$	-
14	$7.90 \cdot 10^3$	0.160	$1.47 \cdot 10^5$	3.89
15	$1.30 \cdot 10^4$	0.180	-	3.17
16	$1.10 \cdot 10^4$	0.150	-	2.00
17	$5.10 \cdot 10^3$	0.0400	-	2.30
18	$3.20 \cdot 10^3$	0.0400	-	2.40
19	$2.20 \cdot 10^3$	0.0400	$2.00 \cdot 10^5$	2.52

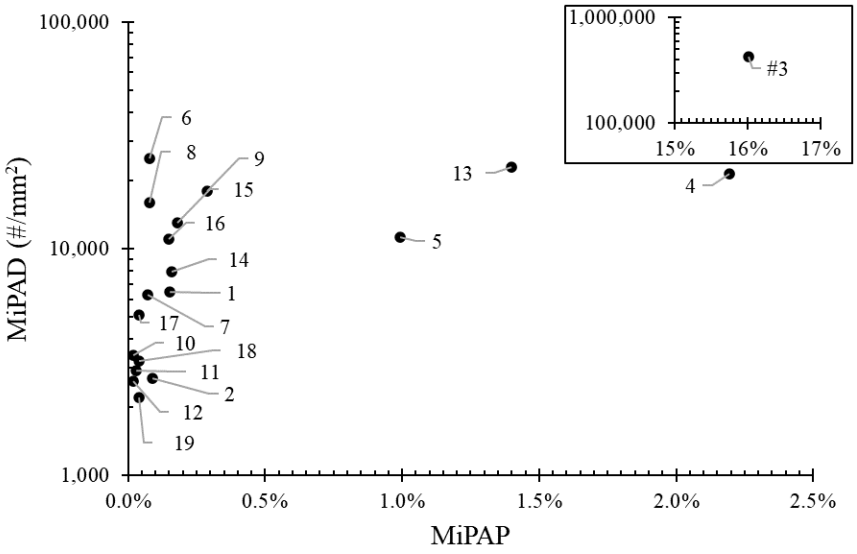

Figure 3-15: MiPAD vs. MiPAP for the outer Ni-P layers of all coatings (#2 is for the outer and inner Ni-P layers).

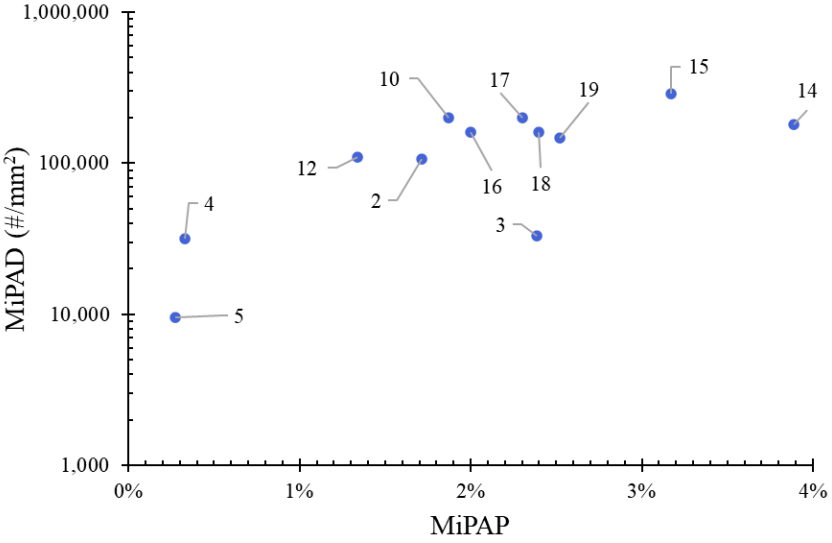

Figure 3-16: MiPAD vs. MiPAP for the Cu strike layers of all coatings.

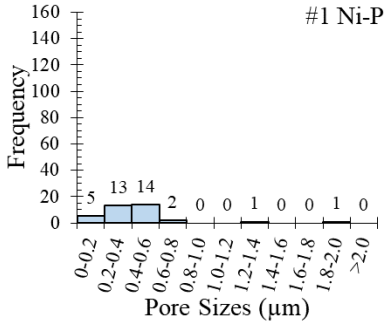

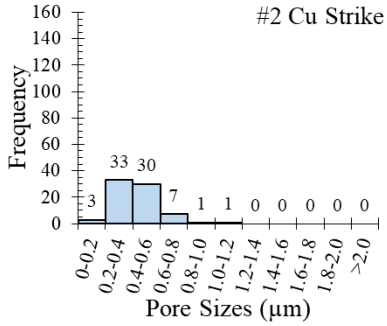
#2 Cu Strike
Frequency
Pore Sizes (µm)
0-0.2
0.2-0.4
0.4-0.6
0.6-0.8
0.8-1.0
1.0-1.2
1.2-1.4
1.4-1.6
1.6-1.8
1.8-2.0
>2.0
3 33 30 7 1 1 0 0 0 0 0

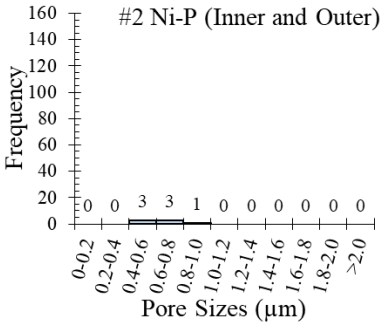
#2 Ni-P (Inner and Outer)
Frequency
Pore Sizes (µm)
0-0.2
0.2-0.4
0.4-0.6
0.6-0.8
0.8-1.0
1.0-1.2
1.2-1.4
1.4-1.6
1.6-1.8
1.8-2.0
>2.0
0 0 3 3 1 0 0 0 0 0 0

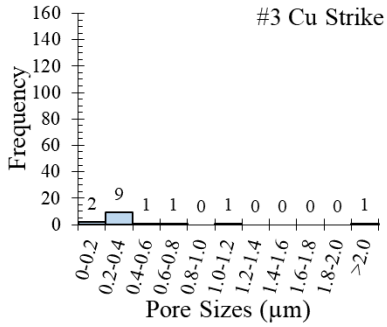
#3 Cu Strike
Frequency
Pore Sizes (µm)
0-0.2
0.2-0.4
0.4-0.6
0.6-0.8
0.8-1.0
1.0-1.2
1.2-1.4
1.4-1.6
1.6-1.8
1.8-2.0
>2.0
2 9 1 1 0 1 0 0 0 0 1

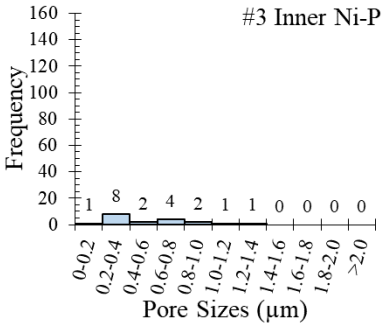
#3 Inner Ni-P
Frequency
Pore Sizes (µm)
0-0.2
0.2-0.4
0.4-0.6
0.6-0.8
0.8-1.0
1.0-1.2
1.2-1.4
1.4-1.6
1.6-1.8
1.8-2.0
>2.0
1 8 2 4 2 1 1 0 0 0 0

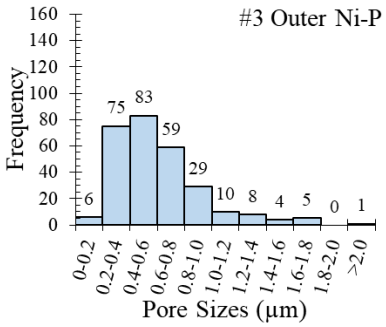
#3 Outer Ni-P
Frequency
Pore Sizes (µm)
0-0.2
0.2-0.4
0.4-0.6
0.6-0.8
0.8-1.0
1.0-1.2
1.2-1.4
1.4-1.6
1.6-1.8
1.8-2.0
>2.0
6 75 83 59 29 10 8 4 5 0 1

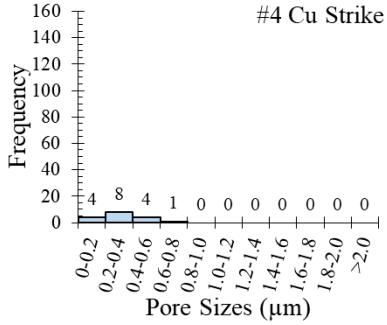
#4 Cu Strike
Frequency
Pore Sizes (µm)
0-0.2
0.2-0.4
0.4-0.6
0.6-0.8
0.8-1.0
1.0-1.2
1.2-1.4
1.4-1.6
1.6-1.8
1.8-2.0
>2.0
4 8 4 1 0 0 0 0 0 0 0

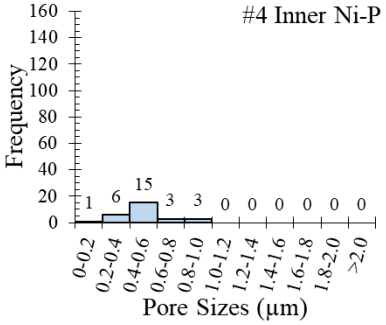
#4 Inner Ni-P
Frequency
Pore Sizes (µm)
0-0.2
0.2-0.4
0.4-0.6
0.6-0.8
0.8-1.0
1.0-1.2
1.2-1.4
1.4-1.6
1.6-1.8
1.8-2.0
>2.0
1 6 15 3 3 0 0 0 0 0 0

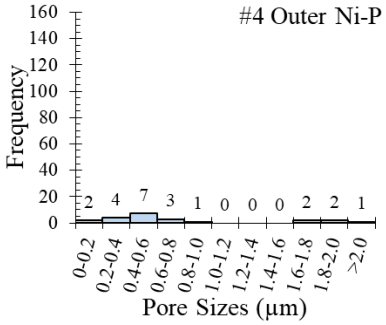
#4 Outer Ni-P
Frequency
Pore Sizes (µm)
0-0.2
0.2-0.4
0.4-0.6
0.6-0.8
0.8-1.0
1.0-1.2
1.2-1.4
1.4-1.6
1.6-1.8
1.8-2.0
>2.0
2 4 7 3 1 0 0 0 2 2 1

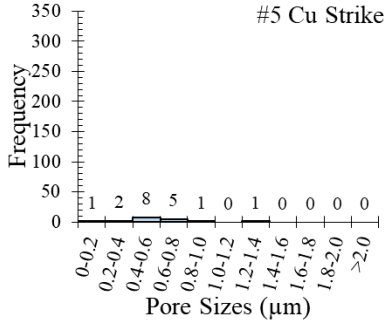
#5 Cu Strike
Frequency
Pore Sizes (µm)
0-0.2
0.2-0.4
0.4-0.6
0.6-0.8
0.8-1.0
1.0-1.2
1.2-1.4
1.4-1.6
1.6-1.8
1.8-2.0
>2.0
1 2 8 5 1 0 1 0 0 0 0

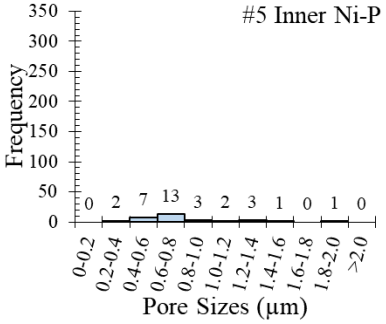
#5 Inner Ni-P
Frequency
Pore Sizes (µm)
0-0.2
0.2-0.4
0.4-0.6
0.6-0.8
0.8-1.0
1.0-1.2
1.2-1.4
1.4-1.6
1.6-1.8
1.8-2.0
>2.0
0 2 7 13 3 2 3 1 0 1 0

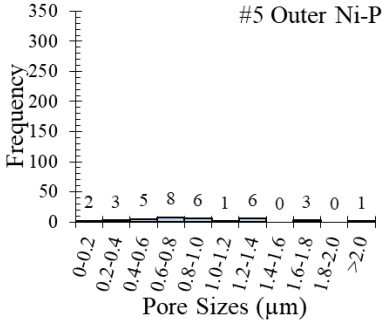
#5 Outer Ni-P
Frequency
Pore Sizes (µm)
0-0.2
0.2-0.4
0.4-0.6
0.6-0.8
0.8-1.0
1.0-1.2
1.2-1.4
1.4-1.6
1.6-1.8
1.8-2.0
>2.0
2 3 5 8 6 1 6 0 3 0 1

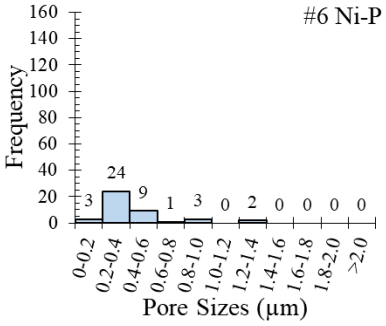
#6 Ni-P
Frequency
Pore Sizes (µm)
0-0.2
0.2-0.4
0.4-0.6
0.6-0.8
0.8-1.0
1.0-1.2
1.2-1.4
1.4-1.6
1.6-1.8
1.8-2.0
>2.0
3 24 9 1 3 0 2 0 0 0 0

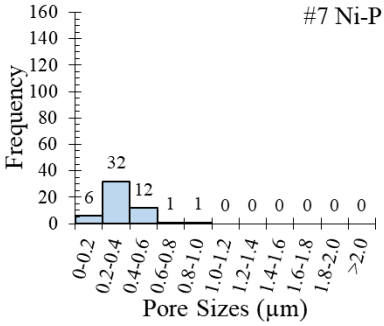
#7 Ni-P
Frequency
160
140
120
100
80
60
40
20
0
6
32
12
1
1
0
0
0
0
0
0
0-0.2
0.2-0.4
0.4-0.6
0.6-0.8
0.8-1.0
1.0-1.2
1.2-1.4
1.4-1.6
1.6-1.8
1.8-2.0
>2.0
Pore Sizes (µm)

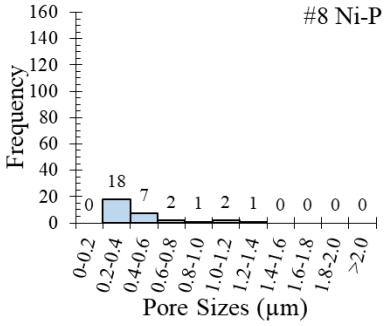
#8 Ni-P
Frequency
160
140
120
100
80
60
40
20
0
0
18
7
2
1
2
1
0
0
0
0
0-0.2
0.2-0.4
0.4-0.6
0.6-0.8
0.8-1.0
1.0-1.2
1.2-1.4
1.4-1.6
1.6-1.8
1.8-2.0
>2.0
Pore Sizes (µm)

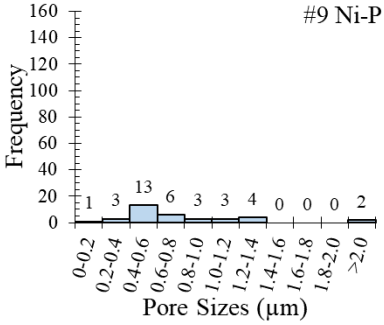
#9 Ni-P
Frequency
160
140
120
100
80
60
40
20
0
1
3
13
6
3
3
4
0
0
0
2
0-0.2
0.2-0.4
0.4-0.6
0.6-0.8
0.8-1.0
1.0-1.2
1.2-1.4
1.4-1.6
1.6-1.8
1.8-2.0
>2.0
Pore Sizes (µm)

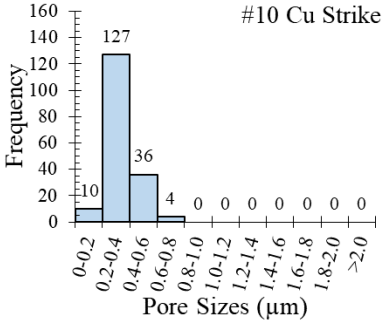
#10 Cu Strike
Frequency
160
140
120
100
80
60
40
20
0
10
127
36
4
0
0
0
0
0
0
0
0-0.2
0.2-0.4
0.4-0.6
0.6-0.8
0.8-1.0
1.0-1.2
1.2-1.4
1.4-1.6
1.6-1.8
1.8-2.0
>2.0
Pore Sizes (µm)

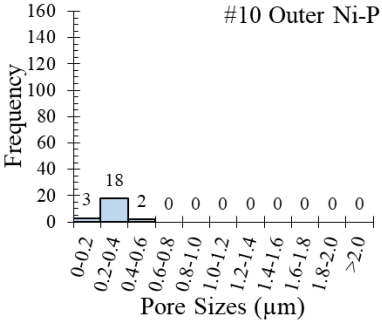
#10 Outer Ni-P
Frequency
160
140
120
100
80
60
40
20
0
3
18
2
0
0
0
0
0
0
0
0
0-0.2
0.2-0.4
0.4-0.6
0.6-0.8
0.8-1.0
1.0-1.2
1.2-1.4
1.4-1.6
1.6-1.8
1.8-2.0
>2.0
Pore Sizes (µm)

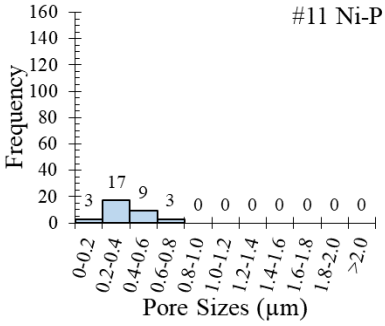
#11 Ni-P
Frequency
160
140
120
100
80
60
40
20
0
3
17
9
3
0
0
0
0
0
0
0
0-0.2
0.2-0.4
0.4-0.6
0.6-0.8
0.8-1.0
1.0-1.2
1.2-1.4
1.4-1.6
1.6-1.8
1.8-2.0
>2.0
Pore Sizes (µm)

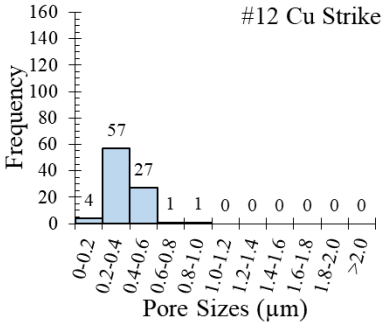
#12 Cu Strike
Frequency
Pore Sizes (µm)
0-0.2
0.2-0.4
0.4-0.6
0.6-0.8
0.8-1.0
1.0-1.2
1.2-1.4
1.4-1.6
1.6-1.8
1.8-2.0
>2.0
4
57
27
1
1
0
0
0
0
0
0

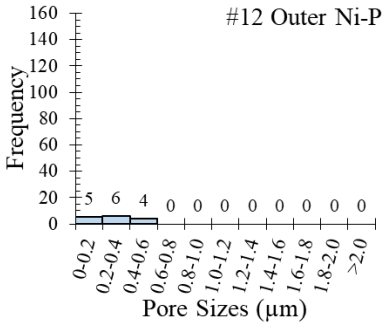
#12 Outer Ni-P
Frequency
Pore Sizes (µm)
5
6
4
0
0
0
0
0
0
0
0

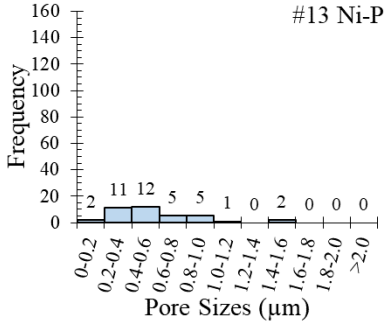
#13 Ni-P
Frequency
Pore Sizes (µm)
2
11
12
5
5
1
0
2
0
0
0

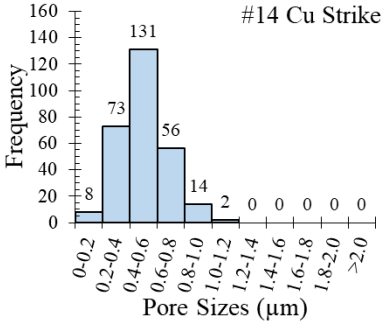
#14 Cu Strike
Frequency
Pore Sizes (µm)
8
73
131
56
14
2
0
0
0
0
0

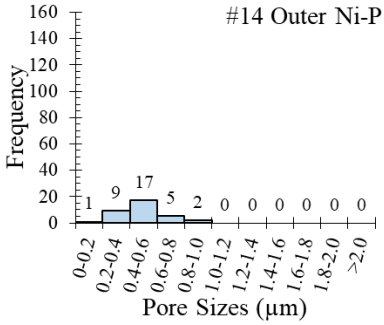
#14 Outer Ni-P
Frequency
Pore Sizes (µm)
1
9
17
5
2
0
0
0
0
0
0

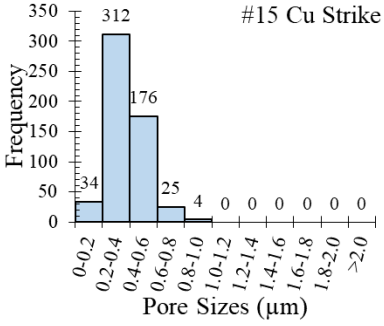
#15 Cu Strike
Frequency
Pore Sizes (µm)
34
312
176
25
4
0
0
0
0
0
0

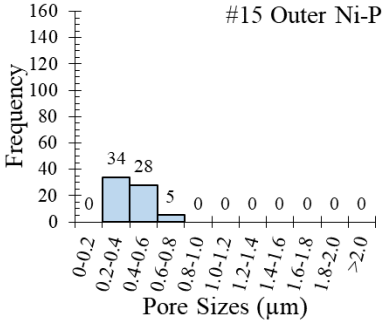
#15 Outer Ni-P
Frequency
Pore Sizes (µm)
0
34
28
5
0
0
0
0
0
0
0

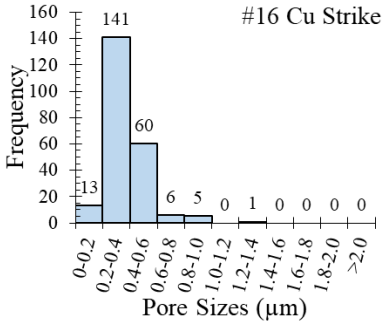
#16 Cu Strike
Frequency
Pore Sizes (µm)
13
141
60
6
5
0
1
0
0
0
0

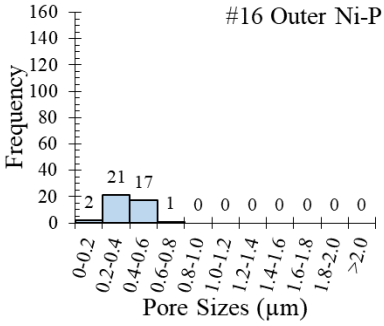
#16 Outer Ni-P
Frequency
Pore Sizes (µm)
2
21
17
1
0
0
0
0
0
0
0

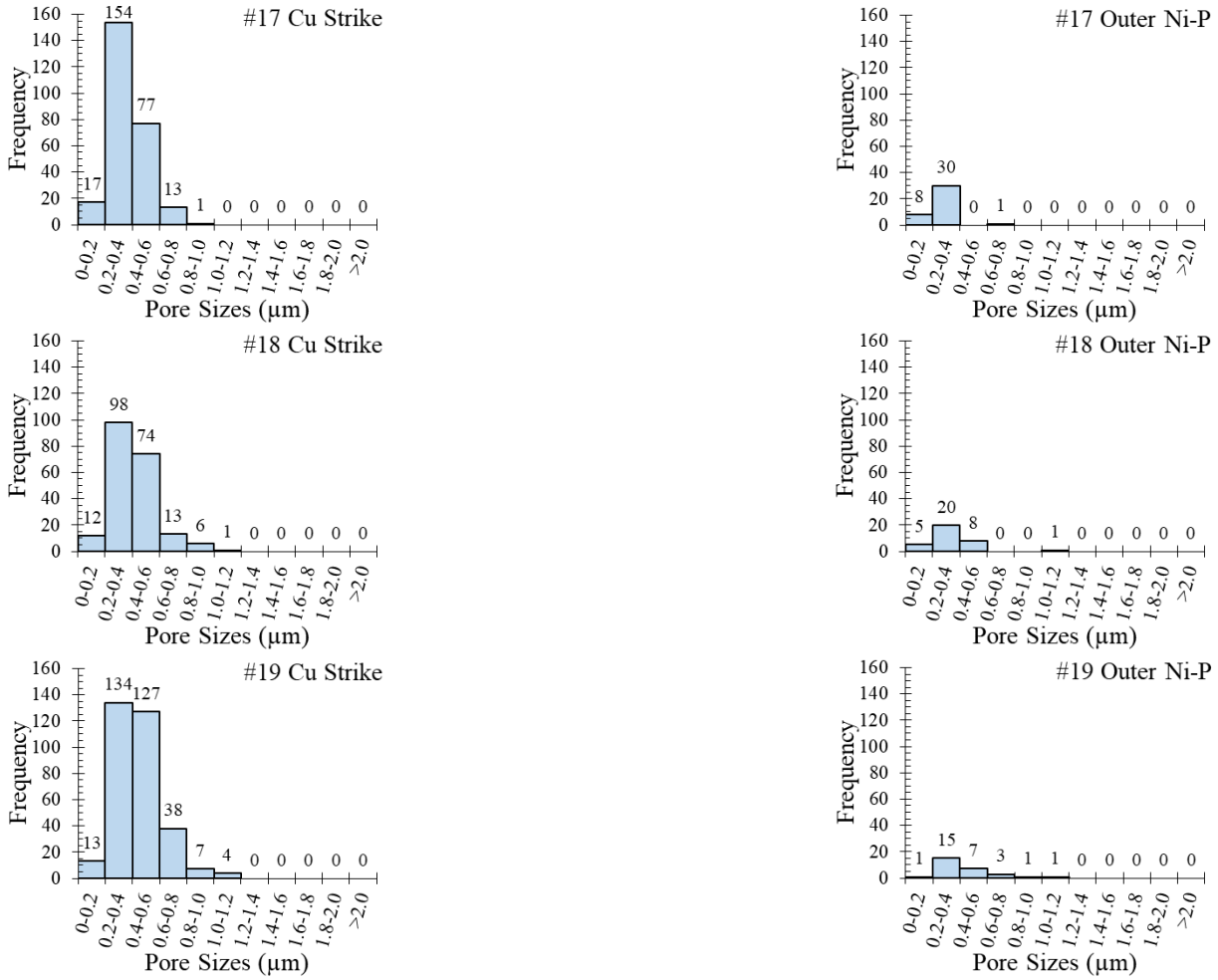

Figure 3-17: Pore size histograms for microscopic porosity.

The reasons behind the MiPAD and MiPAP values were explored by comparative analysis of coatings #6 to #19 to understand the effects of Mg sandblasting grit number, P content in the Ni-P coatings, Cu strike presence, and overall coating thickness on porosity. Coatings #6 to #19 were specially commissioned to understand the effects these plating parameters have on porosity. No error bars are used for these figures as microscopic analysis used data pooled together from several areas, resulting in single number values for MiPAD and MiPAP for each coating. If MiPAD and MiPAP values were calculated for each area, then averages and standard deviations could be calculated and presented. The effect of sand blasting grit number on microscopic porosity was

determined by analyzing the #6, #7, #8, and #11 coatings (Figure 3-18); all other plating parameters other than sand blasting grit number are identical. A larger grit number corresponds to a finer Mg surface finish. No correlation between sandblasting grit number and microscopic porosity was observed. According to Ma and Wang, a coarse substrate surface finish promotes rapid Ni-P formation, which leads to cauliflower-like surface morphology with high porosity [14]. This effect may result in only larger (macroscopic) porosity, which is why no correlation was observed between sandblasting grit number and microscopic porosity. The effect of sandblasting grit number on Cu strike microscopic porosity was not determined since all coatings containing Cu strike layers used 120 grit number sandblasting.

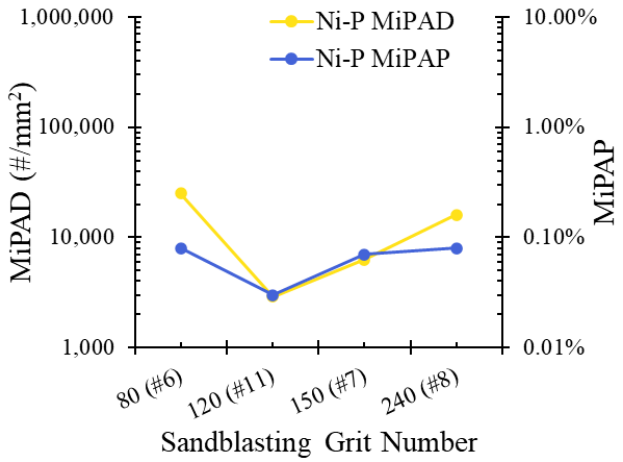

Figure 3-18: Effect of sandblasting grit number on microscopic porosity.

The effect of P content on microscopic porosity was determined by comparing the #9, #11, and #13 coatings; all other plating parameters other than P content were identical. The P content of each coating was measured using EDX analysis of dimple analysis samples at areas where the coating was not polished. The measured values of 2.8, 5.2, and 10.0 wt% P fit the definitions of LPEN, MPEN, and HPEN outlined in Section 3.2.2. The microscopic porosity decreased and then increased as the P content was increased (Figure 3-19). This trend is different from the general consensus in the literature, where a higher P content correlates to lower porosity [26], [76], [77].

This may be explained by Equation 3-6 to Equation 3-9, which outline the most widely accepted mechanism for electroless Ni deposition. Equation 3-6 occurs on a catalytic surface with sufficient applied heat, leading to the hypophosphite ion ($H_2PO_2^-$) reducing to the orthophosphite ion (HPO_3^{2-}) and releasing one H^+ ion and two adsorbed H atoms (H_{ads}) on the catalytic surface. The Ni^{2+} ion from the nickel salt then reacts with the two adsorbed H atoms and deposits Ni on the catalytic surface while releasing two more H^+ ions (Equation 3-7). The $H_2PO_2^-$ ion can also react with one H_{ads} to form one water, one OH^- ion, and deposit one P atom (Equation 3-8). This process likely competes with the process in Equation 3-7 for H_{ads}. The majority of the $H_2PO_2^-$ ions react with water to form H^+, HPO_3^{2-}, and H_2 (Equation 3-9) [26]. Hydrogen evolution during the deposition process may lead to porosity [26], [62]. Since the majority of $H_2PO_2^-$ ion is consumed in Equation 3-9, this reaction is likely more favourable than Equation 3-6 or Equation 3-8. On the other hand, the lower P content of coating #9 indicates that the reaction in Equation 3-8 did not occur as much and that the reaction in Equation 3-9 occurred more. The increased amount of the reaction given by Equation 3-9 relative to that in Equation 3-8 means that coating #9 had more hydrogen evolution during deposition than #11, which explains why it has a higher microscopic porosity. The higher P content of coating #13 means that more of the reaction in Equation 3-8 occurred, which also indicates that more $H_2PO_2^-$ was added to the plating solution. This means that more of the reaction in Equation 3-9 (and more hydrogen evolution) occurred for coating #13 than for coatings #9 or #11, which explains why #13 has a higher microscopic porosity than #9 or #11.

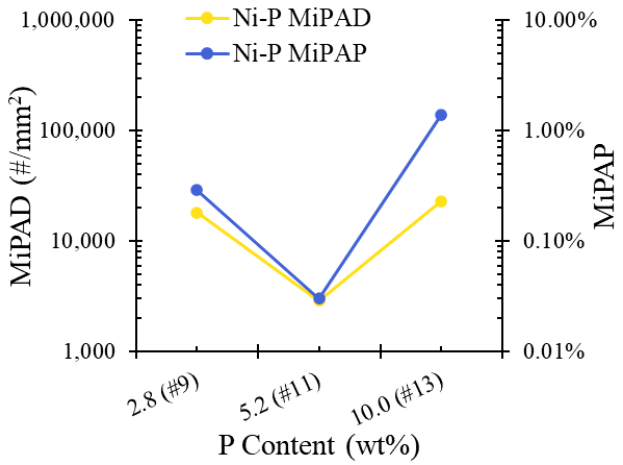

Figure 3-19: Effect of P content on microscopic porosity.

$$H_2PO_2^- + H_2O \longrightarrow H^+ + HPO_3^{2-} + 2H_{ads}$$ Equation 3-6

$$Ni^{2+} + 2H_{ads} \longrightarrow Ni + 2H^+$$ Equation 3-7

$$H_2PO_2^- + H_{ads} \longrightarrow H_2O + OH^- + P$$ Equation 3-8

$$H_2PO_2^- + H_2O \longrightarrow H^+ + HPO_3^{2-} + H_2$$ Equation 3-9

The layer and total thickness for each coating is tabulated in Table 3-5. Coating #14 is the thinnest and coating #19 is the thickest coating.

Table 3-5: Layer thicknesses measured from cross section analysis

Coating Number	Layer Structure	Layer Thicknesses (µm)
1	MPEN Mg	29.4 ± 1.6
2	MPEN Cu Strike MPEN Mg	25.0 ± 1.0 7.0 ± 0.5 14.2 ± 1.5 (46.3 ± 3.0 total)
3	MPEN HPEN Cu Strike Mg	10.5 ± 1.3 13.8 ± 0.9 6.6 ± 0.8 (30.9 ± 3.0 total)

4	LPEN HPEN Cu Strike Mg	8.6 ± 0.7 15.1 ± 1.1 5.9 ± 1.6 (29.6 ± 3.3 total)
5	LPEN HPEN Cu Strike Mg	10.1 ± 0.5 14.5 ± 2.0 4.7 ± 0.6 (29.2 ± 3.1 total)
6	MPEN Mg	34.5 ± 2.9
7	MPEN Mg	34.3 ± 1.7
8	MPEN Mg	33.5 ± 2.0
9	LPEN Mg	32.9 ± 2.3
10	LPEN Cu Strike LPEN Mg	24.1 ± 1.0 4.7 ± 1.1 7.4 ± 1.2 (36.2 ± 3.3 total)
11	MPEN Mg	34.0 ± 1.8
12	MPEN Cu Strike MPEN Mg	25.7 ± 1.7 5.7 ± 0.7 11.4 ± 1.6 (42.8 ± 4.0 total)
13	HPEN Mg	33.4 ± 2.0
14	MPEN Cu Strike MPEN Mg	11.2 ± 0.6 8.2 ± 0.5 9.0 ± 0.7 (28.4 ± 1.8 total)
15	MPEN Cu Strike MPEN Mg	14.0 ± 0.8 9.7 ± 0.3 11.5 ± 1.1 (35.2 ± 2.2 total)

16	MPEN	19.1 ± 0.7
	Cu Strike	7.5 ± 0.4
	MPEN	10.5 ± 0.7
	Mg	(37.1 ± 1.8 total)
17	MPEN	24.3 ± 1.0
	Cu Strike	7.2 ± 0.3
	MPEN	10.6 ± 0.6
	Mg	(42.1 ± 1.9 total)
18	MPEN	30.8 ± 0.8
	Cu Strike	7.1 ± 0.6
	MPEN	10.3 ± 0.7
	Mg	(48.2 ± 2.1 total)
19	MPEN	40.9 ± 1.4
	Cu Strike	7.8 ± 0.5
	MPEN	8.1 ± 1.2
	Mg	(56.8 ± 3.1 total)

The effect of Cu strike presence on microscopic porosity is shown in Figure 3-20. The presence of a Cu strike layer had a negligible effect on microscopic porosity. According to Gray and Luan, when porosity is present in an underlayer, the overlayer will deposit at the same rate at the bottom of the porosity as on the overlayer's top surface, causing porosity to form in the overlayer. This results in underlayer porosity propagating into overlayers [49]. This is shown schematically in Figure 3-21, where because a pore is present in the Cu strike, the Ni-P coating is deposited along the pore's edges, resulting in a smaller pore being propagated into the Ni-P layer. The Cu strike layer of coating #12 has substantially higher microscopic porosity than the Ni-P layer and, as such, it is reasoned that the outer Ni-P microscopic porosity of #12 should be higher than #11, yet this was not observed. One possible explanation is that small porosity (microscopic porosity) is filled in much more easily larger (macroscopic) porosity, and so microscopic porosity in the Cu strike underlayer did not propagate into the Ni-P overlayer, resulting in no increase in microscopic porosity for the Ni-P layer.

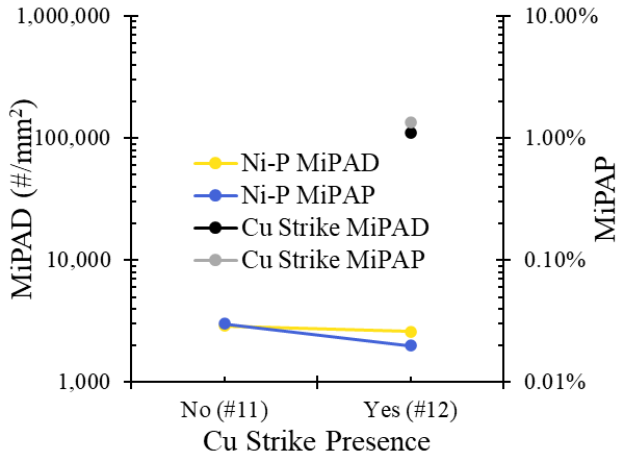

Figure 3-20: Effect of Cu strike presence on microscopic porosity.

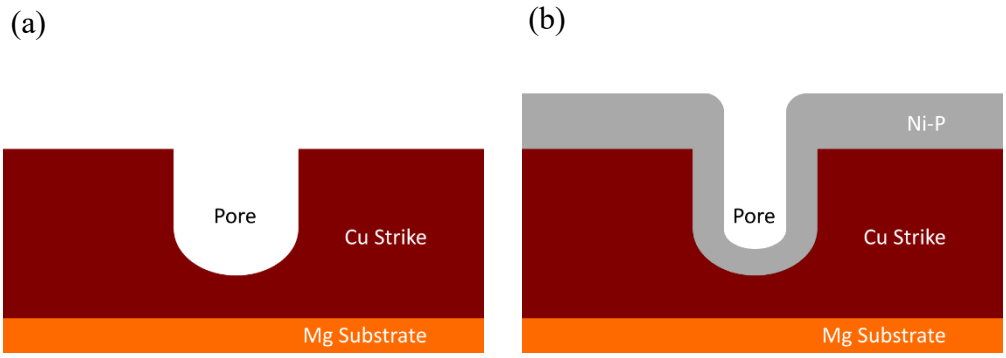

Figure 3-21: Schematic of a) porosity in underlayer (Cu strike) leading to b) pore propagation in the overlayer (Ni-P). Not drawn to scale.

The effect of total coating thickness on microscopic porosity is shown in Figure 3-22a. Ni-P microscopic porosity decreased as total coating thickness increased. The Cu strike microscopic porosity remained stable (Figure 3-22b). The inner Ni-P layer thicknesses are similar, and all have medium P contents. In other words, the "substrate" used for Cu striking was similar for coatings #14 to #19 and any Cu strike porosity differences between these coatings cannot be due to differences in the "substrates". As such, the similar Cu strike porosity across coatings #14 to #19 implies that the Cu strike deposition process is similar if not identical for these coatings. This may be the reason the Cu strike microscopic porosity is similar across coatings #14-#19. Thicker Ni-P outer layers require longer electroless plating times, which allows for more Ni-P to be deposited.

This increases the coating coverage over the Cu strike layers and, over time, the levelling effect of electroless Ni deposition filled in the pores and reduced the microscopic porosity of the coatings, thereby resulting in lower microscopic porosity with higher overall coating thickness [22], [25], [33], [36], [37], [75], [77].

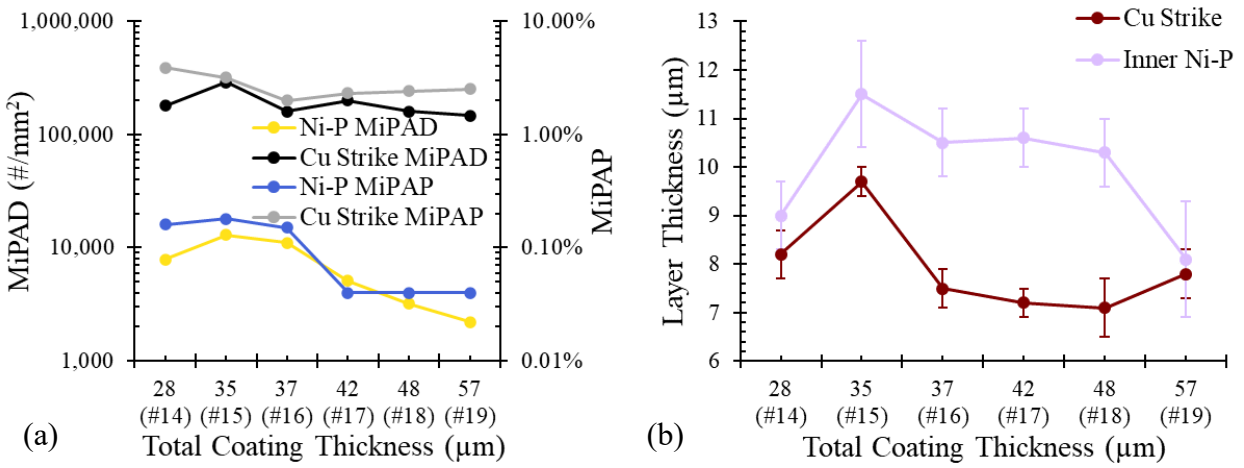

Figure 3-22: a) Effect of total coating thickness on microscopic porosity and b) Cu strike and inner Ni-P thicknesses for coatings #14 to #19 (error bars represent one standard deviation for each data point).

Only total coating thickness and P content had effects on microscopic porosity. This cannot explain why the outer Ni-P microscopic porosity of coating #3 is much higher than that for the others. One possible explanation is that the plating bath for the outer Ni-P layer of coating #3 was contaminated or improperly prepared, thus resulting in high microscopic porosity. The high microscopic porosity of the outer Ni-P layer for coating #3 should be considered an outlier. Apart from #3, coatings #4 and #13 also had high outer Ni-P microscopic porosity, albeit much lower than #3. These results can be rationalized as follows: #4 had LPEN and HPEN layers as well as a low total coating thickness (29.6 ± 3.3 µm) and #13 had a HPEN layer and low total coating thickness (33.4 ± 2.0 µm). The low Ni-P microscopic porosity of coatings #2, #12, and #19 are related to their MPEN layers and high total coating thicknesses (46.3 ± 3.0, 42.8 ± 4.0, and 56.8 ± 3.1 µm, respectively). Microscopic porosity likely does not propagate as easily from underlayers to overlayers. This, for

example, explains why coating #2 had a low outer Ni-P microscopic porosity (<$2.67 \cdot 10^3$ #/mm^2) despite its high Cu strike microscopic porosity ($1.07 \cdot 10^5$ #/mm^2) and why #4 had less Cu strike microscopic porosity than #3 despite the inner Ni-P layer of #4 having higher microscopic porosity than #3. The varying microscopic porosity in the Cu strike layers of the various coatings are, caused by their deposition processes and not by underlayer propagation into the overlayer.

3.3.3 Macroscopic Porosity

The macroscopic porosity of all coatings is tabulated in Table 3-6 and shown in Figure 3-23. MaPAD is displayed using a log-scale so that all data points can be displayed distinctly. Additional macroscopic porosity data are tabulated in Appendix B (Table B-1). Coatings #6 and #13 have the highest macroscopic porosity. Coating #6 has a lower MaPAD than #13, but contains more large pores than #13, resulting in the two having similar MaPAP values (Figure 3-24). Coatings #1, #2, and #19 have the lowest macroscopic porosity. Their MaPAD values are comparable but coating #19 has more larger pores than #1 and #2, resulting in a higher MaPAP value (Figure 3-24).

Table 3-6: Macroscopic porosity analysis results

Coating Number	MaPAD (#/mm^2)	MaPAP (%)
1	3.76	0.0491
2	1.70	0.0324
3	66.3	3.62
4	105	3.68
5	97.1	0.68
6	107	4.53
7	36.0	0.868
8	14.0	0.116
9	67.3	1.35
10	68.7	0.851
11	30.6	0.381
12	69.3	0.818
13	190	4.47
14	113	4.18
15	81.4	1.91
16	61.1	2.14
17	41.6	0.522
18	22.5	0.731
19	5.11	0.143

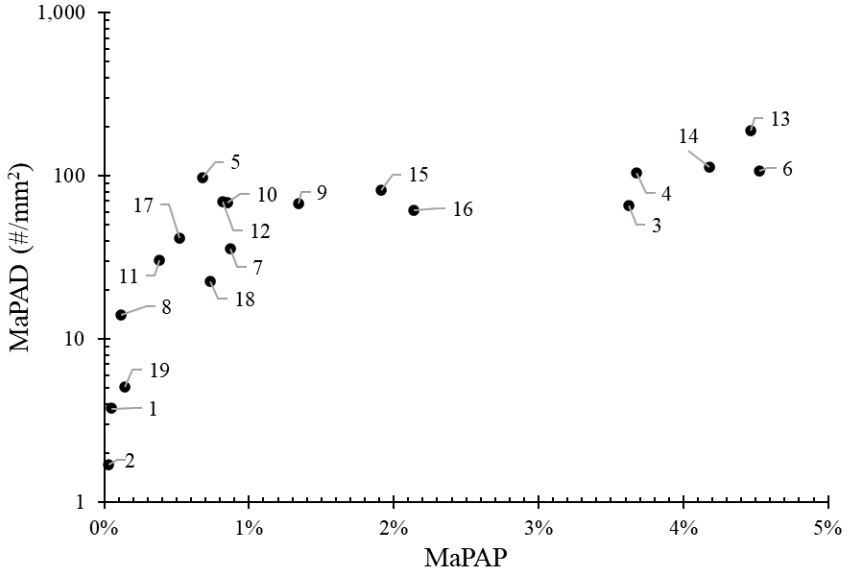

Figure 3-23: MaPAD vs. MaPAP for all coatings.

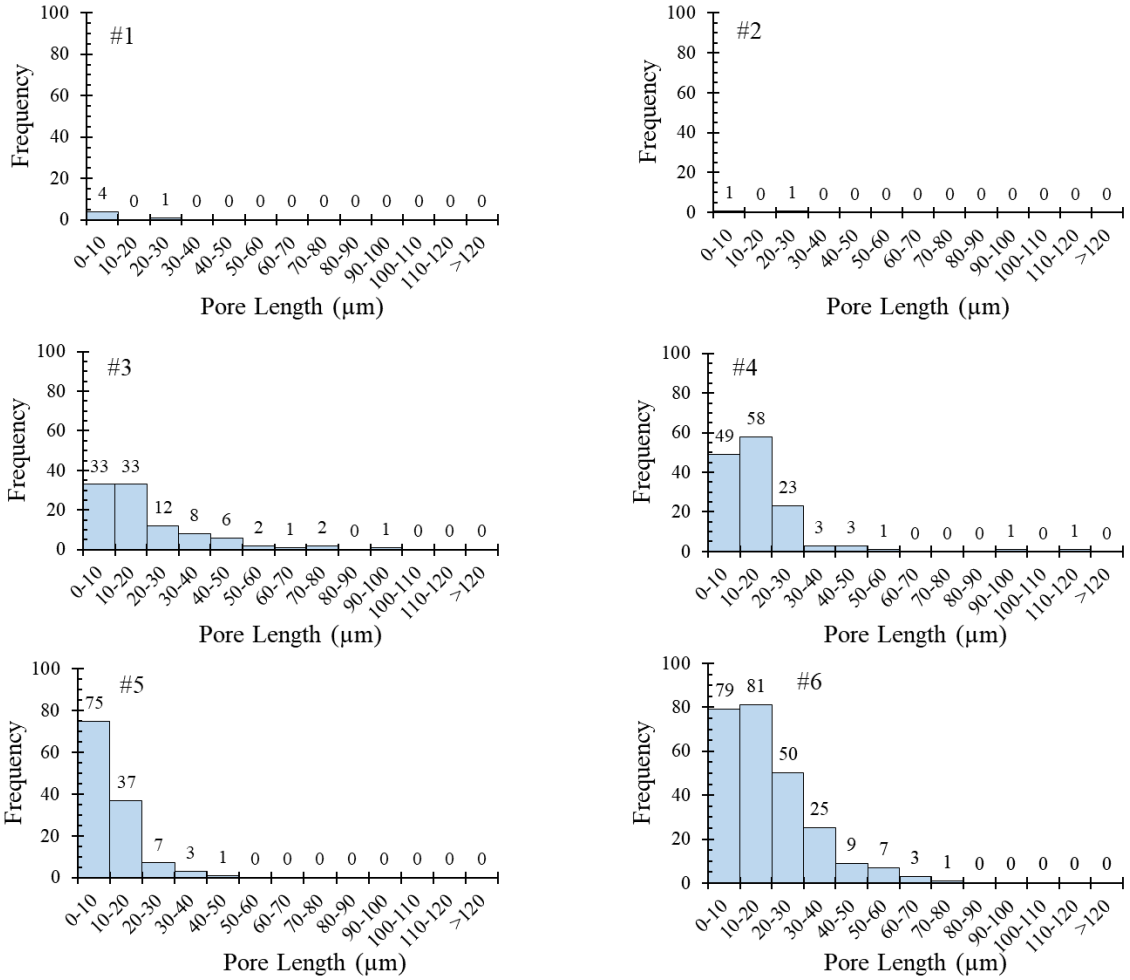

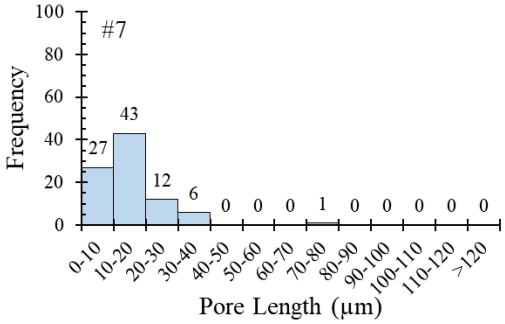
#7
Frequency
Pore Length (μm)
0-10 10-20 20-30 30-40 40-50 50-60 60-70 70-80 80-90 90-100 100-110 110-120 >120
27 43 12 6 0 0 0 1 0 0 0 0 0

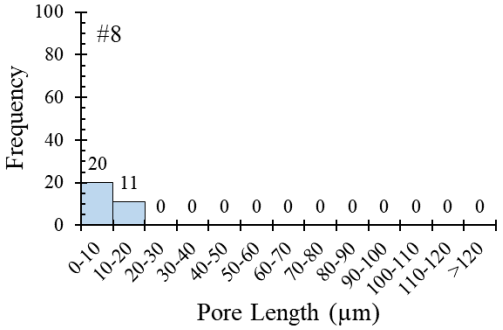
#8
Frequency
Pore Length (μm)
0-10 10-20 20-30 30-40 40-50 50-60 60-70 70-80 80-90 90-100 100-110 110-120 >120
20 11 0 0 0 0 0 0 0 0 0 0 0

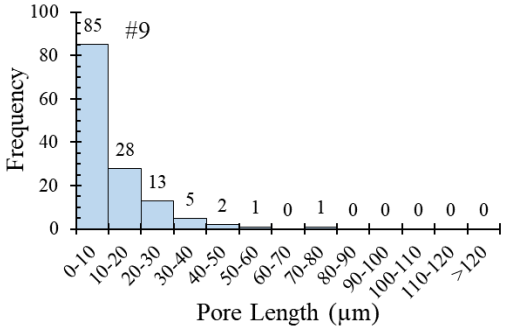
#9
Frequency
Pore Length (μm)
0-10 10-20 20-30 30-40 40-50 50-60 60-70 70-80 80-90 90-100 100-110 110-120 >120
85 28 13 5 2 1 0 1 0 0 0 0 0

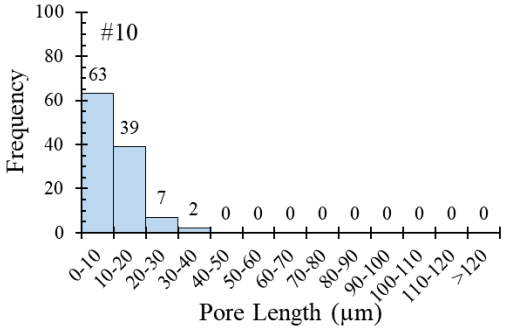
#10
Frequency
Pore Length (μm)
0-10 10-20 20-30 30-40 40-50 50-60 60-70 70-80 80-90 90-100 100-110 110-120 >120
63 39 7 2 0 0 0 0 0 0 0 0 0

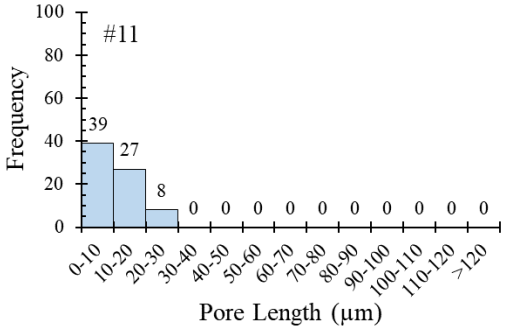
#11
Frequency
Pore Length (μm)
0-10 10-20 20-30 30-40 40-50 50-60 60-70 70-80 80-90 90-100 100-110 110-120 >120
39 27 8 0 0 0 0 0 0 0 0 0 0

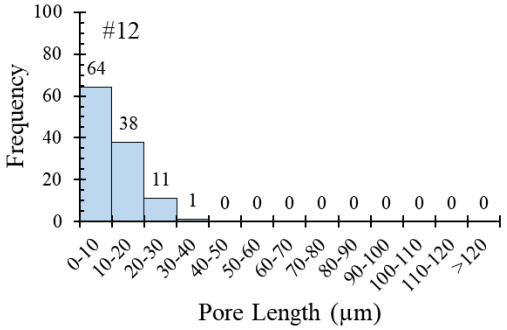
#12
Frequency
Pore Length (μm)
0-10 10-20 20-30 30-40 40-50 50-60 60-70 70-80 80-90 90-100 100-110 110-120 >120
64 38 11 1 0 0 0 0 0 0 0 0 0

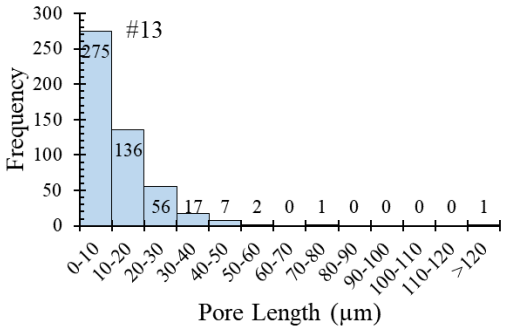
#13
Frequency
Pore Length (μm)
0-10 10-20 20-30 30-40 40-50 50-60 60-70 70-80 80-90 90-100 100-110 110-120 >120
275 136 56 17 7 2 0 1 0 0 0 0 1

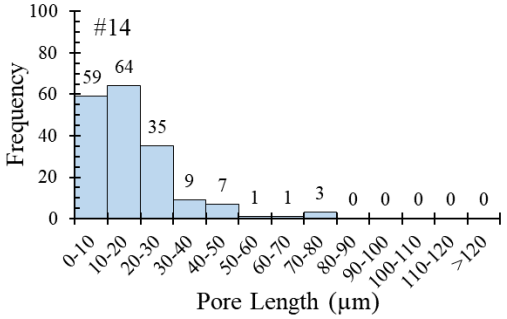
#14
Frequency
Pore Length (μm)
0-10 10-20 20-30 30-40 40-50 50-60 60-70 70-80 80-90 90-100 100-110 110-120 >120
59 64 35 9 7 1 1 3 0 0 0 0 0

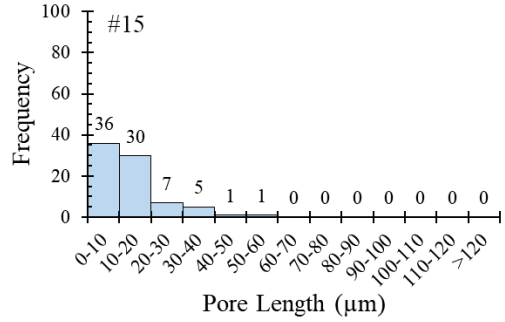
#15
Frequency
Pore Length (μm)
0-10 10-20 20-30 30-40 40-50 50-60 60-70 70-80 80-90 90-100 100-110 110-120 >120
36 30 7 5 1 1 0 0 0 0 0 0 0

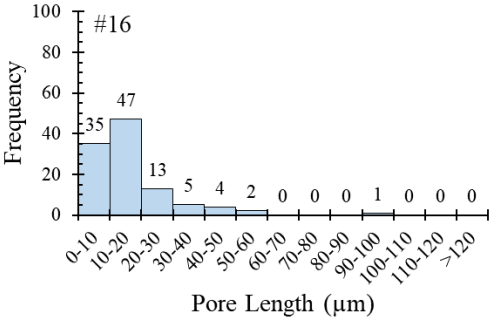
#16
Frequency
Pore Length (μm)
0-10 10-20 20-30 30-40 40-50 50-60 60-70 70-80 80-90 90-100 100-110 110-120 >120
35 47 13 5 4 2 0 0 0 1 0 0 0

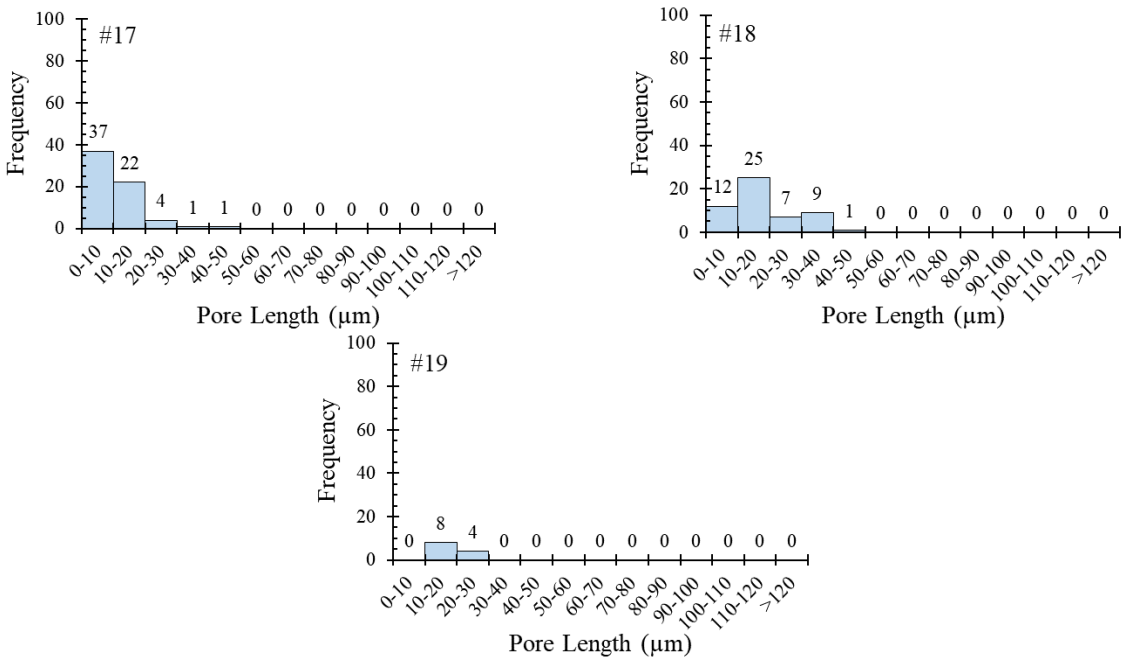

Figure 3-24: Pore size histograms for macroscopic porosity.

To explain the differences in macroscopic porosity between the coatings, the same comparative analysis performed in Section 3.3.2 was performed on coatings #6 to #19 to determine the effect of the plating parameters discussed in Section 3.2.2 on macroscopic porosity. Error bars representing one standard deviation are used in figures displaying the effect of plating parameters on macroscopic porosity. This is possible because, unlike the microscopic porosity analysis, MaPAD and MaPAP values were calculated for each dimple (analogous to each cross section analysis area), with pooled values used in Figure 3-23 and Figure 3-24. This meant that each coating had three sets of MaPAD and MaPAP values (one set for each dimple). As a result, the data points in the figures displaying the effect of plating parameters on macroscopic porosity are averages for the three sets of MaPAD and MaPAP values and the error bars are the standard deviations for these three sets of values. As previously mentioned in Section 3.3.2, rougher Mg surface finishes (low sandblasting grit number) lead to high porosity [14], but since microscopic porosity was not impacted by sandblasting, it was speculated that this effect only occurs for large

(macroscopic) porosity. Larger sandblasting grit number (finer Mg surface finish) resulted in lower macroscopic coating porosity (Figure 3-25). This finding confirms the above speculation that rough surface finish only promotes larger porosity (macroscopic porosity).

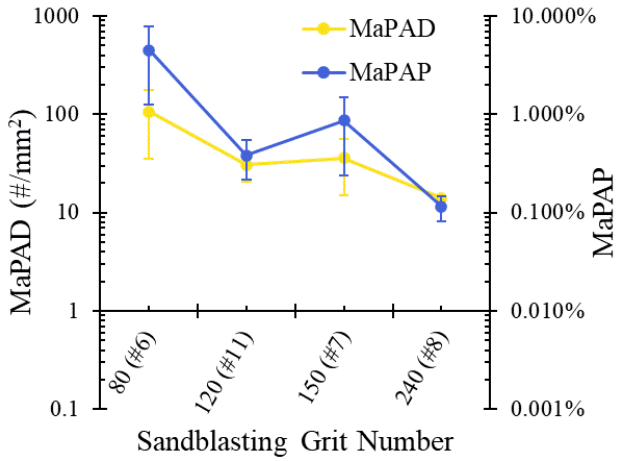

Figure 3-25: Effect of sandblasting grit number on macroscopic porosity. The error bars correspond to one standard deviation.

The effect of P content on macroscopic porosity is shown in Figure 3-26. A similar trend was observed here as for microscopic porosity. The explanation provided in Section 3.3.2 likely applies here also. It is possible that most of the H_2 gas bubbles generated from the reaction in Equation 3-9 during electroless Ni-P deposition are smaller in size and, therefore, generated more microscopic porosity than macroscopic porosity. This could explain why there is a larger difference in microscopic porosity than in macroscopic porosity between coatings #11 and #9 or #13.

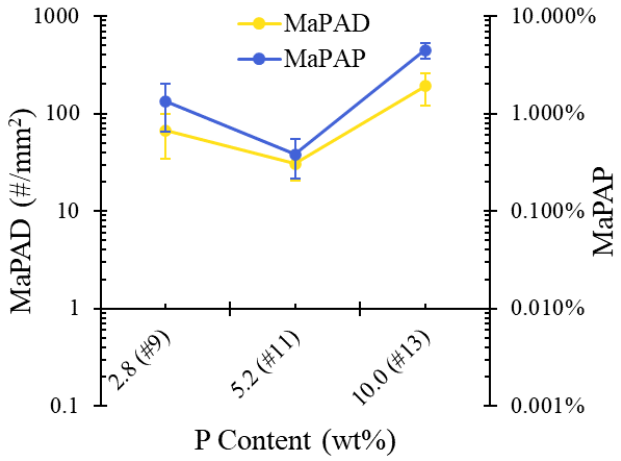

Figure 3-26: Effect of P content on macroscopic porosity. The error bars correspond to one standard deviation.

The presence of Cu strike resulted in more macroscopic porosity in the Ni-P layer (Figure 3-27). Although the macroscopic porosity of the Cu strike layers were not measured, Cu strike layers have substantially higher microscopic porosity than their respective outer Ni-P layers and, as such, it is reasoned that the Cu strike has substantially higher macroscopic porosity than the Ni-P layer also. As previously mentioned in Section 3.3.2, porosity in the underlayer of a coating may propagate to its overlayer [49], but since this was not observed for microscopic porosity, it was proposed that this propagation only occurs for macroscopic porosity. The finding that Cu strike presence led to higher macroscopic porosity in the Ni-P overlayer confirms the conjecture.

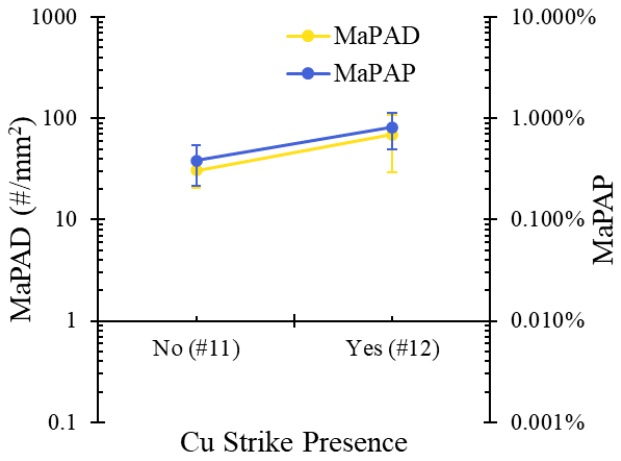

Figure 3-27: Effect of Cu strike presence on macroscopic porosity. The error bars correspond to one standard deviation.

The effect of total coating thickness on porosity was determined by comparing coatings #14 to #19; all other plating parameters were identical. Thicker coatings have lower macroscopic porosity in their Ni-P layers (Figure 3-28). The same explanation provided in Section 3.3.2 likely applies here as well.

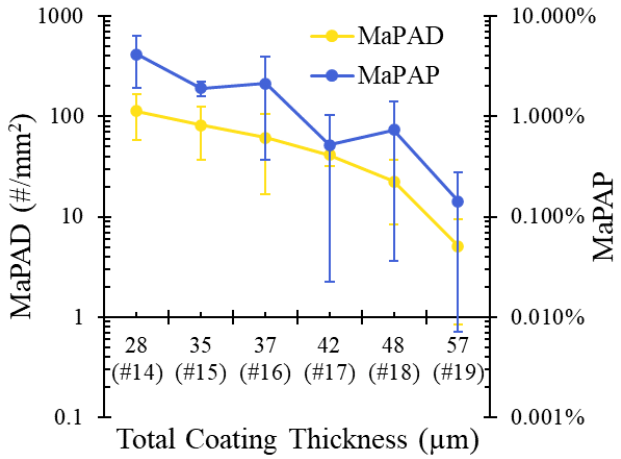

Figure 3-28: Effect of total coating thickness on macroscopic porosity. The error bars represent one standard deviation.

Overall, sandblasting grit number and total coating thickness had greater effects on macroscopic porosity than P content or Cu strike presence. The high macroscopic porosity of coatings #6, #13, and #14 can be attributed to the following: low sandblasting grit number (80) and low total coating thickness (34.5 ± 2.9 µm) for #6; high P content (10.0 wt%) and low total coating thickness (33.4 ± 2.0 µm) for #13; and Cu strike presence and low total coating thickness (28.4 ± 1.8 µm) for #14. The macroscopic porosity reducing effect of two MPEN layers and medium sandblasting grit number (120) in coating #14 were counteracted by the low total coating thickness, leading to #14 having a high macroscopic porosity. The low macroscopic porosity of coatings #1, #2, and #19 can be attributed to the following: medium sandblasting grit number (120) and medium P content for #1; medium sandblasting grit number (120), high overall coating thickness (46.3 ± 3.0 µm), and two MPEN layers for #2; and medium sandblasting grit number (120) and high overall coating

thickness (56.8 ± 3.1 μm) for #19. Despite Cu strike layers being present for coatings #2 and #14, the net effect of high total coating thicknesses and medium sandblasting grit number is a low macroscopic porosity for these two coatings.

3.3.4 Comparing Macroscopic and Microscopic Porosity

Comparing Figure 3-15 and Figure 3-23 show that coatings with high macroscopic porosity also had high microscopic porosity (#3, #4, #13) and coatings with low macroscopic porosity also had low microscopic porosity (#2, #19). Macroscopic and microscopic porosity were both lowest for medium P content and higher total coating thickness. The similar results and trends indicate that macroscopic and microscopic porosity results correlate well with each other. However, higher sandblasting grit number (finer Mg surface finish) had a major effect in reducing macroscopic porosity yet had no difference in reducing microscopic porosity. This indicates that the porosity of a coating cannot be assessed solely using macroscopic porosity or microscopic porosity, and that both methods should be used as they are complementary rather than redundant.

3.4 Summary

In summary, the composition and microstructure of coating #1 was characterized using SEM, EDX, Vickers hardness testing, TEM, and XRD analysis. Coating #1 contained about 6-7 wt% P and is a mixed nanocrystalline/amorphous phase. The Ni-P coating morphology and composition were uniform along the coating surface and throughout most of its thickness, with some P enrichment along the coating/substrate interface, which is consistent with using H_3PO_4 for acid pickling (a common step in the pretreatment process prior to electroless Ni-P plating). The porosity (in terms of pore areal density and pore area percentage, both macroscopic and microscopic) of 19 different Ni-P coatings was characterized using dimple polishing coupled with OM and cross sectional

observation using SEM. Coatings #6, #13, and #14 had the highest macroscopic porosity and coatings #1, #2, #19 had the lowest macroscopic porosity. Coatings #3, #4, and #13 had the highest microscopic porosity and coatings #2, 12, and #19 had the lowest microscopic porosity. The effect of four plating parameters (Mg sandblasting grit number, P content, total coating thickness, and Cu strike presence) were determined by comparing the porosity results of coatings #6 to #19. Higher total coating thickness and medium P content reduced microscopic porosity. Larger sandblasting grit number (finer Mg surface finish) and higher total coating thickness greatly reduced macroscopic porosity, while the lack of a Cu strike layer and medium P content slightly reduced macroscopic porosity. The high microscopic porosity of the Cu strike layers is not caused by the four analyzed parameters, but by their deposition processes. These findings account for the high porosity of coatings #3, #4, and #13 and the low porosity of coatings #2 and #19.

4 Electrochemical Testing

4.1 Introduction

The electrochemical behaviour, especially the corrosion behaviour, of many coatings is contingent on the porosity within the coating. As such, poor corrosion resistance is frequently used to show that a coating has high porosity, and vice-versa. Poor corrosion resistance also means a reduced service lifetime for the coated workpiece. As mentioned in Section 2.8 (Electrocatalytic Activities of Electroless Ni Coatings), electroless Ni-P coatings can catalyze OER and HER, enabling the fabrication and use of electroless Ni-P coated electrodes for electrochemical devices such as secondary metal-air batteries or water electrolysis for hydrogen generation [31]. Stable long-term operation of these devices would, therefore, require high corrosion resistance and low coating porosity. Consequently, this chapter discusses the electrochemical testing methods performed to correlate porosity with corrosion behaviour of the Ni-P coatings [24], [28], [29], [78], [79].

4.2 Experimental

4.2.1 Sample Preparation

Electrochemical samples were prepared using a similar process described in Section 3.2.4 (Plan View SEM and EDX Analysis), with the exception being that the segments are 2 cm long and that these segments were then sectioned across their thickness again to form two smaller segments approximately 1 cm X 0.5 cm X 2 cm in size. A schematic of this process is shown in Figure 4-1. Initially, all electrochemical samples were coated with Buehler EpoThin 2 epoxy to cover surfaces with exposed Mg. Later samples utilised 3M™ Scotch-Weld™ DP110 epoxy as this epoxy hardened much more quickly and adhered to the samples more strongly. The samples tested

electrochemically are tabulated in Table 4-1. After electrochemical testing of coatings #1-#4, #6, and #8, the corrosion measurements were considered to be suspect due to epoxy debonding which exposed the underlying layers of the sample and increased the exposed area of each sample. An order of magnitude calculation was performed to estimate the change in i_{corr} as a result of epoxy debonding and is detailed in Table 4-6 in Section 4.3.1. This calculation assumes a worst case scenario where the epoxy completely debonds, resulting in the exposed area increasing from ~1 cm^2 to 5 cm^2. As such, testing was discontinued. This is explained in greater detail in Sections 4.3.1 and 4.3.2. The effect of exposing the cross section of the coatings to the electrolyte, due to epoxy debonding during corrosion measurements, was assessed using comparative cycle testing of two coating #19 samples. One sample was prepared using the above method and one sample was prepared by applying epoxy on an uncut bar so that an area of 1.8 cm^2 was exposed to the electrolyte. This area was selected to simplify epoxy application and to avoid high current flow damaging the cables during cycle testing, as the larger exposed area necessitated higher current flow to ensure the same current density. If epoxy debonding occurred on the uncut bar sample, then only additional Ni-P would be exposed and the Cu strike would not be exposed to the electrolyte.

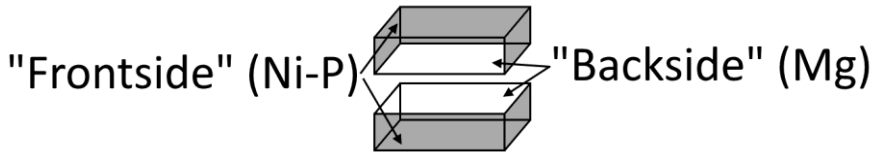

Figure 4-1: Schematic of "backside" and "frontside" of electrochemical samples.

Table 4-1: List of electrochemically tested coatings

Coating Number	1	2	3	4	6	8	19
Layer Structure	MPEN Mg	MPEN Cu Strike MPEN Mg	MPEN HPEN Cu Strike Mg	LPEN HPEN Cu Strike Mg	MPEN Mg	MPEN Mg	MPEN Cu Strike MPEN Mg

4.2.1.1 Buehler EpoThin 2 Epoxy Application

Buehler EpoThin 2 epoxy hardener and Buehler EpoThin 2 epoxy resin were mixed at a mass ratio of approximately 0.45:1 for 2 min using the stem part of a clean cotton applicator. An acrylic paintbrush was then used to paint the 1 cm X 2 cm "backside" faces using the epoxy mixture. The epoxy was allowed to harden in air for a minimum of 9 h before subsequent layers were applied. After the first layer on the "backside" faces hardened, a second layer was applied. After the second "backside" layer hardened, the sides and "frontside" of the sample was painted using the EpoThin 2 epoxy mixture twice (two layers). A Ni-P window was formed, and a circumferential strip of the sample, 3-5 mm wide, was left unpainted to permit electrical contact using alligator clips (Figure 4-2). The paintbrush was cleaned by rinsing and stirring in acetone after each epoxy layer was applied. A photograph was then taken of the prepared sample beside a ruler using a digital camera, and the area of the Ni-P window was calculated using ImageJ. The area values were used for the subsequent electrochemical measurements. The prepared samples were allowed to fully harden over a 24 h period prior to electrochemical testing. All immersion tested samples, except a repeat test of coating #1 (#1 repeat), used this epoxy.

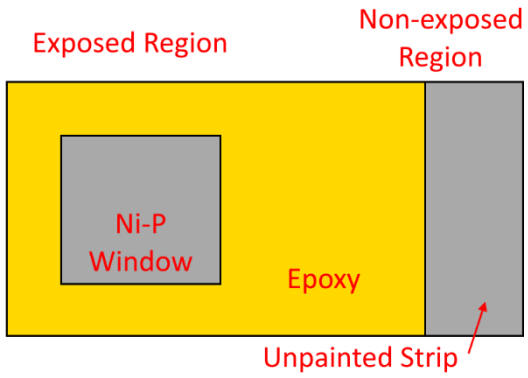

Figure 4-2: Plan-view schematic of "frontside" of electrochemical sample. Not drawn to scale.

4.2.1.2 3M™ Scotch-Weld™ DP110 Epoxy Application

Later electrochemical testing samples used 3M™ Scotch-Weld™ DP110 epoxy instead of Buehler EpoThin 2. The application process is similar to that of EpoThin 2, except that the resin and its hardener were extruded from the manual applicator and manually stirred using the stem of a clean cotton applicator for at least 10 s. The epoxy was smeared onto the sample using the stem of the cotton applicator, and each layer was allowed to harden in air for 20 min on account of the faster hardening time for DP110. The epoxy-covered parts of the cotton applicator were removed using a pair of scissors and the remainder of the applicator was reused for additional epoxy application. The same process to calculate the Ni-P window area in Section 4.2.1.1 was utilized. These samples were also allowed to fully harden over a 24 h period prior to electrochemical testing.

4.2.2 Cell Setup

125 mL of 11 M KOH was poured into a 250 mL plastic beaker, and a 3D printed lid with suitable openings (Figure 4-3) was placed on the beaker. The relative positioning of the electrodes was kept constant by using the lid.

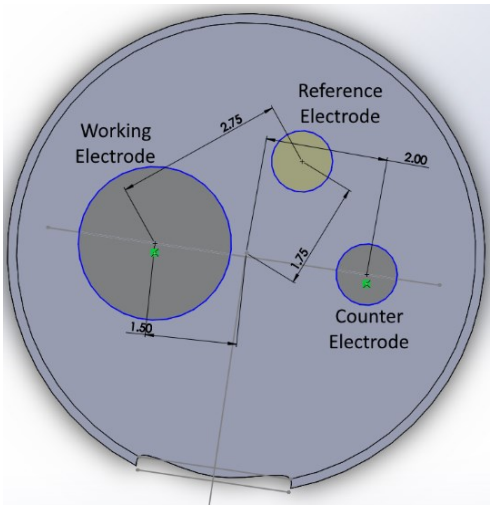

Figure 4-3: Plan view schematic of beaker lid for electrochemical testing (distances are measured in cm).

An alligator clip was used to clamp onto the sample at the unpainted strip, and the exposed region labelled in Figure 4-2 was inserted into the electrolyte while ensuring that the entire Ni-P window was immersed while the unpainted strip was not. The reference electrode was Hg/HgO and the counter electrode was graphite. This setup was used for both immersion and cycling testing, except cycle testing involved gently stirring the electrolyte with a magnetic stirrer. Biologic SP300 and VSP-100 potentiostats were employed for testing.

4.2.3 Immersion Testing

Long term immersion testing was done over a 49-day period, with most sampling occurring every seven days for convenience. First, the samples were held at OCV for 30 min or until the potential fluctuations were less than 1 mV/h, whichever occurred first. The final recorded value during the OCV period is defined as the OCV of the sample for that specific test. The potentiodynamic polarization (PDP) plots of the samples were then measured using a scan rate of 1 mV/s and a potential range of -0.8 to 0.4 V vs. Hg/HgO. The corrosion potential E_{corr} and corrosion current density i_{corr} were then calculated from the PDP plots using EC-Lab; this is explained in further detail in Section 4.2.5. Only coatings #1 to #5 underwent immersion testing because it was determined after testing started that the results were of limited value since corrosion measurements did not change as significantly as those during cycle testing while also taking substantially more time to complete. This is explained in greater detail in Section 4.3.1.

4.2.4 Cycle Testing

An acetic acid test was conducted prior to any electrochemical measurements to determine whether any Mg was exposed from incomplete epoxy coverage of the “backside” or sides or by through-thickness porosity in the coatings. The exposed region of the sample was immersed into glacial

acetic acid and any bubbling caused by H_2 evolution (as shown by Equation 3-1 and Equation 3-2 from Section 3.1 (Introduction) was noted [62]. The sample was then rinsed with deionized water for 15 s and dried with compressed air. Additional epoxy was applied if bubbling was caused by incomplete epoxy coverage of the sides and "backsides", as indicated by bubbling originating from these locations. The sample was inserted into the cell setup described in Section 4.2.2. The cycle testing process is tabulated in Table 4-2. The same OCV and PDP measurement processes described in Section 4.2.3 were used, except that later testing employed a -1.4 to 0.8 V scan range. The larger scan range permitted measurements of additional PDP peaks not present in the range used for immersion testing. The galvanostatic cycling with potential limitation (GCPL) step is tabulated in Table 4-3. E_{we} is the working electrode voltage. The hydrogen evolution reaction (HER) and the oxygen evolution reaction (OER) were induced to simulate the operating conditions for the Ni-P coating, with a 10 s OCV rest period between these steps. This GCPL test process was recommended by the industrial sponsor, Zinc8 Energy Solutions Inc. All successful GCPL steps were 2,000 cycles in duration (the minimum desired lifetime), with one test (coating #3 L) of 3,359 cycles. The acetic acid test was repeated after the cycle testing process to observe if bubbling occurred from the Ni-P window due to porosity or defect formation in the coating.

Table 4-2: Cycle testing process

Steps
OCV 1
PDP 1
OCV 2
GCPL
OCV 3
PDP 2

Table 4-3: GCPL test conditions

Step Name	Step Description
OCV	10 s
HER	-100 mA/cm^2 for 25 s, $E_{we} \geq$ -1.800 V vs. Hg/HgO
OCV	10 s
OER	+100 mA/cm^2 for 40 s, $E_{we} \leq$ 1.500 vs. Hg/HgO

4.2.5 Calculation of E_{corr}, i_{corr}, and CR

E_{corr} and i_{corr} were calculated from the PDP plots using the "Tafel analysis" function from the EC-Lab software. This function uses numerical fitting to determine E_{corr}, i_{corr}, cathodic Tafel slope β_c, and anodic Tafel slope β_a from the Butler-Volmer equation shown in Equation 4-1. I refers to the measured current, I_{corr} is the corrosion current, and E is the electrode potential [80]. An example of the Tafel analysis is shown in Figure 4-4.

$$I = I_{corr}\left(e^{\frac{\log 10(E-E_{corr})}{\beta_a}} - e^{-\frac{\log 10(E-E_{corr})}{\beta_c}}\right) \quad \text{Equation 4-1}$$

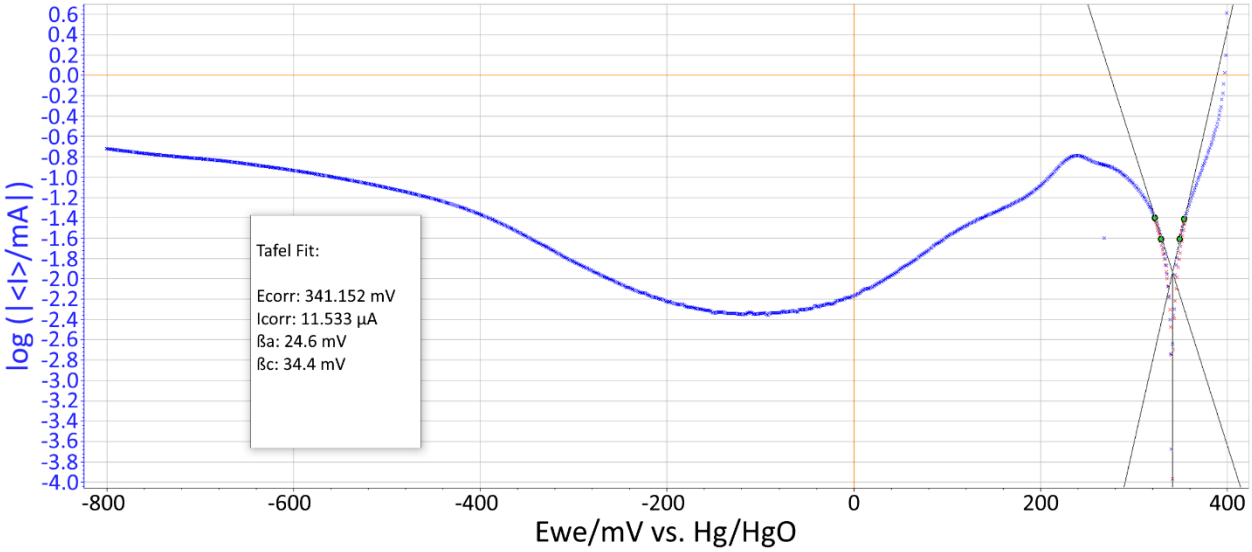

Figure 4-4: Example of numerical fitting by EC-Lab. PDP plot is from day 21 test of immersion tested coating #1.

The corrosion rate CR in nm/day was calculated from i_{corr} using Equation 4-2, where i_{corr} is in A/m^2, ρ is the density of the material being corroded ($8.908 \cdot 10^6$ g/m^3 for pure Ni was assumed),

n is the moles of e^- per moles of metal corroded (2 for pure Ni), and F is the Faraday constant (96, 490 C/mol e^-). The multiplication by 10^6 and division by 365.25 are for unit conversion [73].

$$CR = \frac{i_{corr}\rho}{nF} \cdot \frac{10^6}{365.25} \qquad \text{Equation 4-2}$$

For PDP plots with multiple polarization peaks, the peak with E closest to the OCV value was chosen to define the E_{corr} and i_{corr} values, because OCV is the potential at which thermodynamic equilibrium is achieved [81]. Steady-state corrosion should, therefore, occur at this potential. An example of a PDP plot with multiple peaks is shown in Figure 4-5. The OCV for this example was -634 mV, and so the E peak at -171 mV was utilized for Tafel analysis.

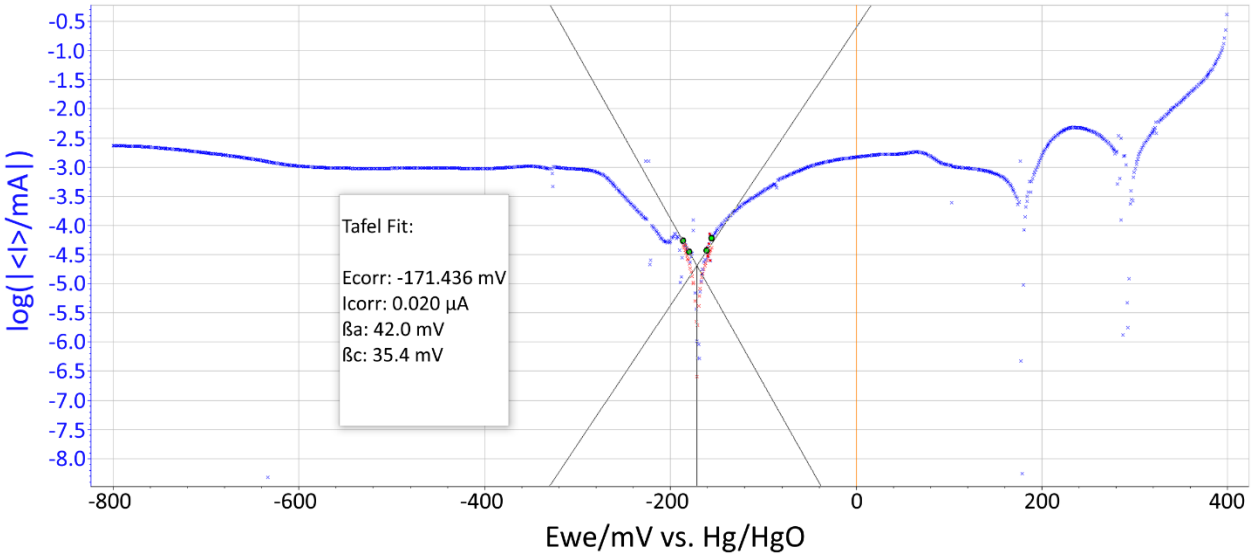

Figure 4-5: Example of numerical fitting by EC-Lab on PDP plot with multiple peaks. Plot is from day 0 test for immersion tested coating #2.

Based on the polarization plot in Figure 4-5, Ni-P corrosion in 11 M KOH exhibits active-passive polarization behaviour. This was determined from the multiple peaks in the PDP plot, which can be explained with the assistance of Figure 4-6 [73], [82]. The first PDP peak, which is used to determine E_{corr} and i_{corr}, is located at the dashed line between areas 1 and 2. The second peak corresponds to primary passivation of the coating (area 4); it is displayed as a peak in the PDP

plots since the potential range for this region is narrow and noise in the data results in a peak. The third peak corresponds to the onset of OER (between areas 6 and 7), which appears as a peak in the PDP plots due to noise once again [82].

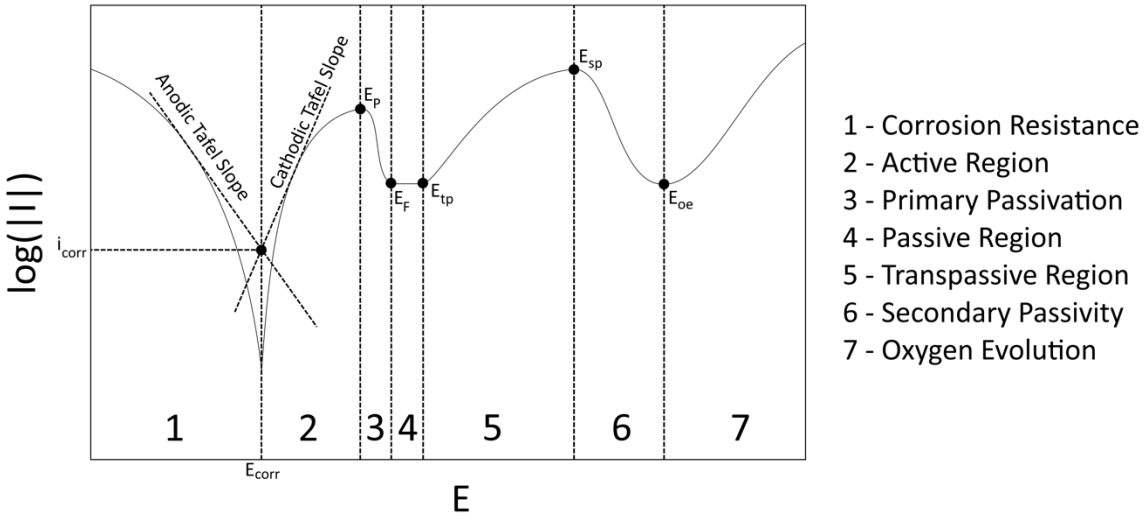

Figure 4-6: Schematic illustrating the appearance of multiple peaks in PDP plots [82]. Not drawn to scale.

4.2.6 Electrolyte Composition

Atomic absorption spectroscopy (AAS, Varian 220FS Double Beam System) was used to analyze the Ni, Mg, and Cu ion concentrations in the electrolytes. 10 mL of freshly made 11 M KOH was used to obtain a baseline concentration for each ion in the electrolyte. For immersion tested samples, approximately 3 mL of the electrolyte was removed following each round of testing (i.e., generally every seven days) for composition analysis. For cycle testing, 7.5 mL of electrolyte was removed after the cycle test finished. Only 3 mL was removed for immersion tested samples as a compromise between obtaining accurate AAS measurements and minimizing electrolyte volume change. Inductively coupled plasma – optical emission spectroscopy (ICP-OES, Thermo Scientific™ iCAP PRO) was used to confirm some of the AAS results. The Ni-P or Cu decrease was calculated using Equation 4-3, where Δt is the decrease in layer thickness in nm, C is the measured ion concentration in ppm, $C_{baseline}$ is the baseline ion concentration, $V_{electrolyte}$ is the

volume of the electrolyte in L, ρ is the density of Ni or Cu (8.908 or 8.96 g/cm^3), and $A_{exposed}$ is the sample area exposed to the electrolyte in cm^2. The multiplication by 10^4 is for unit conversion.

$$\Delta t = \frac{(C - C_{baseline})V_{electrolyte}}{\rho A_{exposed}} \cdot 10^4 \qquad \text{Equation 4-3}$$

4.2.7 SEM and EDX Analysis

All samples were first rinsed in deionized water, ultrasonically cleaned in reagent alcohol for 15 min, and then dried with compress air. For plan-view analyses, carbon tape was applied to the "backside" of the samples with the unpainted strip also in contact with the carbon tape. The "backside" of the samples was pressed onto clean SEM stubs and analyzed with SEM and EDX analysis. The same process described in Section 3.2.5 (Cross Section Sample Preparation and Analysis) was used for cross section analysis. The same SEM conditions, provided in Section 3.2.4 (Plan View SEM and EDX Analysis), were also utilized.

4.3 Results and Discussion

4.3.1 Immersion Testing Results

The variation in OCV, E_{corr}, and CR with immersion time for all immersion tested coatings is shown in Figure 4-7. The average CR and decrease in outer Ni-P layer thickness calculated from the CR, assuming uniform corrosion for all immersion tested coatings, are tabulated in Table 4-4. The layer thickness decrease values were calculated using Equation 4-3. Coating #1 had the highest average CR at 366 nm/day and #3 had the lowest average CR at 38 nm/day. Coating #1, therefore, has the highest Ni-P layer loss at 17.9 µm assuming uniform corrosion, while #3 has the lowest at 1.86 µm. A decrease in thickness by 17.9 µm should result in significant and detectable Ni loss into the electrolyte by AAS and obvious thickness changes in SEM observations of the coating

cross section. These analyses were conducted and are discussed below. Firstly, if a low CR is considered to be the result of low porosity, and by the same argument a high CR is considered to be due to high porosity, then the immersion testing results contradict the porosity results from Section 3.3.2 (Microscopic Porosity) and Section 3.3.3 (Macroscopic Porosity). For example, the #1 coating had fairly low microscopic porosity and the second lowest macroscopic porosity and is, therefore, expected to have a low CR. By contrast, the #3 coating had the highest microscopic porosity and fairly high macroscopic porosity and should, therefore, have a high CR [23], [25], [34], [36], [37], [62], [75], [77]. Consequently, another #1 coating sample was prepared using the newer DP110 epoxy and retested (#1 R in Figure 4-7). The similar results indicate that the high CR for the #1 coating is not caused by deficiencies in the EpoThin 2 epoxy. To ensure that the DP110 epoxy used for the repeat test was not the cause for the high CR, this sample was acetic acid tested before and after immersion testing. No bubbling was observed, indicating that the epoxy successfully prevented Mg exposure to the electrolyte [62]. The OCV and PDP curves for all immersion tested samples are shown in Figure C-1 and Figure C-2 in Appendix C, respectively.

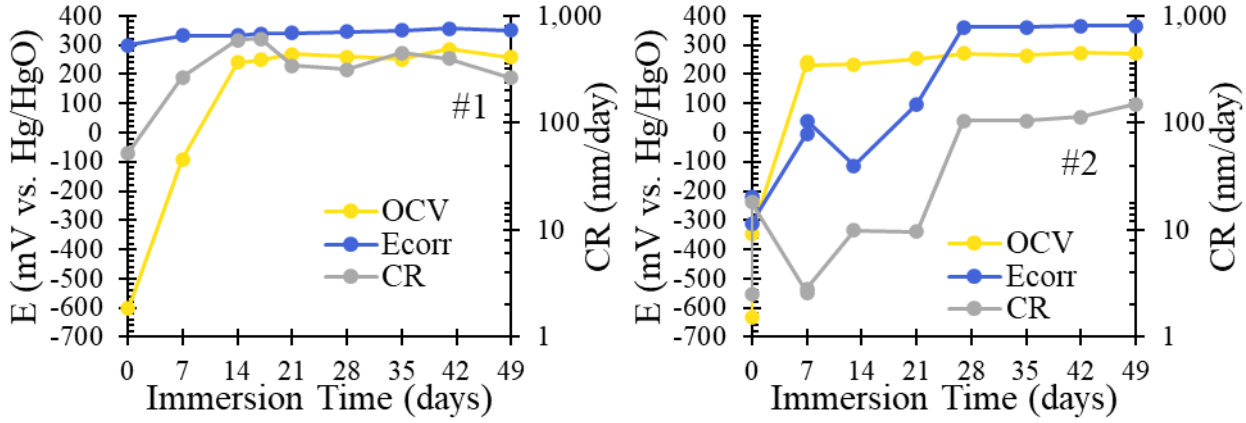

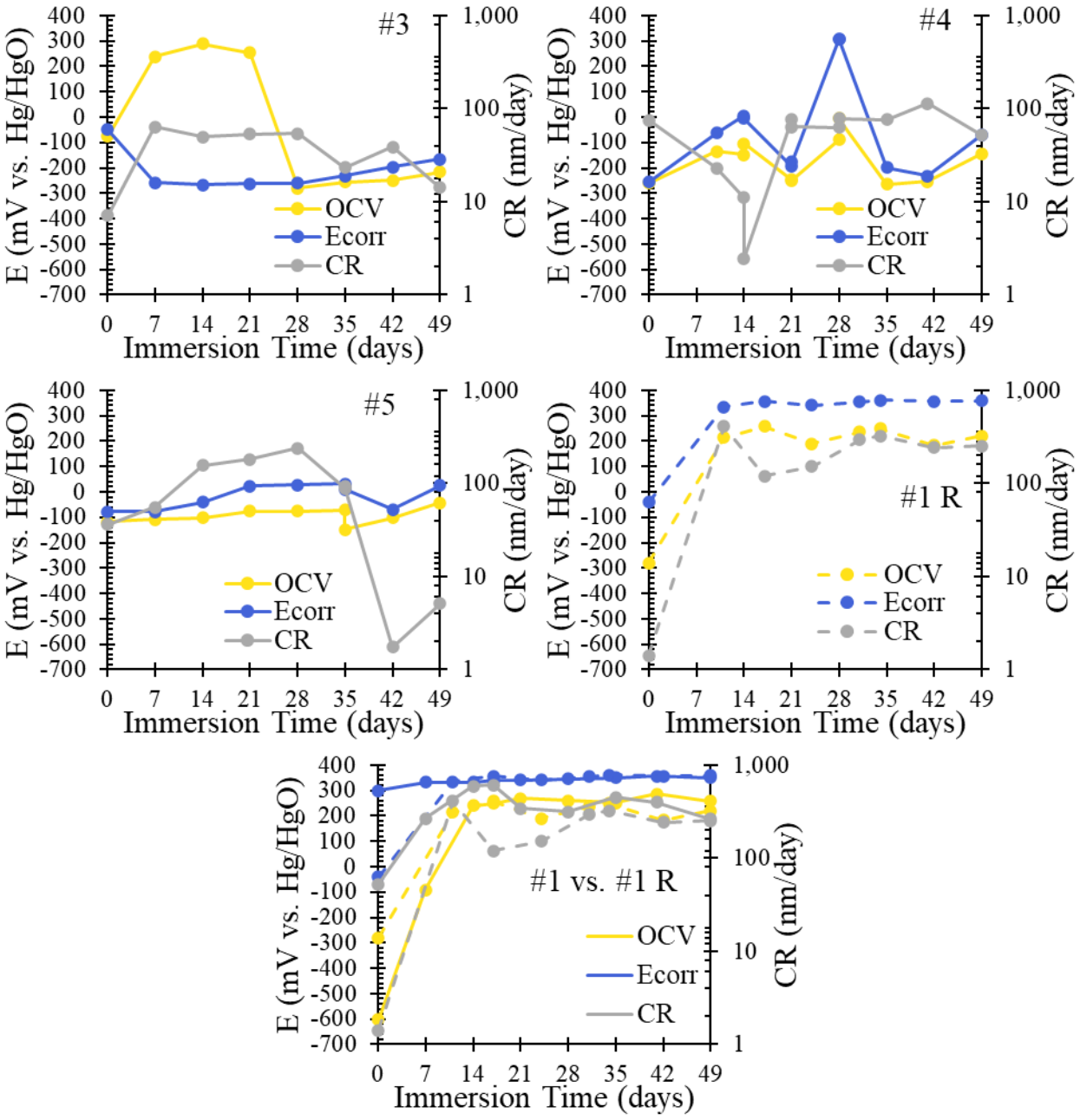

Figure 4-7: Variation with immersion time in OCV, E_{corr}, and CR for immersion tested samples. For the last graph, the results for #1 and #1 R are superimposed; #1 is represented by solid lines and #1 R by dashed lines.

Table 4-4: Average CR and Ni-P thickness decrease assuming uniform corrosion for immersion tested samples

Coating Number	Average CR (nm/day)	Decrease in Ni-P Thickness (μm)
1	366	17.9
2	50.2	2.46
3	38.0	1.86
4	57.6	2.82
5	95.3	4.67
1 R	224	11.0

E_{corr} and i_{corr} increased initially and stabilized for coatings #1, #2, and #1 R during immersion testing. An increase in E_{corr} indicates reduced thermodynamic driving force for corrosion, which should result in a lower CR [21], [25], [37]. This was not observed; one possible explanation can be given with the assistance of Figure 4-8, which shows a polarization curve for an active-passive metal [9], [19]. A fresh 11 M KOH solution, whose cathodic polarization curve is denoted as A in Figure 4-8, is a strongly reducing environment since its O_2 solubility limit is very low [83]. Its intersection with the anodic curve results in $E_{corr,\,A}$ and $i_{corr,\,A}$. As the immersion time is increased, KOH can react with CO_2 present in air and forms carbonates, reducing the KOH concentration [84] and increasing the solubility limit of O_2 in KOH [83]. This makes the electrolytes more oxidizing and shifts the cathodic curve from A to B, which also shifts the intersection point between the anodic and cathodic curves, resulting in $E_{corr,\,B}$ and $i_{corr,\,B}$ which are higher than $E_{corr,\,A}$ and $i_{corr,\,A}$, respectively. This shift in the cathodic polarization curve explains why E_{corr} and i_{corr} can both increase with longer immersion time.

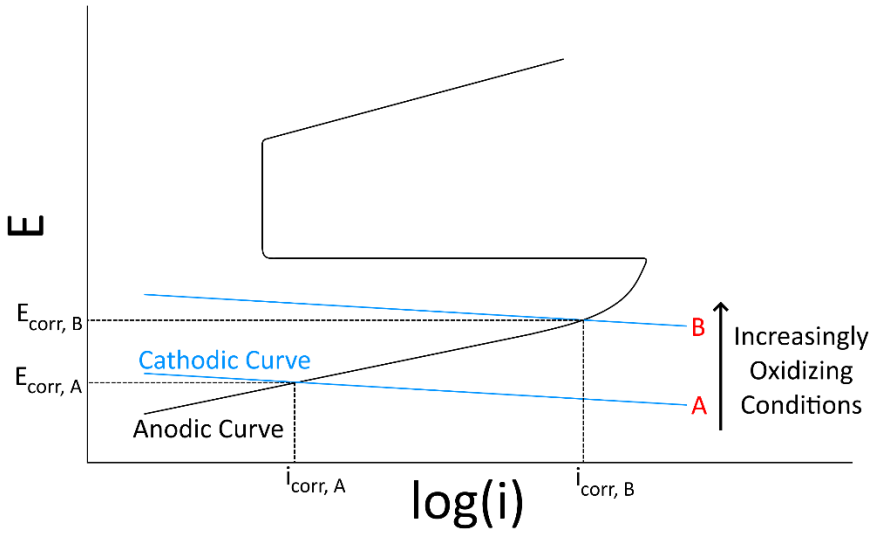

Figure 4-8: Schematic illustrating how i_{corr} can increase with increasing E_{corr}. Not drawn to scale.

Substantial dissolution of the Ni-P and/or Cu strike layers is expected based on the immersion testing results. Correspondingly, the Ni and Cu content in the electrolyte should increase significantly. A calculation of uniform Ni-P or Cu strike thickness loss based on the i_{corr} values and corresponding increase in Ni and Cu concentration in the electrolyte was performed. This calculation assumes corrosion of only Ni-P or only Cu strike. The results are tabulated in Table 4-5. The expected Ni and Cu content increase in the electrolyte is high and should be easily detectable. Additionally, the thickness loss of coatings #1 and #1 R should be detectable by SEM observations. The thickness of coating #1 before testing was 29.4 ± 1.6 µm (Table 3-5). The measured thickness at the exposed regions was 30.8 ± 1.2 µm. As such, there were no measurable differences in Ni-P thickness before and after immersion testing for coating #1, which indicates that there was no measurable amount of Ni-P corrosion. This casts doubt on the accuracy of the CR measurements. Compositional testing of the electrolyte is, therefore, necessary to correlate the discrepancy in measured thickness loss vs. actual thickness loss. The test results are presented below.

Table 4-5: Ni-P and Cu strike uniform thickness loss and equivalent Ni and Cu content increases in electrolyte calculated from CR values

	Lowest Possible Ni-P and Cu Loss	Highest Possible Ni-P and Cu Loss
Corresponding Coating	#3	#1 for Ni-P #5 for Cu Strike
Exposed Area (cm^2)	0.421	1.00 (Ni-P) 0.588 (Cu Strike)
Corresponding Average i_{corr} ($\mu A/cm^2$)	1.29	12.4 (Ni-P) 3.23 (Cu Strike)
Ni-P CR (nm/day)	38.0	366
Uniform Ni-P Thickness Loss (μm)	1.86	17.9
Equivalent Ni Content Increase in Electrolyte (ppm)	5.58	128
Cu Strike CR (nm/day)	40.9	103
Uniform Cu Strike Thickness Loss (μm)	2.00	5.02
Equivalent Cu Content Increase in Electrolyte (ppm)	6.04	21.2

To confirm whether the actual Ni and Cu content increase in the electrolyte matches the calculated values, the Ni, Cu, and Mg ion concentrations in the electrolytes were measured using AAS (Figure 4-9). Sample #1 R was not AAS tested since it exhibited similar corrosion behaviour as #1. The baseline ion concentrations in the 11 M KOH electrolyte are labelled as "BI". The Mg content for all samples remained below the detectability limit of 0.07 ppm, indicating that no Mg corrosion occurred. The Ni content remained stable around the baseline concentration with changes of 0.5 ppm or less, indicating that the Ni-P layers did not corrode or, at least, only marginally. Since coating #1 does not have a Cu strike layer, its highest measured Cu content (0.81 ppm) can be used as a benchmark to evaluate whether Cu corrosion occurred for coatings #2-#5, with content higher than this benchmark indicating corrosion. This benchmark is different from the baseline value shown in Figure 4-9, which was determined from a fresh electrolyte prior to any testing. By this criterion, coatings #2 and #4 experienced Cu corrosion, as their highest measured Cu contents are

1.45 and 4.06 ppm, respectively. The highest measured Cu contents for coatings #3 and #5 are 0.84 and 1.04 ppm, respectively, which indicate slight corrosion of the Cu strike layer. Based on this approach, coatings #2 and #4 exhibited Cu corrosion, with #4 corroding more than #2. The AAS results contradict the calculated Ni and Cu loss values, which indicated that measurable increases of Ni and Cu content in the electrolyte should occur, with Ni content increase in the 5-128 ppm range and Cu content increase in the 6-21 ppm range.

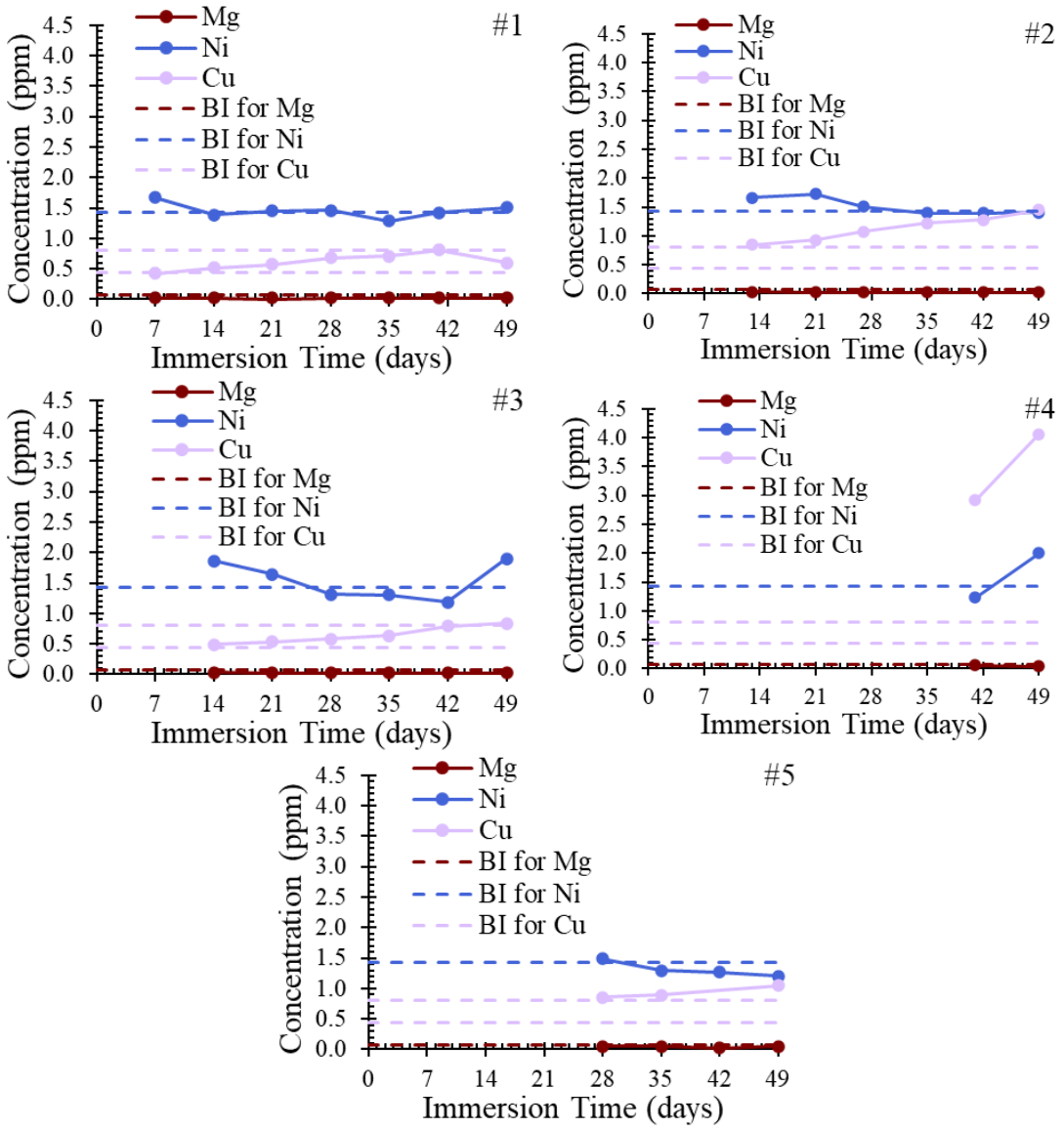

Figure 4-9: AAS results for Mg, Ni, and Cu from immersion tested samples. BI refers to baseline ion concentrations. The upper BI concentration for Cu is the highest measured Cu value from coating #1.

Epoxy debonding was observed for several samples. A significant increase in exposed area due to epoxy debonding could explain the discrepancy in Ni and Cu content increases calculated from CR values and measured from AAS. As a result, an order of magnitude calculation for CR and decrease in layer thickness for the Ni-P coating, assuming complete epoxy debonding, was performed for the coating #1 sample to assess the discrepancy in the CR values calculated assuming no epoxy debonding and complete epoxy debonding. The results are provided in Table 4-6. If complete epoxy debonding occurs, then the exposed area increases from 1.00 to 5.00 cm^2 in the worst case. Given that the I_{corr} remains the same in either case, then the i_{corr} assuming complete epoxy debonding would decrease by a factor of five. This would result in a fivefold reduction in average CR and decrease in Ni-P thickness to 73.1 nm/day and 3.58 μm, respectively. For simplicity, this calculation does not consider that complete epoxy debonding would result in Cu strike or Mg corrosion. As evidenced by the AAS results, Mg corrosion did not occur, but Cu corrosion did occur for coatings with Cu strike layers. Epoxy debonding exposing the coating cross section may explain why Ni-P corrosion was not observed from AAS measurements despite high CR values and may also explain why significant Cu corrosion occurred for coatings containing Cu strike layers. The Cu strike of these coatings corroded preferentially compared with the Mg substrate and Ni-P coating, leading to high localized corrosion, high CR values, and observable Cu corrosion per the AAS measurements. For coating #1, which does not have a Cu strike, the high CR value cannot be explained solely with epoxy debonding, as no changes in coating thickness were measured. A different explanation is required and is provided later.

Table 4-6: Order of magnitude calculation for CR and decrease in thickness for the Ni-P coating from the immersion tested coating #1 sample assuming no epoxy debonding and complete epoxy debonding

	No Epoxy Debonding	Complete Epoxy Debonding
Exposed Area ($cm^{2)}$	1.00	5.00
Average I_{corr} (μA)	12.4	
Average CR (nm/day)	366	73.1
Decrease in Ni-P Thickness (μm)	17.9	3.58

Cross section analysis using SEM and EDX analysis of the immersion tested coating #3 sample was performed to confirm the hypothesis that epoxy debonding resulted in preferential corrosion of the Cu strike layer and to resolve the discrepancy in CR values and AAS measurements (Figure 4-10). Two regions were analyzed: at the edge of the sample where the epoxy had debonded and exposed the Cu strike to the electrolyte and away from the edge, where the epoxy did not debond from the sample. The Cu strike is missing near the edge (Figure 4-10a, Figure 4-10c, and Figure 4-10e) and intact away from the edge of the cross section sample (Figure 4-10b, Figure 4-10d, and Figure 4-10f). These findings indicate that localized Cu corrosion occurred where the epoxy debonded. SEM analysis of the Ni-P layer thicknesses before and after immersion testing found no change, indicating that the Ni-P layer did not corrode. The results confirm that highly localized Cu corrosion occurred due to epoxy debonding, exposing the sectioned faces of the samples to corrosion but do not resolve the discrepancy between high CR values and low/no measured Ni-P corrosion. One explanation for the high CR values is that many PDP curves are noisy around the peaks, resulting in variable Tafel analysis results depending on where the tangent points are selected. An example of this effect is shown in Figure 4-11. Since only a few points are available for Tafel analysis around the peaks, vastly different i_{corr} measurements may occur because selecting slightly different points can result in large differences in Tafel slope values. This problem

is exacerbated by the fact that current density is plotted on a log scale. Consequently, the calculated i_{corr} values can vary significantly (by more than an order of magnitude) from slight changes in where the Tafel slopes intersect. The resulting high variability makes meaningful CR measurements difficult. Mg corrosion was not observed (Figure 4-10e and Figure 4-10f), which is consistent with the AAS results.

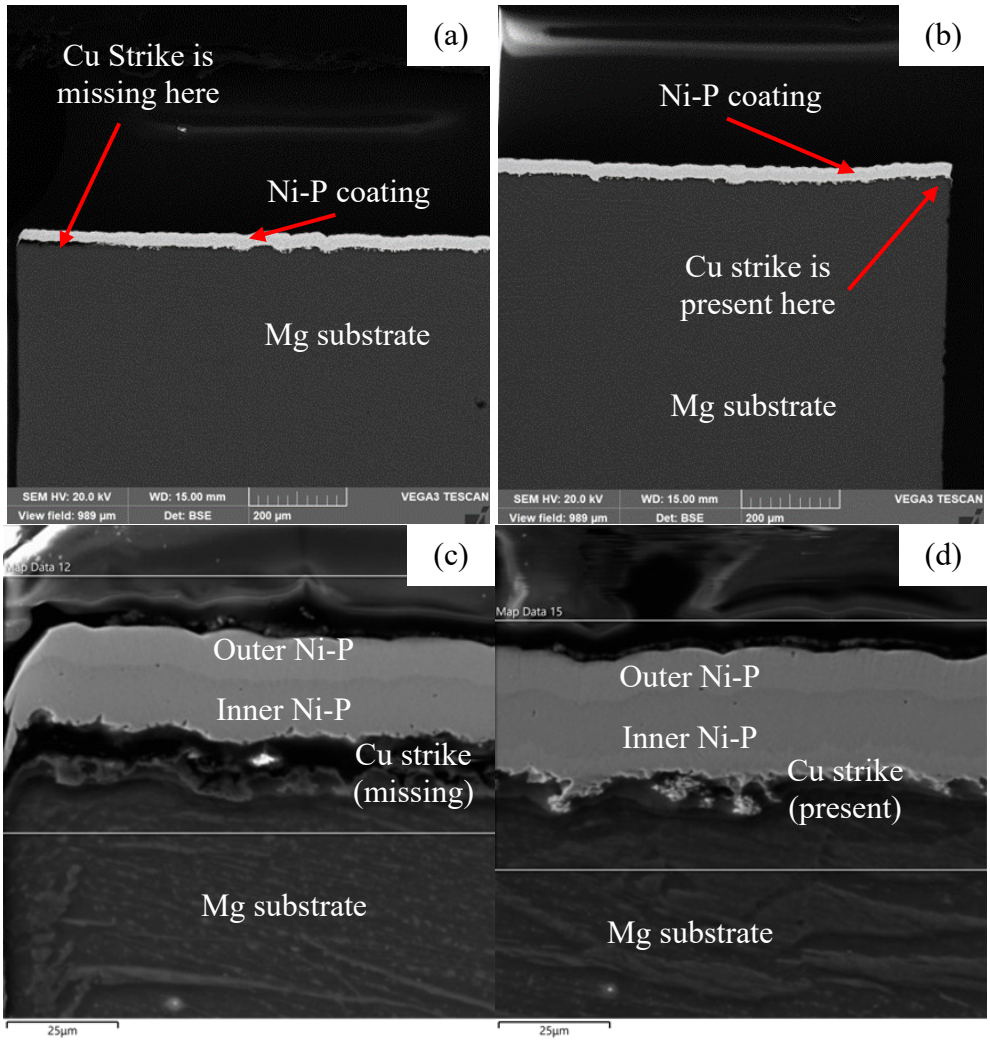

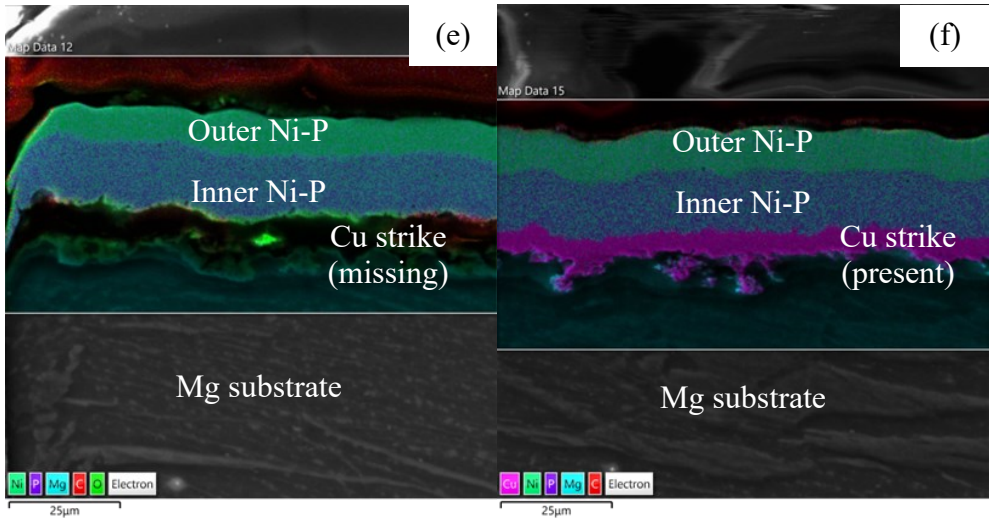

Figure 4-10: SEM BSE cross section micrographs of coating #4 in the vicinity of epoxy debonding; a), c), e) near the edge of the sample and b), d), f) away from the edge of the sample. a), b) Low magnification images; c), d) higher magnification images; e), f) respective EDX overlay maps for c) and d).

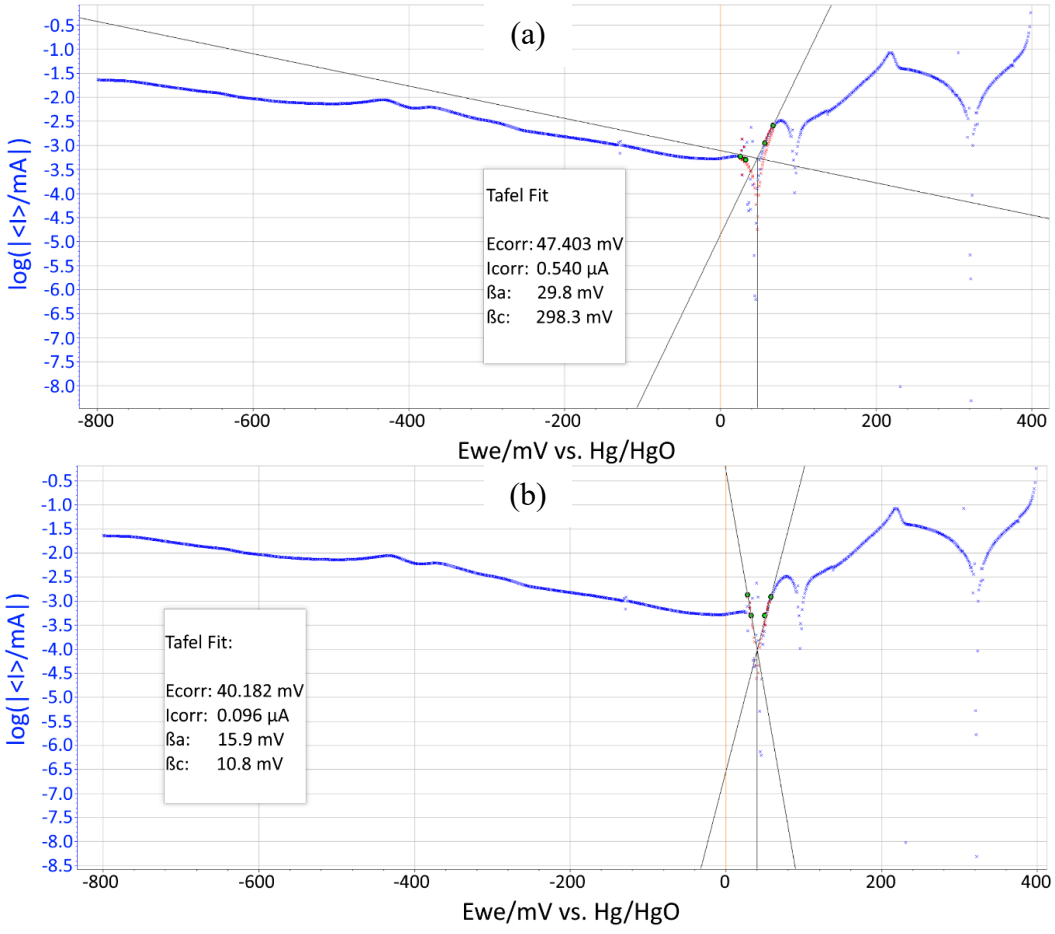

Figure 4-11: Example of high variability in Tafel analysis results caused by PDP plot being noisy around the peaks. This can lead to a) higher i_{corr} values and b) lower i_{corr} values. PDP plot is from day 7 test from the immersion tested coating #2.

The relationship between porosity and day 49 CR for the immersion tested samples is shown in Figure 4-12. Overall, the plots do not follow expected trends of high porosity (in terms of pore areal density or pore area fraction) leading to high CR [24], [28], [29], [78], [79]. This is likely due to epoxy debonding resulting in larger exposed areas, which resulted in calculated i_{corr} being inaccurate, and due to noisy peaks in the PDP plots making meaningful i_{corr} measurements difficult.

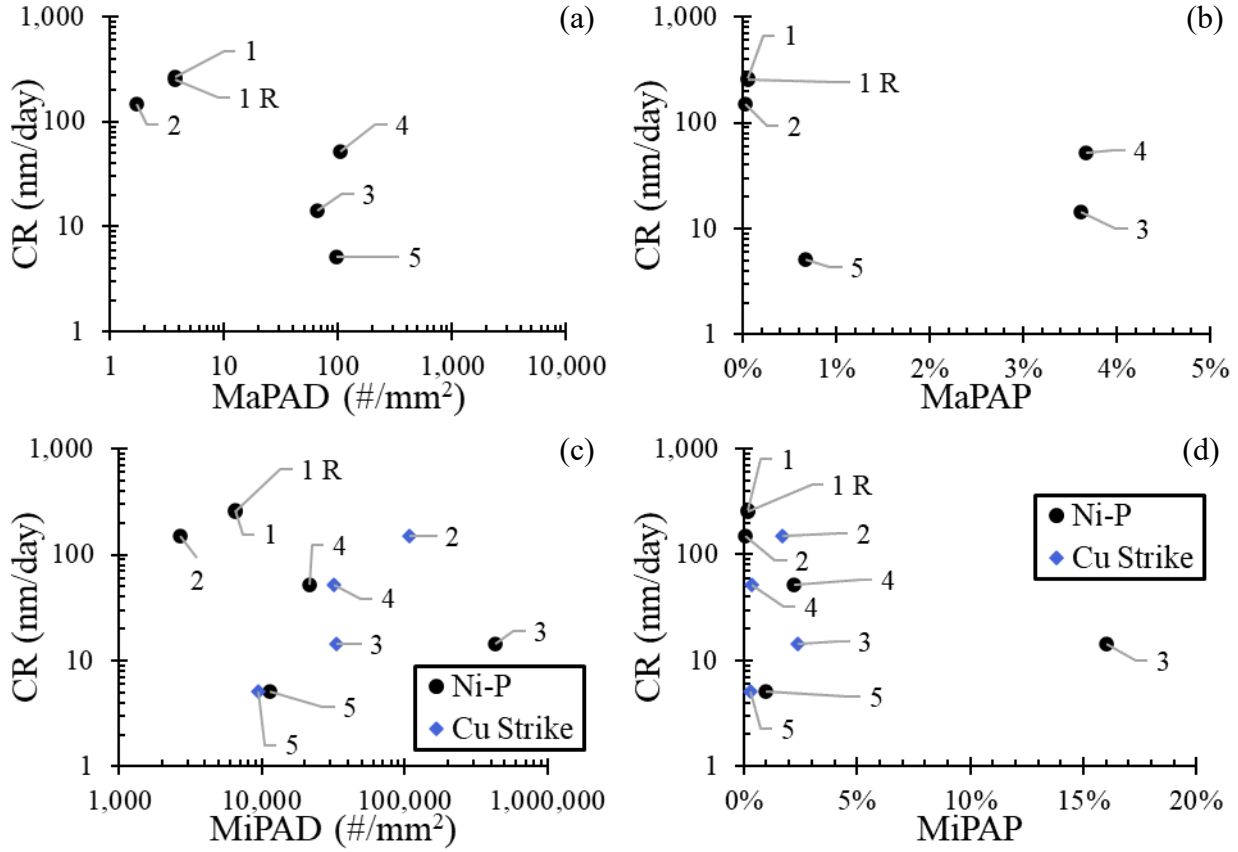

Figure 4-12: Comparison of a) macroscopic pore areal density (MaPAD), b) macroscopic pore area percentage (MaPAP), c) microscopic pore areal density (MiPAD), and d) microscopic pore area percentage (MiPAP) vs. CR at 49th day of immersion testing. Only outer Ni-P layer and Cu strike layer porosity are presented.

4.3.2 Cycle Testing Results

The OCV, E_{corr}, and CR values before and after GCPL for all coatings are shown in Figure 4-13. Another coating #3 sample (#3 L) was tested for 3,359 cycles; this was done to determine the effects of longer cycling. The CR values before and after GCPL are provided in Table 4-7. OCV,

E_{corr}, and CR increased after GCPL for all coatings. Coatings #1, #2, #4, #6, and #8 used DP110 epoxy. Coating #6 had the highest CR after GCPL at $6.80 \cdot 10^3$ nm/day. The CR of coating #3 L ($2.82 \cdot 10^3$ nm/day) is higher than #3 ($1.67 \cdot 10^3$ nm/day), indicating that longer cycling times (more cycles) results in more corrosion of the coating. The CR values from cycle testing are much larger than those from immersion testing, suggesting that GCPL damages the coating more strongly than passive immersion. This was confirmed from SEM observations of the coating surface after testing (Figure 4-14). The immersion tested coating #3 sample (Figure 4-14a) had lower surface porosity than the cycle tested coating #3 sample (Figure 4-14b). The porosity likely formed due to preferential corrosion along Ni-P particle boundaries, so higher porosity indicates greater corrosion attack. The GCPL, OCV, and PDP curves for cycle tested samples are shown in Figure C-3 to Figure C-5, respectively.

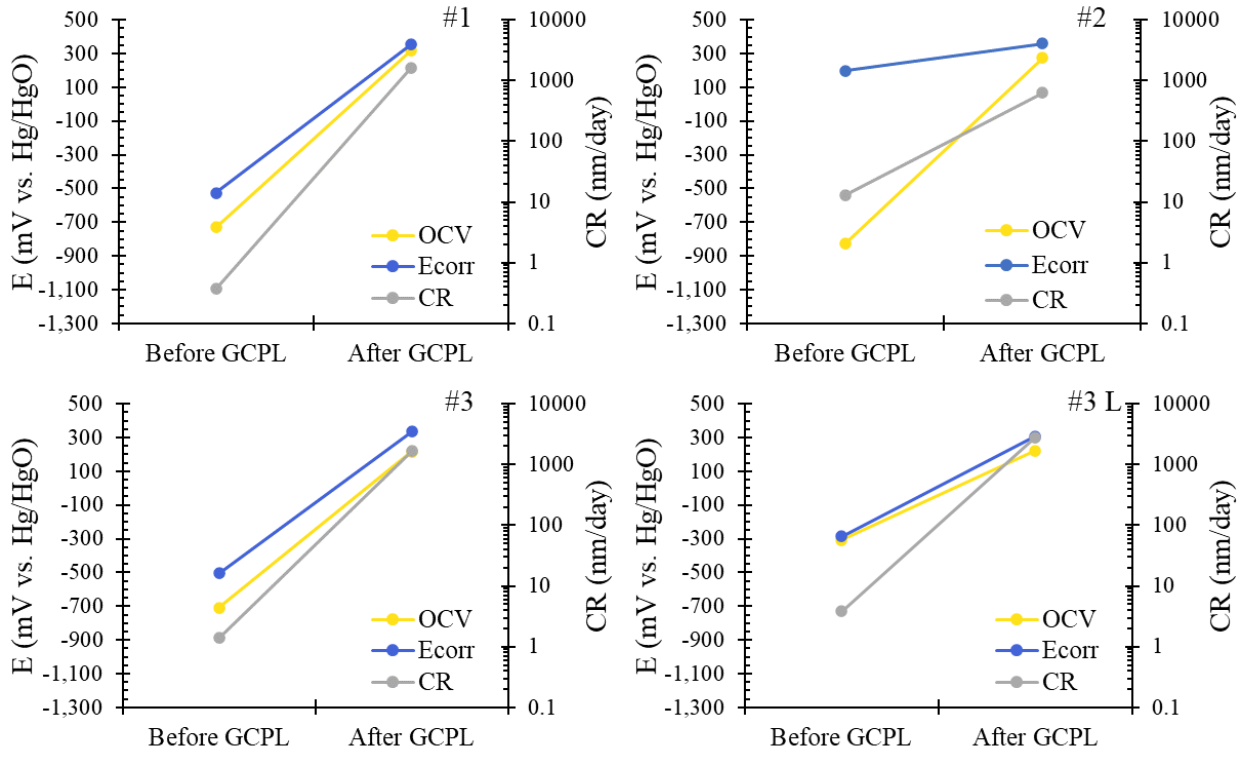

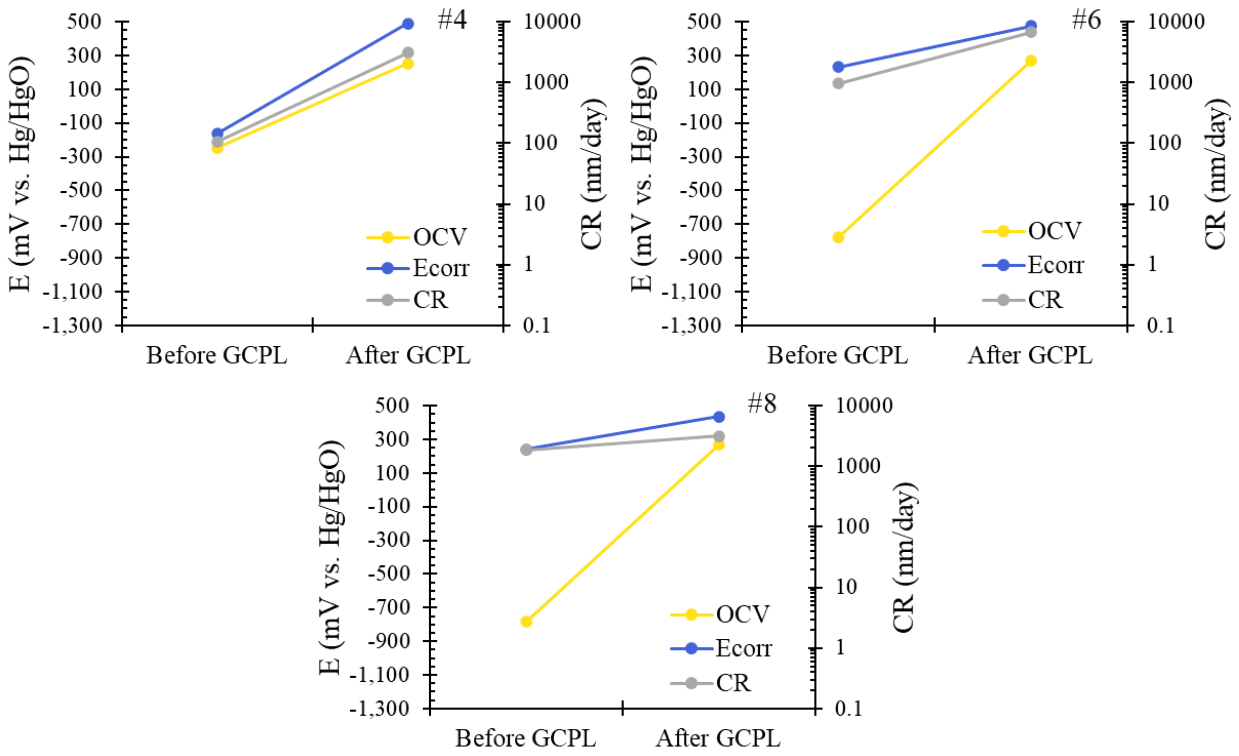

Figure 4-13: OCV, Ecorr, and CR values before and after cycle testing. U denotes uncut bar and L denotes a longer duration cycle test (3,359 cycles).

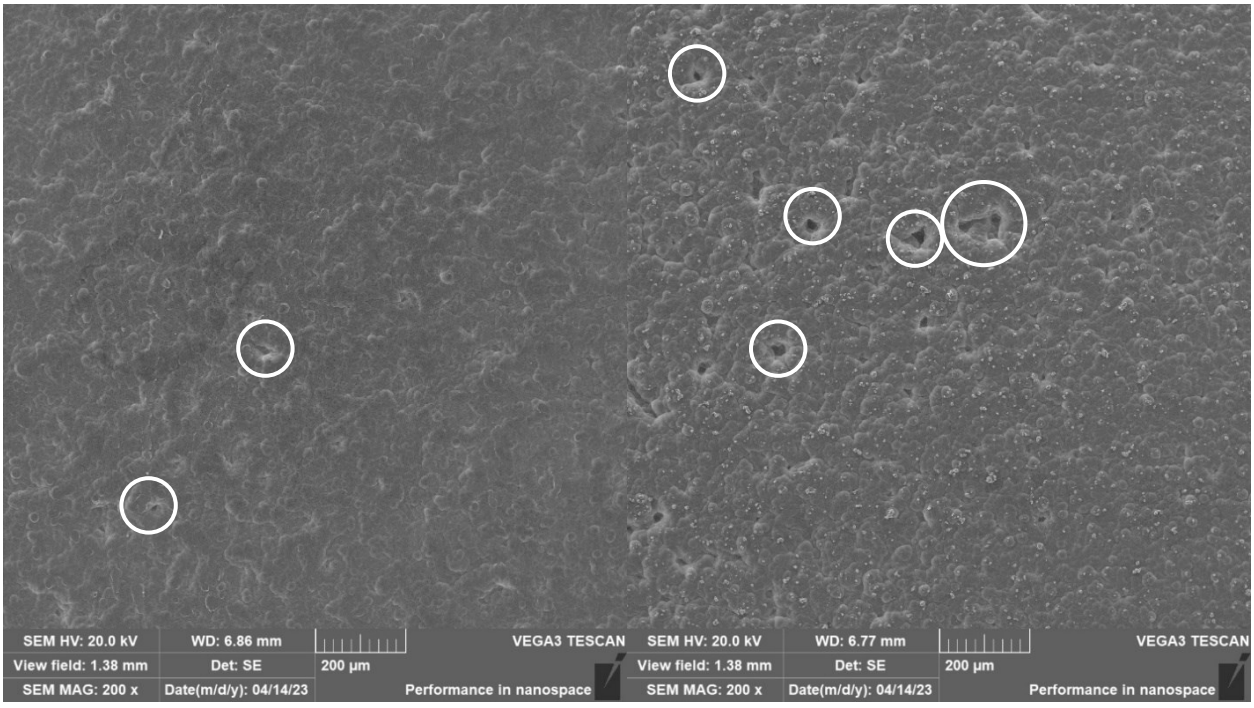

Figure 4-14: SEM SE micrographs of coating #3 a) after immersion testing and b) after cycle testing (2,000 cycles). White circles are used to indicate examples of porosity.

A similar reason as given in Section 4.3.1 can explain why E_{corr} increased alongside i_{corr} during cycle testing. During cycle testing, OER and HER are deliberately induced, resulting in the electrolyte becoming more oxidizing. The increase in oxidizing behaviour during cycle testing is larger than that in immersion testing because O_2 and H_2 are directly formed on the coating surface, resulting in larger increases in oxidizing capabilities. The electrolyte is also open to air and magnetically stirred during cycle testing, enabling larger amounts of CO_2 to be absorbed in solution as well. These factors explain why the increase in E_{corr} from cycle testing is larger than that from immersion testing.

Table 4-7: GCPL CR values before and after testing

Coating #	Before GCPL CR (nm/day)	After GCPL CR (nm/day)
1	$3.71 \cdot 10^{-1}$	$1.60 \cdot 10^{3}$
2	$1.30 \cdot 10^{1}$	$6.26 \cdot 10^{2}$
3	$1.40 \cdot 10^{0}$	$1.67 \cdot 10^{3}$
3 L	$3.84 \cdot 10^{0}$	$2.82 \cdot 10^{3}$
4	$1.07 \cdot 10^{2}$	$3.12 \cdot 10^{3}$
6	$9.58 \cdot 10^{2}$	$6.80 \cdot 10^{3}$
8	$1.88 \cdot 10^{3}$	$3.15 \cdot 10^{3}$

The surface morphology of cycle tested samples changed significantly after testing and some epoxy debonding occurred, as shown in Figure 4-15. A cauliflower-like surface morphology was maintained after testing, with the boundaries between nodules becoming more apparent. All cycle tested samples failed the acetic acid test after cycle testing. Bubbling was observed along the edges between the “frontside” and side faces, where the epoxy had debonded. No bubbling was observed on Ni-P surfaces, only on non-Ni-P surfaces. This indicates that no large defects developed in the Ni-P coatings due to cycle testing. As such, the increase in CR is likely caused by epoxy debonding,

which increased the surface area exposed to the electrolyte (including the coating cross section). To confirm this hypothesis, AAS analysis was performed on the electrolyte for coatings #1-#4 to measure Ni, Cu, and Mg concentration changes (Figure 4-16), where "Before GCPL" values represent baseline ion concentrations. No measurable changes occurred to the Mg and Ni ion concentrations for all electrolytes, indicating that Mg and Ni-P corrosion did not occur. The #3, #3 L, and #4 coatings had significant increases in Cu after cycle testing, indicating that their Cu strike layers corroded. A cross section of the coating #1 sample was analyzed (Figure 4-17) and its Ni-P coating thickness was measured at regions where the sample was exposed to the electrolyte. Ten such locations were measured and averaged. The thickness of the coating before testing was 29.4 ± 1.6 µm (Table 3-5). The measured thickness at the exposed regions is 29.2 ± 1.6 µm. There were no measurable differences in Ni-P thickness before and after cycle testing for the #1 coating, which indicates that there was no measurable amount of Ni-P corrosion; this result is consistent with the AAS results. Since the CR before cycling was ~0.3-0.4 nm/day (negligible) and the CR after cycling was ~1.6 µm/day, the amount of corrosion over the 2 day test period may be too small to be measured reliably given the variation in coating thickness.

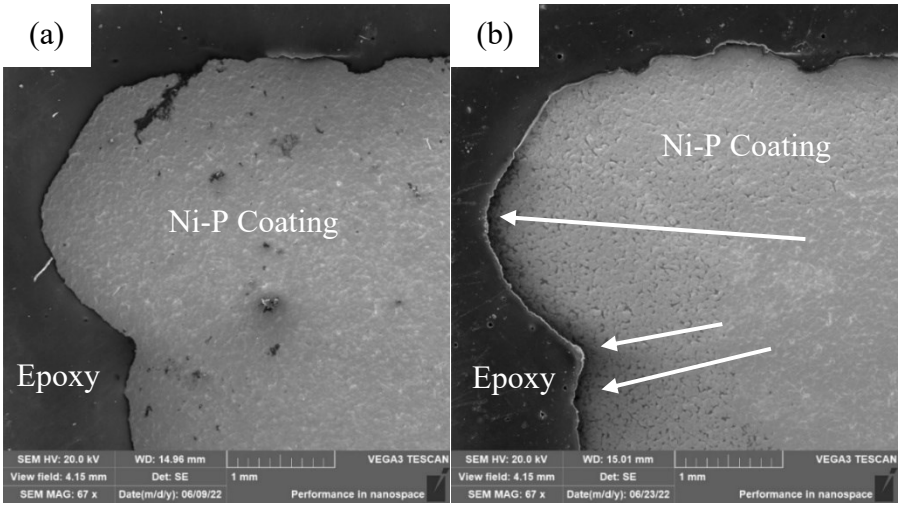

Figure 4-15: Surface morphology of #1 coating a) before and b) after cycle testing. Arrows are used to indicate regions of epoxy debonding.

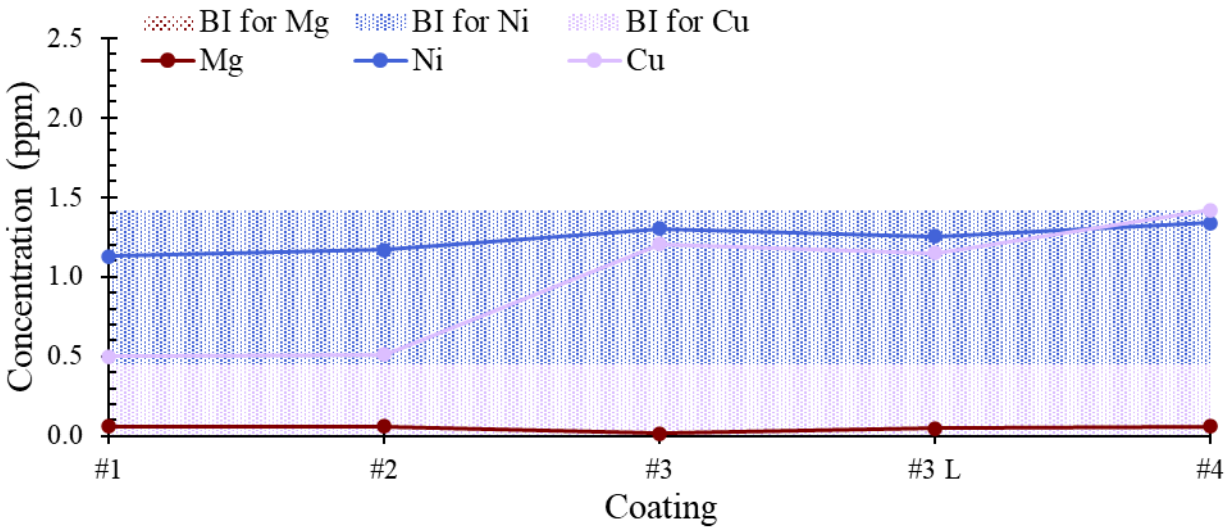

Figure 4-16: AAS results for Mg, Ni, and Cu for cycle tested samples. "BI" refers to baseline ion concentrations.

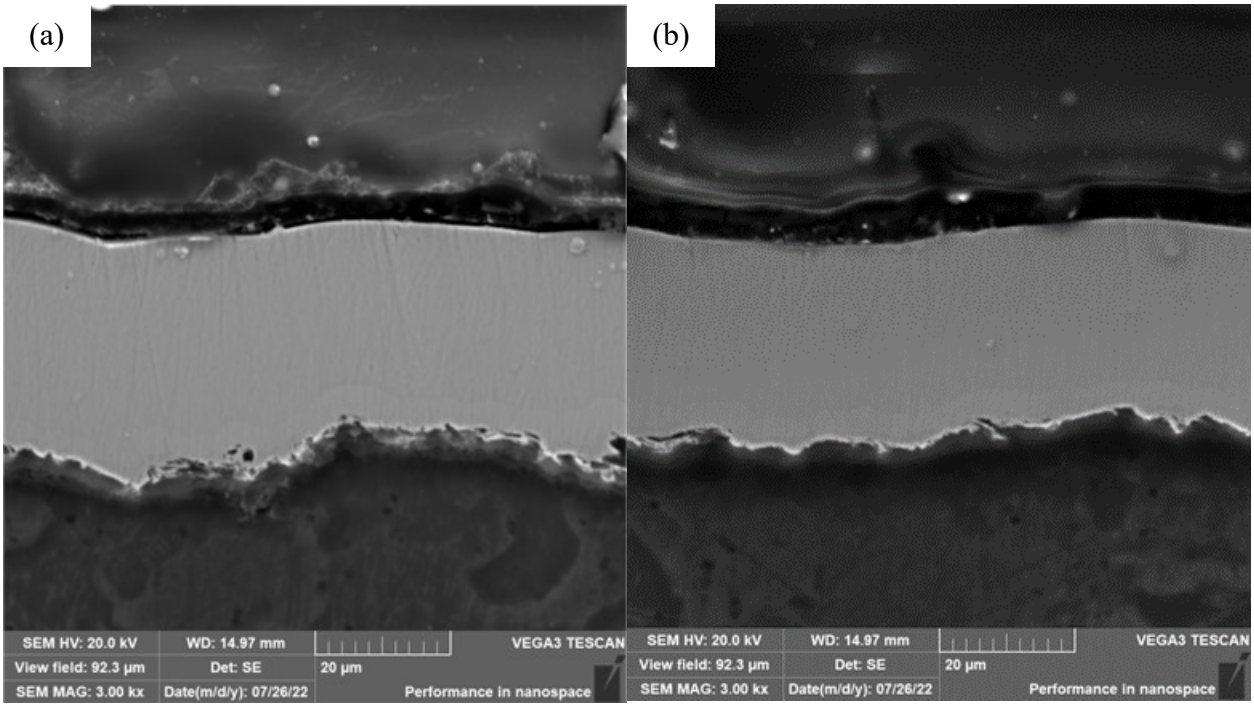

Figure 4-17: Regions used in measuring Ni-P layer thickness for coating #1 at a) non-exposed region and b) exposed region.

The cross section of the coating #3 L sample was analyzed and its outer Ni-P layer thickness was measured at regions where the sample was exposed to the electrolyte (Figure 4-18). 25 locations were measured and averaged. The thickness of the outer Ni-P layer before testing was 10.5 ± 1.3 µm (Table 3-5). The measured thicknesses at the non-exposed and exposed regions are 8.5 ± 0.5

μm and 4.3 ± 0.5 μm, respectively. There was a ~6 μm decrease in Ni-P thickness before and after cycle testing for the #3 L coating, which indicates that there was measurable uniform Ni-P corrosion. This result contradicts the AAS results, which showed essentially no Ni loss (Ni-P corrosion) into the electrolyte. One possible explanation is that since cycle testing involves applied currents, Ni from the outer Ni-P layer is dissolved into solution and is almost immediately electroplated into the porosity of the graphite counter electrode. The graphite counter electrode was not analyzed after testing to confirm this explanation. Only coating #3 L experienced corrosion observable based on SEM analysis. This may be because coating #3 L was cycled for 1,359 cycles longer than other samples. Other samples likely also corroded, but their thickness changes were likely within the standard deviation of the measurements and, therefore, not detectable.

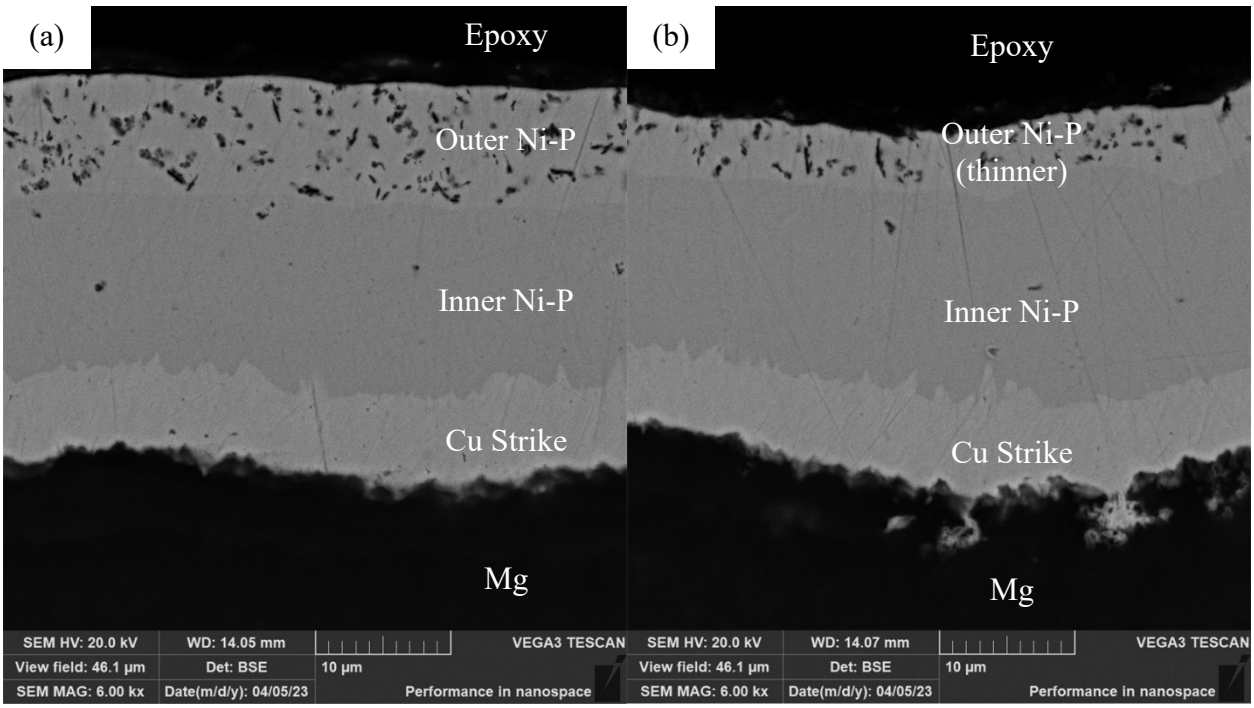

Figure 4-18: SEM BSE images of Ni-P coating #3 L at a) a non-exposed region and b) an exposed region after cycling. A clear decrease in thickness is apparent.

To evaluate the effect of exposing uncoated sample edges to the electrolyte, two samples of coating #19 were prepared. One was prepared using the standard method employed for all other

electrochemical samples (epoxied sectioned bar) and one by applying epoxy around an uncut bar so that an area of 1.8 cm^2 was exposed to the electrolyte. If epoxy debonding occurred for the uncut sample, then the coating cross section, specifically the Cu strike layer, would not be exposed to the electrolyte. In addition, the Mg substrate would not be directly exposed to the electrolyte. The OCV, CR, and E_{corr} values from these samples are shown in Figure 4-19. These values are highly similar, indicating that epoxy debonding did not significantly affect the results.

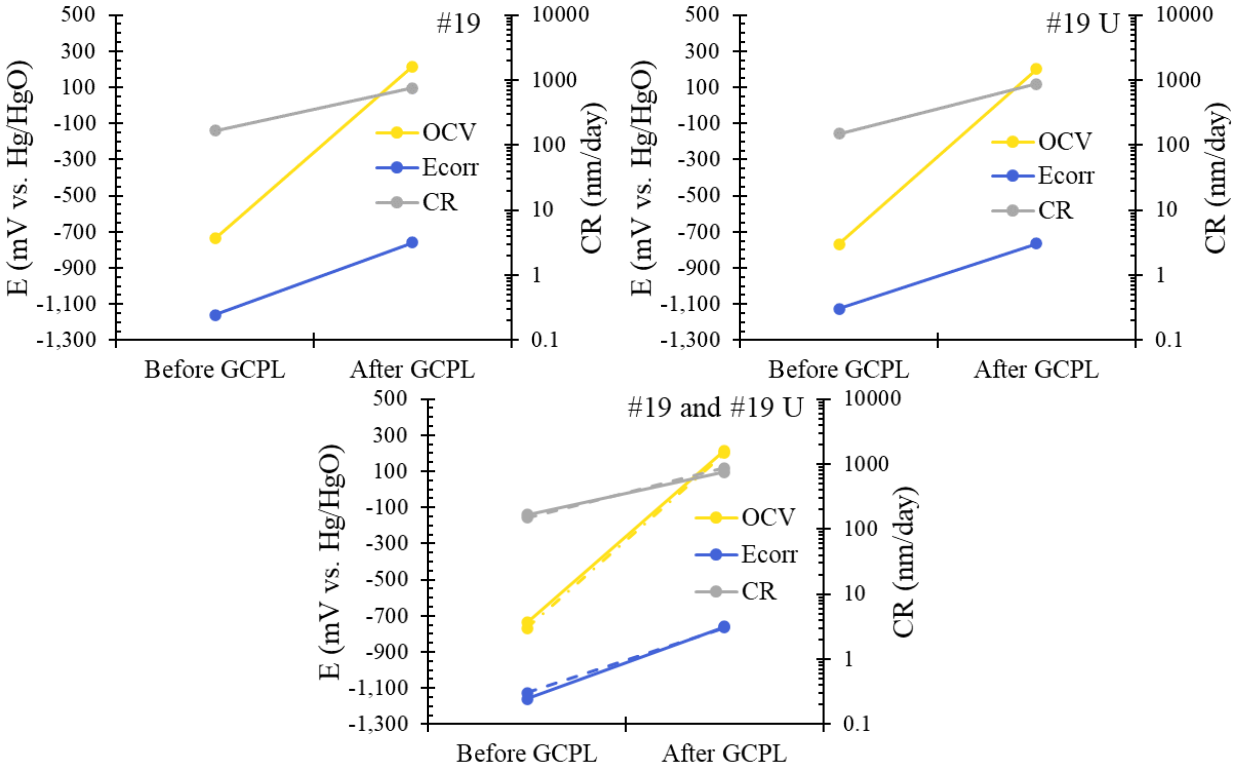

Figure 4-19: OCV, CR, and E_{corr} values before and after cycling for coating #19 samples. U denotes the uncut sample. For the last graph, the results for #19 and #19 U are superimposed; #19 is represented by solid lines and #19 U by dashed lines.

To estimate the lowest and highest possible changes in Ni and Cu content measurements from AAS, the CR values of coatings #19 before GCPL and #19 U after GCPL were used to calculate their equivalent Ni and Cu content increases. Coating #19 before GCPL had the lowest CR, so coupled with its low exposed area, it had the lowest equivalent volumetric loss, which is proportional to Ni or Cu loss into electrolyte. Coating #19 U after GCPL had the largest CR, so

coupled with its large exposed area, it will have the highest Ni or Cu loss into electrolyte. The values are listed in Table 4-8. The thickness loss values, assuming uniform corrosion and Ni and Cu content change in electrolyte (from AAS), were calculated using Equation 4-2 and Equation 4-3. Based on the Ni-P and Cu strike thickness loss calculations, significant amounts of Ni and Cu loss (2-22 and 2-24 ppm, respectively) into the electrolyte were expected. The best-case and worst-case uniform thickness losses for Ni-P and best-case uniform thickness loss for Cu strike are within their respective standard deviation of coating thicknesses, meaning that corrosion cannot be reliably detected using layer thickness measurements from SEM. The electrolytes were analyzed using AAS to determine if the measured Ni and Cu content correlates with the expected Ni or Cu content values in Table 4-8.

Table 4-8: Lowest and highest possible Ni-P and Cu strike uniform thickness loss, their corresponding i_{corr}, and equivalent loss into electrolyte based on uniform thickness loss for coating #19 samples

	Lowest Possible Loss	Highest Possible Loss
Exposed Area (cm^2)	0.844	1.80
Corresponding i_{corr} (mA/cm^2)	5.64	29.5
Ni-P CR (nm/day)	166	872
Uniform Ni-P Thickness Loss (μm)	0.333	1.74
Equivalent Ni Content Increase in Electrolyte (ppm)	2.00	22.4
Cu Strike CR (nm/day)	179	938
Uniform Cu Strike Thickness Loss (μm)	0.358	1.88
Equivalent Cu Content Increase in Electrolyte (ppm)	2.17	24.2

The AAS results for Ni, Cu, and Mg content in the electrolyte are shown in Figure 4-20. There was no measurable loss of Mg and similar amounts of Ni loss for both samples. The results indicate that epoxy debonding did not affect the AAS measurements, since Cu strike corrosion was not observed. The AAS results show that the protective capability of coating #19 is quite good. The

discrepancy in high CR values and low measured corrosion from AAS is likely because of the noisy peaks in the PDP plots. The explanation for this is provided in Section 4.3.1.

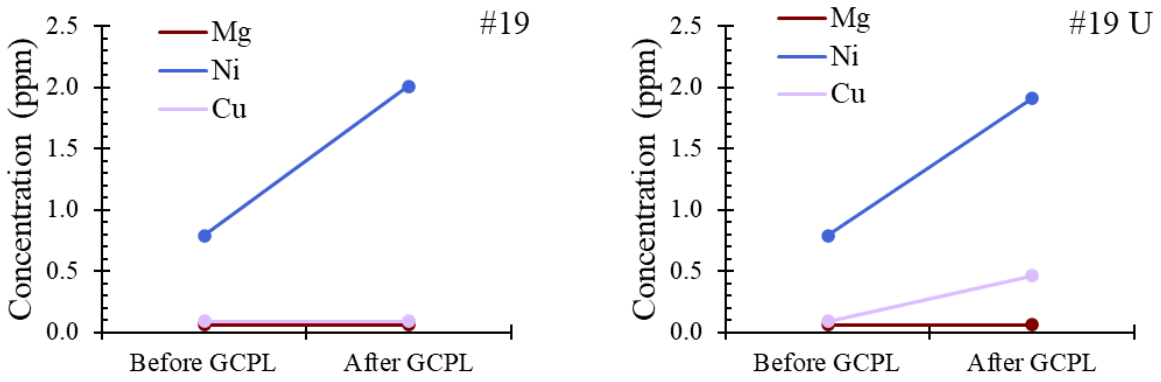

Figure 4-20: AAS results for coating #19 samples. U stands for uncut sample.

The relationship between porosity and CR after cycle testing is shown in Figure 4-21. CR increased with increasing Ni-P macroscopic and microscopic pore density (Figure 4-21a and Figure 4-21c). Overall, the CR increased with increasing Ni-P macroscopic pore area percentage, but there was no trend with microscopic pore area percentage (Figure 4-21b and Figure 4-21d). No trends were observed between CR and Cu strike microscopic pore areal density or microscopic pore area percentage (Figure 4-21c and Figure 4-21d). Since the porosity is not through-thickness, any Ni-P corrosion was likely uniform and minor. This is shown in Figure 4-22, where the coating #1 surface morphology (Figure 4-22a) became notably coarser after cycle testing along Ni-P particle boundaries (Figure 4-22b). As such, higher macroscopic porosity would increase the surface area exposed to the electrolyte, leading to a higher CR value. The trend of increasing CR with increasing macroscopic porosity is, therefore, reasonable. Due to the smaller size of microscopic porosity, higher microscopic porosity did not lead to a significant increase in exposed surface area to electrolyte, which is why the CR did not increase as significantly with increasing microscopic porosity compared with increasing macroscopic porosity. The lack of correlation between CR and

Cu strike microscopic porosity is also expected, as Cu strike corrosion occurred from epoxy debonding and not from electrolyte flow through porosity [2]–[6].

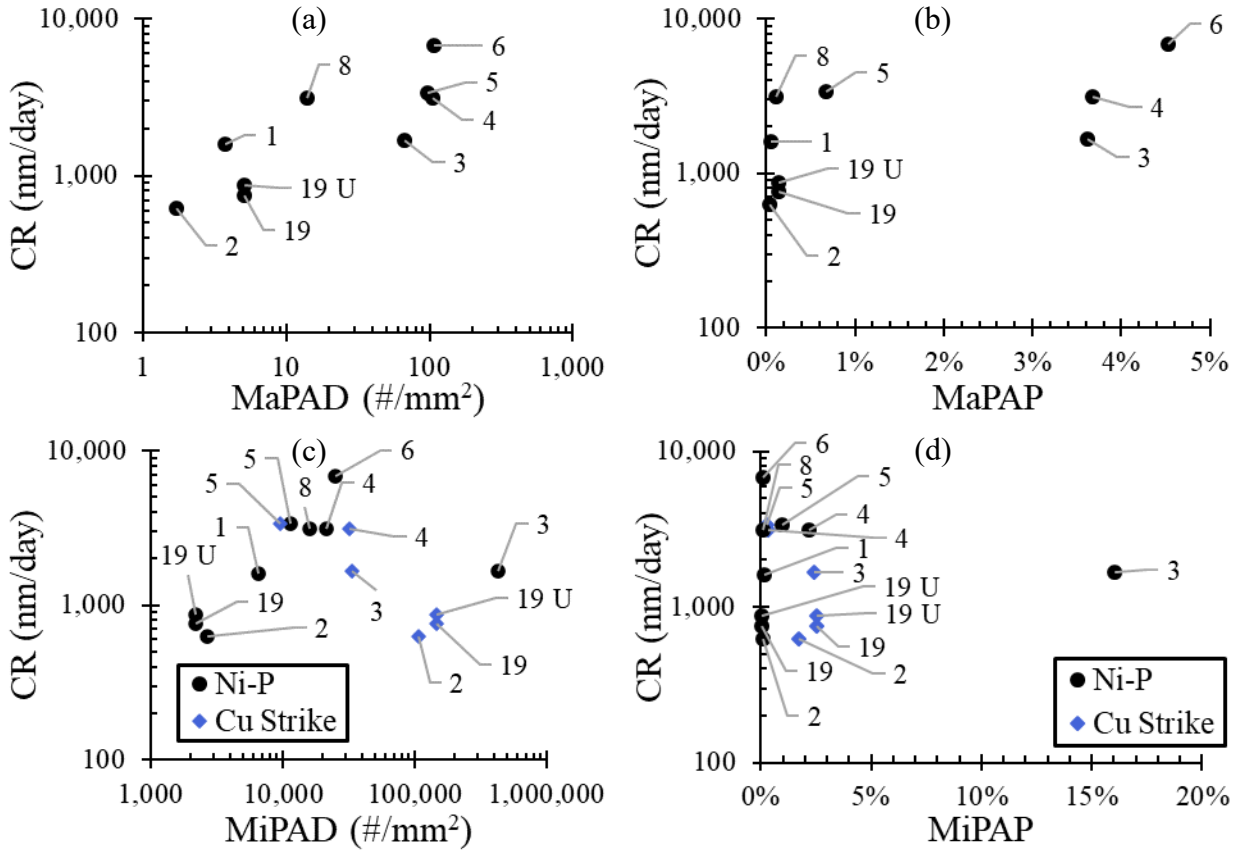

Figure 4-21: Comparison of a) MaPAD b) MaPAP, c) MiPAD, and d) MiPAP vs. CR after cycle testing. Only outer Ni-P layer and Cu strike layer porosity are presented.

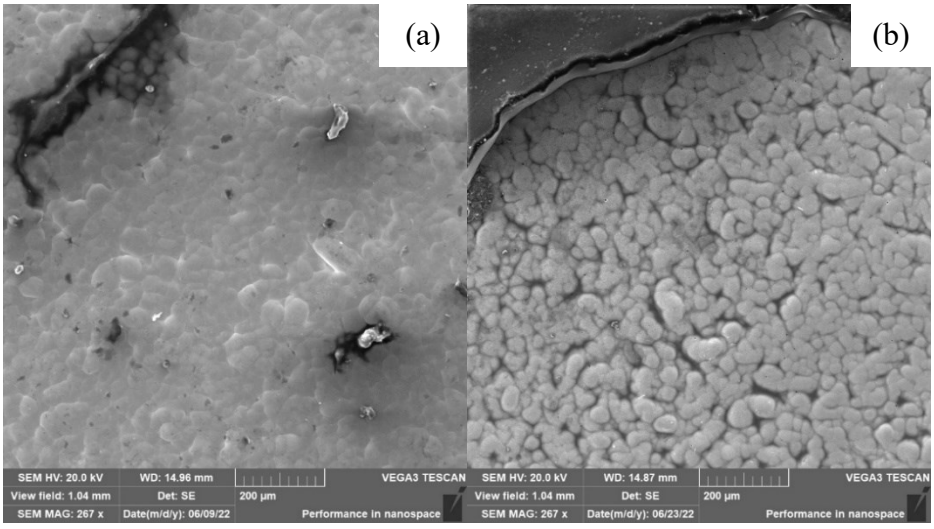

Figure 4-22: Coating #1 a) before cycle testing and b) after cycle testing.

4.3.3 Comparison of AAS with ICP-OES

To confirm the accuracy of the AAS measurements, the electrolyte from some samples, both immersion and cycle tested, were submitted for ICP-OES measurements. A comparison between AAS and ICP-OES results for the cycle tested #1, repeat immersion tested #1, immersion tested #4, and cycle tested #3 L coatings is shown in Figure 4-23. The immersion tested #1 repeat sample was not AAS tested. The #1 coating samples were chosen since they had, at the time of ICP-OES testing, the highest final CR values. The repeat immersion tested #1 coating sample was chosen instead of the original immersion tested sample since DP110 epoxy was used and does not debond as easily as the EpoThin 2 epoxy. The cycle tested #3 L sample was chosen since it underwent the longest GCPL step (3,359 cycles instead of the typical 2,000 cycles) and had, at the time of ICP-OES measurements, the highest after GCPL CR value. The immersion tested #4 sample was chosen since it had the highest measured Cu loss. Coatings #6 and #8 were cycle tested after the ICP-OES measurements were taken. The results have similar trends. Ni and Mg did not dissolve into the electrolyte and coatings containing Cu strike layers have some Cu loss into the electrolyte. ICP-OES showed more Cu loss for coating #4. One possible explanation for this discrepancy is [22] that the Cu content of coating #4 exceeded the Cu concentration used in the standard solutions for flame AAS measurements, resulting in an inaccurate measurement value. Additionally, the small AAS sample volume (~3 mL) for immersion testing electrolytes reduced measurement accuracy, as AAS typically requires > 5mL sample volume for accurate measurements [85], [86].

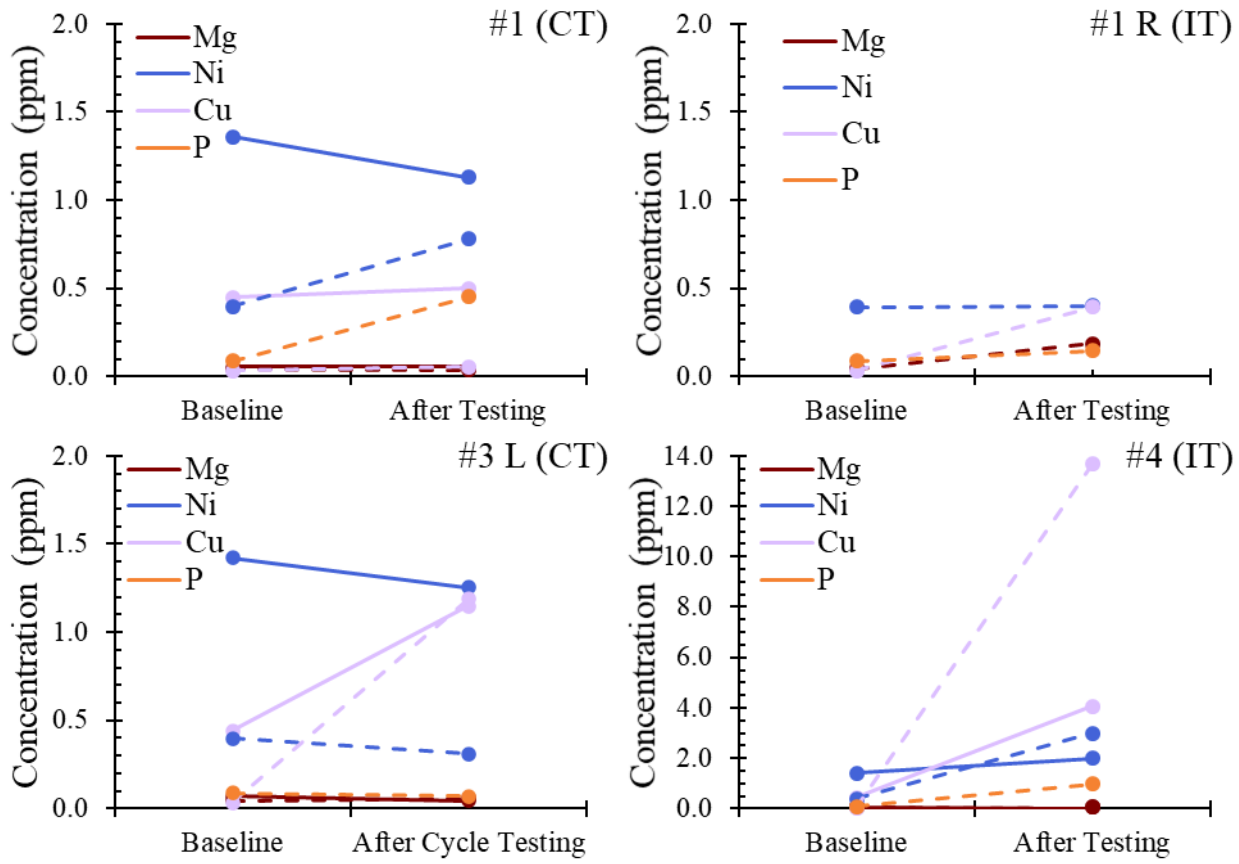

Figure 4-23: Comparison of AAS and ICP-OES results. R refers to a repeat test and L refers to a 3,359 cycle long cycle test. Solid lines are AAS results and dashed lines are ICP-OES results. CT refers to cycle testing and IT refers to immersion testing.

4.4 Summary

The corrosion performance of coatings #1 to #5, #6, #8, and #19 was characterized using immersion testing and/or cycle testing. The electrochemical test results were correlated with porosity results from Chapter 3 (Coating Characterization), SEM/EDX measurements of coating thickness and morphology changes, and compositional analysis using AAS and ICP-OES. Cycle testing induced larger changes in corrosion measurements. Ni-P corrosion rates determined from potentiodynamic polarization plots generally showed a positive correlation with coating porosity. The corrosion rates increased with higher pore areal density and area fractions. Based on SEM analysis, the cycle tested coating #3 L sample, which underwent a 3,359 cycle test compared to

the typical 2,000 cycle test, experienced measurable Ni-P corrosion that was not verified by AAS or ICP-OES analyses. This was attributed to Ni dissolving from the #3 L sample and immediately plating onto the graphite counter electrode due to the applied currents involved during cycle testing. Apart from the cycle tested coating #3 L, SEM, AAS, and ICP-OES analyses showed small or negligible Ni-P corrosion for all samples. Cu strike loss was significant for some samples and was attributed to some epoxy debonding which exposed localized regions of Cu directly to the electrolyte. No Mg loss was detected from SEM, AAS, or ICP-OES analyses, indicating that Mg corrosion did not occur.

5 Nickel Electroplating

5.1 Introduction

Nickel electroplating is a well-established deposition technique applicable to many substrates. The most commonly used Ni plating solution is the Watts bath, which remains in use for electrodeposition of corrosion resistant coatings or electroforming [87]. A modified Watts bath was chosen for electroplating to leverage previous experience by members of the Ivey group, take advantage of its high plating rate to reduce overall plating time, and to obtain highly corrosion resistant coatings for service in highly alkaline environments. Compared to the standard Watts bath, the modified bath used in this work does not utilize pH stabilization to pH 2.0-4.5 or agitation to simplify bath upkeep and setup and contains 0.2 g/L saccharin to refine grain size, reduce tensile internal stress, and increase coating hardness through codeposition of sulfur in the coating [87]. A design of experiments (DoE) approach was taken to optimize the electroplating process. Au coated single crystal Si wafers (Au/Si wafers) were used as substrates in development of the process because they could be cleaved to permit rapid cross sectional characterization.

5.2 Experimental

5.2.1 Sample Preparation

Au/Si wafers, 2 cm X 1 X 0.1 cm in size, were ultrasonically cleaned using reagent alcohol for 5 min and then dried using dry compressed air. The Au coating on the <100> oriented Si wafers was ~200 nm thick and had a ~25 nm thick Ti adhesion layer between the Si substrate and Au coating. Nail polish was applied on the Au coating to isolate an area for electroplating and was allowed to dry for at least 2 h. One region of the Au coating was left unpainted to permit electrical contact

(Figure 4-1). The dimensions of the plating regions were measured using a ruler and the plating region area for each sample was recorded to ensure that the desired current density was applied during electroplating. The wafers with nail polish were rinsed with deionized water and dried using dry compressed air prior to electroplating.

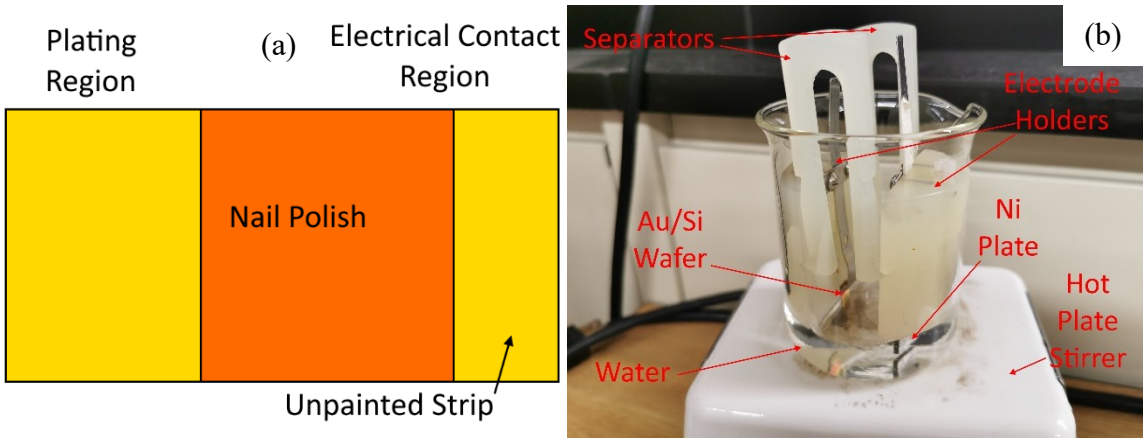

Figure 5-1: a) Plan view schematic of Au/Si wafer after nail polish application and b) labelled image of electroplating setup. Water is used in b) to visually demonstrate typical liquid level of the plating solution.

5.2.2 Electroplating Solution and Electroplating Cell Setup

A modified Watts bath was used for electroplating [87]. The composition of this bath is tabulated in Table 5-1. The chemicals were utilized as supplied. The solution was magnetically stirred at 300 RPM for ~2.5 h at ~40-60ºC on a hot plate stirrer prior to use. After stirring, the magnetic stir bar was removed from the solution and a thermometer was inserted. The temperature control of the hot plate stirrer was adjusted so that temperature of the plating solution (per the thermometer) was kept at ~50ºC. A Ni plate and an electroplating sample were clamped into two electrode holders and inserted into the solution, ensuring that only the Ni plate and plating region of the sample (Figure 5-1a) were in contact with the solution. The clamp was attached to the sample at the electrical contact region (Figure 5-1a). Two plastic separators were used to ensure the Ni plate and sample were parallel to one another. The cables from the power source were attached to the

clamps in the electrode holders, with the Ni plate as the anode and the sample as the cathode (Figure 5-1b). The power supply was turned on and the plating conditions set. After electroplating, the heating element of the hot plate stirrer was turned off, the cables were disconnected from the electrode holders and the plating bath was removed from the stirrer. The electrode holders and separators were removed from the bath and rinsed with deionized water. The sample and Ni plate were unclamped from the electrode holders and rinsed with deionized water. The electrode holders, separators, and Ni plate were left to dry in air. The sample was sonicated in acetone for 5 min and reagent alcohol for 5 min to remove the nail polish and clean the sample, respectively. The cleaned sample was removed from the reagent alcohol and dried using dry compressed air.

Table 5-1: Modified Watts bath composition [87]

Chemical	Supplier	Concentration (g/L)
$NiSO_4 \cdot 6H_2O$	Fisher Scientific	275
$NiCl_2 \cdot 6H_2O$	Fisher Scientific	30
H_3BO_3	MP Biomedicals	45
Saccharin ($C_7H_5NO_3S$)	Sigma-Aldrich	0.2
Operating Conditions		
Average pH at 20ºC		~1.00
Temperature (ºC)		~50

5.2.3 Design of Experiments

A design of experiments (DoE) approach was performed to identify the optimal plating parameters using Design-Expert Version 13 (Design-Expert) by Stat-Ease®. Pulse – on time (t_{ON}) from 2-10 ms and average plating current density (i_{ave}) of 10-40 mA/cm^2 were selected as independent variables. The average thickness (T_{ave}), standard deviation of thickness (T_{SD}), current efficiency

(CE), relative standard deviation of thickness (calculated by dividing the standard deviation of thickness with the average thickness, T_{RSD}), and plating rate (PR) were chosen as dependent variables. The shorthand used for the dependent variables is thickness-derived metrics (TDM). CE was calculated using Equation 5-1 to Equation 5-3, where T_{ave} is in μm, $A_{plating}$ is the plating area in cm^2, ρ_{Ni} is the density of Ni (8.908 g/cm^3), M_{Ni} is the molar mass of Ni (58.6934 g/mol), N_A is the Avogadro constant ($6.0221 \cdot 10^{23}$), i_{ave} is in mA/cm^2, $t_{plating}$ is in min, $q_{plating}$ is the charge used for electrodepositing the coating on the sample, and q_{total} is the total charge delivered to the sample by the power source. The multiplications by 10^{-4} and 60 are for unit conversions.

$$q_{plating} = \frac{T_{ave} A_{plating} \rho_{Ni}}{M_{Ni}} \cdot \frac{2\ mol\ e^-}{1\ mol\ Ni} \cdot N_A \cdot 10^{-4} \quad \text{Equation 5-1}$$

$$q_{total} = i_{ave} A_{plating} t_{plating} \cdot 60 \quad \text{Equation 5-2}$$

$$CE = \frac{q_{plating}}{q_{total}} \quad \text{Equation 5-3}$$

For pulsed current (PC) plating, the total pulse length was fixed to 10 ms, so 2 ms t_{ON} means that the pulse – off time would be 8 ms; 10 ms t_{ON} corresponds to direct current (DC) plating. A response surface design was chosen and a list of runs (tests) was generated that are tabulated in Table 5-2. Empirical models for TDM were developed using t_{ON} and i_{ave} as independent variables. A numerical optimization function in Design-Expert was utilized to select appropriate plating parameters. Thicker (~40 μm) coatings were later plated and characterized from the optimized plating parameters. The procedure is described in greater detail in Section 5.2.5.

Table 5-2: List of DoE runs

Run #	t_{ON} (ms)	i_{ave} (mA/cm^2)
1	5	30
2	2	20
3	10	20
4	2	40
5	10	20
6	8	10
7	5	30
8	2	30
9	5	30
10	8	40
11	10	40
12	5	10

Some preliminary investigation of the viability of electroplating Ni on Au/Si wafers was performed within the Ivey Group by Dr. Anqiang He. From his work, the estimated CE was 73%. Different $t_{plating}$ values were used for i_{ave} to ensure that a T_{ave} of ~4 μm could be obtained. These were calculated based on a CE of 73% and are tabulated in Table 5-3. A target thickness of ~4 μm was chosen to ensure that the plated samples could be easily cleaved without significant plastic deformation of the coatings, as any plastic deformation could distort thickness measurements.

Table 5-3: Corresponding $t_{plating}$ for each i_{ave} to obtain 4 μm T_{ave} assuming 73% CE

i_{ave} (mA/cm^2)	$t_{plating}$ (min)
10	26.7
20	13.4
30	8.9
40	6.7

Ultimately, the goal is to transfer the Ni electroplating process to Mg substrates with the aim of utilizing the coatings in zinc-air regenerative flow batteries. This will be the subject of future work and will be discussed further in Chapter 6 (Conclusions and Future Work). As a preliminary test of the transferability of the process, Ni was electroplated onto the #8 Ni-P coating and the morphology was compared with a similar coating on an Au/Si wafer. The coatings were deposited using 25 mA/m^2 DC plating for 1 h using slight magnetic agitation from the modified Watts bath tabulated in Table 5-1. The preliminary testing occurred before the DoE approach was taken; as such, the parameters used differ from the parameters used in runs #1-#12 or the optimized parameters presented in Sections 5.3.1 to 5.3.3. Plan view images of both coatings are shown in Figure 5-2. The surface roughness of the Ni coating deposited on the Au/Si wafer is smoother because the Au seed layer has a flat, mirror finish, whereas the #8 coating has a coarser surface finish due to its spherical nodular, "cauliflower-like" surface morphology (see Section 3.3.1 – Preliminary Characterization of Coating #1). The surface morphology of the two coatings is otherwise quite similar, which indicates that the optimized Ni coating process developed in this chapter is transferrable to Ni-P substrates. A pretreatment and electroless Ni-P plating procedure is being developed for Mg substrates by the Ivey group. The Mg substrate needs to undergo pretreatment to provide better adhesion of the Ni coating (or other coatings, such as Ni-P, Ni-B, etc.). The purpose of a thin electroless Ni-P layer after pretreatment is to protect the treated Mg surface from oxidation prior to electrodeposition of the thicker coating.

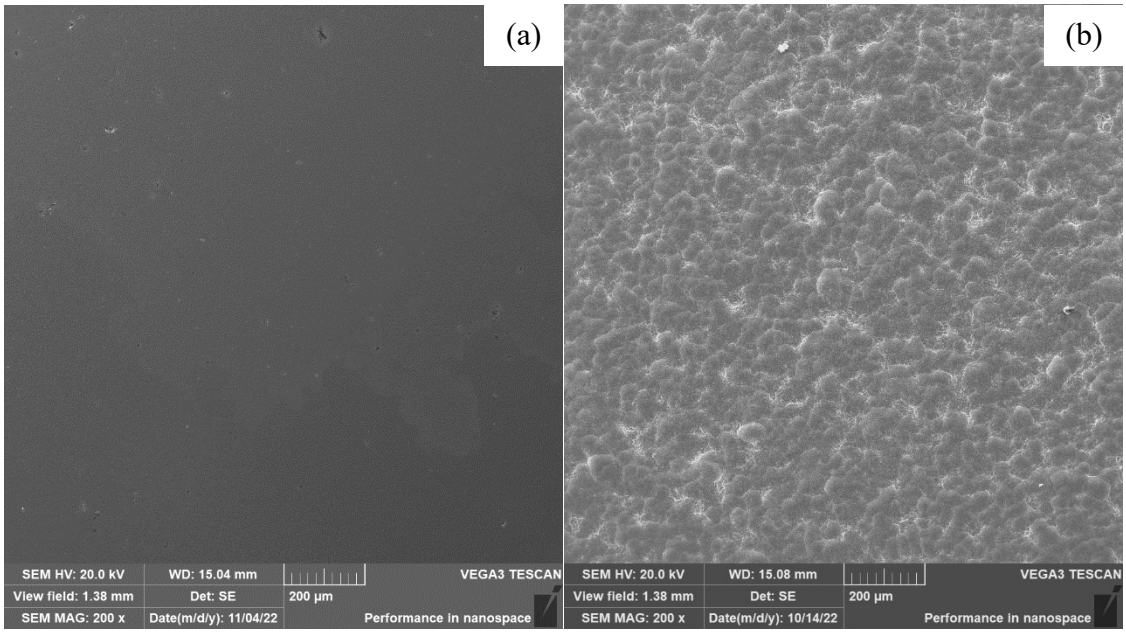

Figure 5-2: Surface morphology of Ni coatings deposited on a) Au/Si wafer and b) coating #8.

5.2.4 Coating TDM and Plan View Characterization

Samples with thin coatings (~4 µm T_{ave}) were cleaved and one half of each sample was placed horizontally on an SEM stub for plan view analysis while the other half was positioned vertically on the stub with the fracture face facing up for cross section analysis. The two halves of each sample were analyzed using an SEM (TESCAN VEGA 3). The accelerating voltage used was 20 kV with a working distance of 7 or 10 mm. At least three locations were selected for cross section analysis and the measured thicknesses across the locations were utilized to calculate TDM values. An example of thickness measurement is shown in Figure 5-3. Additional examples can be found in Figure D-1 in Appendix D.

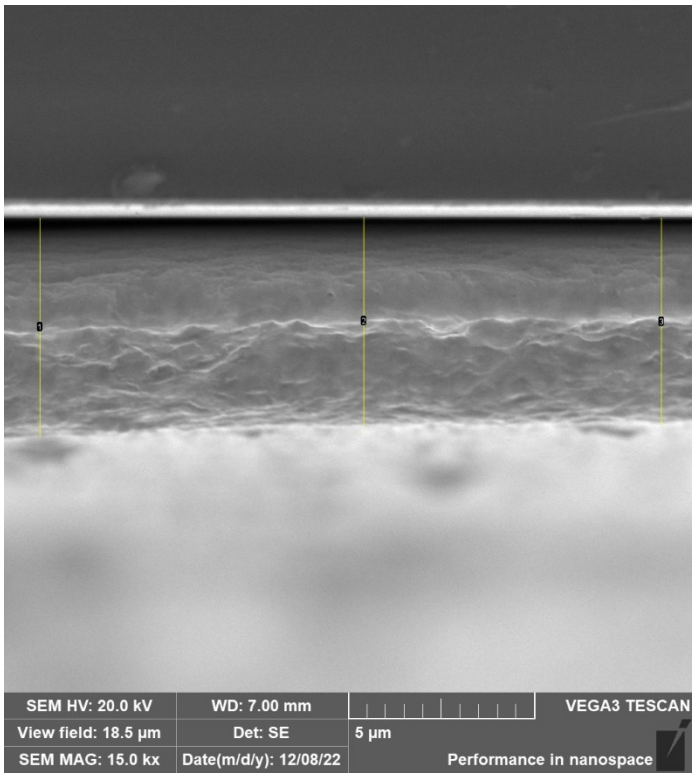

Figure 5-3: Example of thickness measurements (yellow lines) using SEM SE images. The example is from run #2 coating.

To determine the differences in using Au/Si wafers and electroless Ni-P coatings as substrates, Ni coatings were electroplated on Au/Si and on coating #8 using DC plating at 25 mA/cm^2 for 1 h in the preliminary investigations performed by Dr. Anqiang He. The #8 coating was chosen since it had low porosity and was more abundant than coatings #1, #2, or #19, which had lower porosity than #8. The comparison results are discussed in Section 5.3.5.

5.2.5 Characterization of Thick Coatings

Thick (T_{ave} ~40 µm) coatings were deposited on Au/Si wafers using the parameters optimized by the numerical optimization function in Design-Expert. The parameters are described in greater detail in Section 5.3.3. The samples were longitudinally sectioned using a low speed diamond saw using the same process described in Section 3.2.4 (Plan View SEM and EDX Analysis). Cross

sectional samples were then made using one of the halves of each sample; this process is described in Section 3.2.5 (Cross Section Sample Preparation and Analysis). Carbon tape was applied on the top of the cross section samples away from the polished surfaces and the half of each sample not used to make cross sectional samples was pressed onto the carbon tape. This setup allowed for plan views of the coatings to be analyzed alongside the cross sections. The microscopic porosity of these coatings was analyzed using the same process detailed in Section 3.2.6 (Microscopic-Scale Porosity Analysis). The same SEM operating conditions detailed in Section 5.2.4 were utilized. At least four regions were selected for microscopic porosity analysis.

5.3 Results and Discussion

5.3.1 Development of Empirical Models for T_{ave} and T_{SD}

The T_{ave} and T_{SD} values from the DoE runs are tabulated in Table 5-4. T_{ave} ranges from 2-6 µm for all runs, with most runs at ~3 µm. The variation in T_{ave} despite delivering the same electrical charge to each sample indicates that the 73% CE assumption is incorrect. The variation of CE with i_{ave} and t_{ON} is discussed later. Empirical models for T_{ave} and T_{SD} were developed using Design-Expert from data obtained in the 12 runs and are shown in Equation 5-4 to Equation 5-5 and Figure 5-4. The values in blue text in Table 5-4 were excluded while creating the respective empirical models as Design-Expert determined that ignoring these values would improve model fit. DC plating at 10 mA/cm^2 led to the highest T_{ave} (Figure 5-4a), because higher i_{ave} leads to increased hydrogen evolution on the cathode which inhibits electrodeposition and thus reduces the coating thickness. Since PC plating utilizes higher peak current densities than DC plating to ensure the same $t_{plating}$, during t_{on} the applied current density is generally higher than in DC plating, resulting in further hydrogen evolution [88], [89]. This is why shorter t_{ON} results in lower thickness. T_{SD} increases and

then decreases as i_{ave} increases but is lowest for 10 mA/cm^2 (Figure 5-4b). Watson showed that the throwing power (the ability to deposit equal thicknesses for recessed and prominent regions) of Ni plating baths increases slightly with lower i_{ave} (~2 mA/cm^2) and decreases slightly with higher i_{ave} (~43 mA/cm^2) [87]. As mentioned previously, hydrogen evolution increases at high i_{ave}, which inhibits coating deposition. This inhibition may lead to a leveling effect that decreases T_{SD} [87], [89], which may explain why T_{SD} increases and then decreases as i_{ave} is increased. As shown in Figure 5-5, T_{SD} is not affected by t_{ON}. As mentioned previously, PC plating results in higher peak current densities than DC plating, which results in additional hydrogen evolution. The overall increase in hydrogen evolution inhibits coating deposition and likely has a leveling effect, thus resulting in no overall trend between t_{ON} and T_{SD} [87], [89].

Table 5-4: Plating parameters and T_{ave} and T_{SD} values from DoE runs

Run #	i_{ave} (mA/cm^2)	t_{ON} (ms)	$t_{plating}$ (min)	T_{ave} (µm)	T_{SD} (µm)
1	30	5	8.9	3.50	0.257
2	20	2	13.4	4.80	0.681
3	20	10	13.4	3.80	0.163
4	40	2	6.7	2.64	0.0571
5	20	10	13.4	4.85	0.317
6	10	8	26.8	4.03	0.216
7	30	5	8.9	3.16	0.297
8	30	2	8.9	2.19	0.338
9	30	5	8.9	3.05	0.343
10	40	8	6.7	3.33	0.474
11	40	10	6.7	5.89	0.180
12	10	5	26.8	2.76	0.0443

* Values in blue were excluded during the process of creating empirical models to improve model fit with data.

$$T_{ave} = 0.585 + 0.0473 i_{ave} + 0.440 t_{ON} - 0.00790 i_{ave} t_{ON}$$ Equation 5-4

$$T_{SD} = -0.274 + 0.0475 i_{ave} - 0.000929 {i_{ave}}^2$$ Equation 5-5

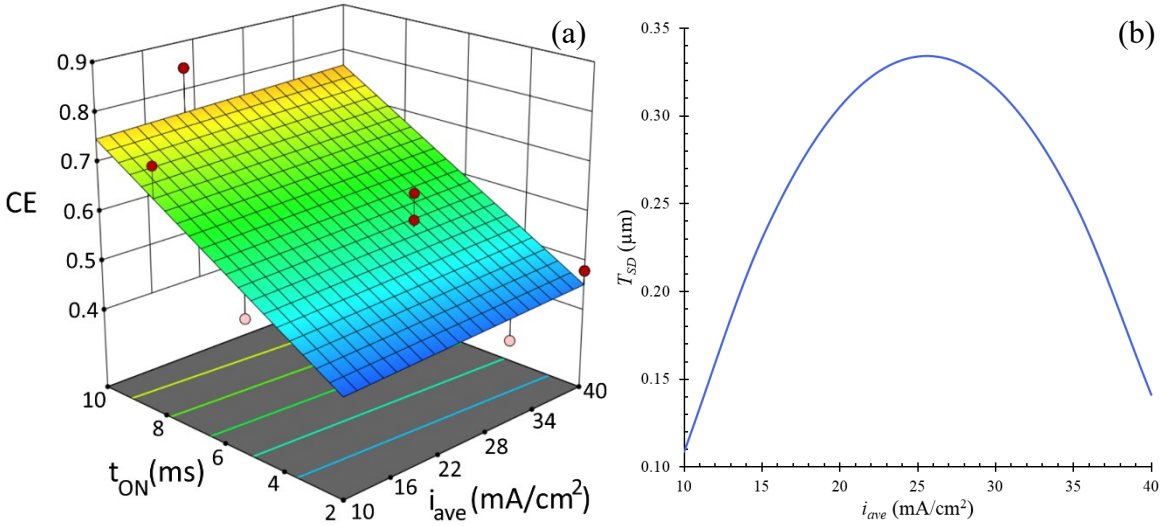

Figure 5-4: Empirical models for T_{ave} and T_{SD} as functions of i_{ave} and t_{ON}.

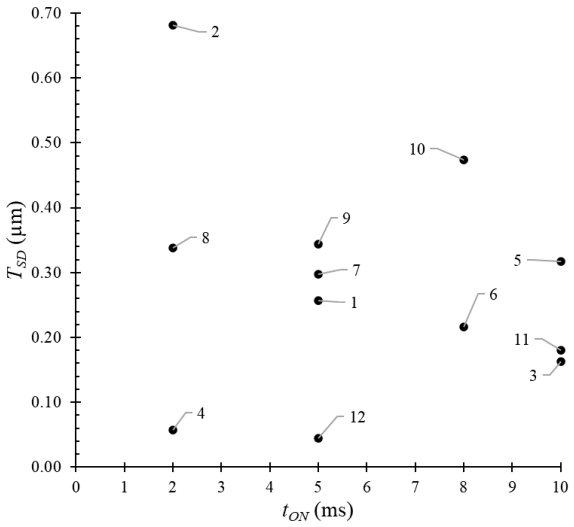

Figure 5-5: T_{SD} variation with t_{ON}. Labels refer to run #.

To test the empirical models listed in Equation 5-4 and Equation 5-5, a numerical optimization function in Design-Expert was utilized to obtain the plating parameters for a T_{ave} of 4 µm while minimizing T_{SD}. Au/Si wafers were coated using these optimized parameters. The parameters with the three highest desirability values and their predicted TDM values are tabulated in Table 5-5.

The desirability values are calculated from the desirability function, which is a statistical calculation that represents how well the optimization can find the desired solution. A desirability value of 1 means that all optimization targets for a solution were met and a value of 0 means that none of the optimization targets for a solution were met.

Table 5-5: Optimized plating parameters used to confirm T_{ave} and T_{SD} model validity and predicted TDM values

Optimized Parameters	i_{ave} (mA/cm$^{2)}$	t_{ON} (ms)	$t_{plating}$ (min)	T_{ave} (µm)	T_{SD} (µm)	Desirability
A	10.0	8.15	26.8	4.00	0.109	0.922
B	10.0	7.60	26.8	3.80	0.109	0.870
C	40.0	10.00	6.7	3.72	0.141	0.809

The predicted and actual TDM values are compared in Table 5-6. Adherence to the target values would indicate that the model can reasonably predict the TDM values. The actual T_{ave} and actual T_{SD} for the coatings from parameters A and C are slightly lower and slightly higher than predicted, respectively. The parameter B coating has slightly higher and slightly lower actual T_{ave} and T_{SD} values than predicted, respectively. Overall, there was a good fit between the models and reality; the models for T_{ave} and T_{SD} are therefore reasonably accurate.

Table 5-6: Predicted vs. actual TDM values for coating deposited from optimized plating parameter A-C

	Optimized Parameters	T_{ave} (µm)	T_{SD} (µm)
Predicted	A	4.00	0.109
Actual		3.56	0.144
Predicted	B	3.80	0.109
Actual		4.16	0.0912
Predicted	C	3.72	0.141
Actual		3.35	0.218

5.3.2 Development of Empirical Models for CE, T_{RSD}, and PR

After confirming that the models for T_{ave} and T_{SD} were reasonably accurate, the CE, T_{RSD}, and PR of runs 1-12 were calculated from the values in Table 5-4 to permit construction of their respective empirical models. The calculated values are provided in Table 5-7. These calculations were done to permit numerical optimization using CE, T_{RSD}, or PR as targets, as CE and PR were deemed more important than T_{ave} since higher CE and PR correspond to better use of electricity and plating time, which reduces overall cost. T_{RSD} was utilized instead of T_{SD} for the new optimization, since it is a normalized metric that permits direct comparison between coatings with different T_{ave} values. The empirical models are shown in Equation 5-6 to Equation 5-8 and Figure 5-6. CE was highest for DC plating at 40 mA/cm^2 but is relatively insensitive to i_{ave}, as DC plating at 40 mA/cm^2 is predicted to only have ~2% higher CE than DC plating at 10 mA/cm^2 (Figure 5-6a). Pulse plating modifies the Nernst diffusion layer into two regimes: a pulsating diffusion layer and a stationary diffusion layer. In the pulsating layer, the Ni^{2+} concentration pulsates at the same frequency as the pulsating current. The short pulse lengths utilized mean that ion transport from the solution to the cathode is consistently disrupted during PC plating, which is why current efficiency is lower for PC plating [87]. The increase in CE with higher i_{ave} is also expected, as higher applied current density increases electron transport to the cathode, which improves CE. Sherwin et al. reported that above a critical i_{ave} ion movement kinetics become diffusion controlled, resulting in a limited number of ions arriving at the cathode to react with the supplied electrons, reducing the overall CE. Since the model for CE does not depict this behaviour, it is likely that the critical i_{ave} for the current system is higher than 40 mA/cm^2 [89]. T_{RSD} increased and then decreased as i_{ave} was increased, which was similar to the behaviour for $T_{SD,}$ but is lowest for 10 mA/cm^2 (Figure 5-6b). The poor fit between T_{SD} and t_{ON} is likely worse than the fit between T_{ave} and t_{ON}, resulting in an

overall lack of fit between T_{RSD} and t_{ON} when calculating T_{RSD} by dividing T_{SD} with T_{ave}. This overall lack of fit is why the empirical model for T_{RSD} does not use t_{ON} as a variable. PR was highest for DC plating at 40 mA/cm^2 (Figure 5-6c). This is reasonable as a higher i_{ave} correlates to more electrons provided per unit time, resulting in a higher PR so long as the CE does not decrease. In other words, as long as the applied i_{ave} is lower than the critical i_{ave}, higher i_{ave} will result in higher PR [89].

Table 5-7: CE, T_{RSD}, and PR values and plating parameters from DoE runs

Run #	i_{ave} (mA/cm^2)	t_{ON} (ms)	$t_{plating}$ (min)	CE (%)	T_{RSD} (%)	PR (µm/h)
1	30	5	8.9	63.4	7.34	23.4
2	20	2	13.4	83.7	14.2	20.6
3	20	10	13.4	66.2	4.30	16.3
4	40	2	6.7	48.1	2.16	23.6
5	20	10	13.4	84.6	6.52	20.8
6	10	8	26.8	73.4	5.37	9.02
7	30	5	8.9	57.8	9.39	21.3
8	30	2	8.9	40.1	15.4	14.8
9	30	5	8.9	55.8	11.2	20.6
10	40	8	6.7	60.8	14.2	22.4
11	40	10	6.7	103	3.06	50.5
12	10	5	26.8	50.3	1.60	6.18

* Values in blue were excluded during process of creating the empirical model for CE to improve model fit with data.

$$CE = 0.347 + 0.000655 i_{ave} + 0.0396 t_{ON} \quad \text{Equation 5-6}$$

$$T_{RSD} = -0.122 + 0.0184 i_{ave} - 0.000362 {i_{ave}}^2 \quad \text{Equation 5-7}$$

$$PR = -7.11 + 0.723 i_{ave} + 1.15 t_{ON} \quad \text{Equation 5-8}$$

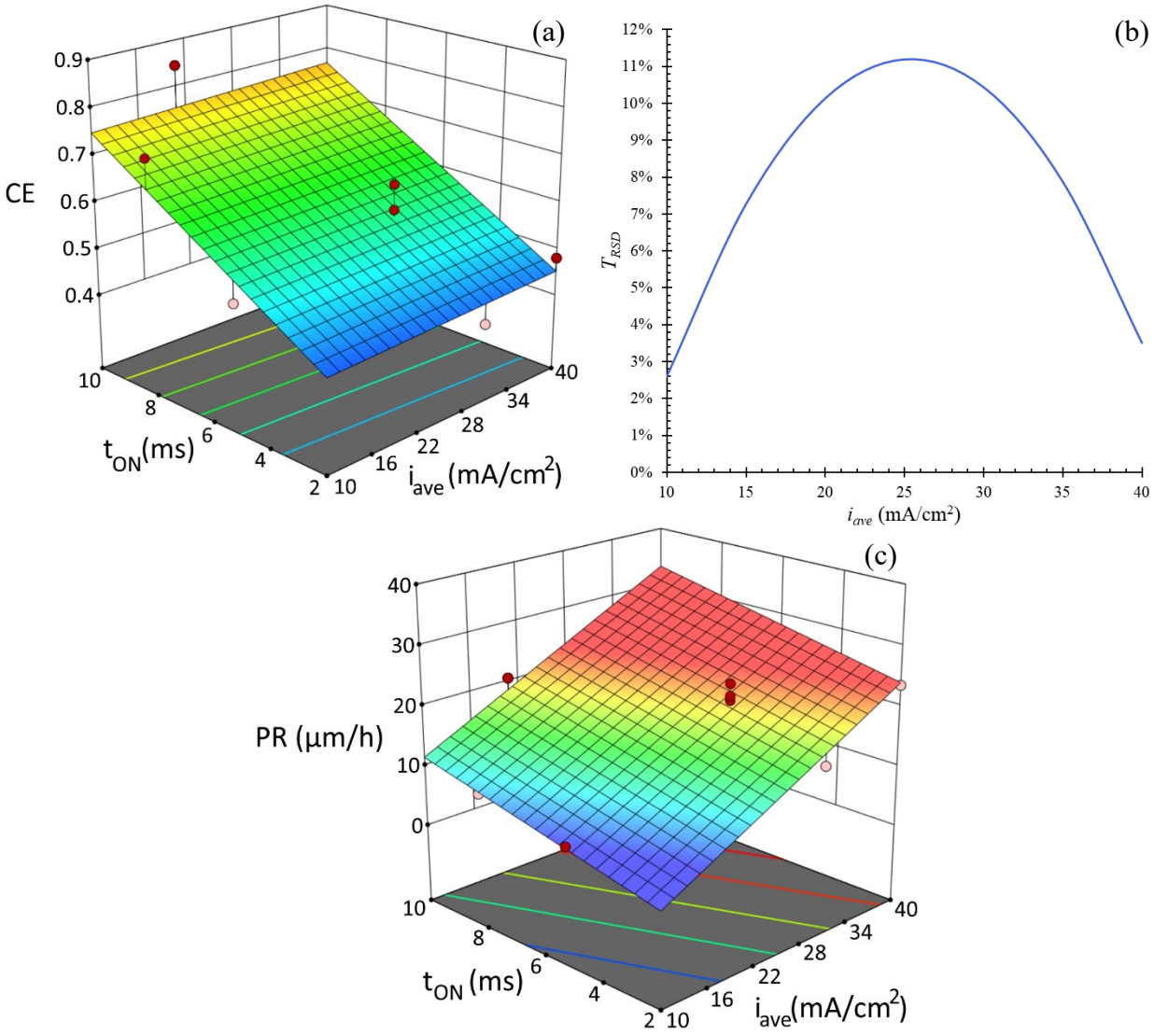

Figure 5-6: Empirical models for a) CE, d) T_{RSD}, and e) PR as functions of i_{ave} and/or t_{ON}.

The models for CE, T_{RSD}, and PR were tested by using numerical optimization to generate plating parameters that can maximize CE and minimize T_{RSD}. These parameters and their respective predicted TDM values are tabulated in Table 5-8. A high CE indicates high utilization of electricity. A low T_{RSD} is an indication of good coating microstructural uniformity and uniform coverage, which are desirable. High PR was not selected as a target since it can be achieved easily by selecting optimized parameters with high i_{ave}. Coatings were deposited from parameters D and E

as these have the highest desirability values. The plating conditions and predicted TDM values are very similar for D and E, so that they essentially provide duplicate tests. Parameters D-F and G-I are essentially DC plating at 10 and 40 mA/cm^2, respectively. Parameters G-I have lower desirability values than D-E because although the CE values for D-I are essentially identical the predicted T_{RSD} values for G-I is about 1% higher than D-F, thus resulting in lower desirability values. A comparison of predicted vs. actual TDM values for coatings D and E is tabulated in Table 5-9. Coating D had a lower T_{ave} and higher T_{SD} than predicted, resulting in a higher T_{RSD} and lower PR than predicted. Coating E had higher T_{SD} and, therefore, T_{RSD} than predicted, with virtually identical predicted and actual PR values. Coating E was plated using a t_{ON} of 9.90 ms instead of 9.95 ms because the power supply resolution for t_{ON} is 0.1 ms, meaning it could be set to 9.9 or 10.0 ms, but not 9.95 ms. Overall, the predicted and actual values are very similar, indicating that the models for CE, T_{RSD}, and PR are reasonably accurate.

Table 5-8: Optimized parameters for high CE and low T_{RSD} used to confirm CE and T_{RSD} model validity and their predicted TDM values

Optimized Parameters	i_{ave} (mA/cm$^{2)}$	t_{ON} (ms)	$t_{plating}$ (min)	T_{ave} (μm)	T_{SD} (μm)	CE (%)	T_{RSD} (%)	PR (μm/h)	Desirability
D	10.0	10.00	26.8	4.67	0.109	75.4	2.59	10.5	0.858
E	10.0	9.95	26.8	4.65	0.109	75.2	2.59	10.4	0.856
F	10.0	9.91	26.8	4.63	0.109	75.0	2.59	10.4	0.854
G	40.0	10.00	6.7	3.72	0.140	75.4	3.51	33.3	0.827
H	40.0	9.92	6.7	3.71	0.140	75.1	3.51	33.2	0.823
I	39.6	10.00	6.8	3.73	0.150	75.4	3.90	32.9	0.813

Table 5-9: Predicted vs. actual TDM values for coatings deposited using optimized plating parameters D and E

	Coatings	T_{ave} (μm)	T_{SD} (μm)	CE (%)	T_{RSD} (%)	PR (μm/h)
Predicted	D	4.67	0.109	75.4	2.59	10.5
Actual		4.19	0.330	76.3	7.89	9.38
Predicted	E	4.65	0.109	75.2	2.59	10.4
Actual*		4.59	0.161	83.6	3.50	10.3

*Coating D used 9.90 ms t_{ON} time because t_{ON} setting for power source only has 0.1 ms resolution

5.3.3 Electrodeposition of Thick Ni Coatings

It was concluded from Chapter 3 (Coating Characterization) that a high coating thickness is correlated with lower porosity. The outer Ni-P layer of coating #19 had very low porosity and a thickness of 40.9 ± 1.4 μm. A coating thickness of 40 μm is therefore sufficient to significantly reduce coating porosity. For this reason, a target T_{ave} of ~40 μm was chosen, as low porosity was achieved without utilizing excessive electricity and long plating times. A high CE and low T_{RSD} were selected as the targets for numerical optimization. Maximizing CE was considered more important than minimizing T_{RSD}, resulting in a "++++" weighting being applied to CE instead of the default "+++" weighting. The default weighting of "+++" was used for T_{RSD}. For reference, the highest and lowest weightings that can be assigned are "+++++" and "+", respectively. The plating parameters with the two highest desirability values and their predicted TDM values are tabulated in Table 5-10. As seen in Table 5-7 and Table 5-9, CE is not constant for all i_{ave}. A higher CE would require lower a $t_{plating}$ to achieve the same coating thickness, and vice-versa. Consequently, the CE and $t_{plating}$ values were revised based on TDM data from runs #1-#12 and parameters A-E and are tabulated in Table 5-11. The CE value for 10.0 mA/cm^2 is the same as the actual CE for coating D. The CE value for 40.0 mA/cm^2 is an average value from all previously deposited coatings that used an i_{ave} of 40.0 mA/cm^2. Note that the developed models are based on the TDM

values obtained from the 12 DoE runs, which had identical q_{total} to ensure a 4 µm T_{ave}. A 40 µm T_{ave} would, therefore, require much higher $q_{plating}$ and the TDM values would be beyond the models' ability to predict. As such, differences are expected between predicted and actual TDM values. Similar to the confirmation plating tests conducted using parameters D and E, the models suggested that DC plating was necessary to maximize CE and minimize T_{RSD}.

Table 5-10: Optimized plating parameters for maximizing CE and minimizing T_{RSD} as determined by Design-Expert and their predicted TDM values

Optimized Parameter	i_{ave} (mA/cm$^{2)}$	t_{ON} (ms)	T_{ave} (µm)	T_{SD} (µm)	CE (%)	T_{RSD} (%)	PR (µm/h)	Desirability
J	10.0	10.00	4.67	0.109	74.9	2.59	11.6	0.842
K	40.0	10.00	3.72	0.140	76.9	3.51	33.3	0.841

Table 5-11: Revised CE and plating times for DC plating at 10 and 40 mA/cm^2

i_{ave} (mA/cm^2)	CE (%)	$t_{plating}$ (min)
10.0	76.3	256.9
40.0	70.6	68.7

The TDM values from the 40 µm T_{ave} coatings deposited from optimized parameters J and K (shortened to coatings J-40 and K-40) are tabulated in Table 5-12. Both parameters J and K were tested because although the predicted $T_{SD,}$ T_{RSD}, and CE of the two were essentially identical, it was uncertain that this prediction would be valid for a T_{ave} of 40 µm. By testing both parameters J and K, the TDM differences between parameters J and K when applied at the practical T_{ave} of 40 µm could be identified. Some plastic deformation of coating J-40 during sectioning and polishing is likely why its CE slightly exceeds 100%. Alternative methods for cross section specimen preparation will be explored for any future electrodeposition work. Coating K-40 had a lower T_{RSD} and higher PR than J-40, while still maintaining high CE. As such, parameter K appears to be optimal. This confirmed that the predicted TDM values are not valid for T_{ave} ~40 µm. To further

confirm that parameter K is optimal, microscopic porosity analysis was performed on coatings J-40 and K-40.

Table 5-12: Actual TDM values from coatings J-40 and K-40

Coating	T_{ave} (μm)	T_{SD} (μm)	CE (%)	T_{RSD} (%)	PR (μm/h)
J-40	52.9	2.02	100.5	3.82	12.4
K-40	45.4	0.822	80.7	1.81	39.7

5.3.4 Microscopic Porosity Characterization of Thick Ni Coatings

An example of microscopic porosity analysis is shown in Figure 5-7. The microscopic porosity results are tabulated in Table 5-13 and the pore size histograms are shown in Figure 5-8. Coatings J-40 and K-40 both have low microscopic pore area percentage (MiPAP) and microscopic pore areal density (MiPAD) values, although K-40 has slightly lower MiPAD and slightly higher MiPAP than J-40. This is because the pores in coating J-40 are generally smaller than in K-40 despite being more numerous, resulting in a lower MiPAP despite the slightly higher MiPAD (Figure 5-8). A comparison of the coating porosity for coatings J-40 and K-40 with coatings #1-#19 is shown in Figure 5-9. Coatings J-40 and K-40 have low MiPAD and MiPAP, which should provide good corrosion resistance [24], [28], [29], [78], [79]. A high thickness, low porosity Ni electroplating process for Au/Si wafer substrates has, therefore, been developed. A Ni-P or Ni-B electroplating process will be developed in future work based on this Ni electroplating process and will be applied to pretreated and electroless Ni-P coated Mg substrates to satisfy the project's ultimate goal of a coating with improved corrosion resistance.

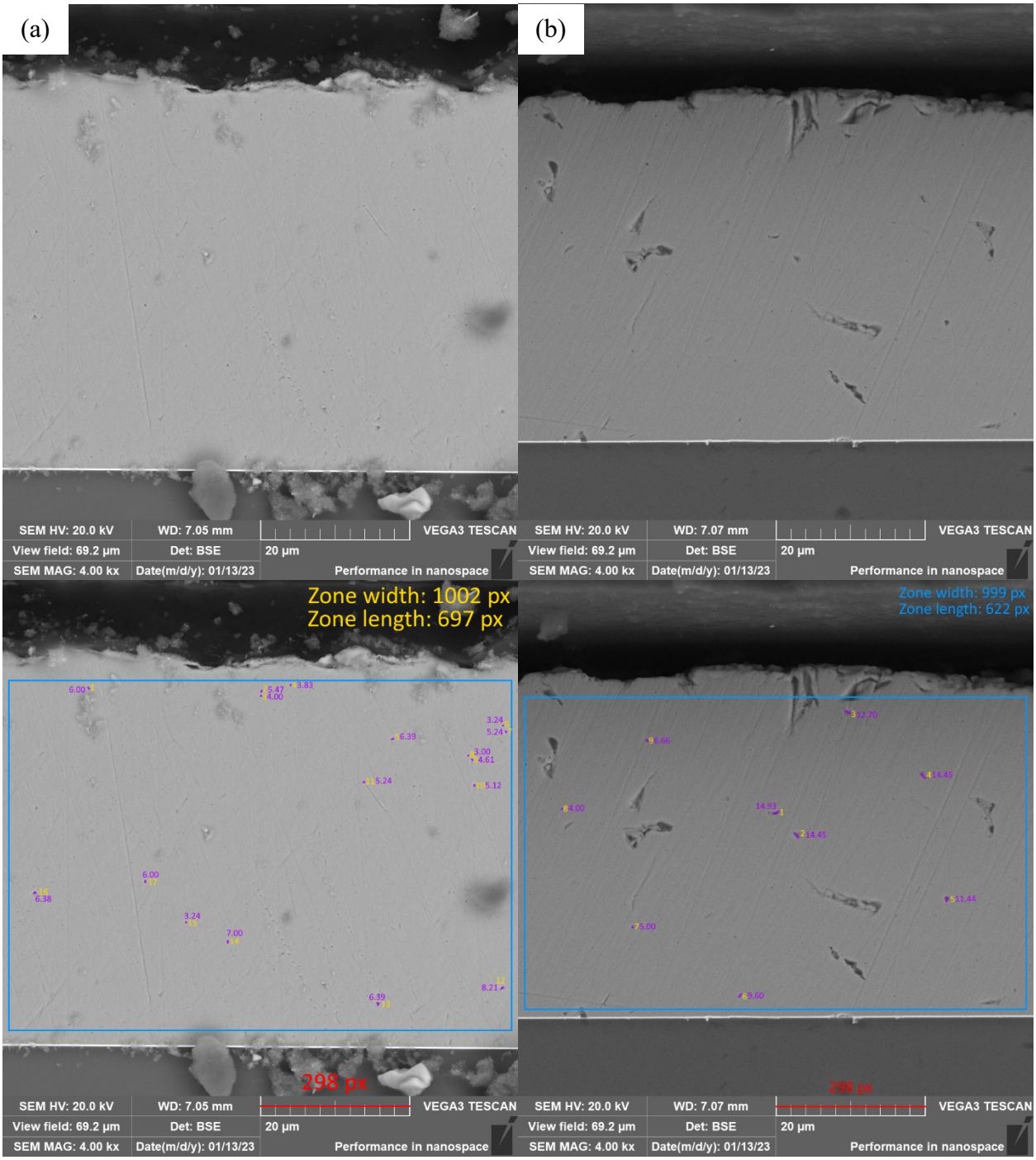

Figure 5-7: SEM BSE images of a) coating J-40 and b) coating K-40 in cross section and c), d) microscopic porosity analysis of the respective areas.

Table 5-13: MiPAD and MiPAP of coatings J-40 and K-40

Coating	MiPAD (#/mm^2)	MiPAP (%)
J-40	$4.59 \cdot 10^3$	0.0952
K-40	$3.78 \cdot 10^3$	0.113

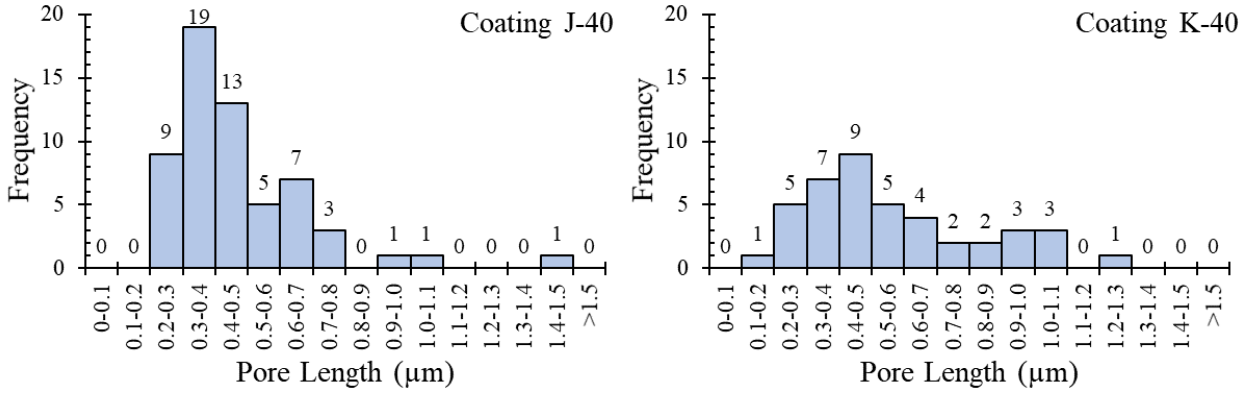

Figure 5-8: Microscopic pore size histograms for J and K coatings.

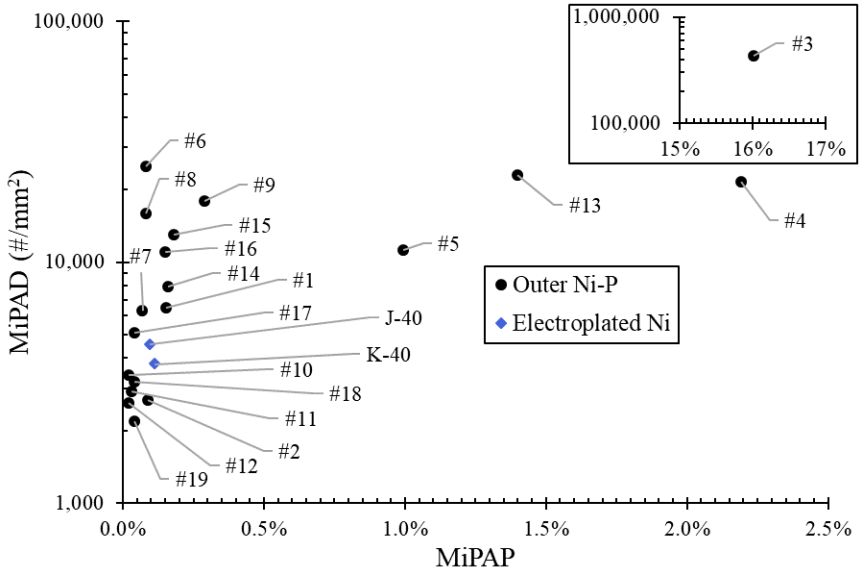

Figure 5-9: Microscopic porosity of coatings #1-#19 and J and K.

5.3.5 Surface Morphology and Composition of Coatings

The surface morphologies of all coatings were documented in plan view images using SEM. All coatings with T_{ave} ~4 µm had similar surface morphology (Figure 5-10). Both run #1 (Figure 5-10a and Figure 5-10b) and parameter D (Figure 5-10c and Figure 5-10d) coatings were flat with small

protrusions visible only at higher magnifications. The flatness of the coatings can be attributed to the smooth Au seed layers, which had a mirror finish. The lighter coloured regions in Figure 5-10a are caused by surface contaminants.

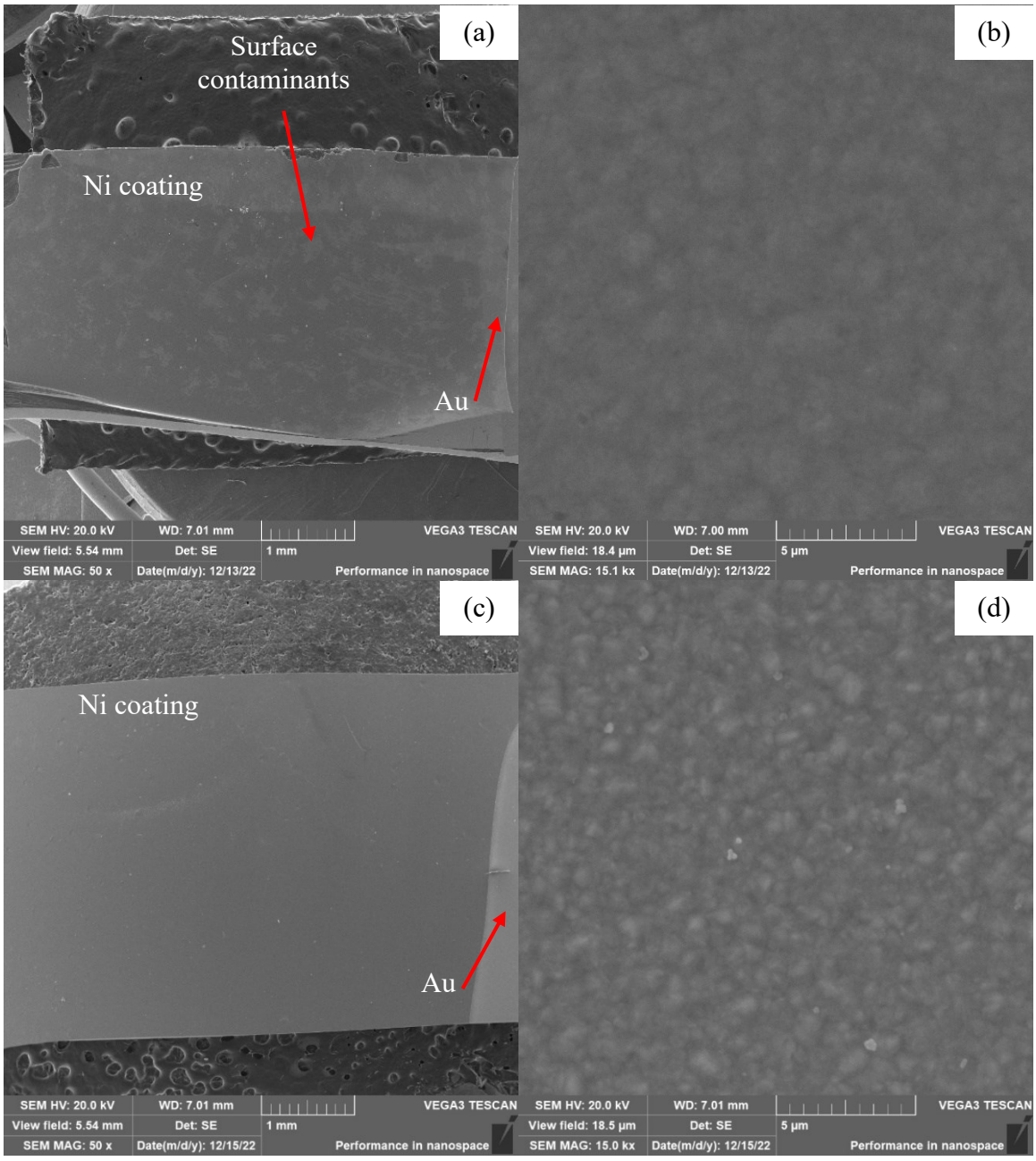

Figure 5-10: Plan view SEM SE images of run #1 coating at a) low and b) high magnification and parameter D coating at c) low and d) high magnification.

The T_{ave} ~40 µm coatings had a slightly different surface morphology at high magnification than the T_{ave} ~4 µm coatings, with the run #1 and J-40 coatings shown as examples (Figure 5-11). Coatings J-40 and K-40 had dimpled features on their surfaces (Figure 5-11b). These are likely caused by a slight increase in surface roughness with longer plating times [87]. The T_{RSD} of run #1-#12 and A-E coatings varies between 1.60% and 15.4% with an average of 7.00%. Coatings J-40 and K-40 have T_{RSD} of 3.82% and 1.81%, respectively, which is within the range mentioned above. The dimpled features in coatings J-40 and K-40 are simply caused by a proportional increase in T_{SD} leading to higher surface roughness.

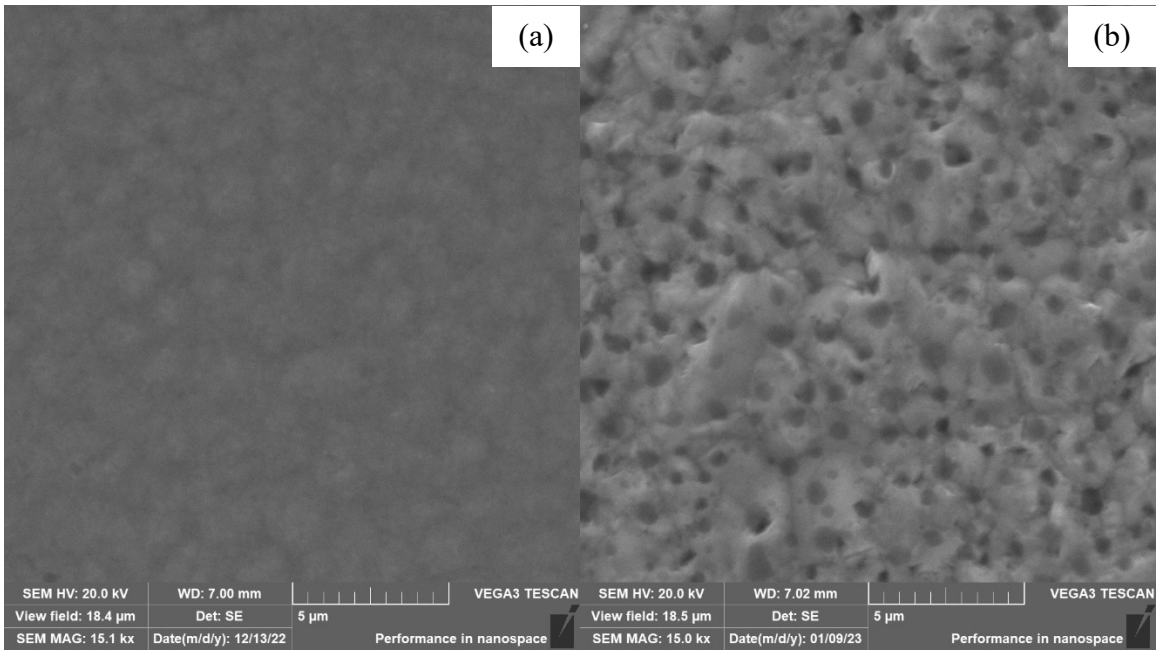

Figure 5-11: SEM SE images of a) run #1 and b) J coatings.

EDX analysis was performed on several coatings, with the results from the coating A coating shown in Figure 5-12 as an example. All coatings are compositionally uniform and composed of pure Ni. The Si and Au peaks are from the substrate and the C peak is from surface contaminants (Figure 5-12b).

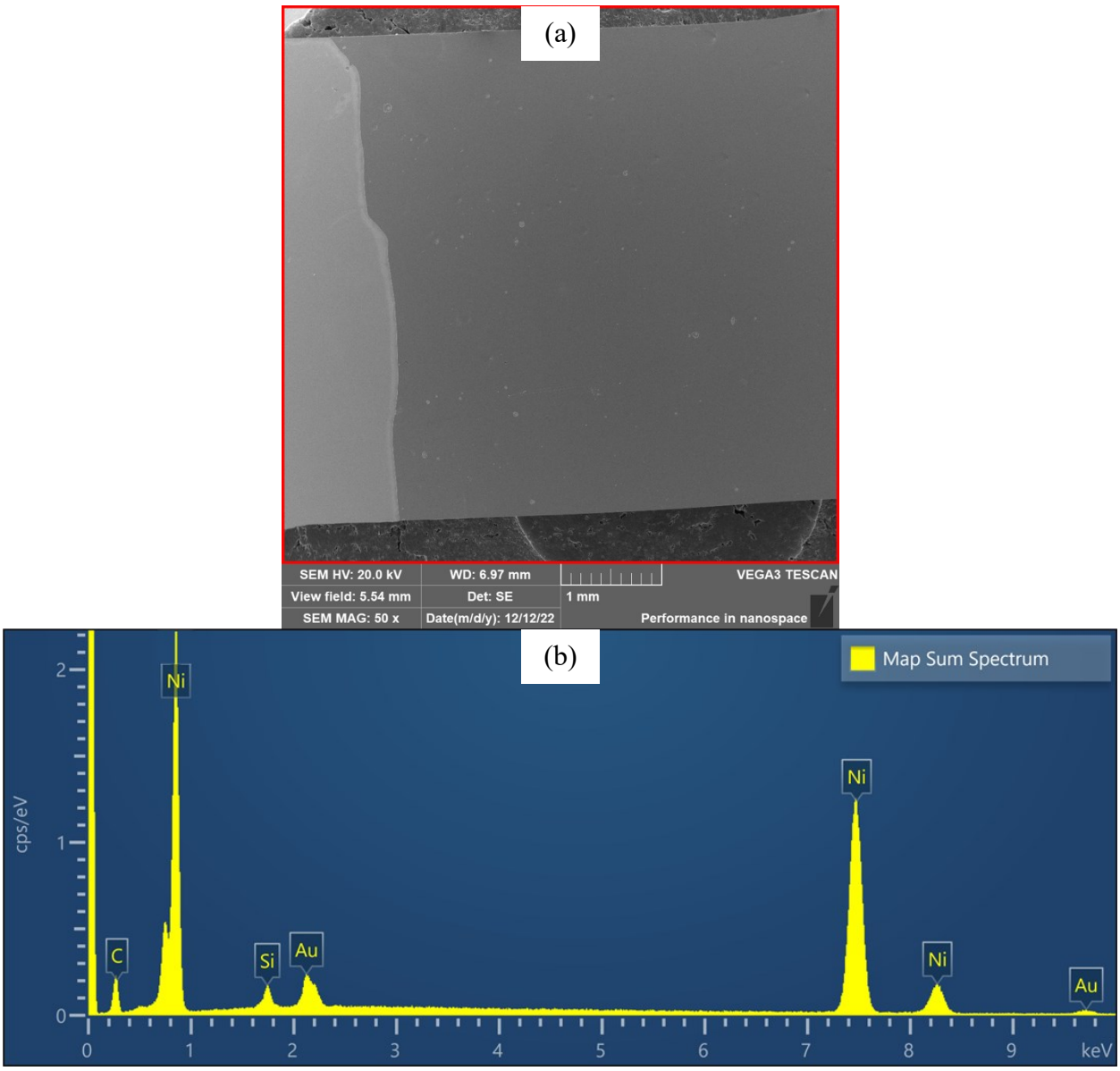

Figure 5-12: a) SEM SE and b) EDX spectrum of coating A. EDX spectrum in b) was taken from red rectangle in a).

5.4 Summary

A Ni electroplating process on Au/Si wafers was developed and optimized. A modified Watts bath (with added saccharin for grain refinement and no pH control for simplified bath operation) was used. Au/Si wafers were utilized for deposition as they could be cleaved to permit rapid characterization. A DoE approach was taken, with Design-Expert 13 software used to generate suggested tests ("runs"). The results were employed to create empirical models for average coating

thickness, standard deviation of coating thickness, plating current efficiency, relative standard deviation of thickness, and plating rate. Numerical optimization from Design-Expert was used to generate optimized plating parameters and predicted metrics. Coatings were deposited using these parameters and the actual metrics were compared against predicted metrics. There was a reasonable fit between predicted and actual values. All coatings deposited in the "runs" and comparisons between predicted and actual metrics were ~4 μm thick to permit cleaving. Two coatings with a target thickness of 40 μm were deposited using parameters optimized for high current efficiency and low relative standard deviation of thickness (parameters J and K). These coatings had low microscopic porosity compared with the electroless Ni-P coatings characterized in Chapter 3 (Coating Characterization). The coating deposited from parameter K (40 mA/cm^2 DC plating) had a lower relative standard deviation of thickness and microscopic porosity than the coating deposited from parameter J (10 mA/cm^2 DC plating) and was considered the optimal parameter for Ni electroplating on Au/Si wafers. The goal of identifying optimal plating parameters for Ni electroplating on Au/Si wafers was, therefore, achieved. In future work, the process will be adapted to include P (to generate Ni-P coatings), with the ultimate goal of electroplating on Mg substrates that have undergone suitable pretreatment and electroless deposition of a Ni-P seed layer to ensure good coating adhesion.

6 Conclusions and Future Work

6.1 Conclusions

This Master of Science degree arose from a partnership between Zinc8 Energy Solutions Inc. (shortened to Zinc8) and the Ivey group. Electroless Ni-P coatings deposited on Mg substrates, utilized in their zinc-air flow batteries (ZAFB), are prone to delamination, which is exacerbated by porosity. The goals of the partnership are to characterize the electroless Ni-P coatings, quantify the porosity present in the Ni-P coatings, and develop improved coatings with longer service lifetimes. The first two goals have been completed, and the third goal is ongoing. Initial work focused on characterizing the microstructure and composition of a standard Ni-P coating, which was similar to other coatings investigated. This was followed by studying the impact of electroless Ni-P plating parameters on porosity in Ni-P coatings on Mg substrates and the effect of porosity on corrosion measurements. Finally, a process was developed to electroplate Ni coatings onto Au-coated Si wafer substrates through a design of experiments (DoE) approach. The new coatings had low porosity and will be adapted to Mg substrates and will incorporate other components, such as P and B. The main achievements of this thesis are highlighted in the following subsections.

6.1.1 Coating Characterization

The standard coating (coating #1) was analyzed in depth using scanning electron microscopy (SEM), energy dispersive x-ray spectroscopy (EDX), transmission electron microscopy (TEM), x-ray diffraction (XRD), and helium ion microscopy (HIM). EDX analysis showed that the P content of coating #1 was 6-7 wt%. TEM and XRD showed that the microstructure of coating #1 was a mixture of amorphous and nanocrystalline phases. These findings confirmed literature consensus

on the relation between P content and the microstructure of electroless Ni-P coatings. The porosity of 19 Ni-P coatings was quantified using microscopic and macroscopic porosity analyses. Microscopic porosity analysis was performed using cross sectional SEM imaging of the samples. Macroscopic porosity analysis was performed using a process developed for this project, which combined dimple polishing with optical microscopy (OM). The two techniques were complementary and yielded consistent results. The effects of Mg sandblasting grit number, P content, Cu strike presence, and total coating thickness on porosity were determined. Thicker coatings and medium P content reduced microscopic porosity. High sandblasting grit number (smaller grit size) and thicker coatings reduced macroscopic porosity. Medium P content and a lack of Cu strike slightly reduced macroscopic porosity.

6.1.2 Electrochemical Testing

Coatings #1-#4, #6, and #8 were electrochemically tested to correlate porosity measurements with corrosion performance. The OCV, E_{corr}, and i_{corr} values of the coatings were used to evaluate corrosion performance. Both immersion (49 days) and cycle testing (2,000 cycles under oxygen evolution reaction (OER) and hydrogen evolution reaction (HER) conditions) were performed, coupled with compositional testing of the electrolyte using atomic absorption spectroscopy (AAS) and inductively coupled plasma optical emission spectroscopy (ICP-OES) and SEM/EDX measurements of coating thickness and morphology changes. The corrosion rates generally increased with increasing porosity. All coatings had significant corrosion rates, based on i_{corr} values determined from electrochemical testing. Apart from coating #1 and #1 R, immersion tested samples had lower corrosion rates than cycle tested samples. However, except for the cycle tested coating #3 L sample, electrolyte compositional testing and SEM/EDX analysis indicated that Ni-

P corrosion was small or negligible. The logarithmic nature of potentiodynamic polarization (PDP) plots (from which i_{corr} was determined) and noisy PDP measurements made meaningful i_{corr} measurements difficult to obtain. Coating #3 L was cycle tested for longer than other samples (3,359 cycles instead of 2,000 cycles) and had measurable Ni-P thickness loss from SEM observations but no observable increase in Ni content from AAS or ICP-OES measurements. It is proposed that Ni dissolved from the coating #3 L sample during cycle testing is plated onto the graphite counter electrode. This assertion will be tested in future work. Localized corrosion of the Cu was significant for some samples. This was attributed to localized regions of Cu being exposed directly to the electrolyte during testing due to epoxy debonding. Mg loss was not detected for any samples.

6.1.3 Nickel Electroplating

A Ni electroplating process using a modified Watts bath was developed for deposition on Au-coated Si wafers. A DoE approach was used to generate recommended plating conditions and the results were employed to create empirical models for various coating metrics. Numerical optimization of these models was used to generate optimal plating parameters. DC plating at 40 mA/cm^2 was determined to be optimal and a 40 μm coating was deposited from this parameter had low microscopic porosity. The electroplating process is being adapted for Mg substrates and for electrodeposition of Ni alloy coatings.

6.2 Future Work

6.2.1 Analysis of Graphite Counter Electrode

The graphite counter electrode used in electrochemical testing should be analyzed via SEM and EDX methods to verify if Ni deposition is occurring on or within it. Confirmation of Ni deposition

would resolve the paradox of high corrosion rates from electrochemical testing and observed Ni-P thickness loss for the cycle testing coating #3 L sample, but lack of Ni detection via AAS or ICP-OES analysis.

6.2.2 Cross Section Analysis of Electrochemical Samples

Cross section SEM/EDX analysis was conducted only on the immersion tested coating #4, cycle tested coating #1, and cycle tested coating #3 L samples. All electrochemical samples should be analyzed so that their coating thickness measurements can be compared against the CR values and AAS and/or ICP-OES measurements. These comparisons can help determine the validity of the CR values for estimating actual Ni-P thickness loss.

6.2.3 Longer Duration Cycle Testing

The cycle tested coating #3 L sample had measurable Ni-P thickness loss from SEM after cycle testing for 3,359 cycles, whereas the cycle tested coating #1 sample had no measurable change in Ni-P thickness after 2,000 cycles. This may be due to the much longer cycle count for coating #3 L. Cycle testing with only 2,000 cycles may be insufficient to cause measurable Ni-P thickness changes. Longer duration cycle testing (> 3,000 cycles) should be conducted for all samples, with corresponding SEM measurements of coating thickness changes.

6.2.4 Additional Cycle Testing

All coatings should be cycle tested, as cycle testing induces more significant changes in corrosion measurements and is much faster than the 49-day immersion testing. Additional cycle testing results would permit a more thorough correlation between corrosion and porosity measurements.

6.2.5 Electrodeposition on Ni-P Coatings

A pretreatment process for Mg substrates is being developed within the Ivey research group. Mg is highly reactive and oxidizes readily. Coatings deposited on the native Mg oxide layer have poor adhesion. A pretreatment process prevents Mg oxidation and permits a well adhering coating to be deposited. After pretreatment, a thin electroless Ni-P coating will be deposited on the Mg substrate. Ni coatings will then be deposited on the electroless Ni-P coating, followed by electrochemical testing. These coatings will go a long way in satisfying the partnership goal of an improved (low porosity) coating. The Ni electroplating process is being adapted for use on the new substrates.

6.2.6 Electrodeposition of Ni Alloy Coatings

Ni alloy coatings could provide higher hardness and wear resistance than pure Ni coatings, which may be useful in improving the service lifetime of the coated electrode in ZAFBs. The modified Watts bath used for Ni electroplating is being adapted to deposit Ni-P coatings. Other Ni alloys such as Ni-B could also be explored.

6.2.7 Electrocatalytic Activity of Improved Coating

The electrocatalytic activity of any new coating towards OER and HER should be determined to ensure that the ZAFB do not suffer a significant decrease in electrochemical performance. Improvements towards OER catalytic activity and decreases towards HER catalytic activity would improve the overall electrochemical performance of the ZAFB. These may be achieved with amorphous microstructures.

References

[1] X. Han *et al.*, "Metal–Air Batteries: From Static to Flow System," *Adv Energy Mater*, vol. 8, no. 27, pp. 1–28, 2018, doi: 10.1002/aenm.201801396.

[2] J. Cho, S. Jeong, and Y. Kim, "Commercial and research battery technologies for electrical energy storage applications," *Prog Energy Combust Sci*, vol. 48, pp. 84–101, 2015, doi: 10.1016/j.pecs.2015.01.002.

[3] Md. A. Rahman, X. Wang, and C. Wen, "High Energy Density Metal-Air Batteries: A Review," *J Electrochem Soc*, vol. 160, no. 10, pp. A1759–A1771, 2013, doi: 10.1149/2.062310jes.

[4] L. Collins, "New zinc-air battery is 'cheaper, safer and far longer-lasting than lithium-ion,'" *Recharge*, no. June 2020, p. 1, 2020, [Online]. Available: https://www.rechargenews.com/transition/new-zinc-air-battery-is-cheaper-safer-and-far-longer-lasting-than-lithium-ion/2-1-812068

[5] S. I. Smedley and X. G. Zhang, "A regenerative zinc-air fuel cell," *J Power Sources*, vol. 165, no. 2, pp. 897–904, 2007, doi: 10.1016/j.jpowsour.2006.11.076.

[6] M. Buchtík, M. Krystỳnová, J. Másilko, and J. Wasserbauer, "The effect of heat treatment on properties of Ni-P coatings deposited on a AZ91 magnesium alloy," *Coatings*, vol. 9, no. 7, 2019, doi: 10.3390/coatings9070461.

[7] A. Thakur, S. Gharde, and B. Kandasubramanian, "Electroless nickel fabrication on surface modified magnesium substrates," *Defence Technology*, vol. 15, no. 4, pp. 636–644, 2019, doi: 10.1016/j.dt.2019.04.006.

[8] J. Wang, X. Pang, and H. Jahed, "Surface protection of Mg alloys in automotive applications: A review," *AIMS Mater Sci*, vol. 6, no. 4, pp. 567–600, 2019, doi: 10.3934/matersci.2019.4.567.

[9] Y. Bai *et al.*, “A brief review about surface treatment of magnesium alloys,” *Materials Science Forum*, vol. 724, pp. 307–310, 2012, doi: 10.4028/www.scientific.net/MSF.724.307.

[10] M. Bestetti and A. Da Forno, “Electroless and Electrochemical Deposition of Metallic Coatings on Magnesium Alloys Critical Literature Review,” *Magnesium Alloys - Corrosion and Surface Treatments*, pp. 153–184, 2011.

[11] M. T. Y. Paul, B. B. Yee, D. R. Bruce, and B. D. Gates, “Hexagonal Arrays of Cylindrical Nickel Microstructures for Improved Oxygen Evolution Reaction,” *ACS Appl Mater Interfaces*, vol. 9, no. 8, pp. 7036–7043, 2017, doi: 10.1021/acsami.6b14129.

[12] G.-H. Ao *et al.*, “Construction of Hierarchical Porous Architecture on Ni Foam for Efficient Oxygen Evolution Reaction Electrode,” *Front Mater*, vol. 8, no. October, pp. 1–8, 2021, doi: 10.3389/fmats.2021.726270.

[13] M. Ghamari and A. A. Amadeh, “Wear and corrosion resistance of AZ91 magnesium alloy coated by pulsed current electrodeposited Ni–Al2O3nanocomposite,” *Transactions of the Institute of Metal Finishing*, vol. 95, no. 2, pp. 114–120, 2017, doi: 10.1080/00202967.2017.1265760.

[14] B. Ma and R. Wang, “Tuning interface to improve corrosion resistance of electroless Ni-P coating on AZ31B alloy,” *Metals (Basel)*, vol. 8, no. 5, 2018, doi: 10.3390/met8050328.

[15] C. A. Huang, T. H. Wang, T. Weirich, and V. Neubert, “A pretreatment with galvanostatic etching for copper electrodeposition on pure magnesium and magnesium alloys in an alkaline copper-sulfate bath,” *Electrochim Acta*, vol. 53, no. 24, pp. 7235–7241, 2008, doi: 10.1016/j.electacta.2008.04.074.

[16] Z. Liu and W. Gao, “Scratch Adhesion Evaluation of Electroless Nickel Plating on Mg and Mg Alloys,” *Int J Mod Phys B*, vol. 20, no. 25, 26, 27, pp. 4637–4642, 2006.

[17] R. Bellemare, “Direct plating of magnesium with electroless nickel,” *National Association for Surface Finishing Annual Technical Conference 2009, SUR/FIN 2009*, no. February, pp. 77–87, 2009.

[18] S. Y. Jian, J. K. Chang, K. F. Lin, T. Y. Chen, J. H. Yuan, and M. Der Ger, “Characteristic V-Mn conversion coating in reinforcing corrosion resistance of electroless Ni-P coated LZ91 Mg alloy,” *Surf Coat Technol*, vol. 394, no. April, p. 125724, 2020, doi: 10.1016/j.surfcoat.2020.125724.

[19] N. Ghavidel, S. R. Allahkaram, R. Naderi, M. Barzegar, and H. Bakhshandeh, “Corrosion and wear behavior of an electroless Ni-P/nano-SiC coating on AZ31 Mg alloy obtained through environmentally-friendly conversion coating,” *Surf Coat Technol*, vol. 382, no. September 2019, 2020, doi: 10.1016/j.surfcoat.2019.125156.

[20] H. Huo, Y. Li, and F. Wang, “Corrosion of AZ91D magnesium alloy with a chemical conversion coating and electroless nickel layer,” *Corros Sci*, vol. 46, no. 6, pp. 1467–1477, 2004, doi: 10.1016/j.corsci.2003.09.023.

[21] J. Zhang *et al.*, “Electroless deposition and characterization of a double-layered Ni-B/Ni-P coating on AZ91D Mg alloy from eco-friendly fluoride-free baths,” *Surf Coat Technol*, vol. 342, no. March, pp. 178–189, 2018, doi: 10.1016/j.surfcoat.2018.02.105.

[22] Z. Liu and W. Gao, “Electroless nickel plating on AZ91 Mg alloy substrate,” *Surf Coat Technol*, vol. 200, no. 16–17, pp. 5087–5093, 2006, doi: 10.1016/j.surfcoat.2005.05.023.

[23] R. Ambat and W. Zhou, “Electroless nickel-plating on AZ91D magnesium alloy: Effect of substrate microstructure and plating parameters,” *Surf Coat Technol*, vol. 179, no. 2–3, pp. 124–134, 2004, doi: 10.1016/S0257-8972(03)00866-1.

[24] N. El Mahallawy, A. Bakkar, M. Shoeib, H. Palkowski, and V. Neubert, “Electroless Ni-P coating of different magnesium alloys,” *Surf Coat Technol*, vol. 202, no. 21, pp. 5151–5157, 2008, doi: 10.1016/j.surfcoat.2008.05.037.

[25] W. X. Zhang, Z. H. Jiang, G. Y. Li, Q. Jiang, and J. S. Lian, “Electroless Ni-Sn-P coating on AZ91D magnesium alloy and its corrosion resistance,” *Surf Coat Technol*, vol. 202, no. 12, pp. 2570–2576, 2008, doi: 10.1016/j.surfcoat.2007.09.023.

[26] D. W. Baudrand, “Electroless Nickel Plating,” *Surface Engineering*, vol. 5, pp. 290–310, 1994, doi: 10.31399/asm.hb.v05.a0001264.

[27] L. Yang, J. Li, Y. Zheng, W. Jiang, and M. Zhang, “Electroless Ni-P plating with molybdate pretreatment on Mg-8Li alloy,” *J Alloys Compd*, vol. 467, no. 1–2, pp. 562–566, 2009, doi: 10.1016/j.jallcom.2007.12.041.

[28] C. Gu, J. Lian, J. He, Z. Jiang, and Q. Jiang, “High corrosion-resistance nanocrystalline Ni coating on AZ91D magnesium alloy,” *Surf Coat Technol*, vol. 200, no. 18–19, pp. 5413–5418, 2006, doi: 10.1016/j.surfcoat.2005.07.001.

[29] Y. D. He, H. F. Fu, X. G. Li, and W. Gao, “Microstructure and properties of mechanical attrition enhanced electroless Ni-P plating on magnesium alloy,” *Scr Mater*, vol. 58, no. 6, pp. 504–507, 2008, doi: 10.1016/j.scriptamat.2007.10.051.

[30] W. J. Cheong, B. L. Luan, and D. W. Shoesmith, “Protective coating on Mg AZ91D alloy - The effect of electroless nickel (EN) bath stabilizers on corrosion behaviour of Ni-P deposit,” *Corros Sci*, vol. 49, no. 4, pp. 1777–1798, 2007, doi: 10.1016/j.corsci.2006.08.025.

[31] M. T. Y. Paul, B. B. Yee, D. R. Bruce, and B. D. Gates, “Hexagonal Arrays of Cylindrical Nickel Microstructures for Improved Oxygen Evolution Reaction,” *ACS Appl Mater Interfaces*, vol. 9, no. 8, pp. 7036–7043, 2017, doi: 10.1021/acsami.6b14129.

[32] H. T. Hsu and T. J. Yang, “Improvement of corrosion resistance of AZ91D magnesium alloy by nickel plating,” *Procedia Eng*, vol. 36, pp. 279–284, 2012, doi: 10.1016/j.proeng.2012.03.041.

[33] J. S. Lian, G. Y. Li, L. Y. Niu, C. D. Gu, Z. H. Jiang, and Q. Jiang, “Electroless Ni-P deposition plus zinc phosphate coating on AZ91D magnesium alloy,” *Surf Coat Technol*, vol. 200, no. 20–21, pp. 5956–5962, 2006, doi: 10.1016/j.surfcoat.2005.09.007.

[34] W. X. Zhang, Z. H. Jiang, G. Y. Li, Q. Jiang, and J. S. Lian, “Electroless Ni-P/Ni-B duplex coatings for improving the hardness and the corrosion resistance of AZ91D magnesium alloy,” *Appl Surf Sci*, vol. 254, no. 16, pp. 4949–4955, 2008, doi: 10.1016/j.apsusc.2008.01.144.

[35] C. Gu, J. Lian, G. Li, L. Niu, and Z. Jiang, “Electroless Ni-P plating on AZ91D magnesium alloy from a sulfate solution,” *J Alloys Compd*, vol. 391, no. 1–2, pp. 104–109, 2005, doi: 10.1016/j.jallcom.2004.07.083.

[36] W. X. Zhang, N. Huang, J. G. He, Z. H. Jiang, Q. Jiang, and J. S. Lian, “Electroless deposition of Ni-W-P coating on AZ91D magnesium alloy,” *Appl Surf Sci*, vol. 253, no. 11, pp. 5116–5121, 2007, doi: 10.1016/j.apsusc.2006.11.022.

[37] W. X. Zhang, J. G. He, Z. H. Jiang, Q. Jiang, and J. S. Lian, “Electroless Ni-P layer with a chromium-free pretreatment on AZ91D magnesium alloy,” *Surf Coat Technol*, vol. 201, no. 8, pp. 4594–4600, 2007, doi: 10.1016/j.surfcoat.2006.09.312.

[38] D. Seifzadeh and Z. Rajabalizadeh, “Environmentally-friendly method for electroless Ni-P plating on magnesium alloy,” *Surf Coat Technol*, vol. 218, no. 1, pp. 119–126, 2013, doi: 10.1016/j.surfcoat.2012.12.039.

[39] Y. W. Song, D. Y. Shan, and E. H. Han, “High corrosion resistance of electroless composite plating coatings on AZ91D magnesium alloys,” *Electrochim Acta*, vol. 53, no. 5, pp. 2135–2143, 2008, doi: 10.1016/j.electacta.2007.09.026.

[40] L. P. Wu, J. J. Zhao, Y. P. Xie, and Z. D. Yang, “Progress of electroplating and electroless plating on magnesium alloy,” *Transactions of Nonferrous Metals Society of China (English Edition)*, vol. 20, no. SUPPL. 2, pp. s630–s637, 2010, doi: 10.1016/S1003-6326(10)60552-3.

[41] G. L. Song, "'Electroless' deposition of a pre-film of electrophoresis coating and its corrosion resistance on a Mg alloy," *Electrochim Acta*, vol. 55, no. 7, pp. 2258–2268, 2010, doi: 10.1016/j.electacta.2009.11.078.

[42] Z. Liu and W. Gao, "The effect of substrate on the electroless nickel plating of Mg and Mg alloys," *Surf Coat Technol*, vol. 200, no. 11, pp. 3553–3560, 2006, doi: 10.1016/j.surfcoat.2004.12.001.

[43] R. Petro and M. Schlesinger, "Direct Electroless Deposition of Low Phosphorous Ni-P Films on AZ91D Mg Alloy," *J Electrochem Soc*, vol. 159, no. 7, pp. D455–D461, 2012, doi: 10.1149/2.069207jes.

[44] H. Zhao, Z. Huang, and J. Cui, "A new method for electroless Ni-P plating on AZ31 magnesium alloy," *Surf Coat Technol*, vol. 202, no. 1, pp. 133–139, 2007, doi: 10.1016/j.surfcoat.2007.05.001.

[45] B. Zhang, "History–From the Discovery of Electroless Plating to the Present," in *Amorphous and Nano Alloys Electroless Depositions*, 1st ed.Amsterdam: Elsevier Inc., 2016, pp. 3–48. doi: 10.1016/b978-0-12-802685-4.00001-7.

[46] H. J. Luo, B. N. Song, Y. H. Liu, and G. C. Yao, "Electroless Ni-P plating on Mg-Li alloy by two-step method," *Transactions of Nonferrous Metals Society of China (English Edition)*, vol. 21, no. 10, pp. 2225–2230, 2011, doi: 10.1016/S1003-6326(11)60999-0.

[47] J. Chen, D. H. Bradhurst, S. X. Dou, and H. K. Liu, "The effect of chemical coating with Ni on the electrode properties of Mg2Ni alloy," *J Alloys Compd*, vol. 280, no. 1–2, pp. 290–293, Oct. 1998, doi: 10.1016/S0925-8388(98)00731-2.

[48] Z.-C. Wang, L. Yu, F. Jia, and G.-L. Song, "Effect of Additives and Heat Treatment on the Formation and Performance of Electroless Nickel-Boron Plating on AZ91D Mg Alloy," *J Electrochem Soc*, vol. 159, no. 7, pp. D406–D412, 2012, doi: 10.1149/2.012207jes.

[49] J. E. Gray and B. Luan, “Protective coatings on magnesium and its alloys - A critical review,” *J Alloys Compd*, vol. 336, no. 1–2, pp. 88–113, 2002, doi: 10.1016/S0925-8388(01)01899-0.

[50] T. Pearson and M. del Mar Cordero-Rando, “Pretreatment of Magnesium Substrates for Electroplating,” US20070039829A1, 2007

[51] B. Zhang, “Green Electroless Plating,” in *Amorphous and Nano Alloys Electroless Depositions*, 1st ed.Amsterdam: Elsevier Inc., 2016, pp. 383–409. doi: 10.1016/b978-0-12-802685-4.00007-8.

[52] B. L. Luan and J. E. Gray, “Acousto-immersion coating and process for magnesium and its alloy,” 2003

[53] B. Zhang, “Electroless Plating Baths of Metals, Binary Alloys, and Multicomponent Alloys,” in *Amorphous and Nano Alloys Electroless Depositions*, 1st ed.Amsterdam: Elsevier Inc., 2016, pp. 51–106. doi: 10.1016/b978-0-12-802685-4.00002-9.

[54] G. Cui, N. Li, D. Li, J. Zheng, and Q. Wu, “The physical and electrochemical properties of electroless deposited nickel-phosphorus black coatings,” *Surf Coat Technol*, vol. 200, no. 24, pp. 6808–6814, 2006, doi: 10.1016/j.surfcoat.2005.10.015.

[55] H. Huo, Y. Li, and F. Wang, “AZ91D 镁合金化学镀镍,” *Journal of Chinese Society for Corrosion and Protection*, vol. 22, no. 1, pp. 14–17, 2002.

[56] Z. Zhang *et al.*, “Studies on influence of zinc immersion and fluoride on nickel electroplating on magnesium alloy AZ91D,” *Appl Surf Sci*, vol. 255, no. 17, pp. 7773–7779, Jun. 2009, doi: 10.1016/j.apsusc.2009.04.169.

[57] H. Luo, M. Leitch, H. Zeng, and J. L. Luo, “Characterization of microstructure and properties of electroless duplex Ni-W-P/Ni-P nano-ZrO2 composite coating,” *Materials Today Physics*, vol. 4, pp. 36–42, Mar. 2018, doi: 10.1016/j.mtphys.2018.03.001.

[58] S. M. A. Shibli, M. Ameen Sha, B. L. Anisha, D. Ponnamma, and K. K. Sadasivuni, "Effect of phosphorus on controlling and enhancing electrocatalytic performance of Ni–P–TiO2–MnO2 coatings," *Journal of Electroanalytical Chemistry*, vol. 826, pp. 104–116, Oct. 2018, doi: 10.1016/j.jelechem.2018.08.021.

[59] P. Shoghi, D. Seifzadeh, M. Gholizadeh-Gheshlaghi, and A. Habibi-Yangjeh, "Pretreatment-free Ni−P plating on magnesium alloy at low temperatures," *Transactions of Nonferrous Metals Society of China (English Edition)*, vol. 28, no. 12, pp. 2478–2488, Dec. 2018, doi: 10.1016/S1003-6326(18)64894-0.

[60] R. Petro and M. Schlesinger, "Direct Electroless Deposition of Ni-P-Zn Films on AZ91D Mg Alloy," *J Electrochem Soc*, vol. 160, no. 9, pp. D349–D353, 2013, doi: 10.1149/2.050309jes.

[61] M. Heshmati, D. Seifzadeh, P. Shoghi, and M. Gholizadeh-Gheshlaghi, "Duplex Ni-Zn-Cu-P/Ni-P electroless coating on magnesium alloy via maleic acid pretreatment," *Surf Coat Technol*, vol. 328, pp. 20–29, 2017, doi: 10.1016/j.surfcoat.2017.08.027.

[62] J. Li, Y. Tian, Z. Huang, and X. Zhang, "Studies of the porosity in electroless nickel deposits on magnesium alloy," *Appl Surf Sci*, vol. 252, no. 8, pp. 2839–2846, 2006, doi: 10.1016/j.apsusc.2005.04.028.

[63] S. Alleg, A. Boussaha, W. Tebib, M. Zergoug, and J. J. Suňol, "Microstructure and Magnetic Properties of NiP Alloys," *J Supercond Nov Magn*, vol. 29, no. 4, pp. 1001–1011, Apr. 2016, doi: 10.1007/s10948-016-3397-2.

[64] C.-C. Hu and A. Bai, "Composition control of electroplated nickel-phosphorus deposits," *Surf Coat Technol*, vol. 137, pp. 181–187, 2001.

[65] S. Surendran, S. Shanmugapriya, S. Shanmugam, L. Vasylechko, and R. Kalai Selvan, "Interweaved Nickel Phosphide Sponge as an Electrode for Flexible Supercapattery and Water Splitting Applications," *ACS Appl Energy Mater*, vol. 1, no. 1, pp. 78–92, 2018, doi: 10.1021/acsaem.7b00006.

[66] ASTM International, “Standard Specification for Autocatalytic (Electroless) Nickel-Phosphorus Coatings on Metal,” *Annual Book of ASTM Standards*, vol. i, pp. 1–14, 2015, doi: 10.1520/B0733-15.2.

[67] X. Guo *et al.*, “Amorphous Ni-P with hollow dendritic architecture as bifunctional electrocatalyst for overall water splitting,” *J Alloys Compd*, vol. 765, pp. 835–840, Oct. 2018, doi: 10.1016/j.jallcom.2018.06.321.

[68] W. Yu *et al.*, “Toward a new generation of low cost, efficient, and durable metal-air flow batteries,” *J Mater Chem A Mater*, vol. 7, no. 47, pp. 26744–26768, 2019, doi: 10.1039/c9ta10658h.

[69] A. Khor *et al.*, “Review of zinc-based hybrid flow batteries: From fundamentals to applications,” *Mater Today Energy*, vol. 8, pp. 80–108, 2018, doi: 10.1016/j.mtener.2017.12.012.

[70] C. Hu *et al.*, “Nickel phosphide electrocatalysts for hydrogen evolution reaction,” *Catalysts*, vol. 10, no. 2, Feb. 2020, doi: 10.3390/catal10020188.

[71] S. Q. Guo, L. F. Hou, C. L. Guo, and Y. H. Wei, “Characteristics and corrosion behavior of nickel-phosphorus coatings deposited by a simplified bath,” *Materials and Corrosion*, vol. 68, no. 4, pp. 468–475, Apr. 2017, doi: 10.1002/maco.201609155.

[72] N. Iranipour, R. Azari Khosroshahi, and N. Parvini Ahmadi, “A study on the electroless Ni-P deposition on WE43 magnesium alloy,” *Surf Coat Technol*, vol. 205, no. 7, pp. 2281–2286, Dec. 2010, doi: 10.1016/j.surfcoat.2010.09.006.

[73] S. A. Bradford, *Corrosion Control*, 1st ed. Boston, MA: Springer US, 1993. doi: 10.1007/978-1-4684-8845-6.

[74] ASTM International, “Standard Test Method for Measurement of Thickness of Metallic Coatings by Measurement of Cross Section with a Scanning Electron Microscope,” 2021. doi: 10.1520/B0748-90R21.

[75] ASTM International, “Standard Specification for Autocatalytic (Electroless) Nickel-Phosphorus Coatings on Metal,” *Annual Book of ASTM Standards*, vol. i, no. Reapproved 2009, pp. 1–14, 2021, doi: 10.1520/B0733-21.2.

[76] R. N. Duncan, “The metallurgical structure of electroless nickel deposits: Effect on coating properties,” *Plating and Surface Finishing*, vol. 83, no. 11, pp. 65–69, 1996.

[77] R. Parkinson, “Properties and applications of electroless nickel,” 1997.

[78] M. Buchtík, P. Kosár, J. Wasserbauer, J. Tkacz, and P. Doležal, “Characterization of electroless Ni-P coating prepared on a wrought ZE10 magnesium alloy,” *Coatings*, vol. 8, no. 3, Mar. 2018, doi: 10.3390/coatings8030096.

[79] V. Ezhilselvi, J. N. Balaraju, and S. Subramanian, “Chromate and HF free pretreatment for MAO/electroless nickel coating on AZ31B magnesium alloy,” *Surf Coat Technol*, vol. 325, pp. 270–276, Sep. 2017, doi: 10.1016/j.surfcoat.2017.06.049.

[80] Gamry Instruments, “Getting Started with Electrochemical Corrosion Measurement rev 2,” 2017. [Online]. Available: http://www.gamry.com/App_Notes/Understandin%0Ahttps://www.gamry.com/application-notes/corrosion-coatings/basics-of-electrochemical-corrosion-measurements/

[81] J. Zhang, R. N. Carter, P. T. Yu, W. Gu, F. T. Wagner, and H. A. Gasteiger, “FUEL CELLS – PROTON-EXCHANGE MEMBRANE FUEL CELLS | Catalysts: Life-Limiting Considerations,” in *Encyclopedia of Electrochemical Power Sources*, Elsevier, 2009, pp. 626–638. doi: 10.1016/B978-044452745-5.00234-3.

[82] N. Makuch, “The importance of phase composition for corrosion resistance of borided layers produced on nickel alloys,” *Materials*, vol. 13, no. 22, pp. 1–16, Nov. 2020, doi: 10.3390/ma13225131.

[83] R. E. Davis, G. L. Horvath, and C. W. Tobias, “The solubility and diffusion coefficient of oxygen in potassium hydroxide solutions,” *Electrochim Acta*, vol. 12, no. 3, pp. 287–297, 1967, doi: 10.1016/0013-4686(67)80007-0.

[84] N. F. A. Firman, A. Noor, M. Zakir, Maming, and A. F. Fathurrahman, “Absorption of carbon dioxide into potassium hydroxide: Preliminary study for its application into liquid scintillation counting procedure,” *Egypt J Chem*, vol. 64, no. 9, pp. 4907–4912, Sep. 2021, doi: 10.21608/ejchem.2021.66304.3506.

[85] Thermo Elemental, “AAS, GFAAS, ICP or ICP-MS? Which technique should I use?,” Franklin, MA, 2001.

[86] G. Bagherian, M. Arab Chamjangali, H. Shariati Evari, and M. Ashrafi, “Determination of copper(II) by flame atomic absorption spectrometry after its perconcentration by a highly selective and environmentally friendly dispersive liquid–liquid microextraction technique,” *J Anal Sci Technol*, vol. 10, no. 1, Dec. 2019, doi: 10.1186/s40543-019-0164-6.

[87] M. Schlesinger and M. Paunovic, Eds., *Modern electroplating*, 5th ed. Hoboken, New Jersey: Wiley, 2010.

[88] S. Zhang, J. Yu, Z. Liu, Y. Yin, and C. Qiao, “Numerical and Experimental Investigation of the Effect of Current Density on the Anomalous Codeposition of Ternary Fe-Co-Ni Alloy Coatings,” *Materials*, vol. 15, no. 17, Sep. 2022, doi: 10.3390/ma15176141.

[89] C. Sherwin, S. Bhat, and S. P. Hebbar, “Effects of Current Density on Surface Morphology and Coating Thickness of Nickel Plating on Copper Surface,” 2021.

[90] A. L. Olsen and S. T. Halvorsen, “Method for the Electrolytical Metal Coating of Magnesium Articles,” US4349390, 1982

Appendix A: Additional Information Regarding Pretreatment and Plating Bath Compositions

Table A-1: Olsen et al. patent for zinc immersion followed by copper striking and nickel electroplating [40], [90]

Mechanical Pretreatment	Unspecified process or time	
Degreasing	Organic solvent such as trichloroethylene, perchloroethylene, or trichloroethane, unspecified time	
Pickling	$HOOCCOOH \cdot 2H_2O$	2-10 g/L
	Fluortensid FT 248 (wetting agent)	0.5 g/L
	Temperature	10-40°C
	Time	5-120 s
Activation	$K_4P_2O_7$ or $Na_4P_2O_7$	10-200 g/L
	Na_2CO_3 for pH adjustment	Up to 50 g/L
	Fluortensid FT 248 (wetting agent)	0.5 g/L
	pH	10.0-11.5
	Temperature	20-80°C
	Time	0.5-3 min
Chemical Zincating	$ZnSO_4 \cdot 7H_2O$	50 g/L
	$K_4P_2O_7$	150 g/L
	KF	7 g/L
	Na_2CO_3	5 g/L
	pH	10.2-10.5
	Temperature	60-65°C
	Time	3 min
Copper Strike	Copper	40-45 g/L
	Free KCN	20-25 g/L
	Ultinal ® (brightening agent)	Unspecified

	pH	12-13
	Temperature	60℃
	Cathode current density	2 A/dm^2
	Deposit thickness	15 μm
Nickel Electroplating	Duplalux G ® (brightening agent)	Unspecified
	Cathode current density	3 A/dm^2
	Deposit thickness	10 μm

Table A-2: Example from Pearson et al.'s patent [50]

Alkaline Degreasing	NaOH	25 g/L
	Sodium gluconate	25 g/L
	Voltage	6 V
	Temperature	65°C
	Time	3 min
Zinc Electroplating	$ZnSO_4$	55 g/L
	$K_4P_2O_7$	150 g/L
	KF	7 g/L
	Na_2CO_3	5 g/L
	Current density	1 A/dm^2
	Temperature	60°C
	Time	5 min
Copper Electroplating	CuCN	Unspecified
	Current density	2 A/dm^2
	Time	15 min
Nickel Electroplating	Unspecified bright nickel plating solution	
	Current density	4 A/dm^2
	Time	20 min
Chromium Electroplating	Unspecified bright chromium plating solution	
	Current density	10 A/dm^2
	Time	6 min
Dry	Unspecified drying procedure	

Table A-3: Wang et al chromate and fluoride-free zinc immersion pretreatment bath [48]

Mechanical Cleaning	Abraded successively with 350, 1500 and 2000 grit SiC emery paper	
Alkaline Degreasing	Na_2CO_3	20 g/L
	$Na_3PO_4 \cdot 12H_2O$	20 g/L
	Polyethylene glycol monoalkyl phenyl ester	5 mL/L
	Temperature	75°C
	Time	5-10 min
Acid Pickling	CH_3COOH	20 mL/L
	$NaNO_3$	40 g/L
	Temperature	25°C
	Time	5 s
Zinc Immersion	$ZnSO_4 \cdot 7H_2O$	30 g/L
	Tetrasodium pyrophosphate decahydrate	120 g/L
	Na_2CO_3	5 g/L
	NaF	5 g/L
	Temperature	65°C
	Time	3-10 min

Table A-4: Pretreatment process utilising MDP for depositing Ni-Sn-P, Ni-W-P and Ni-B/Ni-P coatings developed by Zhang et al. [25], [34], [36], [37]

Mechanical Cleaning	Grinding with 2000 grit SiC paper	
Alkaline Cleaning	NaOH	45 g/L (for Ni-Sn-P, and Ni-B/Ni-P composite coating) 10% (for Ni-W-P)
	$Na_3PO_4 \cdot 12H_2O$	10 g/L
	Temperature	65°C
	Time	20 min (for Ni-P only) 15 min
MDP Conversion Coating	$Mn(H_2PO_4)_2$	0.5 g/L 5 g/L (for Ni-B/Ni-P composite coating only)
	H_3PO_4 (85% V/V)	15 mL 150 mL/L (for Ni-B/Ni-P composite coating only)
	$C_2H_4O_2$	20 mL 200 mL/L (for Ni-B/Ni-P composite coating only)
	Ethanol	50 mL 500 mL/L (for Ni-B/Ni-P composite coating only)
	HNO_3 (80% V/V)	5 mL 50 mL/L (for Ni-B/Ni-P composite coating only)
	Temperature	Room temperature
	Time	2 min

Table A-5: Luan and Gray Cu immersion and electroless Ni-P baths [52]

Cu Immersion	$CuSO_4 \cdot 5H_2O$	125 g/L
	HF	100 mL/L
	Temperature	25℃
	Time	5 min
	Sonicating Frequency	35 kHz
Electroless Ni-P Plating	$NiSO_4 \cdot 6H_2O$	30 g/L
	$NaH_2PO_2 \cdot H_2O$	20 g/L
	$NaCH_3COO$	20 g/L
	pH	4.5
	Temperature	75℃
	Time	1 h

Table A-6: Ambat and Zhou pretreatment process [23]

Mechanical Polishing	Wet grinding with 1000 grit SiC paper	
	Diamond wheel polishing with 6 μm diamond paste	
Ultrasonic Degreasing	Performed in acetone	
Alkaline Degreasing	NaOH	10%
	Temperature	60℃
	Time	5 min
Pickling	H_2CrO_4	6%
	HNO_3	5%
	Time	45 s
Activation	HF (70%)	250 mL/L
	Time	10 min

Table A-7: Ambat and Zhou's electroless Ni-P plating bath [23]

$NiCO_3 \cdot 2Ni(OH)_2 \cdot 4H_2O$	9.7 g/L
Citric acid	5.2 g/L
NH_4HF_2	7.5 g/L
HF	11 mL/L
H_2NCSNH_2 (Thiourea, TU)	1 mg/L
$NaH_2PO_2 \cdot H_2O$	20 g/L
NH_4OH	To adjust pH
pH	7-8
Temperature	80°C
Agitation	Mild mechanical

Table A-8: Pretreatment process used by Huo et al. [20]

Mechanical Polishing	Grinding with 1000 grit emery paper	
Ultrasonic Bath	Acetone	
Stannate Conversion Coating	NaOH	10 g/L
	$Na_2SnO_3 \cdot 3H_2O$	50 g/L
	$NaCH_3COO \cdot 3H_2O$	10 g/L
	Temperature	90°C
	Time	60 min, moderate stirring
Sensitization	$SnCl_2$	10 g
	HCl	5 mL
	H_2O	1000 mL
	Temperature	Room temperature
	Time	1-2 min, specimen shaken
Activation	$PdCl_2$	0.5 g
	C_2H_5OH	500 mL
	H_2O	500 mL
	Temperature	Room temperature
	Time	10-60 s, specimen shaken
Reduction	$NaH_2PO_2 \cdot H_2O$	30 g/L
	Temperature	Room temperature
	Time	10-60 s, specimen shaken

Table A-9: Huo et al.'s electroless Ni-P plating bath [20], [55]

$Ni(CH_3COO)_2 \cdot 4H_2O$	
NaH_2PO_2	
Citric acid	
pH	6.9
Time	2 h

Table A-10: Lian et al. pretreatment procedure [33]

Mechanical Cleaning	Grinding with 1500 grit SiC papers	
Alkaline Degreasing	KOH	10.5 g/L
	Temperature	60°C
	Time	3-5 min
Phosphating	H_3PO_4	17.5 g/L
	ZnO	3.2 g/L
	NaF	1.7 g/L
	Nitroguanidine	0.2 g/L
	Tartaric acid	2.2 g/L
	$NaNO_3$	2.5
	$NaMoO_4$	0-2.5
	pH	2.13-3
	Temperature	45°C
	Time	2-3 min

Table A-11: Zhao et al. 8604 organosilicon interlayer application process [44]

Step	Process	Time
1	Acid pre-cleaning with 30 mL/L of HNO_3 at room temperature	1.5 min
2	Water cleaning	
3	Drying in drying oven	
4	Immerse sample vertically in 8604 organosilicon heat-resistant varnish	
5	Hang dry in air	30 min
6	Oven dry in air at 180°C	60 min
7	Surface roughening with 600 g/L NaOH aqueous solution	30 min
8	Immerse in Pd colloid activator at 25°C	10 min
9	Dissolve colloid in 100 mL of HCl and 900 mL deionized water at 40°C	1 min

Table A-12: Zhao et al. electroless Ni-P plating bath [44]

$NiSO_4 \cdot 6H_2O$	16 g/L
$Na_2H_2PO_2$	16 g/L
$Na_4P_2O_7$	60 g/L
NH_4OH	8 mL/L
Surfactant	20 mg/L
Stabilizer	4 µg/L
pH	9.5
Temperature	50°C
Time	60 min

Table A-13: Yang et al. pretreatment process [27]

Mechanical Cleaning	Abrading with 1500 grit SiC paper	
Ultrasonic Cleaning	Performed in acetone	
Alkaline Cleaning	NaOH	50 g/L
	$Na_3PO_4 \cdot 12H_2O$	10 g/L
	Temperature	60°C
	Time	10-20 min
Molybdate Pretreatment	$Na_2MoO_4 \cdot 2H_2O$	20 g/L
	pH	5.5 ± 0.5
	Temperature	Room temperature
	Time	3 min

Table A-14: Seifzadeh and Rajabalizadeh pretreatment process [38]

Mechanical Polishing	Utilised emery papers	
Alkaline Degreasing	NaOH	10 mL/L
	$Na_3PO_4 \cdot H_2O$	10 mL/L
	Time	15 min
Pickling	HNO_3	50 mL/L
	Time	30 s
CLP Conversion Coating	$Ce(NO)_3$	0.4 g/L
	$La(NO)_3$	0.4 g/L
	$KMnO_4$	25 g/L
	Temperature	Room temperature
	Time	15 min

Table A-15: Ghavidel et al. pretreatment process [19]

Mechanical Cleaning	Abraded with sandpapers up to 1200 grit	
Ultrasonic Degreasing	Unknown compound(s)	
	Time	5 min
$NaHCO_3$ Conversion Coating	$NaHCO_3$	Saturated
	Temperature	25°C
	Time	60 min
Water Cleaning	Rinsed with deionized water	

Table A-16: Ghavidel et al. Ni-P/nano-SiC plating bath [19]

$NiSO_4 \cdot 6H_2O$	20 g/L
$Na_2H_2PO_2 \cdot H_2O$	22 g/L
Trisodium citrate dihydrate	10 g/L
NH_4HF_2	10 g/L
TU	1 mg/L
Unknown surfactant	10 mg/L
SiC NPs	0.5, 1, 2, 4 g/L
pH	7
Temperature	75°C
Time	1 h

Table A-17: He et al. pretreatment process [29]

Mechanical Polishing	Grinding with up to 1200 grit SiC paper	
Ultrasonic Degreasing	Performed in ethanol	
Alkaline Wash	NaOH	50 g/L
	Na_3PO_4	10 g/L
	Temperature	60°C
	Time	15 min
Pickling	CrO_3	125 g/L
	HNO_3	110 mL/L
	Time	50 s
	Temperature	Room temperature
Activation	HF (40%)	385 mL/L
	Time	10 min
	Temperature	Room temperature

Table A-18: He et al MAEP bath [29]

$NiCO_3 \cdot 2Ni(OH)_2 \cdot 4H_2O$	10 g/L
Citric acid monohydrate	5 g/L
HF (40%)	12 mL/L
NH_4HF_2	10 g/L
$NaH_2PO_2 \cdot H_2O$	20 g/L
NH_4OH	30 mL/L
TU	1 mg/L
Al_2O_3 balls (1-1.5 mm in diameter)	
pH	6.5 ± 1.0
Temperature	80 ± 2℃
Time	60 min

Table A-19: Heshmati et al. maleic acid pretreatment process for AM60B [61]

Mechanical Cleaning	Sequential abrading with 600 to 2000 grit SiC emery papers	
Ultrasonic Degreasing	Performed in acetone	
	Temperature	Room temperature
	Time	15 min
Acid Etching	HNO_3 (69-71%)	50 mL/L
	Time	30 s
Maleic Acid Pretreatment	Maleic acid anhydride	3 g/L
	Time	2 min

Table A-20: Heshmati et al. electroless Ni-P and Ni-Zn-Cu-P plating baths for Ni-Zn-Cu-P/Ni-P composite coating [61]

Electroless Ni-P Plating Bath	$NiSO_4 \cdot 6H_2O$	15 g/L
	$Na_2H_2PO_2 \cdot H_2O$	14 g/L
	$NaCH_3COOH$	13 g/L
	NH_4HF_2	8 g/L
	HF (40% V/V)	12 mL/L
	TU	1 ppm
	NH_3 (30%)	For pH adjustment
	pH	6.4
	Temperature	65℃
	Time	1 h
Electroless Ni-Zn-Cu-P Plating Bath	$NiSO_4 \cdot 6H_2O$	25 g/L
	$Na_2H_2PO_2 \cdot H_2O$	30 g/L
	$ZnSO_4 \cdot 7H_2O$	2 g/L
	$CuSO_4 \cdot 5H_2O$	0.2 g/L
	$NaCH_3COOH$	47 g/L
	NH_4HF_2	8 g/L
	HF (40% V/V)	12 mL/L
	TU	1 ppm
	NH_3 (30%)	For pH adjustment
	pH	10
	Temperature	70℃
	Time	2 h

Table A-21: Successful plating baths used by Petro and Schlesinger [43]

	Composition (g/L)						
	S1	S2	S3	S4	S5	S6	S7
$Ni(CH_3COO)_2 \cdot 4H_2O$	9.940	-	-	9.940	-	-	-
$NiSO_4 \cdot 6H_2O$	-	10.499	-	-	10.499	-	6.299
$Ni(H_2NSO_3)_2 \cdot 4H_2O$	-	-	12.899	-	-	12.899	-
$ZnSO_4 \cdot 7H_2O$	-	-	-	-	-	-	4.594
Trisodium citrate dihydrate	23.500						
$NaH_2PO_2 \cdot H_2O$	17.500						
NaOH	1.250			-	-	-	-
NH_4OH (mL/L)	12.5				37.5		40.0
Average pH (before deposition, at 20°C)	11.81	11.98	11.85	11.86	11.92	11.93	11.69
Operating Temperature	68-72°C						

Table A-22: Unsuccessful plating baths used by Petro and Schlesinger [43]

	Composition (g/L)					
	F1	F2	F3	F4	F5	F6
$NiSO_4 \cdot 6H_2O$	29.00	-	-	-	10.499	
$NiCl_2 \cdot 6H_2O$	-	9.495		-	-	-
$Ni(CH_3COO)_2 \cdot 4H_2O$	-	-	-	9.940	-	-
Disodium succinate dihydrate	15.000	-	-	-	-	-
Succinic acid	1.300	-	-	-	-	-
Trisodium citrate dihydrate	23.500					
$NaH_2PO_2 \cdot H_2O$	17.000			17.500		
NaOH	-	1.250	-	1.9375	1.875	11.910
NH_4OH (mL/L)	-	12.5	37.5	-	-	-
$(NH_4)_2SO_4$	-	-	-	-	-	19.250
Average pH (before deposition, at 20°C)	5.40	11.86	11.77	12.32	11.97	11.30
Operating Temperature	68-72°C					

Table A-23: Wang et al. electroless Ni-B plating bath [48]

$Ni(CH_3COO)_2 \cdot 4H_2O$	30 g/L
Ethylenediamine	100 mL/L
NaOH	46 g/L
$NaBH_4$	0.8 g/L
TU	0.5-2 mg/L
Sodium saccharine dihydrate	1-4 g/L
pH	13.6
Temperature	85℃
Time	1 h

Table A-24: Petro and Schlesinger Ni-P-Zn plating baths [60]

	Composition (g/L)			
	25% Zn	35% Zn	50% Zn 1	50% Zn 2
$NiSO_4 \cdot 6H_2O$	7.87425	6.82435	5.2495	6.82435
$ZnSO_4 \cdot 7H_2O$	2.87125	4.01975	5.7425	7.46525
Trisodium citrate dihydrate	23.500			
$NaH_2PO_2 \cdot H_2O$	17.500			
NH_4OH (mL/L)	37.5	37.5	62.5	50.0
Average pH (before deposition, at 20℃)	11.61	11.63	11.96	11.63
Operating temperature	68-72℃			

Table A-25: Zhang et al. electroless Ni-Sn-P plating bath [25]

$NiSO_4 \cdot 6H_2O$	15 g/L
$Na_2SnO_3 \cdot 3H_2O$	4 g/L
$Na_2H_2PO_2 \cdot H_2O$	20 g/L
Trisodium citrate dihydrate	80 g/L
NH_4HF_2	15 g/L
H_2NCSNH_2	0.001 g/L
pH	9.0 ± 0.2
Temperature	90 ± 2℃

Table A-26: Zhang et al.'s electroless Ni-W-P plating bath [36]

$NiSO_4 \cdot 6H_2O$	15 g/L
$Na_2H_2PO_2 \cdot H_2O$	20 g/L
Na_2CO_3	20 g/L
Na_2WO_4	10 g/L
Trisodium citrate dihydrate	40 g/L
NH_4HF_2	8 g/L
TU	1 mg/L
pH	9.0
Temperature	80 ± 2℃

Table A-27: Hsu and Yang pretreatment process [32]

Ultrasonic Cleaning	Performed in isopropyl alcohol for 10 min	
Alkaline Degreasing	Unknown composition	
	Temperature	60°C
	Time	2 min
Acid Pickling	Unknown composition and operational conditions	
Surface Activation	Unknown composition and operational conditions	
Zincating	Unknown composition and operational conditions	
Cu Striking	Unknown Cu strike solution	
	Pure Cu anode (99.99%)	
	Current density	5 A/dm^2
	Temperature	Room temperature
	Time	10 min

Table A-28: Hsu and Yang electroless Ni-P and Ni electroplating baths [32]

Electroless Ni-P Plating	$NiSO_4 \cdot 6H_2O$	20 g/L
	$Na_2H_2PO_2 \cdot H_2O$	27 g/L
	Succinic acid	16
	Unknown stabilizer	0.54 ppm
	pH	4.80
	Temperature	80°C
	Time	40 min
Ni Electroplating	$NiSO_4 \cdot 6H_2O$	240 g/L
	$NiCl_2$	45 g/L
	H_3BO_3	30 g/L
	Unknown brightener	10 mL/L
	Current density	1.0 A/dm^2
	Temperature	55°C
	Time	Not specified

Table A-29: Gu et al. pretreatment process [35]

Mechanical Cleaning	Abrading with 1500 grit SiC paper	
Alkaline Cleaning	NaOH	45 g/L
	$Na_3PO_4 \cdot 12H_2O$	10 g/L
	Temperature	65°C
Pickling	CrO_3	125 g/L
	HNO_3 (70% V/V)	100 mL/L
	Temperature	Room temperature
	Time	Variable (0-60 s)
Activation	HF (40% V/V)	350 mL/L
	Temperature	Room temperature
	Time	10 min

Table A-30: Gu et al. direct electroless Ni-P plating bath [35]

$NiSO_4 \cdot 6H_2O$	15 g/L
$NaH_2PO_2 \cdot H_2O$	14 g/L
$NaCH_3COO$	13 g/L
HF (40% V/V)	12 mL/L
NH_4HF_2	8 g/L
TU	1 mg/L
pH	6.4 ± 0.2
Temperature	82 ± 2°C
Time	1 h

Table A-31: Gu et al. NC Ni electroplating bath [28]

NC Ni Electroplating	$NiSO_4 \cdot 6H_2O$	250-300 g/L
	$NiCl_2 \cdot 6H_2O$	30-40 g/L
	H_3BO_3	30-45 g/L
	Saccharin	0.1-0.2 g/L
	Current Density	3 A/dm^2
	pH	5
	Temperature	50°C
	Time	30 min

Table A-32: Pretreatment process used by Luo et al. [46]

Alkaline Degreasing	NaOH	25 g/L
	Na_2CO_3	20 g/L
	$Na_3PO_4 \cdot 12H_2O$	20 g/L
	Temperature	60°C
	Time	8-10 min
Acid Cleaning	CH_3COOH	5 g/L
	Temperature	20°C
	Time	90 s
Activation	H_3PO_4 (85%)	50-60 mL/L
	NH_4HF_2	100-200 g/L
	Temperature	25°C
	Time	8-12 min

Table A-33: Luo et al. two-step electroless Ni-P plating baths [46]

First Electroless Plating Step	$NiCO_3 \cdot 2Ni(OH)_2 \cdot 4H_2O$	10 g/L
	$NaH_2PO_2 \cdot H_2O$	20 g/L
	HF (40%)	10 mL/L
	Lactic acid	15 mL/L
	NH_4HF_2	10 g/L
	Unknwon Surfactant	Proper
	TU	1 mg/L
	$NH_3 \cdot H_2O$ (25%)	Adjust pH to 6
	pH	6
	Temperature	80°C
	Time	10 min
Second Electroless Plating Step	$NiSO_4 \cdot 6H_2O$	30 g/L
	$NaH_2PO_2 \cdot H_2O$	20 g/L
	HF (40%)	10 mL/L
	Lactic acid	15 mL/L
	NH_4HF_2	10 g/L
	Surfactant	Proper
	TU	1 mg/L
	pH	4
	Temperature	80°C
	Time	60 min

Table A-34: Zhang et al. Ni-P and Ni-B plating baths for Ni-B/Ni-P composite coating [34]

Ni-P	$NiSO_4 \cdot 6H_2O$	15 g/L
	$Na_2H_2PO_2 \cdot H_2O$	26 g/L
	$NaC_2H_3O_2$	13 g/L
	HF (40% V/V)	12 mL/L
	NH_4HF_2	8 g/L
	TU	1 mg/L
	pH	5.0 ± 0.2
	Temperature	90 ± 2°C
	Time	40 min
Ni-B	$NiCl_2 \cdot 6H_2O$	0.127 M
	Ethylenediamine	1.5 M
	$NaBH_4$	0.021 M
	NaOH	2.25 M
	TU	$1.32 \cdot 10^{-5}$ M
	pH	> 13
	Temperature	85 ± 2°C
	Time	4 h

Table A-35: Two-step activation procedure used by Zhang et al. [21]

Mechanical Cleaning	Sequential polishing with 400 to 1200 grit SiC emery papers	
Ultrasonic Degreasing	Performed in acetone	
	Temperature	25 ± 2°C
	Time	10 min
Alkaline Degreasing	NaOH	50 g/L
	$Na_3PO_4 \cdot 12H_2O$	10 g/L
	Temperature	60 ± 2°C
	Time	10 min
Acid Pickling	H_3PO_4 (85%)	600 cm^3/L
	HNO_3 (68%)	30 cm^3/L
	Temperature	25 ± 2°C
	Time	1 min
Activation 1	$K_4P_2O_7$	160 g/L
	Na_2CO_3	20 g/L
	$KF \cdot 2H_2O$	11 g/L
	Temperature	40 ± 2°C
	Time	2.5 min
Activation 2	H_3PO_4	180 g/L
	NH_4HF_2	95 g/L
	Temperature	25 ± 2°C
	Time	2.5 min

Table A-36: Zhang et al. electroless Ni-B and Ni-P plating baths for Ni-P/Ni-B composite coating [21]

Ni-B Plating	$NiCl_2 \cdot 6H_2O$	25 g/L
	Ethylenediamine	50 cm^3/L
	Trisodium citrate dihydrate	30 g/L
	NaOH	90 g/L
	$NaBH_4$	0.8 g/L
	TU	1 mg/L
	pH	11.0
	Temperature	75 ± 2°C
Ni-P Plating	$NiSO_4 \cdot 6H_2O$	20 g/L
	$Na_2H_2PO_2 \cdot H_2O$	20 g/L
	Citric acid monohydrate	5 g/L
	TU	0.001 g/L
	$NH_3 \cdot H_2O$ (25%)	Used to adjust pH to 5.5
	Temperature	85 ± 2°C

Table A-37: Song et al. pretreatment process [39]

Mechanical Cleaning	Grinding with 1000 grit SiC emery paper
Ultrasonic Degreasing	Performed in acetone Unspecified temperature and time
Alkaline Degreasing	Unspecified process, temperature, or time
Acid Pickling	Unspecified process, temperature, or time
Activation	Unspecified process, temperature, or time

Table A-38: Song et al. Ni-P-ZrO_2 plating, Ni electroplating, and Ni-P plating baths [39]

Electroless Ni-P Plating	$NiCO_3 \cdot 2Ni(OH)_2 \cdot 4H_2O$	11 g/L
	$NaH_2PO_2 \cdot H_2O$	23 g/L
	Sodium citrate	12 g/L
	KF	8 g/L
	Buffer agent	12.5 g/L
	Stabilizer	2 mg/L
	pH	6.0
	Temperature	80°C
	Time	30 min
Electroless Ni-P-ZrO_2 Plating	Same as electroless Ni-P plating, but with 5 g/L of ZrO_2 (20 nm) NPs added to plating bath	
Ni Electroplating (Watts Solution)	$NiSO_4$	220 g/L
	NaCl	12 g/L
	H_3BO_3	33 g/L
	Na_2SO_4	25 g/L
	$MgSO_4$	35 g/L
	pH	5.0
	Temperature	Room temperature
	Cathodic current density	1.0 A/dm^2

Table A-39: Pretreatment, zincating, and copper plating processes used by Ghamari and Amadeh [13]

Mechanical Cleaning	Water Jet	
	2000 grit SiC paper	
Degreasing	NaOH	20 g/L
	Temperature	60°C
	Time	5 min
Pickling	$HCrO_3$	180 g/L
	Time	5 min
Activation	NH_4HF_2	30 g/L
	H_3PO_4	120 g/L
	Temperature	Ambient
	Time	25 s
Zincating	$ZnSO_4 \cdot H_2O$	30 g/L
	NaP_2O_7	120 g/L
	NaF	5 g/L
	Na_2CO_3	5 g/L
	pH	10.2-10.4
	Rotational speed	150 RPM
	Temperature	85°C
	Time	10 min
Cu Electroplating	CuCN	40 g/L
	KCN	70 g/L
	KF	30 g/L
	Na_2CO_3	5 g/L
	pH	10.2
	Current density	2 A/dm^2
	Temperature	55°C
	Time	15 min

Table A-40: Ghamari and Amadeh pulsed current electroplating bath [13]

$NiSO_4$	300 g/L
$NiCl_2$	45 g/L
H_3BO_3	45 g/L
SDS	1 g/L
Saccharin	1 g/L
γ-Al_2O_3 NPs	0 or 5 g/L
Temperature	50°C
pH	4.5
Duty Cycle	30%
Frequency	10 Hz
On/Off Times	0.03s / 0.07s
Rotational Speed	150 RPM

Table A-41: Alkaline $CuSO_4$ bath used by Huang et al. [15]

$CuSO_4$	40 g/L
Potassium sodium tartrate	150 g/L
H_3BO_3	20 g/L
NaOH	Add until 10 pH
Galvanostatic Etching Anodic Current Density	50 mA/cm^2
Cu Electroplating Charge Density	24 C/cm^2

Table A-42: Alleg et al. Ni-P electroplating bath [63]

$NiSO_4 \cdot 6H_2O$	0.2 M
$NaH_2PO_2 \cdot H_2O$	0.1 M
H_3BO_3	0.005 M
Saccharin	0.005 M
NaCl	0.7 M
pH	3-4
Temperature	70 ± 2 ℃
Potential	-1.3 to -1 V
Time	10 or 20 min

Table A-43: Hu and Bai Ni-P electroplating bath [64]

$NiSO_4 \cdot 6H_2O$	330 g/L
$NiCl_2$	45 g/L
$NaH_2PO_2 \cdot H_2O$	0.5-1M
H_3BO_3	37 g/L
NaOH	For pH adjustment
HCl	For pH adjustment
pH	1-4
Temperature	20-50 ℃
Current density	50-250 mA/cm^2
Stirring rate	200-400 RPM
Delivered charge	120 C/cm^2

Appendix B: Additional Examples of SEM BSE Micrographs of Cross Sections, Macroscopic Porosity Data, and Examples of Dimples from All Coatings

#1

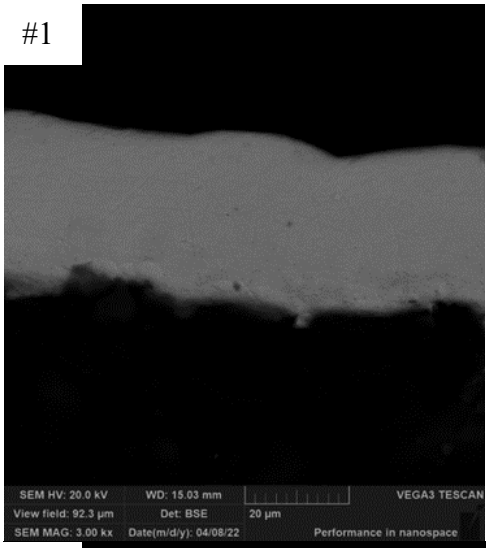

#2

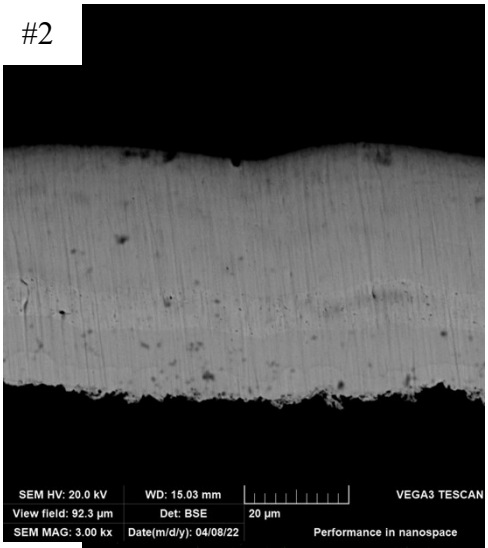

#3

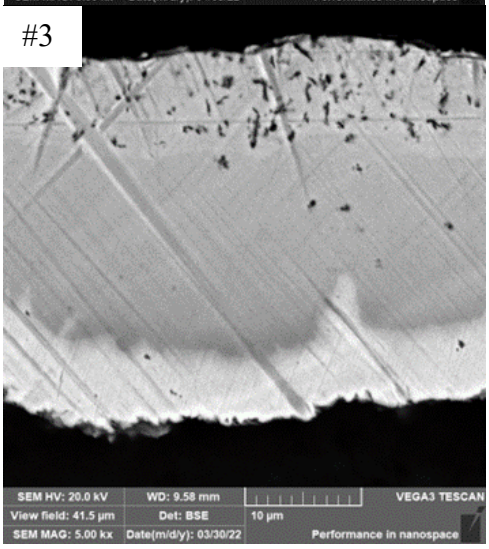

#4

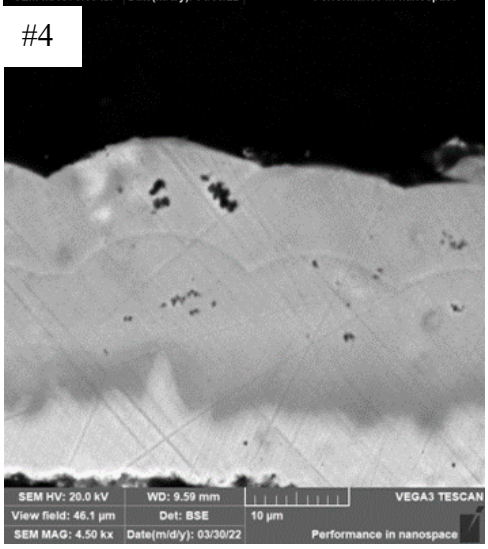

#5

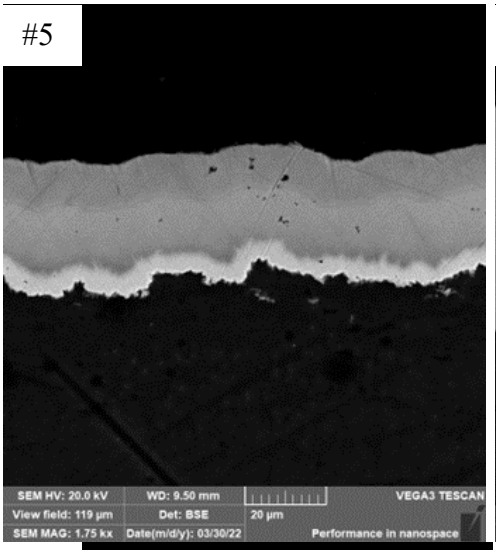
SEM HV: 20.0 kV
WD: 9.50 mm
VEGA3 TESCAN
View field: 119 µm
Det: BSE
20 µm
SEM MAG: 1.75 kx
Date(m/d/y): 03/30/22
Performance in nanospace

#6

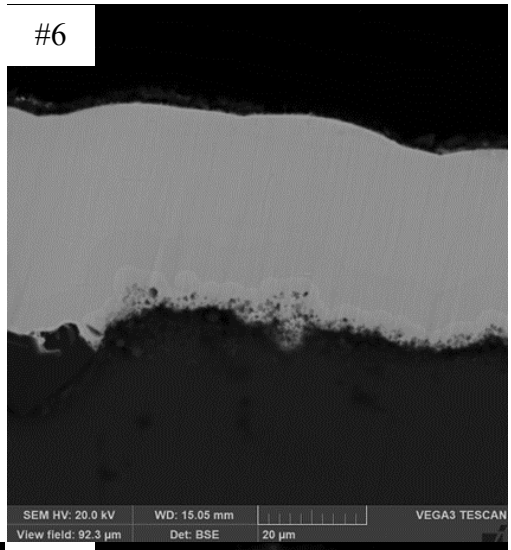
SEM HV: 20.0 kV
WD: 15.05 mm
VEGA3 TESCAN
View field: 92.3 µm
Det: BSE
20 µm

#7

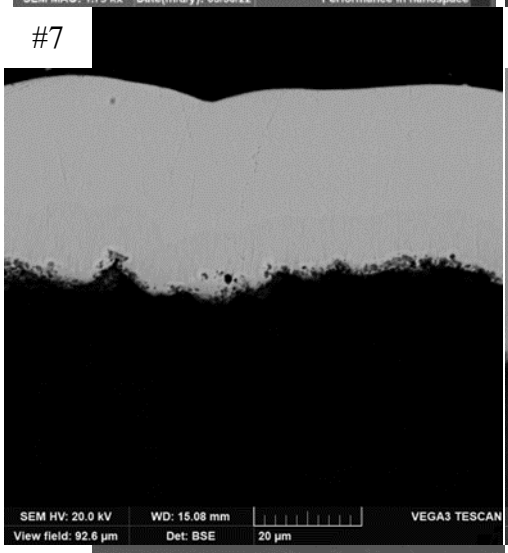
SEM HV: 20.0 kV
WD: 15.08 mm
VEGA3 TESCAN
View field: 92.6 µm
Det: BSE
20 µm

#8

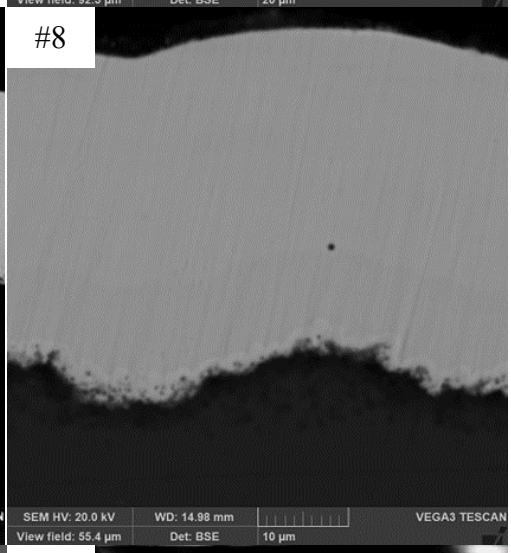
SEM HV: 20.0 kV
WD: 14.98 mm
VEGA3 TESCAN
View field: 55.4 µm
Det: BSE
10 µm

#9

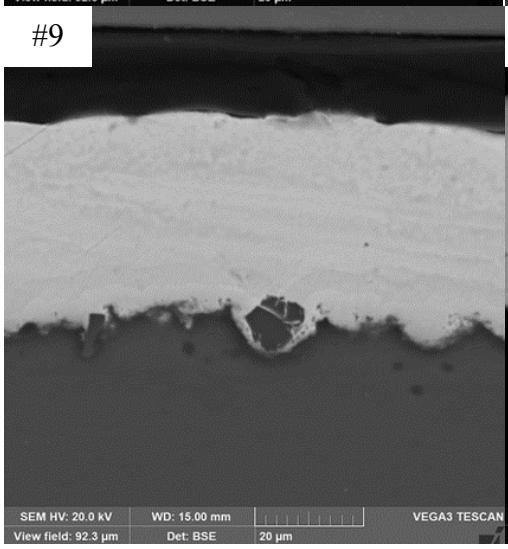
SEM HV: 20.0 kV
WD: 15.00 mm
VEGA3 TESCAN
View field: 92.3 µm
Det: BSE
20 µm

#10

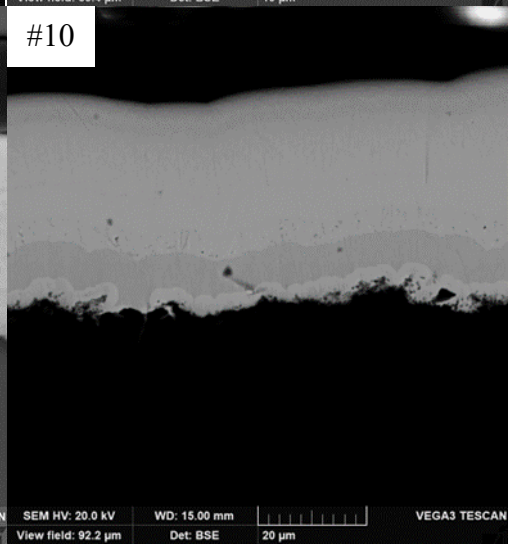
SEM HV: 20.0 kV
WD: 15.00 mm
VEGA3 TESCAN
View field: 92.2 µm
Det: BSE
20 µm

#11

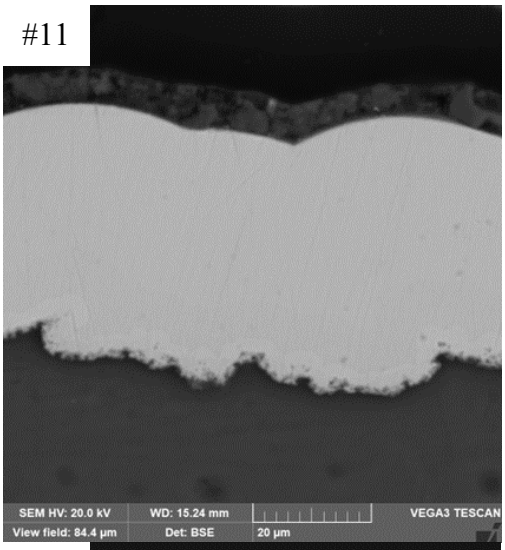

#12

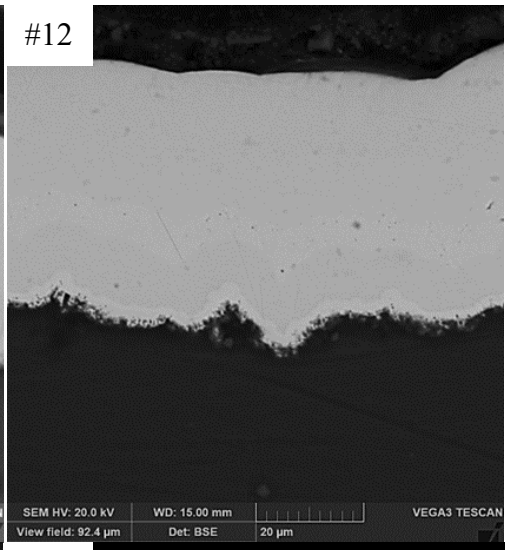

#13

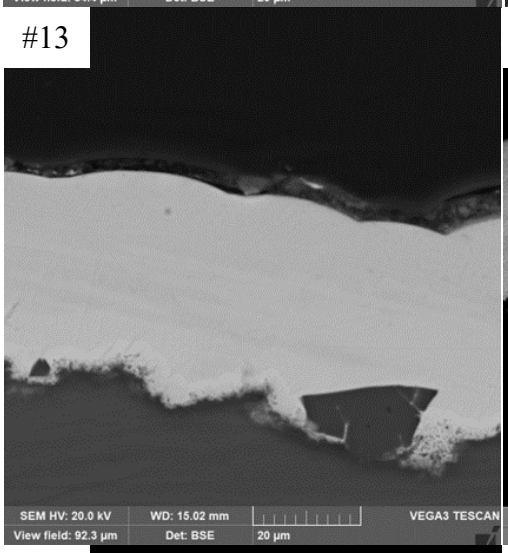

#14

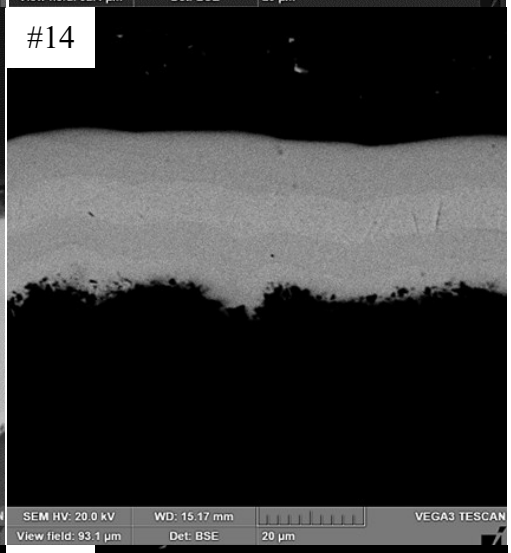

#15

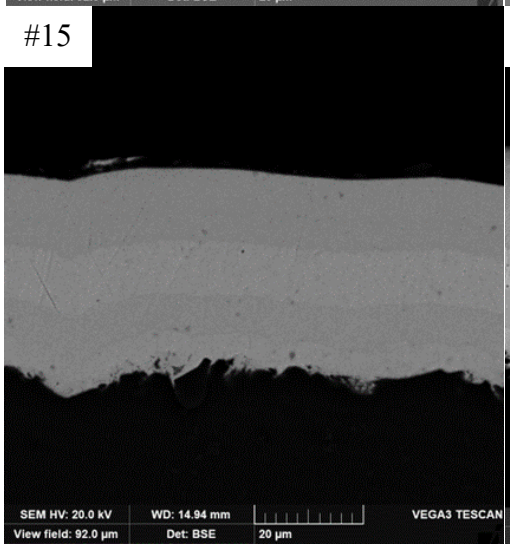

#16

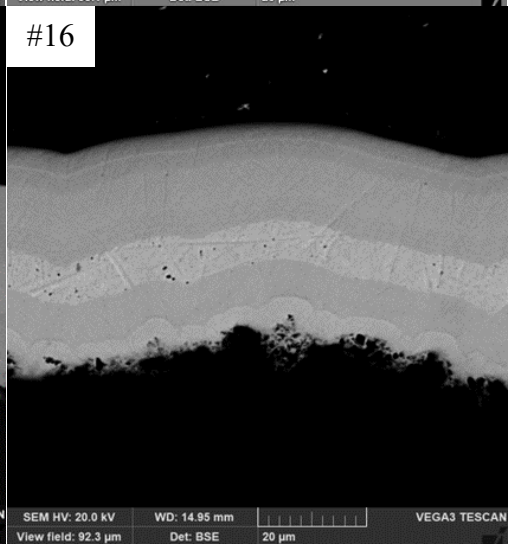

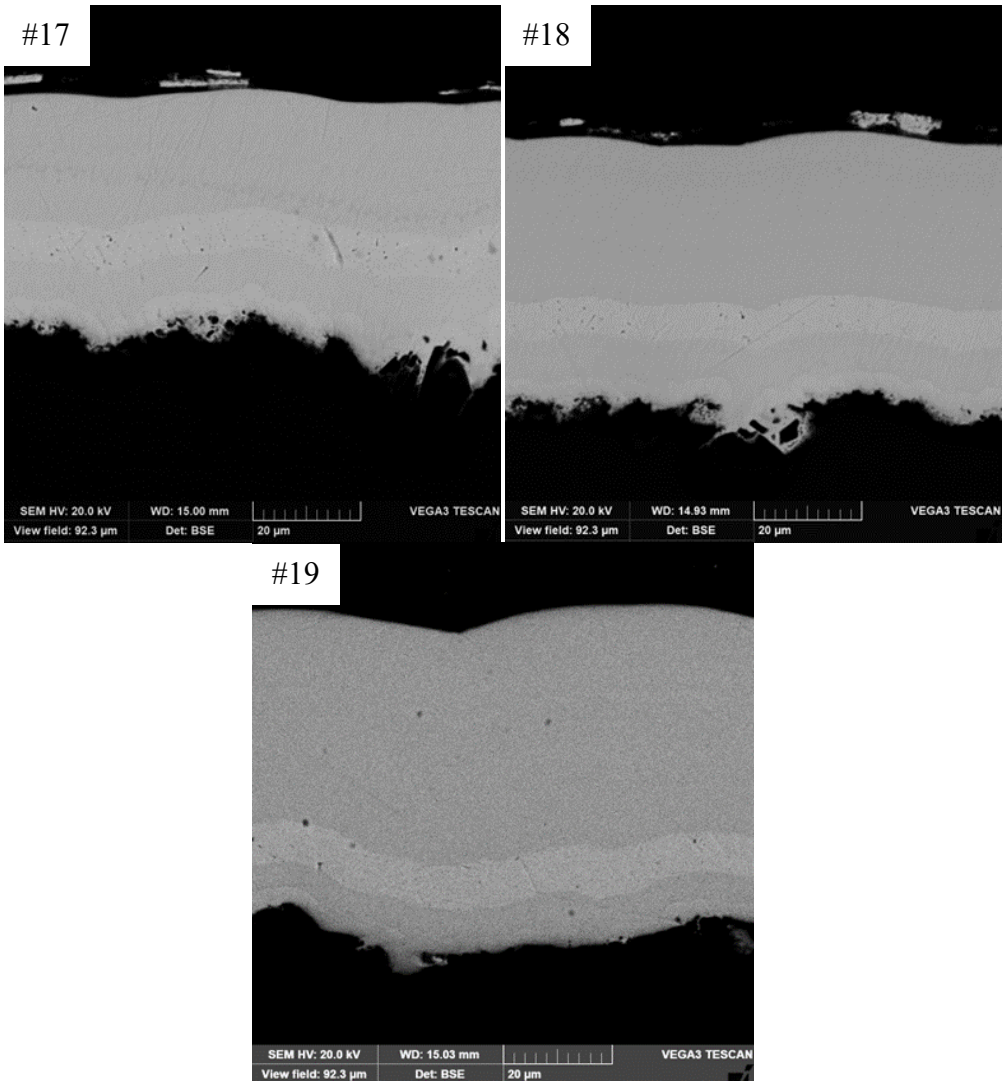

Figure B-1: Examples of SEM BSE micrographs of cross sections of all coatings.

Table B-1: Additional macroscopic porosity data

Coating Number	Analyzed Region Area (mm^2)	Total Number of Pores	Total Pore Area (μm^2)
1	1.33	5	$6.54 \cdot 10^2$
2	1.18	2	$3.83 \cdot 10^2$
3	1.48	98	$5.35 \cdot 10^4$
4	1.33	139	$4.88 \cdot 10^4$
5	1.27	123	$1.41 \cdot 10^4$
6	2.38	255	$1.08 \cdot 10^5$
7	2.47	89	$2.15 \cdot 10^4$
8	2.21	31	$2.55 \cdot 10^3$
9	2.01	135	$2.70 \cdot 10^4$
10	1.62	111	$1.37 \cdot 10^4$
11	2.42	74	$9.23 \cdot 10^3$
12	1.65	114	$1.35 \cdot 10^4$
13	2.60	495	$1.16 \cdot 10^5$
14	1.59	179	$6.65 \cdot 10^4$
15	0.983	80	$1.88 \cdot 10^4$
16	1.75	107	$3.74 \cdot 10^4$
17	1.56	65	$8.16 \cdot 10^3$
18	2.40	54	$1.75 \cdot 10^4$
19	2.35	12	$3.35 \cdot 10^3$

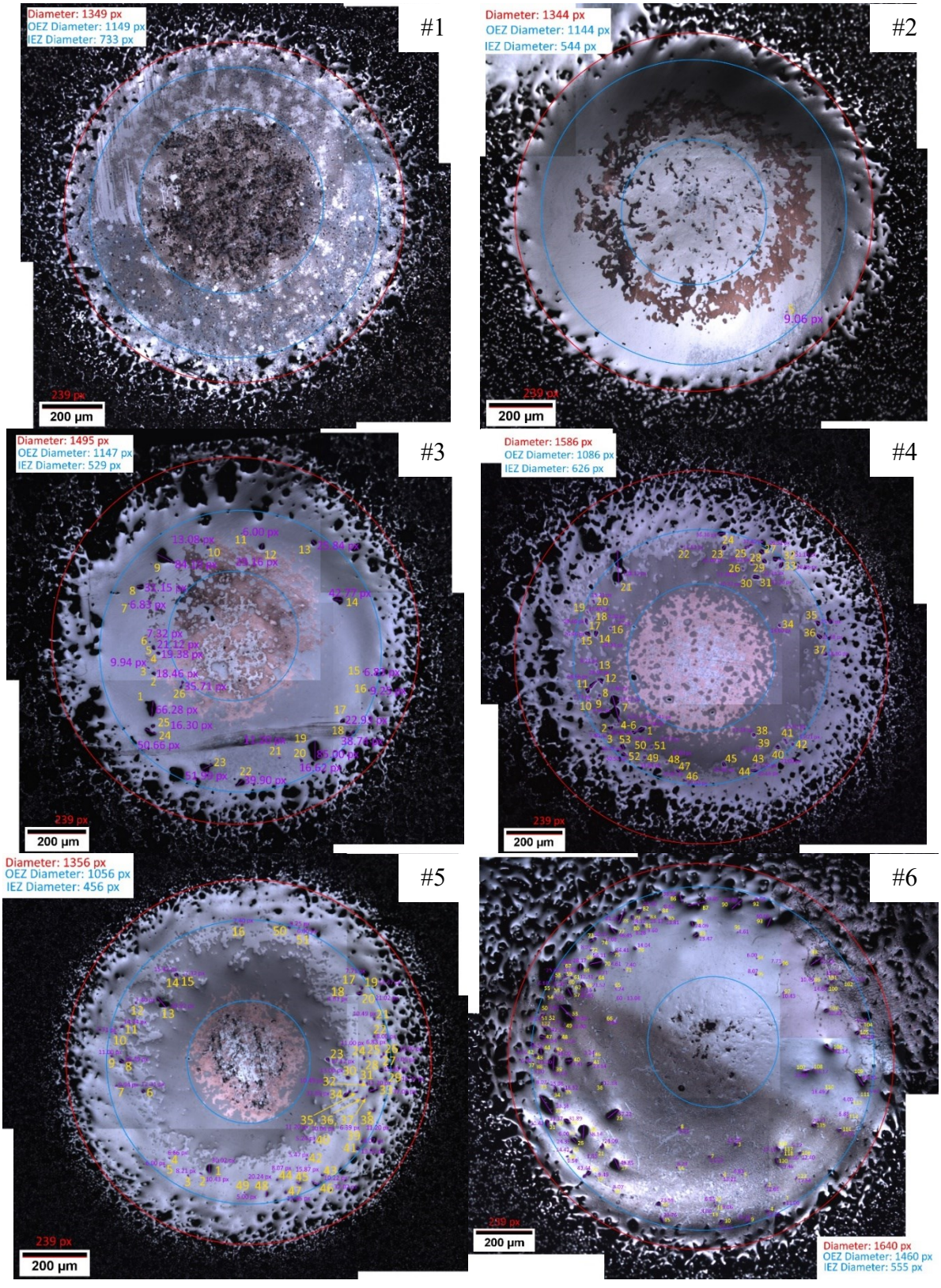
Diameter: 1349 px
OEZ Diameter: 1149 px
IEZ Diameter: 733 px
#1
239 px
200 µm
Diameter: 1344 px
OEZ Diameter: 1144 px
IEZ Diameter: 544 px
#2
9.06 px
239 px
200 µm
Diameter: 1495 px
OEZ Diameter: 1147 px
IEZ Diameter: 529 px
#3
239 px
200 µm
Diameter: 1586 px
OEZ Diameter: 1086 px
IEZ Diameter: 626 px
#4
239 px
200 µm
Diameter: 1356 px
OEZ Diameter: 1056 px
IEZ Diameter: 456 px
#5
239 px
200 µm
#6
239 px
200 µm
Diameter: 1640 px
OEZ Diameter: 1460 px
IEZ Diameter: 555 px

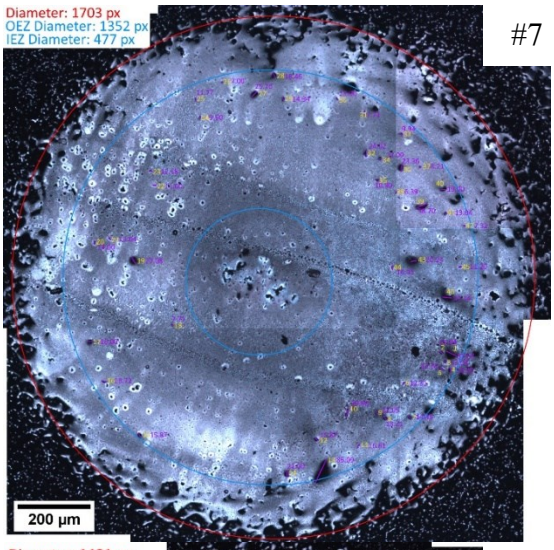
Diameter: 1703 px
OEZ Diameter: 1352 px
IEZ Diameter: 477 px
200 µm

#7

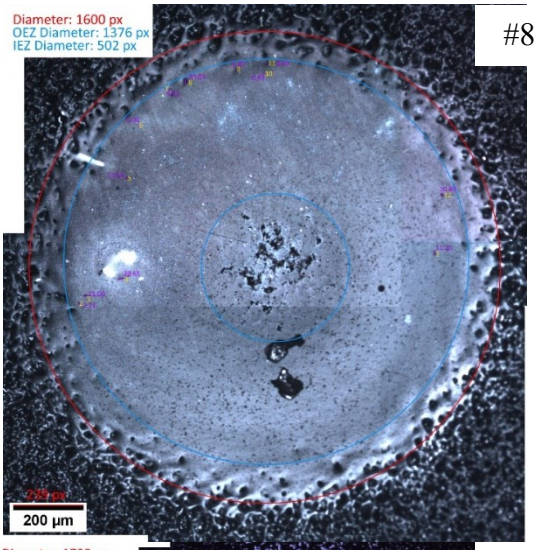
Diameter: 1600 px
OEZ Diameter: 1376 px
IEZ Diameter: 502 px
200 µm

#8

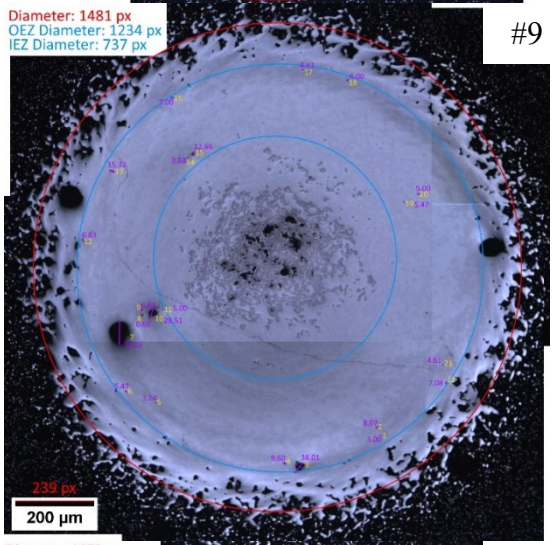
Diameter: 1481 px
OEZ Diameter: 1234 px
IEZ Diameter: 737 px
239 px
200 µm

#9

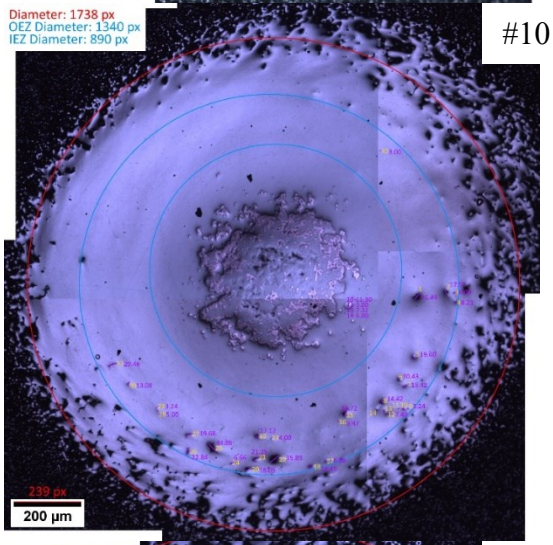
Diameter: 1738 px
OEZ Diameter: 1340 px
IEZ Diameter: 890 px
239 px
200 µm

#10

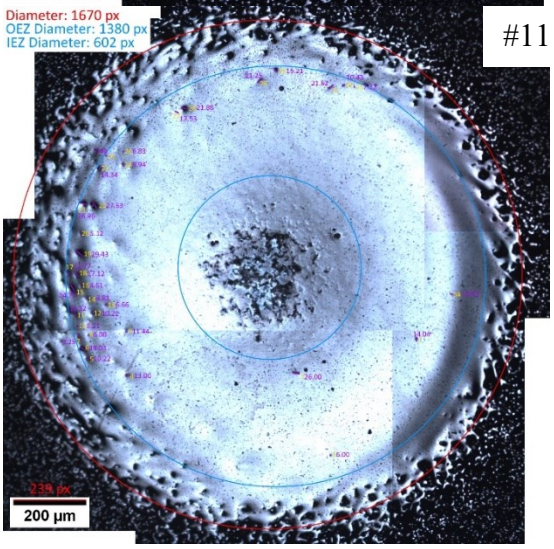
Diameter: 1670 px
OEZ Diameter: 1380 px
IEZ Diameter: 602 px
239 px
200 µm

#11

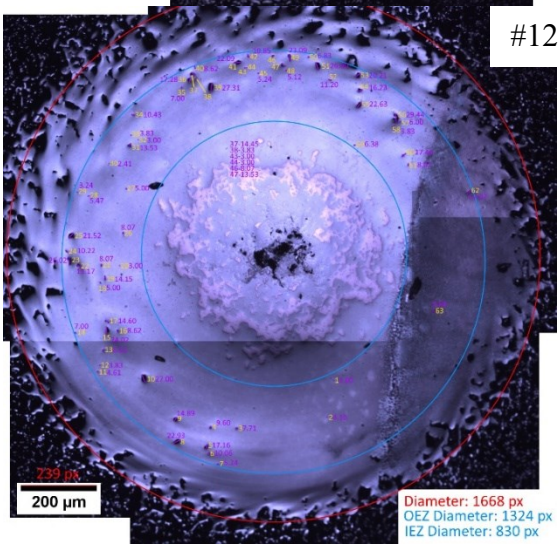
239 px
200 µm
Diameter: 1668 px
OEZ Diameter: 1324 px
IEZ Diameter: 830 px

#12

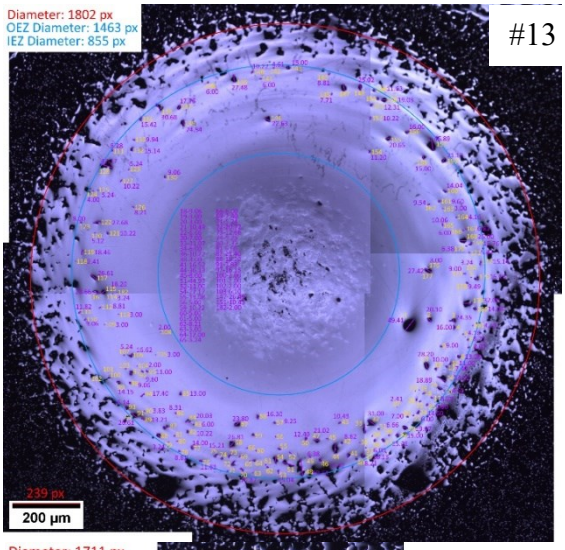

#13

#14

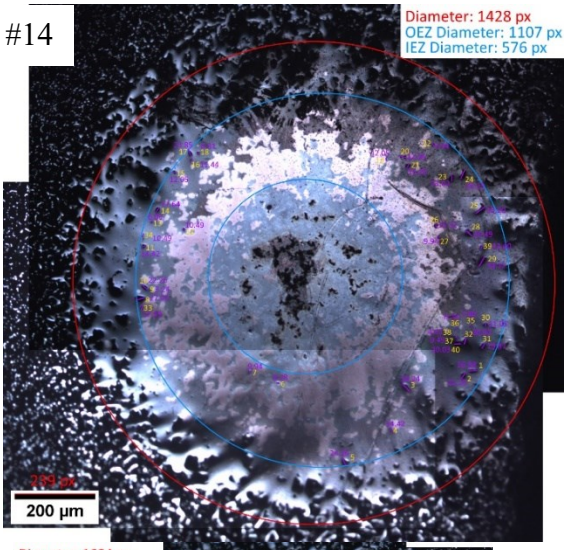

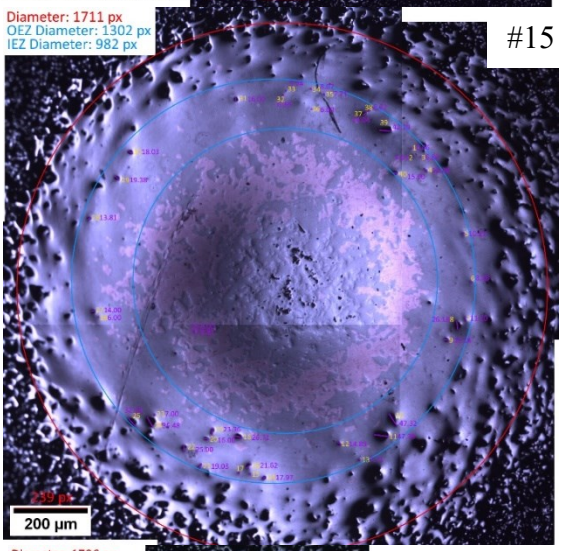

#15

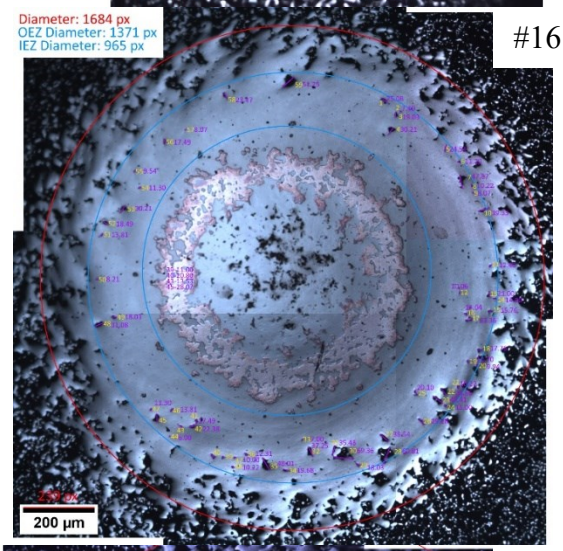

#16

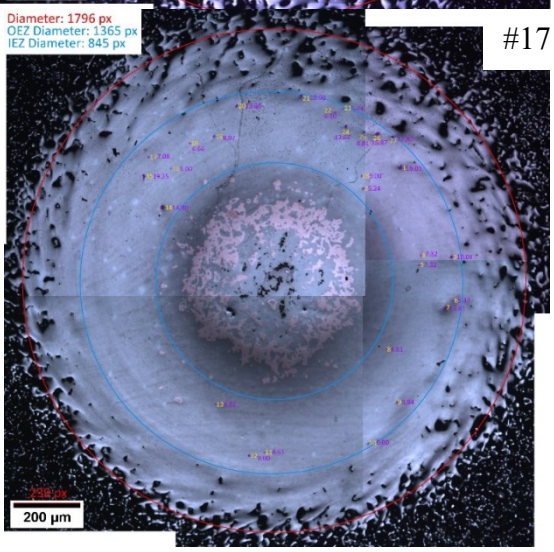

#17

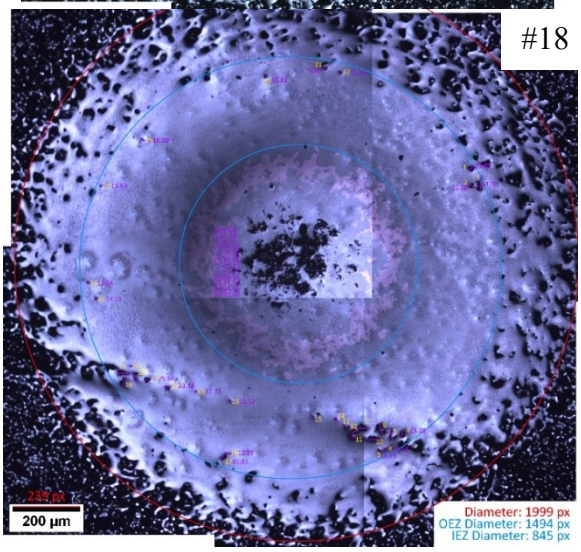

#18

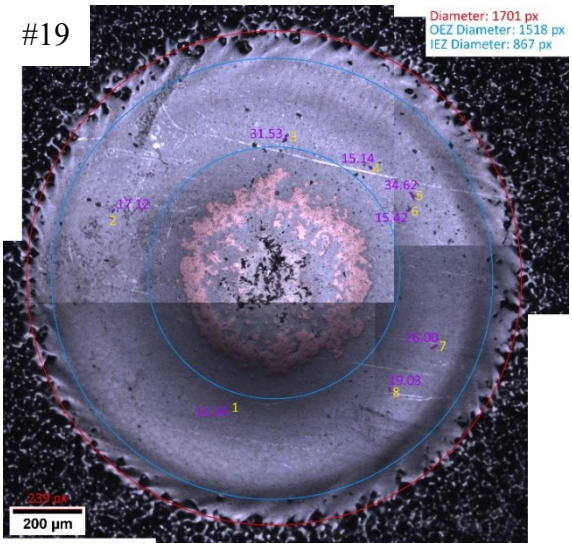

Figure B-2: Examples of dimples from all coatings.

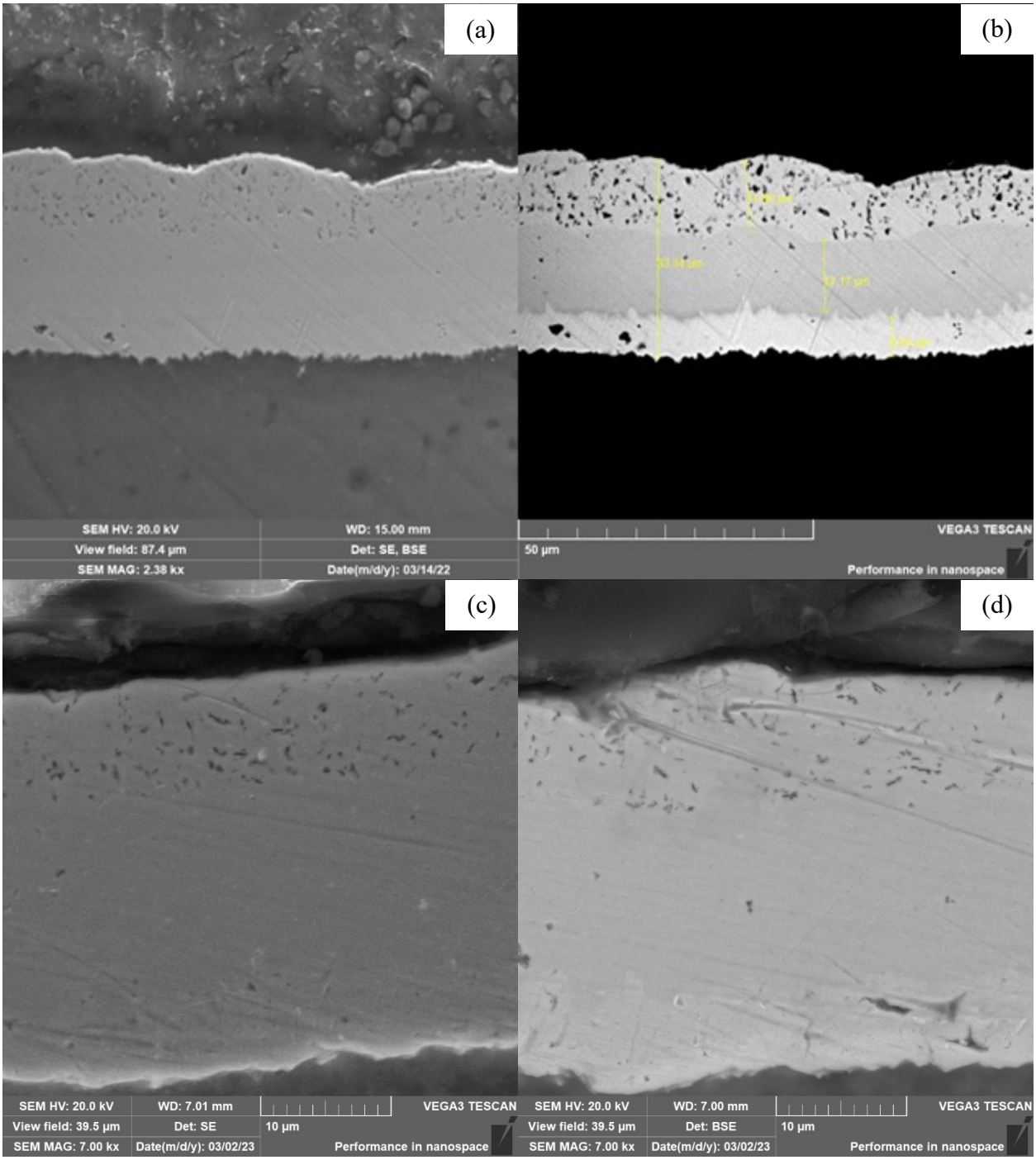

Figure B-3: SEM micrographs of first coating #3 cross section sample in a) SE and b) BSE modes and second coating #3 cross section sample in c) SE and d) BSE modes.

Appendix C: OCV, PDP, and GCPL Graphs for Immersion and Cycle Tested Samples

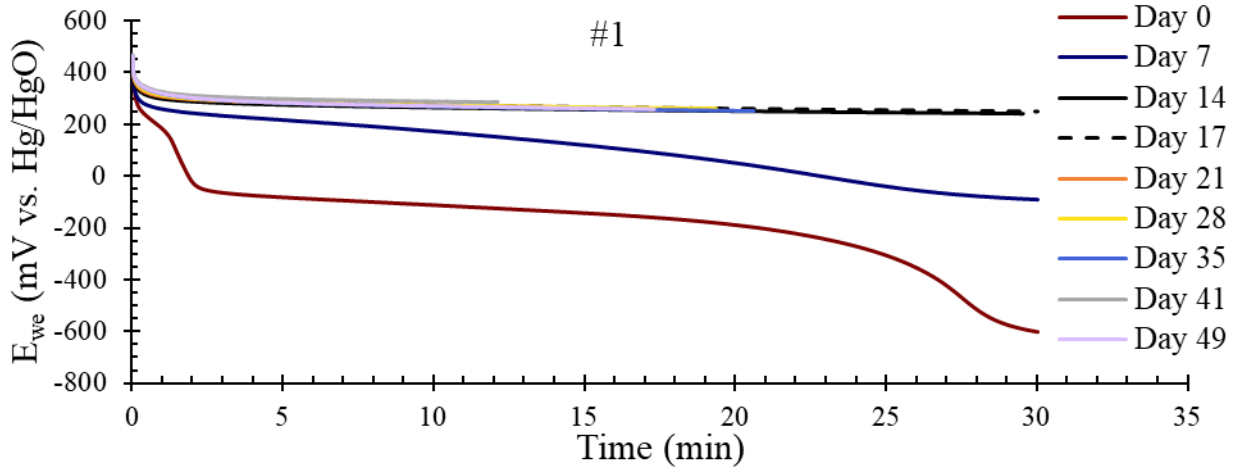

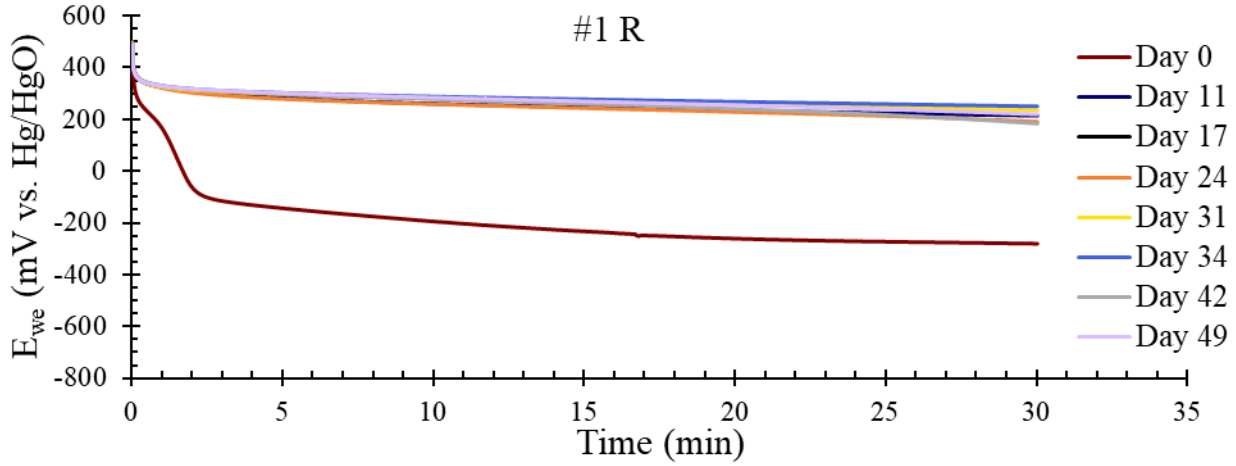

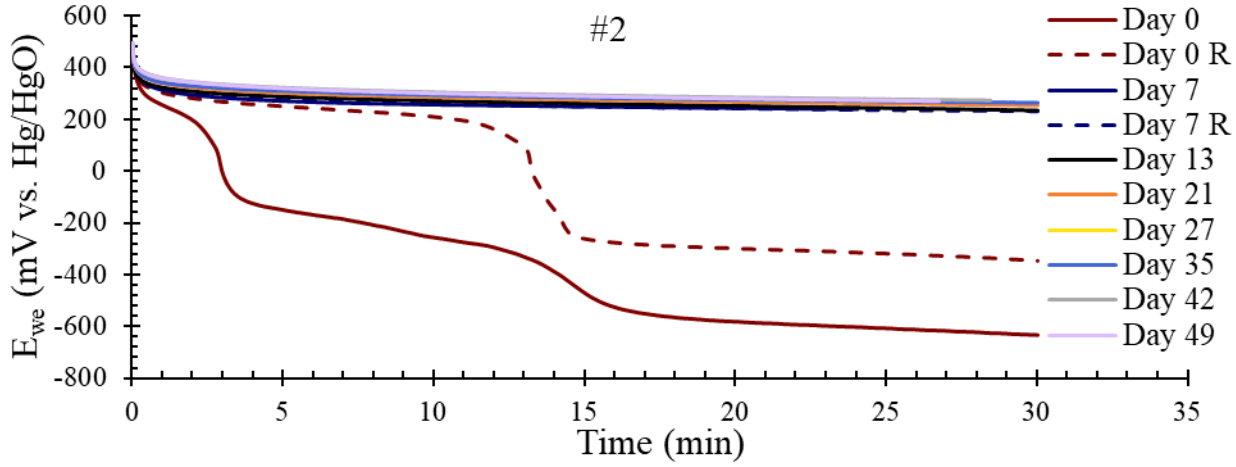

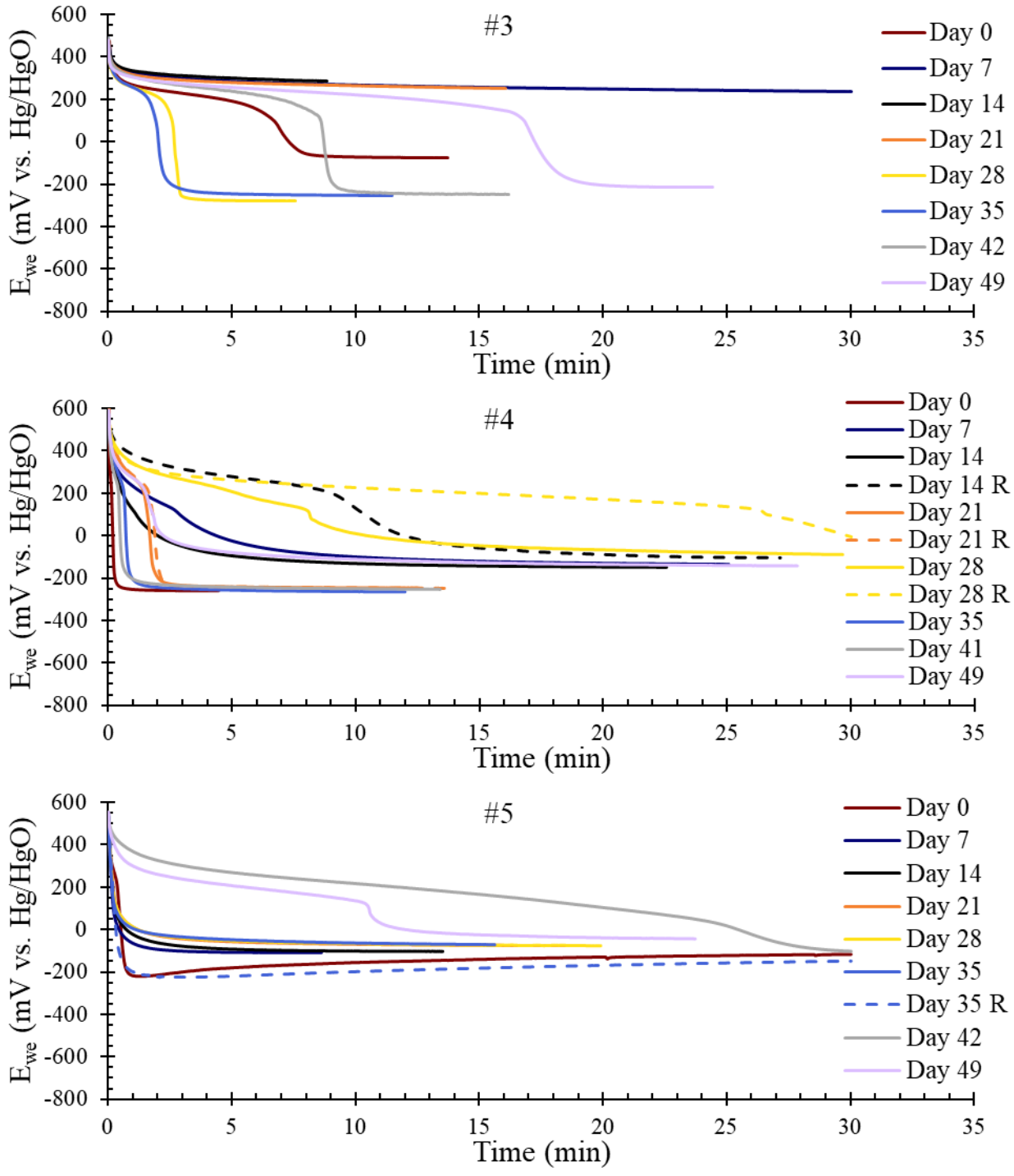

Figure C-1: OCV curves for immersion tested samples. R refers to repeat tests.

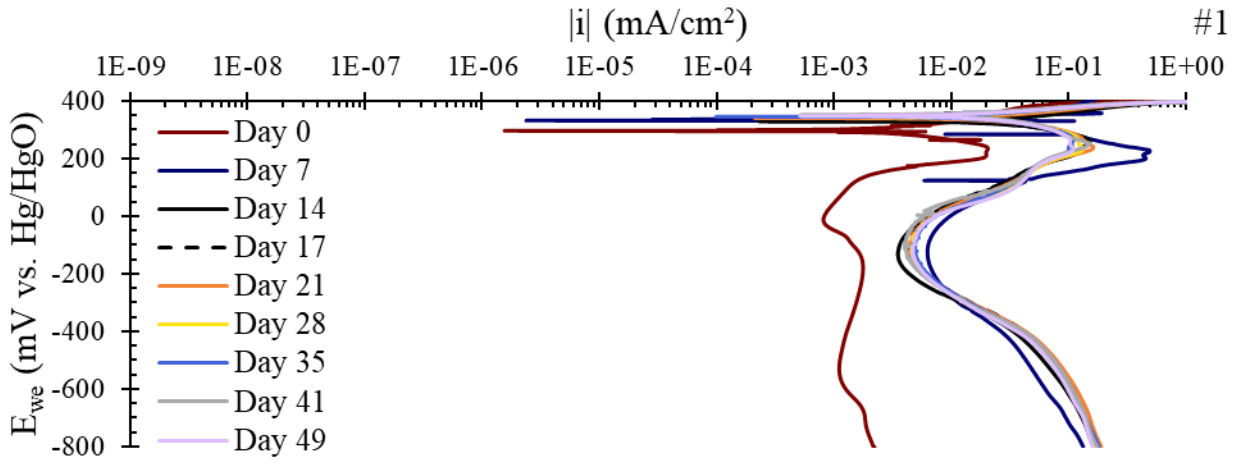
|i| (mA/cm²)
#1
1E-09
1E-08
1E-07
1E-06
1E-05
1E-04
1E-03
1E-02
1E-01
1E+00
400
200
0
-200
-400
-600
-800
E_we (mV vs. Hg/HgO)
Day 0
Day 7
Day 14
Day 17
Day 21
Day 28
Day 35
Day 41
Day 49

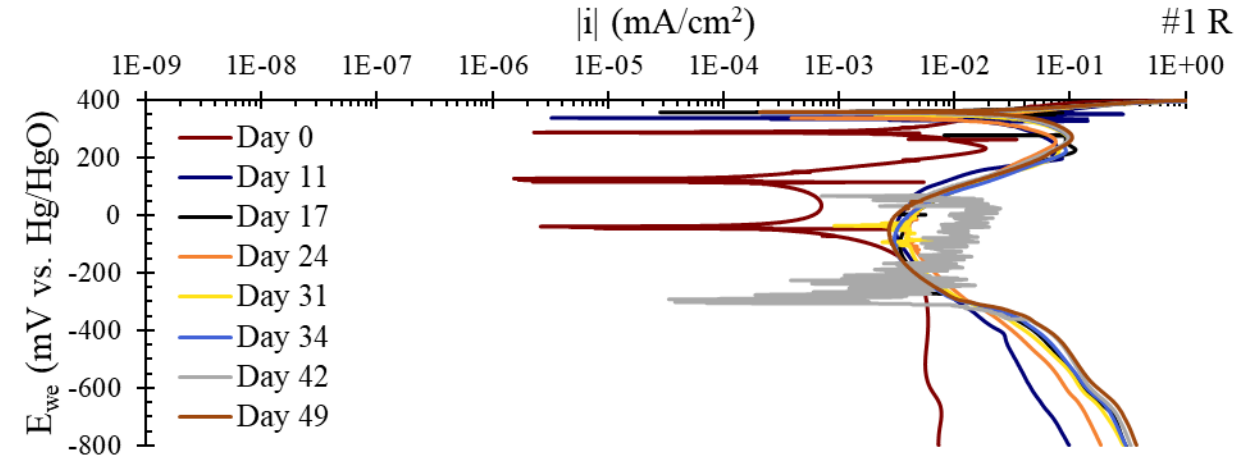
|i| (mA/cm²)
#1 R
1E-09
1E-08
1E-07
1E-06
1E-05
1E-04
1E-03
1E-02
1E-01
1E+00
400
200
0
-200
-400
-600
-800
E_we (mV vs. Hg/HgO)
Day 0
Day 11
Day 17
Day 24
Day 31
Day 34
Day 42
Day 49

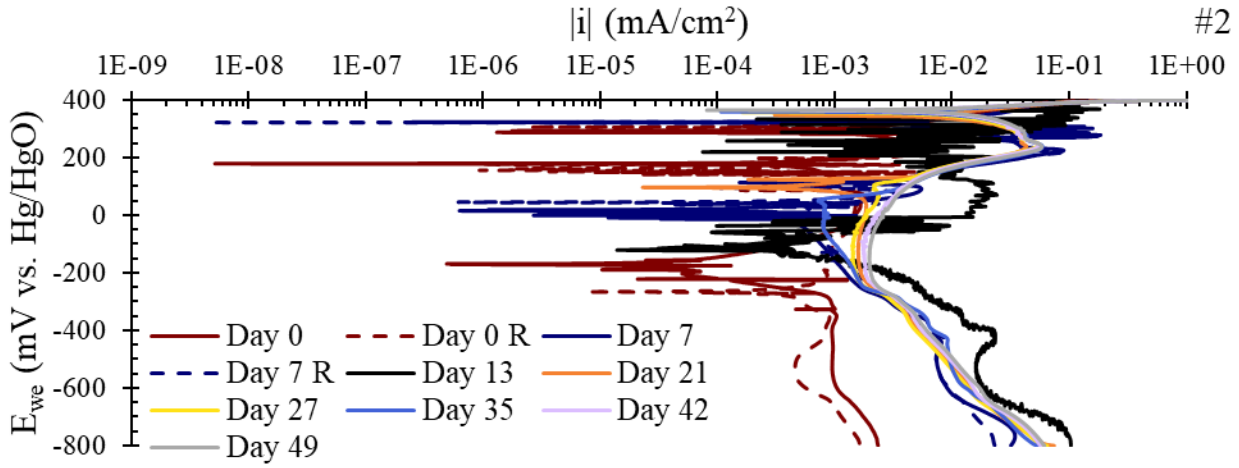
|i| (mA/cm²)
#2
1E-09
1E-08
1E-07
1E-06
1E-05
1E-04
1E-03
1E-02
1E-01
1E+00
400
200
0
-200
-400
-600
-800
E_we (mV vs. Hg/HgO)
Day 0
Day 0 R
Day 7
Day 7 R
Day 13
Day 21
Day 27
Day 35
Day 42
Day 49

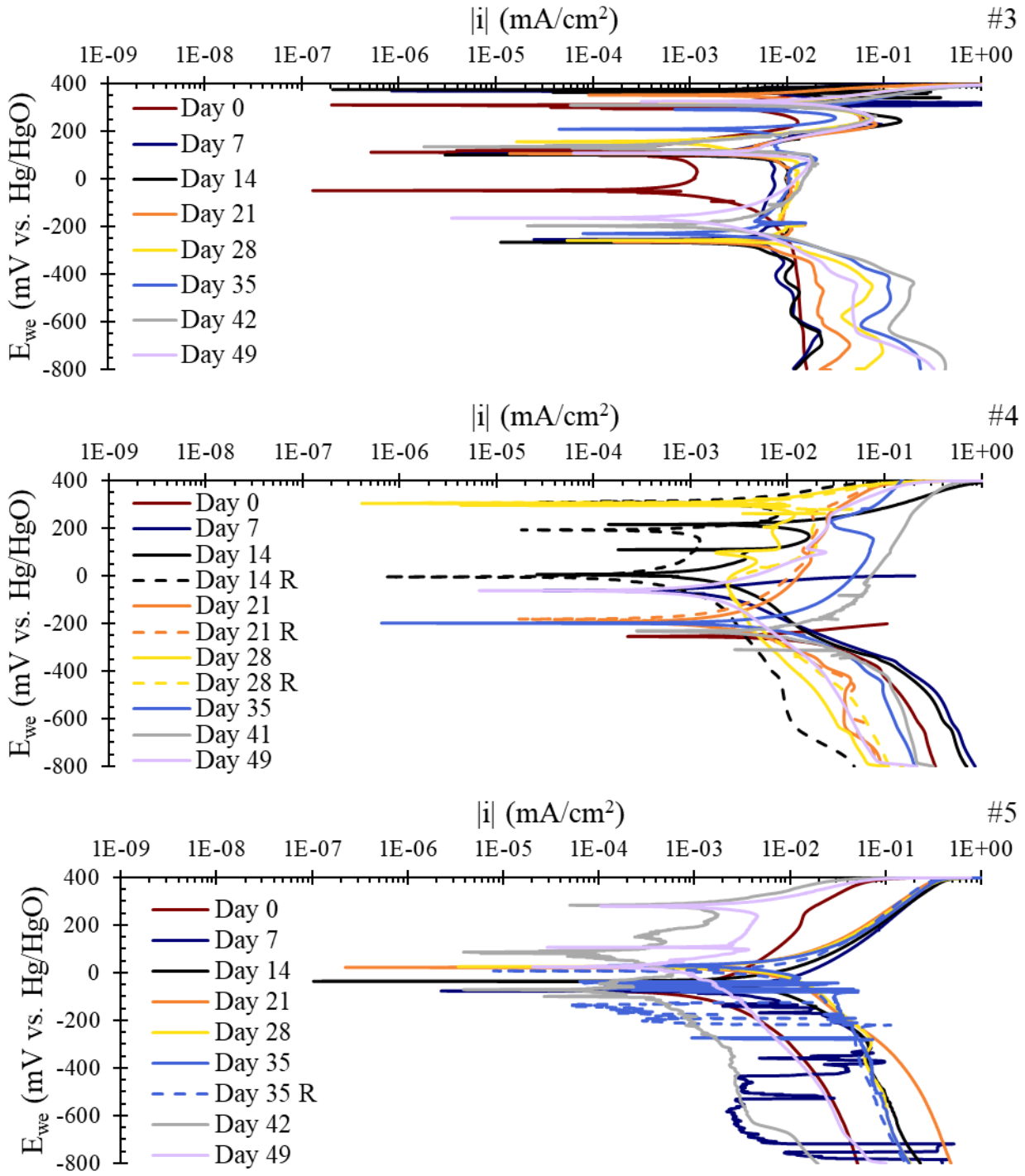

Figure C-2: PDP curves for immersion tested samples. R refers to repeat tests.

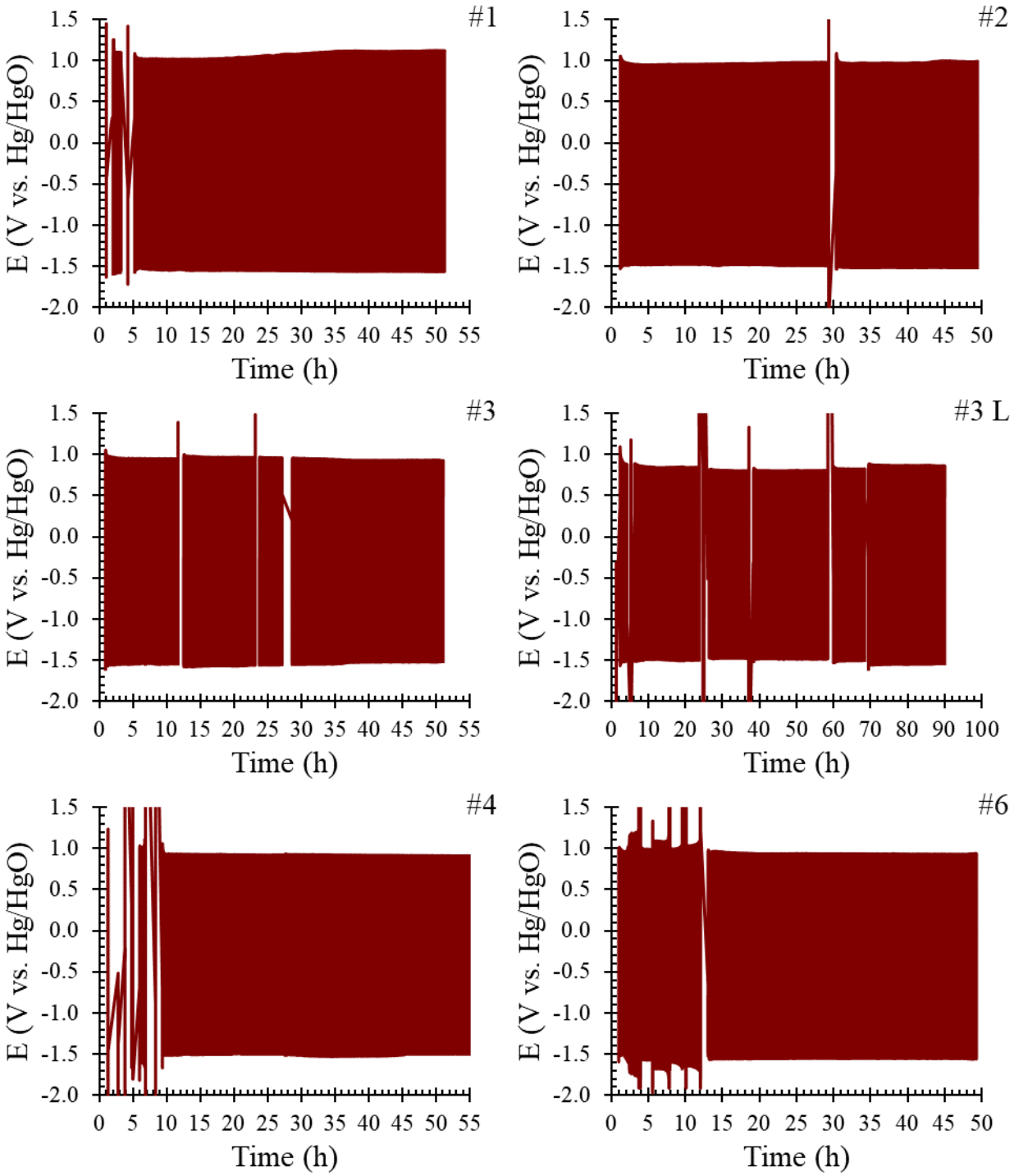
#1
#2
#3
#3 L
#4
#6
E (V vs. Hg/HgO)
Time (h)
1.5
1.0
0.5
0.0
-0.5
-1.0
-1.5
-2.0
0 5 10 15 20 25 30 35 40 45 50 55
0 5 10 15 20 25 30 35 40 45 50
0 10 20 30 40 50 60 70 80 90 100

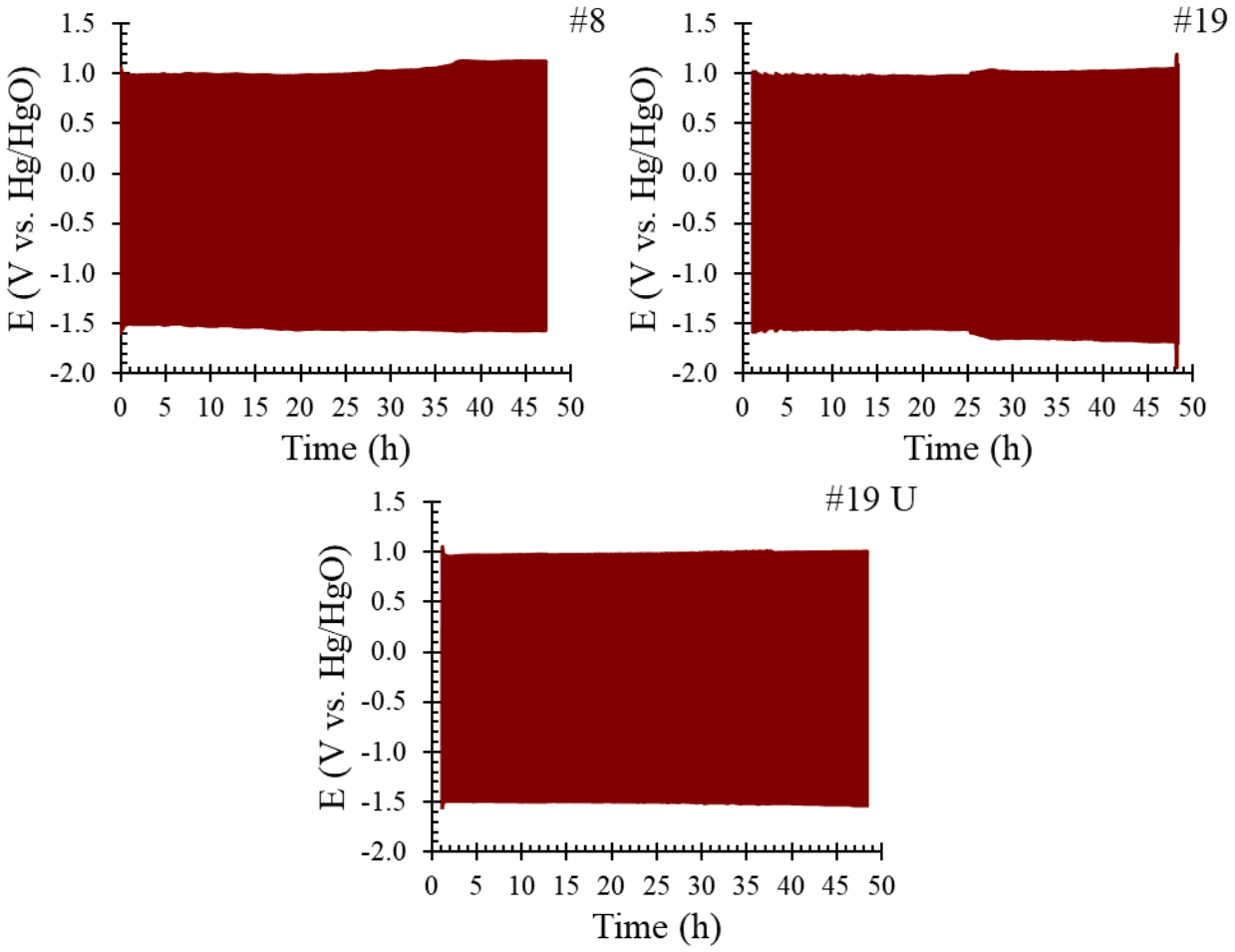

Figure C-3: GCPL test results. U denotes uncut sample and L denotes 3,359 cycle test.

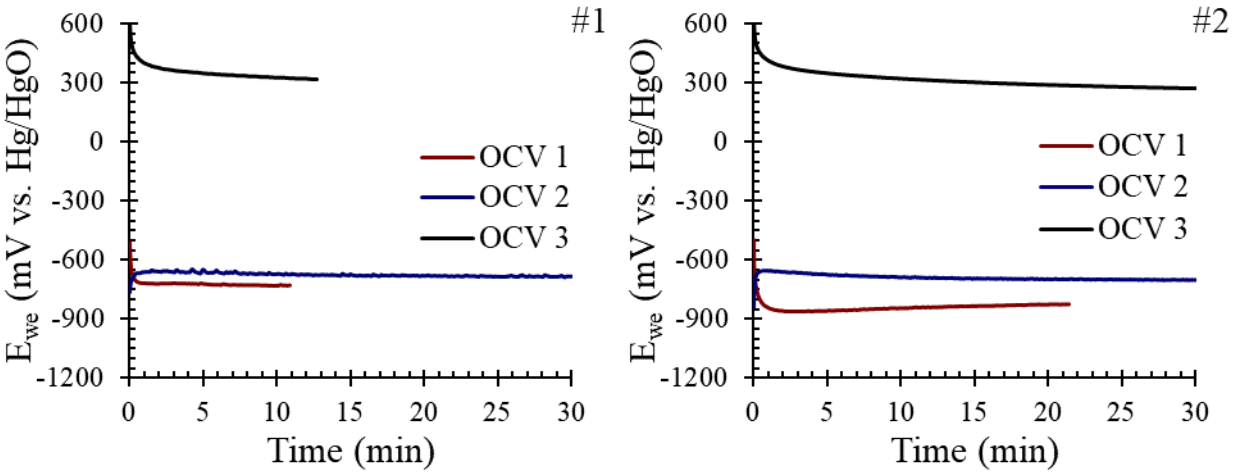

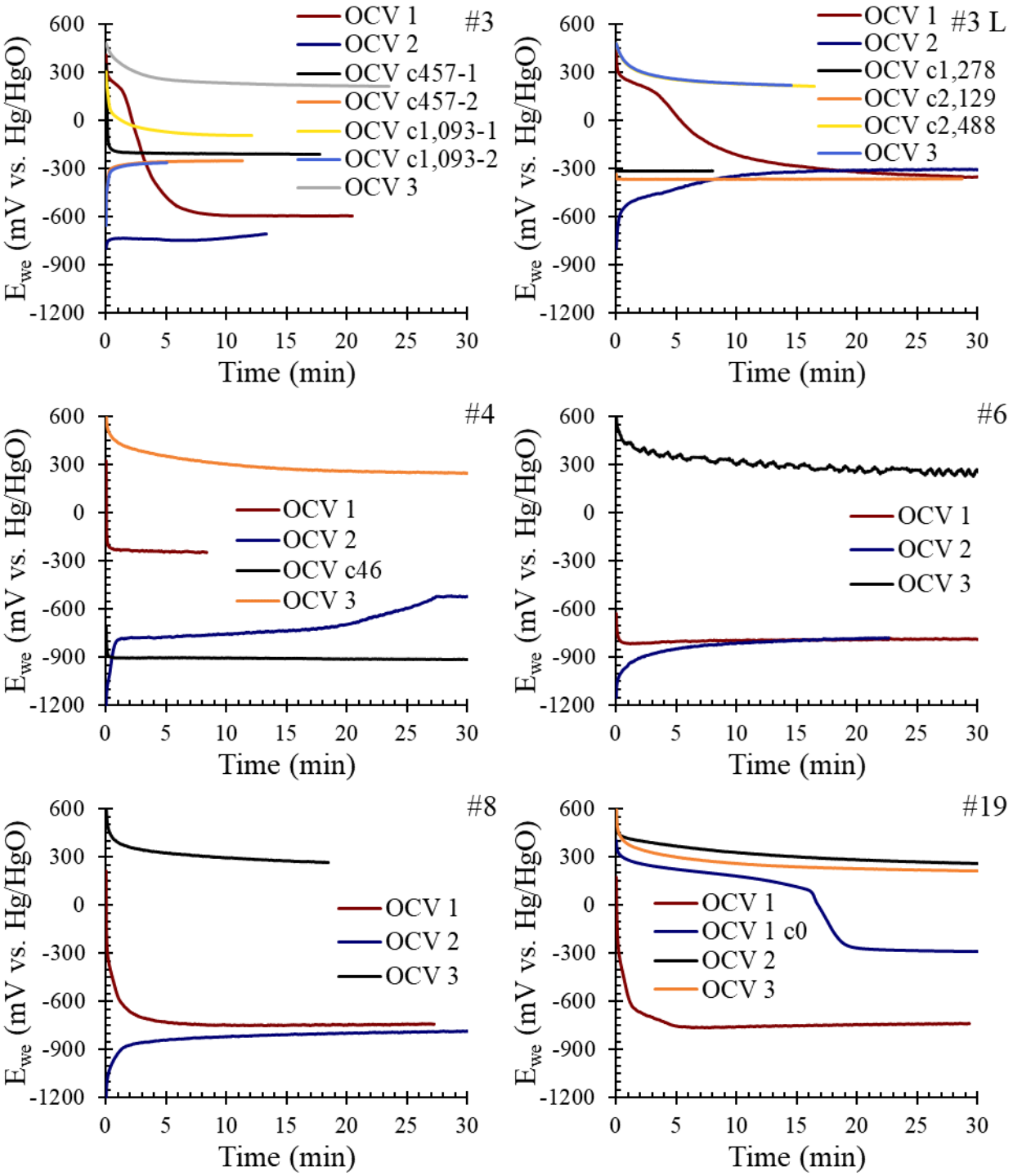
#3
OCV 1
OCV 2
OCV c457-1
OCV c457-2
OCV c1,093-1
OCV c1,093-2
OCV 3
#3 L
OCV 1
OCV 2
OCV c1,278
OCV c2,129
OCV c2,488
OCV 3
#4
OCV 1
OCV 2
OCV c46
OCV 3
#6
OCV 1
OCV 2
OCV 3
#8
OCV 1
OCV 2
OCV 3
#19
OCV 1
OCV 1 c0
OCV 2
OCV 3
E_we (mV vs. Hg/HgO)
Time (min)

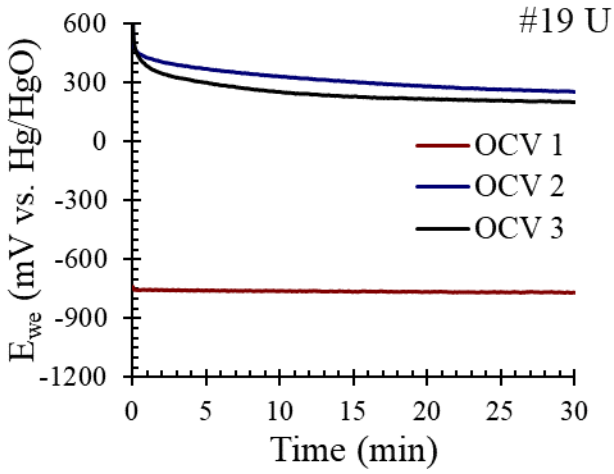

Figure C-4: OCV curves for cycle tested samples. Note that c stands for cycle number, _-1 and _-2 refer to before and after PDP measurement conducted at the cycle number, U denotes uncut sample, and L denotes 3,359 cycle test.

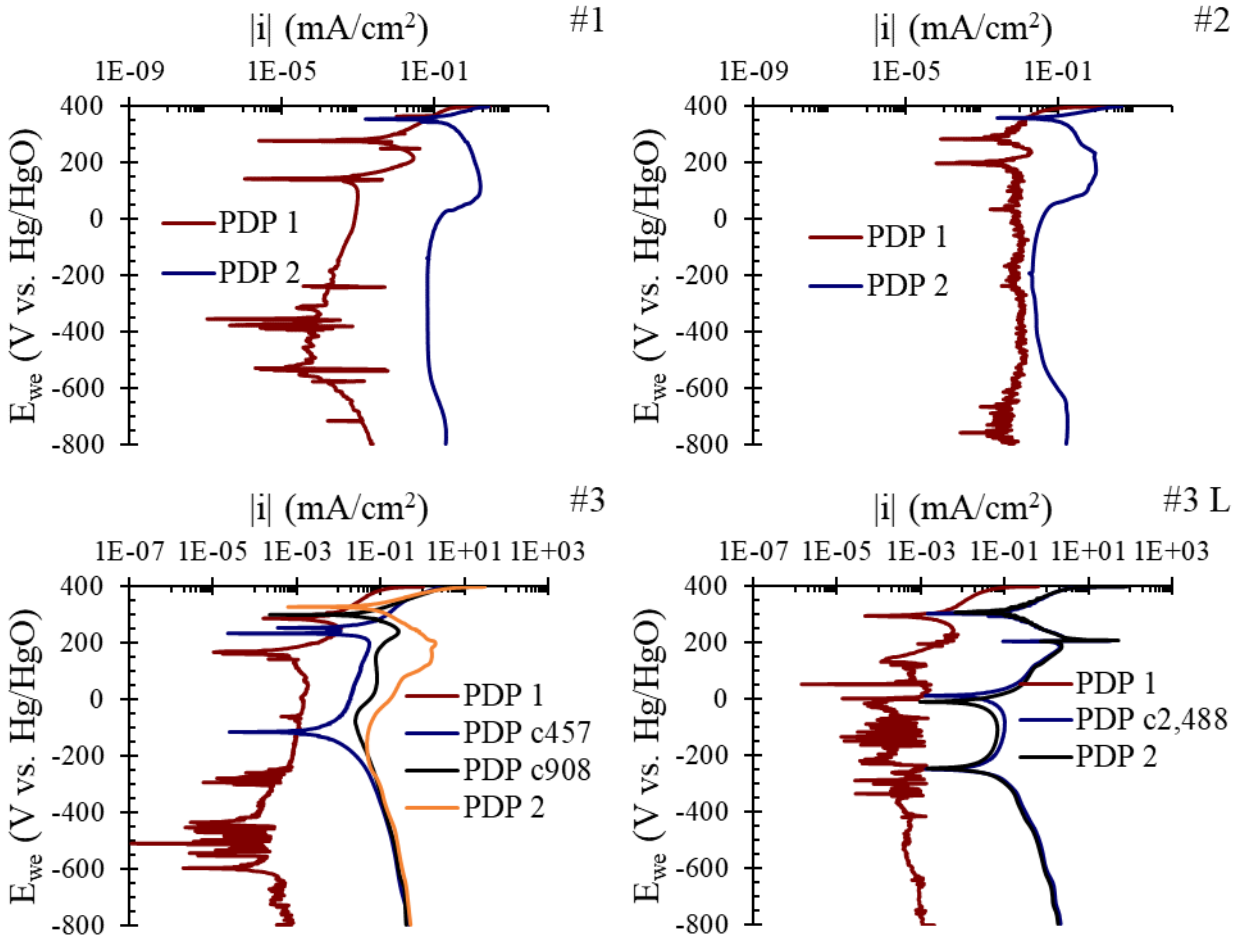

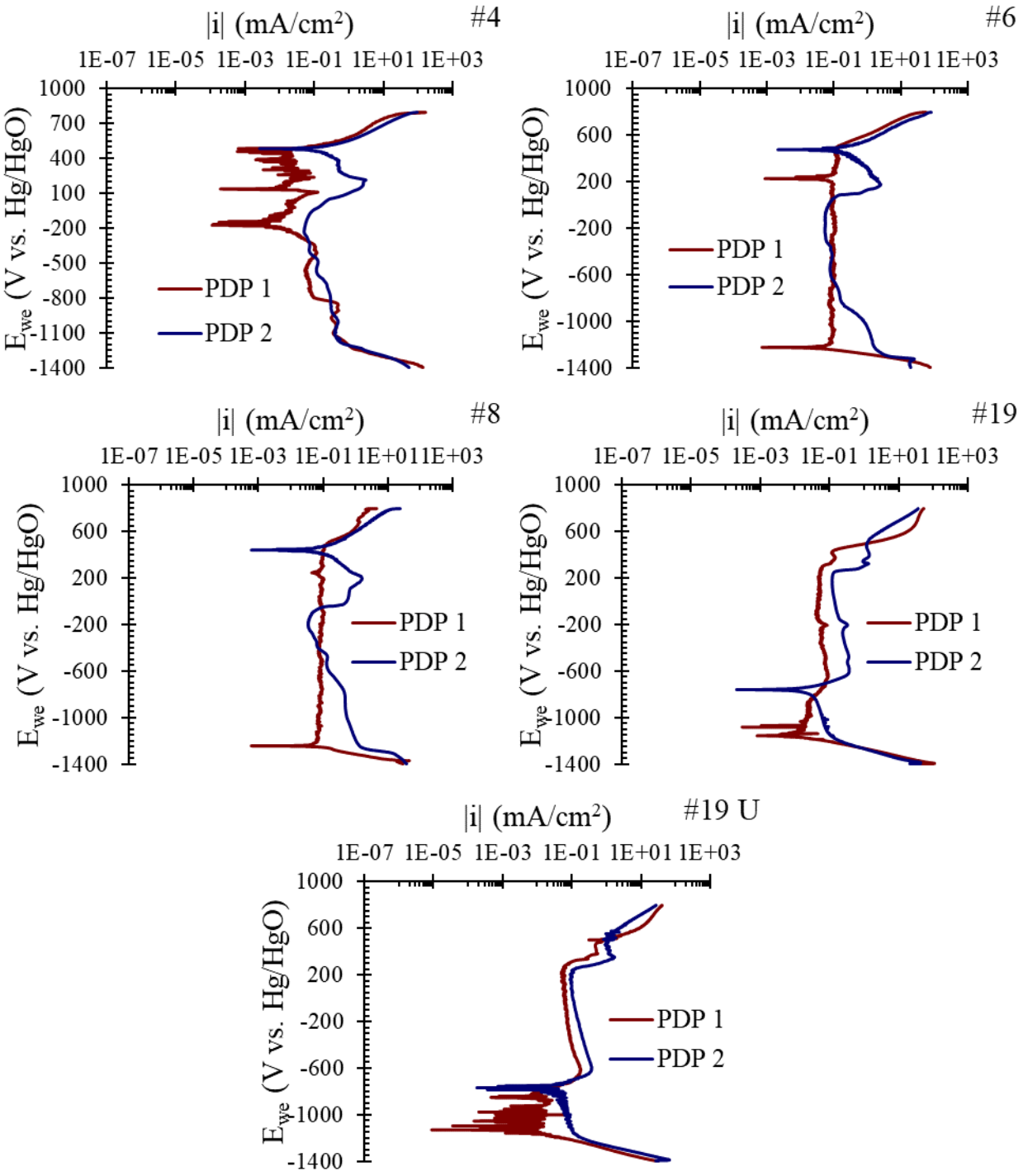

Figure C-5: PDP curves for cycle tested samples. Note that c denotes cycle number, U denotes an uncut sample, and L denotes 3,359 cycle test.

Appendix D: Plan View and Cross Section Micrographs of Ni Deposits

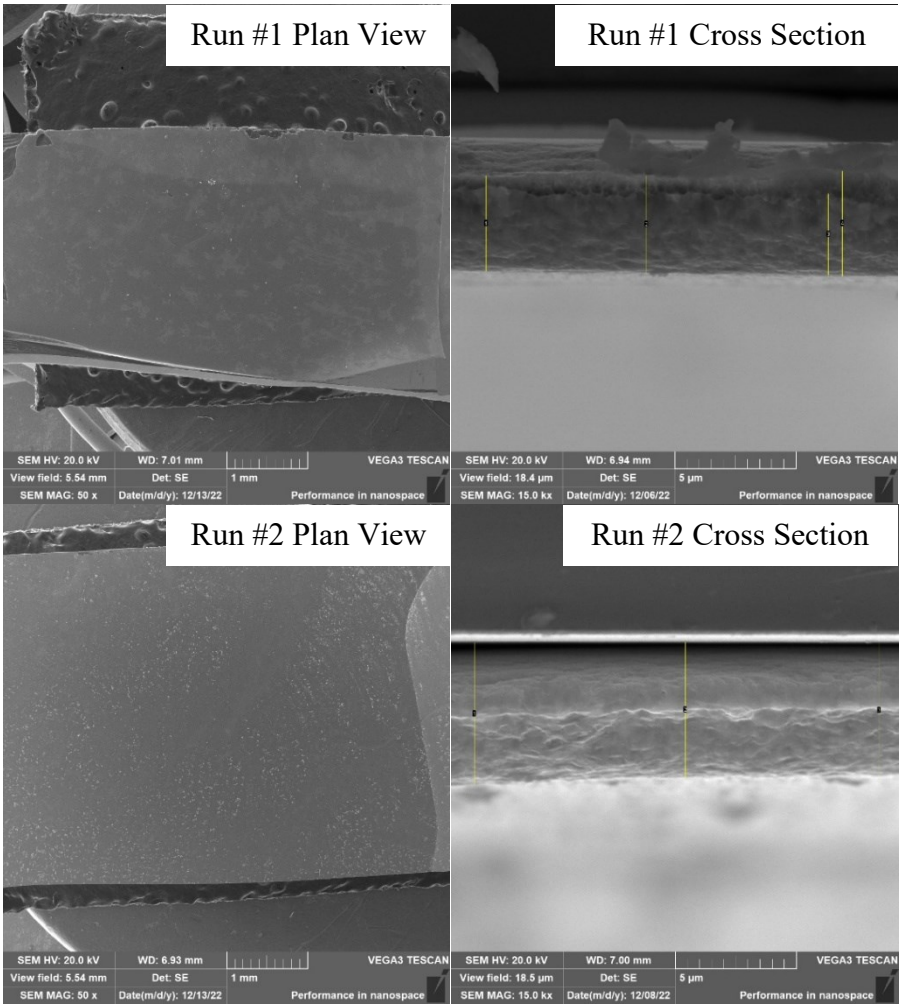

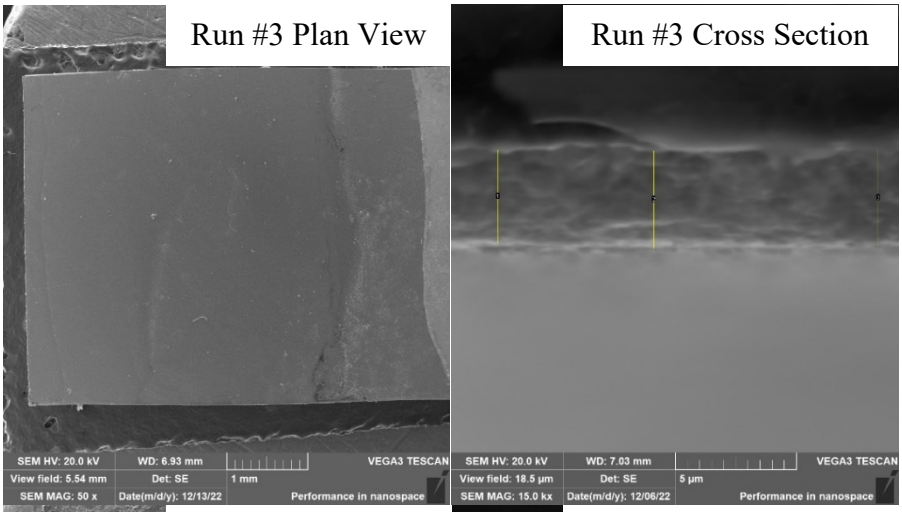
Run #3 Plan View
SEM HV: 20.0 kV
WD: 6.93 mm
VEGA3 TESCAN
View field: 5.54 mm
Det: SE
1 mm
SEM MAG: 50 x
Date(m/d/y): 12/13/22
Performance in nanospace

Run #3 Cross Section
SEM HV: 20.0 kV
WD: 7.03 mm
VEGA3 TESCAN
View field: 18.5 µm
Det: SE
5 µm
SEM MAG: 15.0 kx
Date(m/d/y): 12/06/22
Performance in nanospace

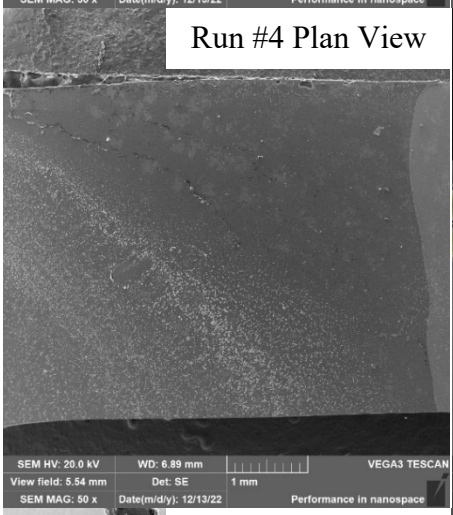
Run #4 Plan View
SEM HV: 20.0 kV
WD: 6.89 mm
VEGA3 TESCAN
View field: 5.54 mm
Det: SE
1 mm
SEM MAG: 50 x
Date(m/d/y): 12/13/22
Performance in nanospace

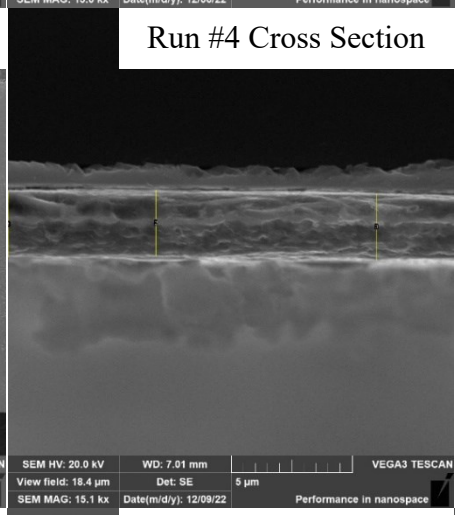
Run #4 Cross Section
SEM HV: 20.0 kV
WD: 7.01 mm
VEGA3 TESCAN
View field: 18.4 µm
Det: SE
5 µm
SEM MAG: 15.1 kx
Date(m/d/y): 12/09/22
Performance in nanospace

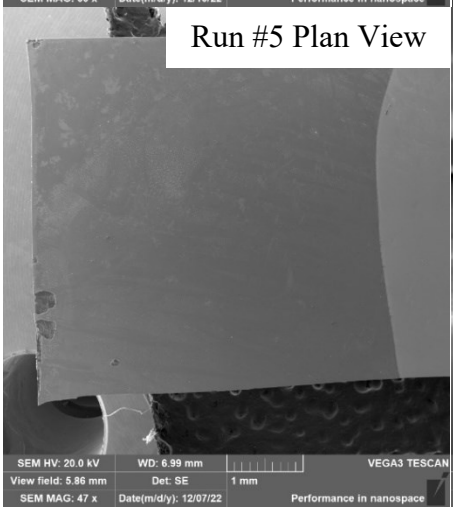
Run #5 Plan View
SEM HV: 20.0 kV
WD: 6.99 mm
VEGA3 TESCAN
View field: 5.86 mm
Det: SE
1 mm
SEM MAG: 47 x
Date(m/d/y): 12/07/22
Performance in nanospace

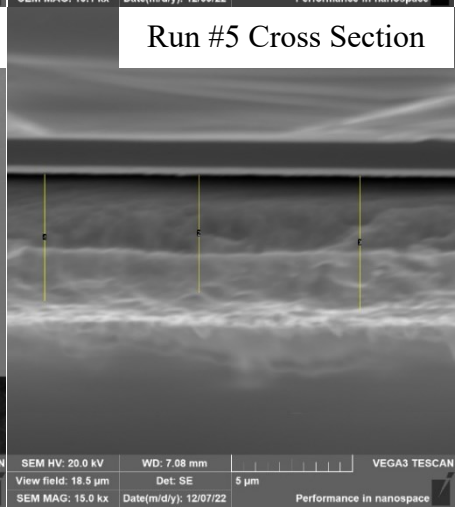
Run #5 Cross Section
SEM HV: 20.0 kV
WD: 7.08 mm
VEGA3 TESCAN
View field: 18.5 µm
Det: SE
5 µm
SEM MAG: 15.0 kx
Date(m/d/y): 12/07/22
Performance in nanospace

Run #6 Plan View

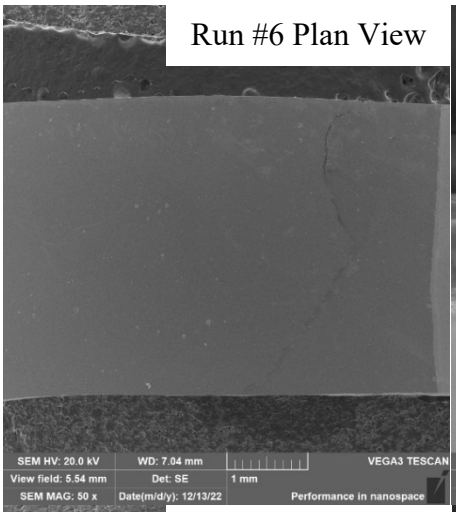

Run #6 Cross Section

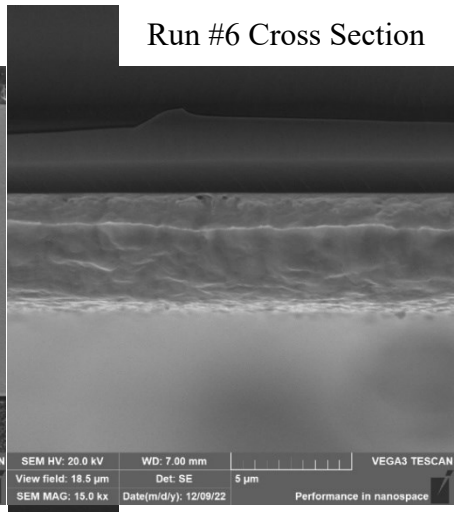

Run #7 Plan View

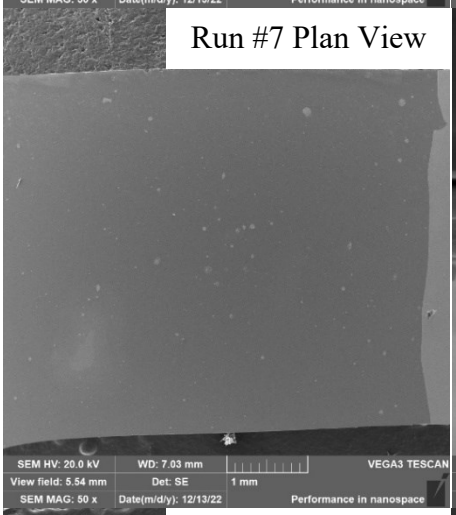

Run #7 Cross Section

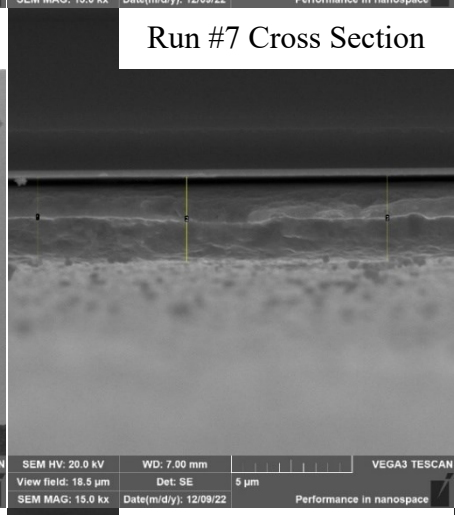

Run #8 Plan View

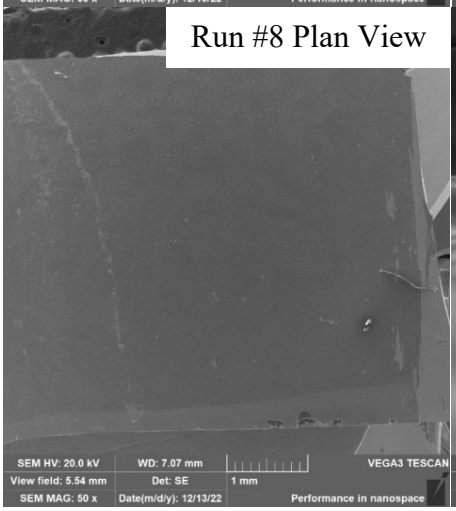

Run #8 Cross Section

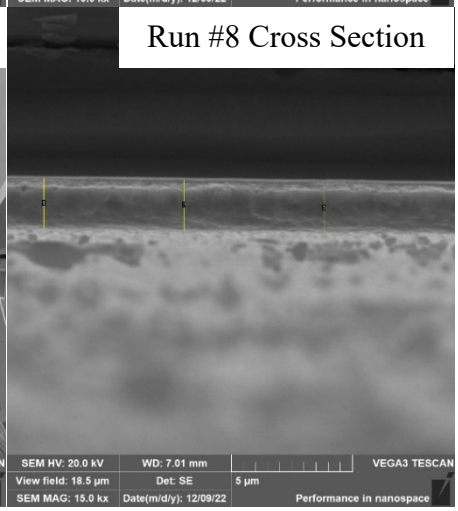

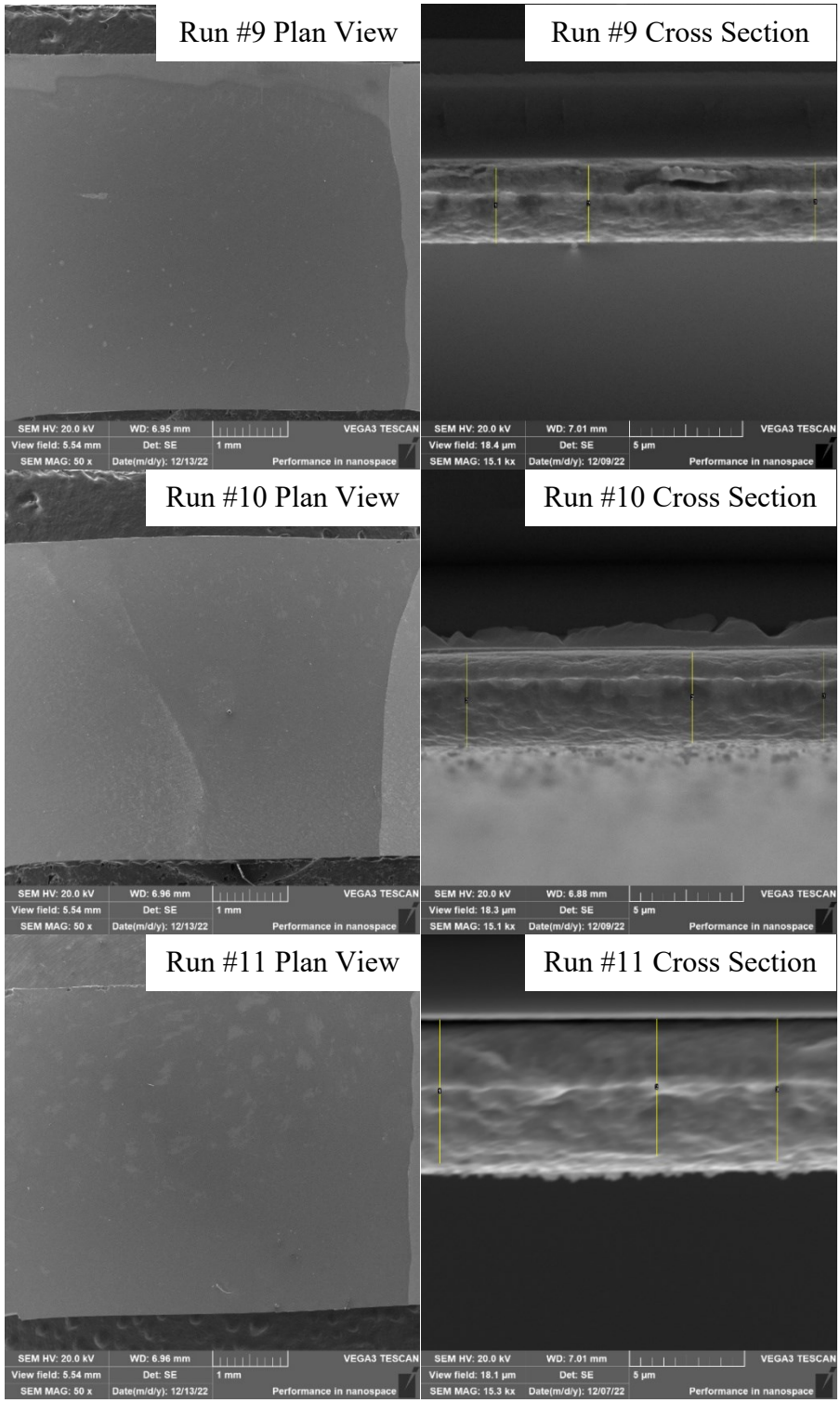
Run #9 Plan View
Run #9 Cross Section
Run #10 Plan View
Run #10 Cross Section
Run #11 Plan View
Run #11 Cross Section

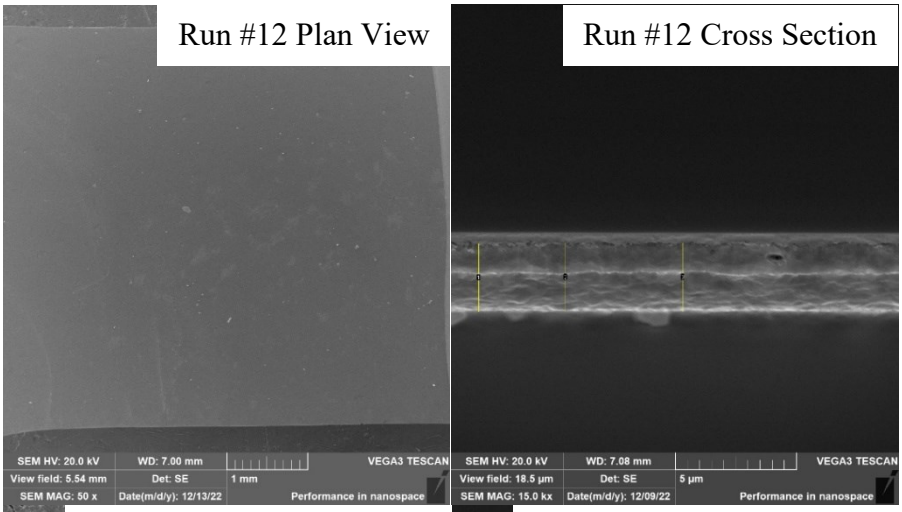
Run #12 Plan View
SEM HV: 20.0 kV
WD: 7.00 mm
VEGA3 TESCAN
View field: 5.54 mm
Det: SE
1 mm
SEM MAG: 50 x
Date(m/d/y): 12/13/22
Performance in nanospace

Run #12 Cross Section
SEM HV: 20.0 kV
WD: 7.08 mm
VEGA3 TESCAN
View field: 18.5 µm
Det: SE
5 µm
SEM MAG: 15.0 kx
Date(m/d/y): 12/09/22
Performance in nanospace

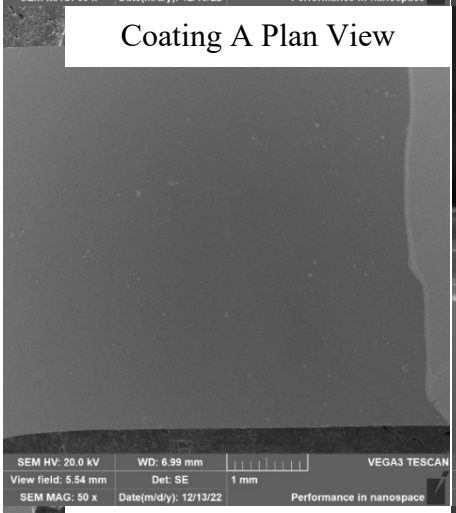
Coating A Plan View
SEM HV: 20.0 kV
WD: 6.99 mm
VEGA3 TESCAN
View field: 5.54 mm
Det: SE
1 mm
SEM MAG: 50 x
Date(m/d/y): 12/13/22
Performance in nanospace

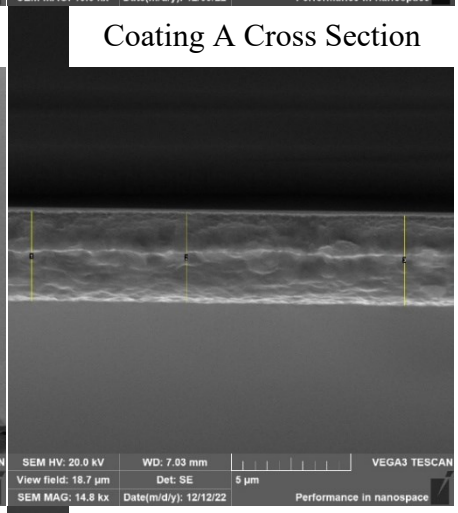
Coating A Cross Section
SEM HV: 20.0 kV
WD: 7.03 mm
VEGA3 TESCAN
View field: 18.7 µm
Det: SE
5 µm
SEM MAG: 14.8 kx
Date(m/d/y): 12/12/22
Performance in nanospace

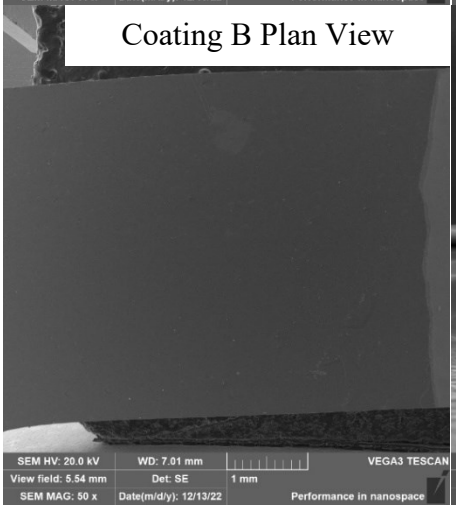
Coating B Plan View
SEM HV: 20.0 kV
WD: 7.01 mm
VEGA3 TESCAN
View field: 5.54 mm
Det: SE
1 mm
SEM MAG: 50 x
Date(m/d/y): 12/13/22
Performance in nanospace

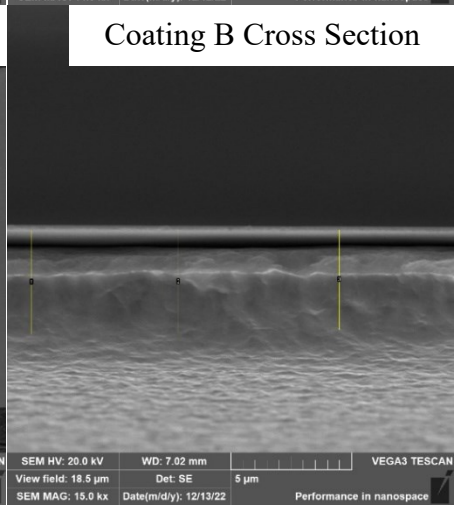
Coating B Cross Section
SEM HV: 20.0 kV
WD: 7.02 mm
VEGA3 TESCAN
View field: 18.5 µm
Det: SE
5 µm
SEM MAG: 15.0 kx
Date(m/d/y): 12/13/22
Performance in nanospace

Coating C Plan View

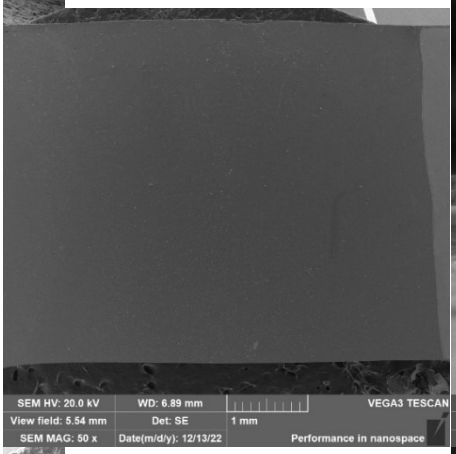

Coating C Cross Section

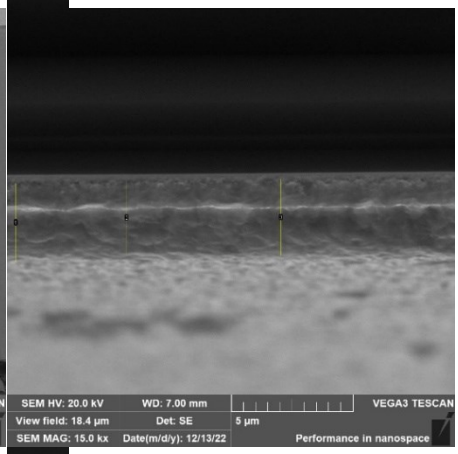

Coating D Plan View

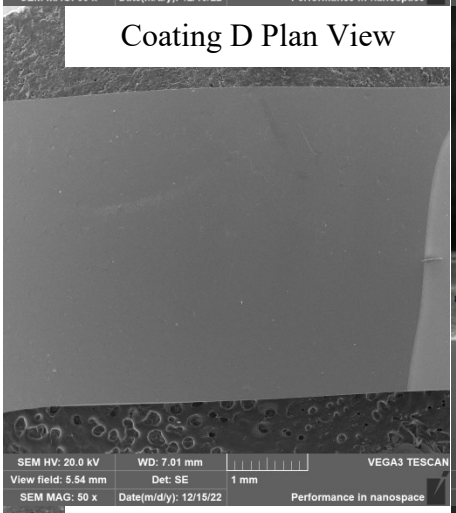

Coating D Cross Section

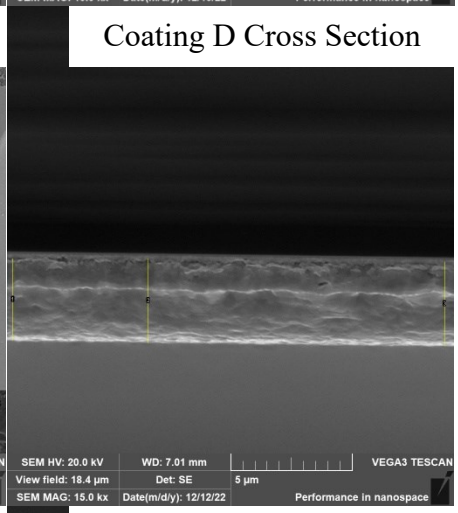

Coating E Plan View

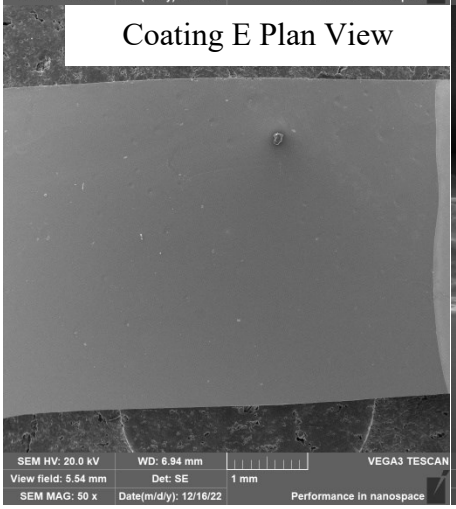

Coating E Cross Section

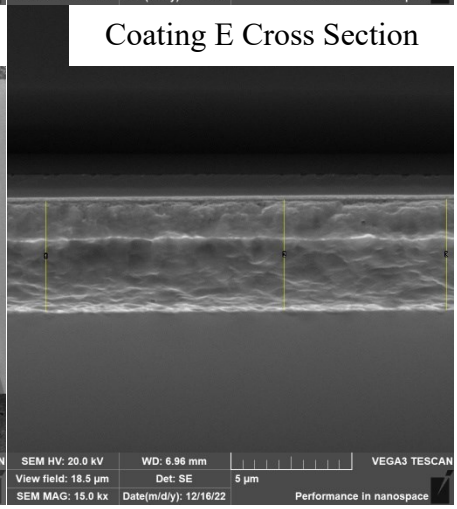

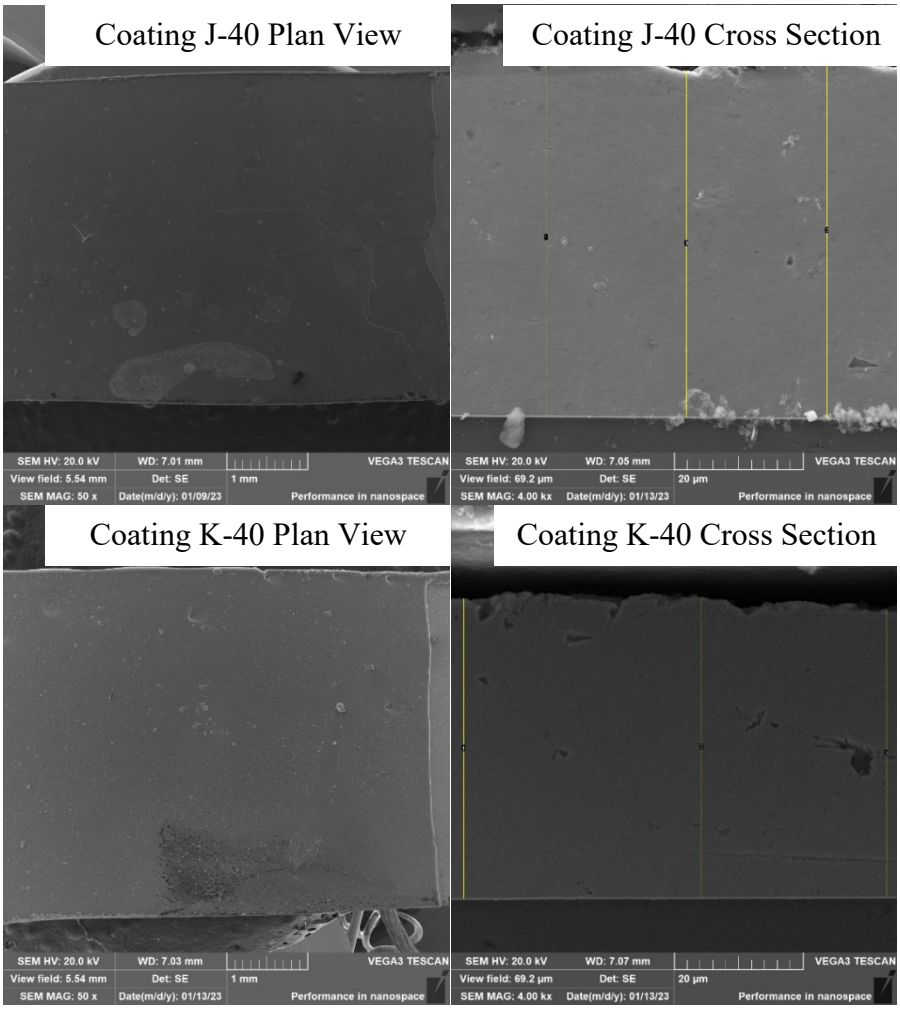

Figure D-1: Examples of plan view (left) and thickness measurements (right) for all Ni coatings.